Diverse applications of glucose derived functionalized carbon nanostructures

A thesis submitted for the degree of

Doctor of Philosophy

By

Dinesh Jagadeesan

Chemistry and Physics of Materials Unit

Jawaharlal Nehru Centre for Advanced Scientific Research

(A Deemed University)

Bangalore, India.

July 2009


Dedicated to my
parents and teachers

DECLARATION

I hereby declare that the matter embodied in the thesis entitled "**Diverse** A**pplications of glucose derived functionalized carbon nanostructures**" is the result of investigations carried out by me at the Chemistry and Physics of Materials Unit, Jawaharlal Nehru Centre for Advanced Scientific Research, India under the supervision of Dr. M. Eswaramoorthy and that it has not been submitted elsewhere for the award of any degree or diploma.

In keeping with the general practice in reporting the scientific observations, due acknowledgement has been made whenever the work described is based on the findings of other investigators. Any omission that might have occurred due to oversight or error in judgement is regretted.

Dinesh Jagadeesan

CERTIFICATE

I hereby certify that the work described in this thesis entitled "**Diverse** a**pplications of glucose derived functionalized carbon nanostructures**" has been carried out by Mr. Dinesh Jagadeesan under my supervision at the Chemistry and Physics of Materials Unit, Jawaharlal Nehru Centre for Advanced Scientific Research, India and that it has not been submitted elsewhere for the award of any degree or diploma.

Dr. Eswaramoorthy Muthusamy

(Research Supervisor)

ACKNOWLEDGEMENTS

It is my pleasure to acknowledge the valuable support extended by many people during my research at JNCASR.

One of many things that I would fondly cherish about JNCASR is my interactions with Prof. C. N. R. Rao. Though my interactions with him were brief, its impact would be everlasting. I thank Prof. C. N. R. Rao for the passion he ignited in me for excellence. I am grateful to him for the interests that he had shown in my research work from time to time in the form of many valuable suggestions. I consider it an honour to have worked with him on a few research problems and co-authored three publications.

I thank my research supervisor Dr. M. Eswaramoorthy who has the credit of introducing me into the world of research. I must admit that the academic freedom that I enjoyed under his supervision helped me to learn beyond the conventional. His constant interactions especially during manuscript preparation had often put me back to the working bench. But I do realize it to be the best way to achieve perfection in science - my sincere thanks to him for the opportunity.

I thank the following faculties namely Prof. G. U. Kulakrni, Prof. S. Balasubramanyam, Prof. A. Sundaresan of CPMU, Prof. S. K. Pati of TSU and Prof. N. Ravishankar of MRC, (IISc) for their courses during my first year. I thank Prof. S. M. Shivprasad, Prof. N. Chandrabhas, Dr. A. Govindaraj, Dr. T. Maji and Prof. K. S. Narayan for useful discussions on various topics. I also thank Prof. Umesh Waghmare of TSU, whose counsel and cooperation was valuable during my tenure as a student member of security advisory committee.

I thank Prof. A. Sundaresan, Dr. V. K. Mangalam, Mr. Pranab and Mr. Madhu for magnetic measurements and useful discussions. I also thank Ms. A. Gomathi and Mr. V. P.

Bhat for helping me with Raman spectroscopy measurements; Mr. Gopal, Dr. T. Bhuvana and Ms. B. Radha for their help in using the microscopes.

I sincerely thank Prof. T. K. Kundu with whom we collaborated on the intracellular trafficking using nanomaterials. He had been generous in allowing me to get trained in his lab for few months in cell culture. I also thank his student Ms. R. Selvi for her time and guidance in my training and other lab members of transcription and disease lab (MBGU) for their cooperation. I thank Prof. M. S. Inamdar, Dr. Kavitha Siva and Ms. Parvathy of vascular biology lab (MBGU) for their help in biocompatibility studies on bioactive glass.

I thank the timely help of the technical staff namely Ms. N. R. Selvi (for FESEM), Mrs. T. Usha (for TEM), Mr. Vasu (for UV, PL, IR, TGA), Mr. Anil (for XRD), Mr. Basavaraj (for SEM), Mrs. B. S. Suma (for Confocal microscope), Mr. Srinath, Mr. Srinivasa Rao and Mr. Srinivas (for technical assistance). The assistance provided by Mr. Arokianathan, Mr. Moorthy and Mr. Sunil is also appreciated.

The services provided by JNCASR library, complab, academics and administration were indispensible. I have also used the facilities of IISc Library, SERC and National Nanoscience Initiative during my research work. In particular, I would like to thank Mr. Amit of Nanocentre, whom I will ever remember for his wonderful work attitude.

I thank my friends Mr. Sanil (Liverpool), Mr. A. Trishul (IITM), Mr. R. Sridharan (Cambridge), Dr. V. Ramanathan (Seoul), Dr. Venkat (IISc), Dr. S. Angapanne (CLCR), Dr. K. P. K. Menon, Mr. K. L. Gurunatha, (Toulouse), Mr. S. Rajashekarayya (Bristol) and Mr. Sandeep (NIMS) for sending me the pdf versions of research articles not subscribed at JNCASR.

I also thank all my lab mates Mr. Saikrishna, Mr. K. K. R. Datta, Mr. Kalyan and Mr. Piyush for their cooperation and help. I also acknowledge all the visiting scientists and students (POCE and SRF) for their contributions.

I thank my seniors Dr. G. V. Pavan, Dr. R. Thomas, Dr. A. Dutta and Dr. A. Thirumurugan for useful discussions on my research problems. Cheers to all my friends who gave me company in treats and tours – the best part of my stay here.

My heartfelt gratitude to my guru Bhagwan Sri Sathya Sai Baba without whose blessings, I would not have achieved this. The good will and encouragement of my brother and sister in law, sacrifices and struggles of my parents have helped me to stay focus on my goal and I pray to remain worthy of their love. This thesis is a humble offering to my parents and teachers.

In the end, I would say that Ph.D life was a roller-coaster filled with ups and downs. Nevertheless, the ride was fun and I thank the company of all those who made it a memorable one.

PREFACE

This thesis presents the diverse applications of carbon nanostructures which are rich in surface functional groups like –COOH, -CHO and –OH and are derived from glucose by hydrothermal route. Unlike other carbon materials, they do not require any further chemical treatment to functionalize the surface. The synthesis does not involve any toxic reagents and therefore can be applied to various applications in biology too.

The chapter 1 introduces the carbon nanostructures, their properties and mechanistic studies that have been performed by us and other workers in this field. Further the use of functional carbon nanostructures as templates to prepare various inorganic hollow structures has been described in this chapter. Chapter 2 deals in detail the synthesis of functionalized carbon nanotubes from glucose and their templating action in obtaining GaN nanotube brushes. Coating of inorganic nanostructures like Fe_3O_4 and silica with functional carbon nanostructure has also been discussed. Chapter 3 describes the synthesis of single crystalline α-Fe_2O_3 nanocups using spherical carbon nanostructures as template. The cup-like morphology was obtained from spherical structure through buckling process and their magnetic properties showed shape dependent behaviour. Chapter 4 investigates the use of carbon spheres to make macro-mesoporous bioactive glass and its influence in the growth of hydroxyapatite nanocrystals. The enrichment of calcium and phosphate ions on the surfaces of carbon spheres by their functional groups and the generation of local heat during their calcinations help to promote the formation of hydroxyapatite nanocrystals in the as-synthesized bioactive glass. The results could have implications in bone implant materials. The interaction of carbon spheres with the cells, their mechanism of entry, preference to the nucleus of the mammalian cell and cytotoxicity in the context of delivering a therapeutic molecule are the contents of chapter 5. Chapter 6 is a slight deviation from the main stream work on materials although the common theme carbon is still the focus. In this chapter,

attempts were made to convert naturally available, inorganic carbon source namely carbonates into methane in the presence of transition metals and metal oxides as catalysts.

TABLE OF CONTENTS

DECLARATION I

CERTIFICATE II

ACKNOWLEDGEMENTS III

PREFACE VI

TABLE OF CONTENTS VIII

LIST OF ABBREVIATIONS XIV

1. Introduction

1.1.Allotropes of carbon 2

1.2.Carbon nanostructures 4

1.3.Characterizing carbon nanostructures 6

1.4.Applications of carbon materials 10

1.5.Functionalized carbon materials derived from carbohydrates 12

1.6.Glucose derived carbon – synthesis, structure and properties 13

1.7.Applications of HC 22

a. Materials synthesis 22

b. Catalysis 23

c. Energy and fuel cells 23

1.8. Conclusions 24

1.9. References 24

2. Use of amorphous carbon nanostructures as templates to synthesise hollow inorganic nanostructures

Summary 30

2.1.Introduction 31

2.2.Scope of the present investigation 34

2.3.Experimental section 35

a. Materials 35

b. Synthesis of CSP 35

c. $ZnAl_2O_4$ hollow spheres 36

d. SiO_2 hollow spheres 36

e. SnO_2 hollow spheres 37

f. Synthesis of Fe_3O_4 nanoparticles 37

g. Synthesis of Fe_3O_4 and $MnFe_2O_4$ submicron spheres 37

h. Synthesis of mesoporous SiO_2 spheres 38

i. Synthesis of inorganic core and carbon shell nanostructures 38

j. Synthesis of amorphous carbon nanotube brushes (a-CNT) 38

k. Synthesis of GaN nanotube brushes 39

2.4.Characterization 39

2.5.Results and discussion 40

2.6.Conclusions 57

2.7.References 58

3. Tuning the morphology of iron oxide nanocontainers from spherical templates

Summary 62

3.1.Introduction 63

3.2.Scope of the present investigation 65

3.3.Experimental section 65

a. Materials 65

b. Synthesis of spherical carbonaceous templates 65

c. Formation of thixotropic gel by hydrolytic polymerisation 66

d. Maintaining the relative humidity 66

3.4.Characterization 68

3.5.Results and discussion 68

3.6.Conclusions 81

3.7.References 81

4. Carbon spheres assisted synthesis of hierarchically porous bioactive glass

Summary 85

4.1.Introduction 86

4.2.Scope of the present Investigation 89

4.3.Experimental section 90

a. Materials 90

b. Synthesis of amorphous carbon additive 90

c. Synthesis of hierarchically porous bioactive glass 91

d. Synthesis of simulated body fluid (SBF) 91

e. *In vitro* studies 92

f. Preliminary biocompatibility test of MBG, MBGH and MBGH-3d samples on human fibroblasts cells *in vitro* 92

4.4.Characterization 93

4.5.Results and discussion 93

4.6.Conclusions 109

4.7.References 109

5. Intrinsically fluorescent carbon spheres as a new class of nuclear targeting vectors

Summary 112

5.1.Introduction 113

5.2.Scope of the present investigation 114

5.3.Experimental section 116

a. Synthesis of carbon nanospheres 116

b. Zeta potential measurements 116

c. Confocal microscopy imaging 116

d. Adsorption of CTPB on CSP 117

e. Preparation of the DMEM medium 117

f. Cell revival 117

g. Maintenance of cell culture 118

h. Preparation of the cover slips 119

i. Seeding the cells for experiments 119

j. Preparation of the samples for confocal microscopy studies 119

k. Effect of serum on the uptake of CSP 120

l. Temperature dependent uptake of CSP 120

m. ATP dependent uptake of CSP 120

n. ATP dependent uptake of CSP 121

o. Cytotoxicity of CSP 121

5.4.Results and discussions 121

5.5.Conclusions 135

5.6.References 135

6. Investigation of the conversion of inorganic carbonates to methane

Summary 138

6.1.Introduction 139

a. The hydrogen economy 141

b. Nuclear energy 144

c. The methanol economy 146

d. The fuel cell technology 148

6.2.Scope of the present investigation 150

6.3.Experimental Section 150

a. Materials 151

b. Synthesis of carbonates 151

c. Preparation of the catalyst 153

d. Characterization 153

e. Estimation of carbonates 153

f. Experimental setup for catalytic conversion of metal carbonates 153

g. Sample packing 155

h. Gas lines and plumbing 156

i. GC – configuration and measurement details 156

6.4.Results and discussion 157

6.5.Conclusions 173

6.6.References 173

LIST OF PUBLICATIONS 178

LIST OF ABBREVIATIONS

SEM – Scanning Electron Microscope

FESEM – Field Emission Scanning Electron Microscope

EDX – Energy Dispersive X-ray

TEM – Transmission Electron Microscope

HREM – High Resolution Transmission Electron Microscopy

ED – Electron Diffraction

FTIR – Fourier Transform Infrared Spectroscopy

TGA – Thermogravimetric Analysis

CLSM – Confocal Laser Scanning Microscope

XRD – X-ray Diffraction

FC – Field Cooled

ZFC – Zero Field Cooled

UV-vis – Ultraviolet and visible

PL – Photoluminescence

BET – Brunauer Emmett Teller theory of N_2 adsorption

FFT – Fast Fourier Transform

FWHM – Full Width at Half Maximum

HC – Carbon derived from hydrothermal treatment of aqueous carbohydrate solution

CSP – Carbon spheres derived from glucose.

CNT – Carbon nanotubes (graphitic)

a-CNT – Carbon nanotubes prepared from glucose (amorphous)

PCM – Polycarbonate membrane

TEOS - Tetraethylorthosilicate

PDADMAC – poly(diallyldimethylammonium) chloride

MBG – Mesoporous Bioactive Glass

MBGH – Hierarchically Mesoporous Bioactive Glass

SBF – Simulated Body Fluid

HCA – Hydeoxycarbonate apatite

CTPB – (N-(4-chloro-3-trifluoromethylphenyl-2-ethoxybenzamide)

CTPB-CSP – Carbon spheres adsorbed with CTPB molecule

HAT – Histone acetyltransferases

HDAC – Histone deacetyltransferases

DNA – Deoxyribonucleic acid

DMEM – Dulbeccos Modified Eagle's Medium

DMSO – Dimethyl sulfoxide

FBS – Foetal Bovine Serum

FCS – Foetal Calf Serum

PBS – Phosphate Buffer Solution

MTT – 3-(4,5-Dimethyl-2-thiazolyl)-2,5-diphenyl-2H-tetrazolium bromide

MTS – 3-(4,5-dimethylthiazol-2-yl)-5-(3-carboxymethoxyphenul)-2-(4-sulfophenyl)-2-H-tetrazolium

PEG – Polyethyleneglycol

Chapter 1

Introduction

Chapter 2

Use of amorphous carbon nanostructures as templates to synthesise hollow inorganic nanostructures

Chapter 3

Tuning the morphology of iron oxide nanocontainers from spherical templates

Chapter 4

Carbon spheres assisted synthesis of hierarchically porous bioactive glass

Chapter 5

Intrinsically fluorescent carbon spheres as a new class of nuclear targeting vectors

Chapter 6

Investigation of the conversion of inorganic carbonates to methane

Relevance to further chapters

This thesis presents the diverse applications of functionalized carbon nanostructures derived from glucose by hydrothermal route. Chapter 1 introduces the carbon nanostructures, their properties and mechanistic studies that have been performed by us and other workers in this field. Further the use of functional carbon nanostructures as templates to prepare various inorganic hollow structures has been described in this chapter. Chapter 2 deals in detail the synthesis of functionalized carbon nanotubes from glucose and their templating action in obtaining GaN nanotube brushes. Coating of inorganic nanostructures like Fe_3O_4 and silica with functional carbon nanostructure has also been discussed. Chapter 3 describes the synthesis of single crystalline α-Fe_2O_3 nanocups using spherical carbon nanostructures as template. The cup-like morphology was obtained from spherical structure through buckling process and their magnetic properties showed shape dependent behaviour. Chapter 4 investigates the use of carbon spheres to make macro-mesoporous bioactive glass and its influence in the growth of hydroxyapatite nanocrystals. The enrichment of calcium and phosphate ions on the surfaces of carbon spheres by their functional groups and the generation of local heat during their calcinations help to promote the formation of hydroxyapatite nanocrystals in the as synthesiszed bioactive glass. The results could have implications in bone implant materials. The interaction of carbon spheres with the cells, their mechanism of entry, preference to the nucleus of the mammalian cell and cytotoxicity in the context of delivering a therapeutic molecule are the contents of chapter 5. Chapter 6 is a slight deviation from the main stream work on materials although the common theme carbon is still the focus. In this chapter, attempts were made to convert naturally available, inorganic carbon source namely carbonates into methane in the presence of transition metals and metal oxides as catalysts.

1. Introduction

Carbon plays a unique role in nature. The formation of carbon in stars as a result of the merging of three α-particles is a crucial process that leads to the formation of other heavier elements in the universe.[1] Being the fourth most abundant element in the universe by mass after hydrogen, helium, and oxygen, it is present in all known life forms, and in the human body.[2] The unique diversity of organic compounds and their unusual polymer-forming ability (catenation) at the temperatures commonly encountered on earth, make this element the chemical basis of life. Of all the naturally existing elements, carbon has the highest melting and sublimation point.[3] Although thermodynamically prone to oxidation, carbon resists oxidation more effectively than elements such as iron and copper. At standard temperature and pressure, it resists all but the strongest oxidizers. It does not react with sulfuric acid, hydrochloric acid, chlorine or any alkalis.

1.1. Allotropes of carbon:

An interesting aspect of carbon is its existence in different forms or *allotropes* that include the hardest naturally occurring substance like diamond and also one of the softest known substances like graphite. Under ambient conditions the graphite phase with strong in-plane trigonal bonding is the stable phase. Under the application of high pressure and temperature transformation to metastable diamond structure takes place. Once the pressure is released, diamond remains essentially stable under ambient conditions although, in principle, it will very slowly transform back to the thermodynamically stable graphite. However, a quick transformation to graphite phase is also possible by exposing the diamond to perturbations like irradiation and heat.[3]

The fundamental differences in the properties of graphite and diamond arise from their orbital hybridization and crystal structures (Figure 1). The sp^2 hybrid orbitals which are planar favor the graphitic structure while tetrahedral sp^3 hybrid orbitals favor the diamond structure.

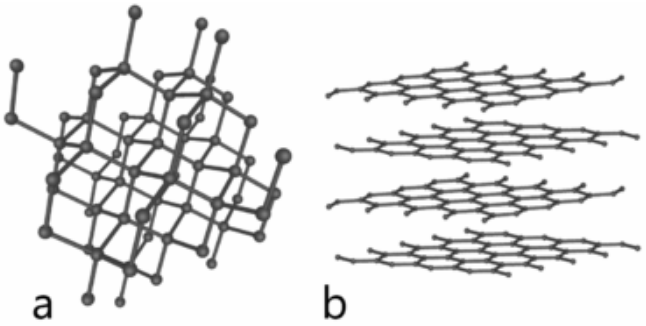

Figure 1: Crystal structure of two major allotropes of carbon a) diamond and b) graphite (source: http://en.wikipedia.org/wiki/File:Diamond_and_graphite.jpg)

Graphite, which is completely made up of sp^2 hybridized carbon occur as stacked layers with hexagonally arranged atoms in each layer. The interplanar distance between two successive layers is 3.353 Å. The weak interactions between the planes are responsible for its soft mechanical properties. On the other hand, in diamond, every carbon atom is surrounded by four other carbon atoms at the corners of a regular tetrahedron with a cube edge length of 3.567 Å. The cubic structure of diamond is viewed as two interpenetrating fcc lattice. The nearest C-C bond in diamond is 1.544 Å, nearly 10 % larger than in graphite.[3] However the high atomic density of diamond (56% higher than the graphite) due to the crystal structure is responsible for its strong mechanical properties.[3]

Though bulk carbon is primarily divided into diamond and graphite, a number of other allotropes are also known. A classification of carbon materials based on the nature of carbon atoms present may be more predictive of the existence of new forms of carbon that are presently unknown to mankind. For example, diamond has atoms that are 100% sp^3 hybridized, while graphite is made of carbon 100 % sp^2 hybridized. The former is an insulator with a very large band gap (5.5 eV) while the latter is a conductor (around 0.25 eV).[4] The two examples give the clue about the possible existence of carbon with millions of permutations and combinations of sp^2 and sp^3 hybridized carbon atoms. Diamond like carbon (DLC) and glassy carbon are classic examples which has a mixture of sp^2 and sp^3 carbon atoms.[3a] Another form of carbon with a mixture of sp^2 and sp^3 hybridized carbon is well- known as

amorphous carbon, a highly disordered network of carbon atoms that have predominantly sp^2 bonding, besides a small proportion of sp^3 bonds.[5] In such materials the ordering exists on a length scale of 10 Å. Two parameters i) carbon bonding and ii) the hydrogen content as impurities are essential in characterizing the short range order.[5] Thus amorphous carbon is made up of clusters of sp^2 carbons and clusters of sp^3 carbons with hydrogen impurities to passivate the dangling bonds.

While all these structures are essentially 3D bulk structures, the recent thrust on the materials science at nanometer length scales have brought into focus the existence of a number of carbon structures of reduced dimensions. They include materials like graphene, carbon nanotubes and fullerene. A classification based on the dimensions is given below.

1.2. Carbon nanostructures:

The three most important allotropic forms of carbon of low dimensions, namely, graphene (2D), carbon nanotubes (1D) and fullerene (0D) are derived from graphite. Graphene, a one-atom-thick planar sheet of sp^2-bonded carbon atoms in a honeycomb crystal lattice was synthesized recently by the micromechanical cleavage of bulk graphite.[6] Though it is not difficult to imagine the existence of graphene given our knowledge on graphite from ancient times, it is rather puzzling to find in nature their closed structural analogues namely, fullerenes and carbon nanotubes. The discovery of carbon nanostructures were pioneered by Kroto,[7] Krätschamer[8] and Ijima[9a] and was developed by many other researchers.

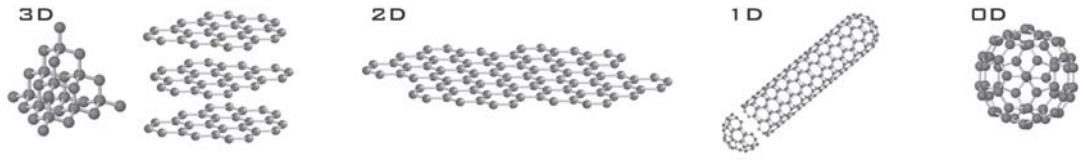

Figure 2: Cartoon representation of carbon allotropes in reduced dimensions (Materials Today, 2007, 10, 20)

Fullerenes are closed-cage carbon molecules with three-coordinate carbon atoms tiling the spherical or nearly spherical surfaces. The best known structure $C_{60,}$ with a truncated icosahedra structure is formed by twelve pentagonal rings and twenty hexagonal rings. The

existence of curvature due to cyclopentane rings in fullerenes is explained by the presence of corannule structures. Corannule is a polycyclic aromatic hydrocarbon consisting of a cyclopentane ring fused with 5 benzene rings (Figure 3).

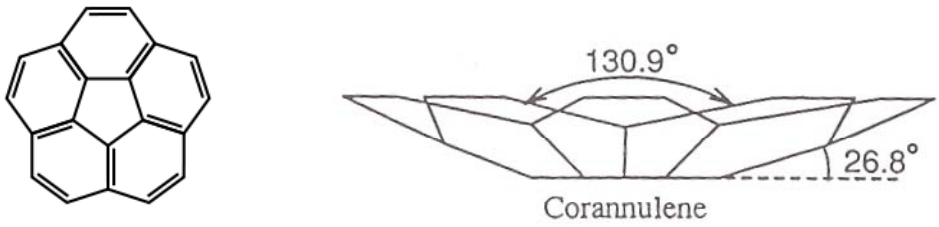

Figure 3: Structure of corannulene that explains the formation of curvature in carbon nanostructures. (Ref 4)

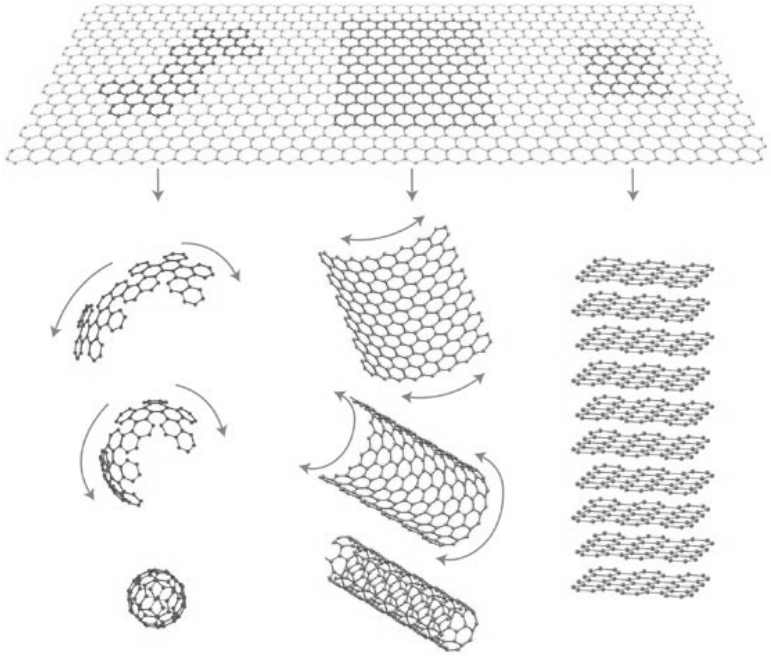

Figure 4: Formation of carbon nanostructures from graphene monolayer (Materials Today, 2007, 10, 20).

It is possible to construct fullerenes and other carbon nanostructures from graphene (Figure 4). Carbon nanotube can be of single walled (SWNT - no graphitic layers around the tubule) or double/multiwalled (DWNT/MWNT) (Figure 5). A carbon nanotube can be visualized by cutting a C_{60} molecule along the centre and spacing the two resultant hemispherical corannulenes by a narrow strip of rolled graphene of the diameter similar to that of the base circle of the corannulene (Figure 6). The theoretical model of rolling the

graphene strip to form a carbon nanotube also explains its chirality due to different possible ways of rolling.

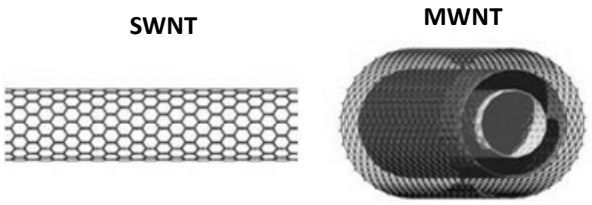

Figure 5: Structure of single walled carbon nanotube (SWNT) and Multi walled carbon nanotube (MWNT) (Source: http://www.nanotechnologies.qc.ca/projets/nanotubes/images/en/SWCNT_MWCNT_schema.jpg)

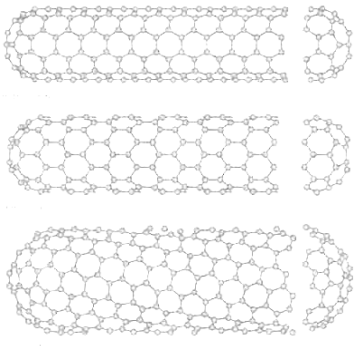

Figure 6: Schematic formation of carbon nanotubes from graphene and corannulene structures. (Source: http://www.geocities.com/nanotubes_report/introcnt.htm)

1.3. Characterizing carbon nanostructures:

Characterization of carbon nanostructures is one of the primary steps that succeed a successful synthesis. The tool that can be used for the characterization depends on the type of information one is looking for. For example, some of the basic criteria that are considered important are morphology, yield, impurities, crystallinity, surface area, optical properties etc. In this regard, transmission electron microscopy (TEM) has served a huge purpose in characterizing the morphology and microstructure of the carbon nanostructures. It has been possible to measure the lattice fringes of crystalline carbon nanostructures like MWNT or nanodiamonds using high resolution TEM. It is also used to differentiate SWNT, DWNT and MWNT.[9b] Electron energy loss spectroscopy is also widely used in the study of doped carbon nanostructures.[9c] There are also studies which involve *in situ* study of growth mechanisms of CNTs using a TEM.[9d] To some extent the yield can also be estimated by observing the sample

at a lower magnification. In Figure 7, TEM images of various carbon nanostructures are shown.

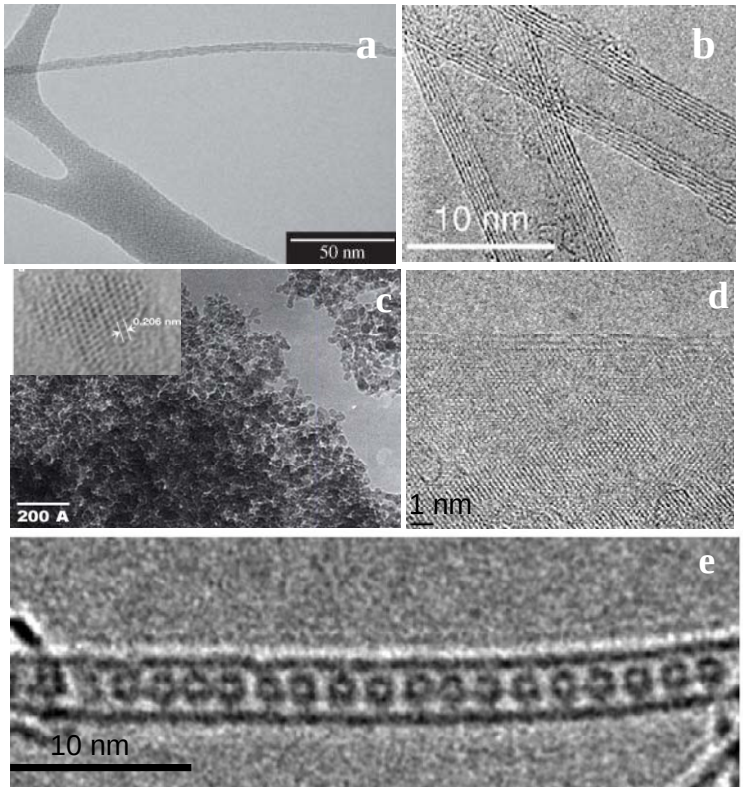

Figure 7: TEM images a) SWNT (Materials Research, 2008, doi: 10.1590/S1516-14392008000300019)**,** b) MWNT (J. Phys. Chem. 2000, B104, 2794), c) Nanodiamonds, Inset HREM. (*Appl Phys Lett*, 2008, 93, 132115), d) Graphene (*Nature*, 2007, 446, 60-63). e) Fullerene encapsulated SWNT (*Jpn. J. Appl. Phys.* 2005, 44, L1341).

The next important step involves the estimation of the purity of the sample which predominantly depends on the type of impurity present in the sample. This step is vital in developing the synthesis conditions to obtain samples of better quality. For example, the CNTs are usually associated with metal catalyst particles and amorphous carbon as impurities. While TEM gives some basic idea on the type of impurity present, thermo gravimetric analysis (TGA) is also widely used to study the presence of amorphous carbon and metal impurities. Atomic Force Microscopy (AFM) has also been regularly used to determine the number of layers in the synthesized graphene samples using the step height. BET adsorption

isotherm is another routine characterization tool to determine the surface area of the nanofoams, CNTs and graphene.

One of the most powerful, generic and non-destructive tool to characterize all the allotropes of carbon is Raman spectroscopy (Figure 8). Raman Scattering studies were first used by Tuinstra and Koenig[10] to characterize several forms of carbons including single–crystal graphite, pyrolytic graphite, activated charcoal and carbon blacks. In their studies all disordered graphite samples showed two prominent Raman features with peaks at 1580 and 1355 cm^{-1}. They assigned the dominant peak at 1580 cm^{-1} to the in-plane E_{2g} Raman-allowed vibration. The second peak at 1355 cm^{-1} was identified with in-plane disorder-induced scattering from graphitic modes.[11] The position, width and relative intensity of these bands are modified according to the carbon forms.

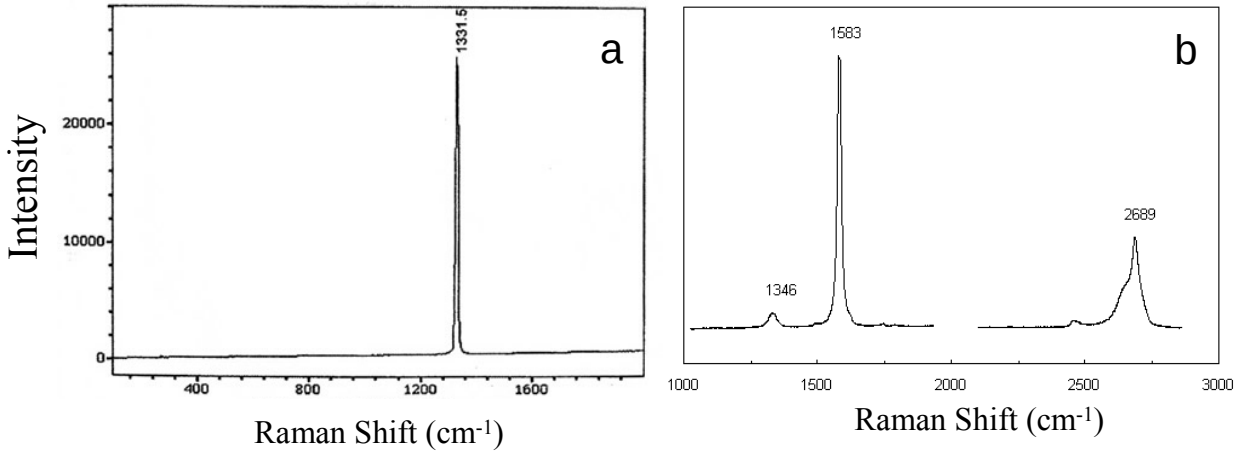

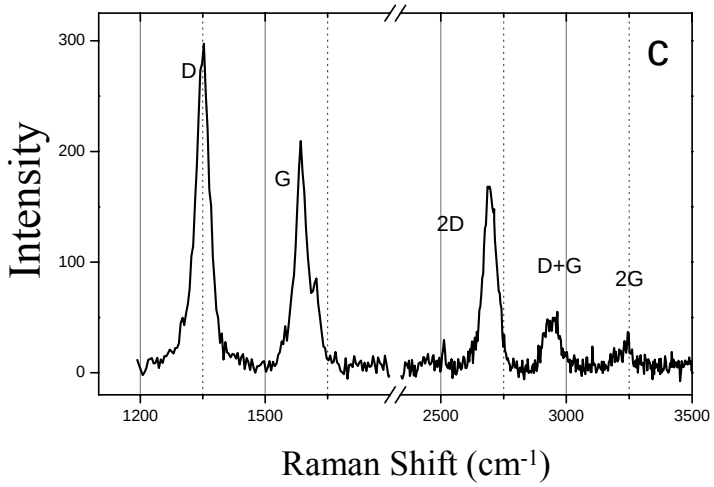

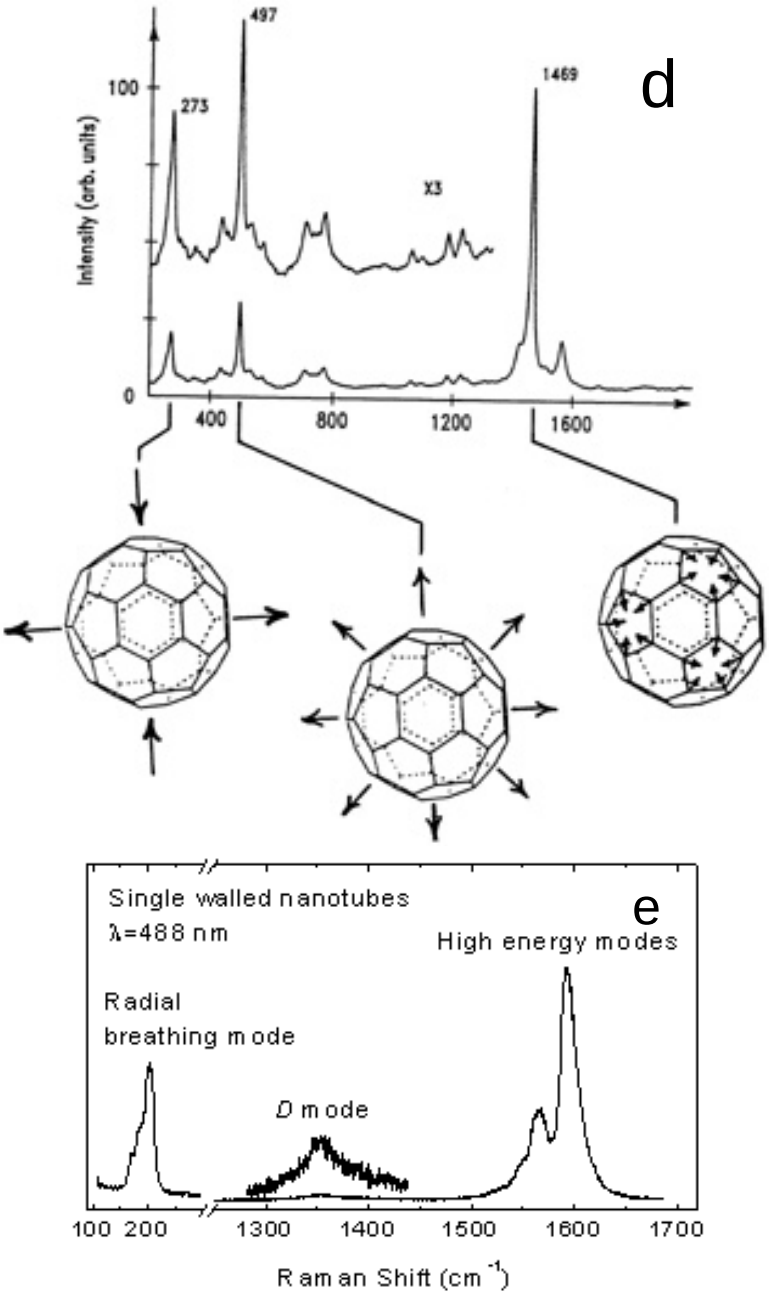

Figure 8: Raman spectra of various carbon allotropes a) diamond,[10] b) graphite,[11] c) graphene,[12] d) fullerene,[12] e) carbon nanotube.[12]

Raman studies on diamond materials show a sharp peak at 1332 cm^{-1}, typical for the sp^3-bonded carbon. Graphene shows two main Raman features, including the G band at 1580 cm^{-1} and the 2D band (the overtone of the disorder induced D band; also called G2 band) at 2700 cm^{-1}. The shape of the 2D Raman band can be used to identify the number of graphene layers.[12] Raman spectroscopy has also been used as a characterisation tool for pristine and doped fullerenes. The band at 496 cm^{-1} is the purely radial A_g mode. The high frequency band

at 1469 cm^{-1} is due to the pentagons of fullerenes and is called pentagonal pinch mode. This band is very often associated with the photochemically induced polymeric state of C_{60}.[12] In the case of carbon nanotubes, the five most important Raman features are identified as the following:[12] (i) a low-frequency peak < 200 cm^{-1} characteristic of A_{1g} "radial breathing mode" is also sensitive to the diameter of nanotube, (ii) D band (disordered/ill organized graphite) at 1340 cm^{-1}, (iii) a high frequency G band between 1500 and 1600 cm^{-1} corresponding to the in-plane stretching mode of graphite (iv) the first overtone of D mode (G' mode) between 2450 and 2650 cm^{-1} and (v) a combination of D and G modes between 2775 and 2950 cm^{-1}.

1.4. Applications of carbon materials:

Most forms of bulk carbon and their solid variants like carbon black, kish graphite, carbon whiskers, fibers, carbon black, exfoliated graphite, carbon foam, activated charcoal have been known to mankind for many decades.[3a] They have been extensively used in various applications involving adsorption or substrate for catalysts and even in biomedical applications. Highly oriented pyrolytic graphite (HOPG) is yet another material which has been commonly used when atomically flat conducting substrates are required for scanning probe measurements. Diamond like carrbon is known to be hard, chemically inert, insulating, IR transparent and biologically compatible.[13] These are also highly resistant to acids. For example, a normal graphite is reduced to a powder by a mixture of concentrated sulfuric and nitric acids at room temperature, the glassy carbon is unaffected by such treatment, even after several months.

The advent of nanomaterials in the last few decades has indeed changed the outlook of possible applications that the carbon materials were once expected to perform. The two-dimensional form of carbon, graphene, which was only obtained recently, received a great deal of attention. Electrons in graphene which behave like mass-less relativistic particles can lead to a number of very peculiar electronic properties ranging from an anomalous quantum Hall effect to the absence of localization making it a futuristic material capable of replacing

silicon in the electronic device applications.[14] Though many more interesting properties of graphene are yet to be unravelled, for now, the large scale synthesis of a single layer graphene itself remains a challenging issue.

Fullerenes were first discovered in the experiments of Kroto et al.[7] But following the development of better routes of synthesis by Krätschamer et al,[8] the activity in the field increased dramatically. As of today, fullerenes (C_{60} and related materials) have shown many exceptional properties some of which are expected to lead to practical applications. The nonlinear optical properties in the excited triplet state gives rise to optical limiting devices and photorefractive devices, while the photoinduced charge transfer between C_{60} and polymer in composites gives rise to photoconductivity applications, photodiodes and photovoltaic devices.[15-19] Catalytic applications of C_{60} include CH_4 activation[20] and conversion of H_2S to sulphur.[21] There are also reports on the fullerene (only C_{60}) catalysed oxidation reaction of organic solvents.[22]

Carbon nanotubes were discovered in 1991 by S. Ijima.[9a] Soon after this the carbon nanotubes found applications in a number of fields ranging from supercapacitors, batteries, sensors, drug delivery, composites etc. The graphitic structure of carbon nanotubes gives them hydrophobicity, robustness, electronic and optical properties. However, for applications like integration of metal, semiconducting nanoparticles, dyes, drugs onto their surface, the primary requirement is to provide the surface of the carbon nanotubes with chemical handles like –OH, -COOH, $-NH_2$, -SH groups etc. A stable and uniform dispersion of carbon nanotubes in water or any organic solvents is also a case in which the surface functionalization plays an important role. In the past, this has been achieved either by non covalent interactions or through covalent chemistry. Molecules like long chain alkane thiols, polycyclic compounds interact through van der Waals interaction along the sides of the nanotubes.[23] While this technique is relatively easier to employ, it is severely hampered by its strength of interaction and also difficulty in transferring the nanotubes to the aqueous

medium. Electrostatic interactions have also been exploited by using polyelectrolytes to glue the carbon nanotubes and the target material/molecule.[24]

Another popular way of functionalizing carbon nanotubes is by using covalent chemistry. Continuous reflux or microwave heating of carbon nanotubes in strong acids or H_2O_2, $KMnO_4$, O_3, OsO_4, RuO_4 etc have known to introduce –COOH groups on their surface.[25,26] But they are also known to shorten the nanotubes and cause open ends. Prato's studies of the organic functionalization of carbon nanotubes are more recent and perhaps more relevant in medicinal chemistry.[27] The functionalization was based on the 1,3-dipolar cycloaddition of azomethine ylides. The method offers advantages of introducing wide range of functional groups which could be homogenously distributed. There is no doubt that carbon nanotube has occupied a very prestigious position among the materials with futuristic implications. But, the energy consuming synthesis and extensive chemical steps of surface functionalization of carbon nanotubes can be substituted by suitable alternatives in certain applications where the functionalization plays a critical role. The rationale in the search of better alternative must look for the carbon precursor with high ratio of heteroatoms like oxygen or nitrogen. The availability of the precursor, cost and energetics in the synthesis of carbon nanostructures must also be considered. A sweeter alternative was to use glucose - a commonly available, non-toxic, less expensive carbohydrate as the carbon precursor to obtain highly nanostructures at a lower temperature. Also the as synthesized materials retain a number of functional groups of the precursors on the surface.

1.5. Functionalized carbon materials derived from carbohydrates:

The simplest form of carbohydrates, are either polyhydroxyaldehydes (aldoses) or polydyroxyketones (ketoses). They are linked up with each other by glycosidic bonds to form di, tri, oligo or polysaccharides.[28] The mode of glycosidic linkage between the monosaccharides has been known to dictate the function of the eventually formed polysaccharides. Thus, ranging from energy storage to structural integrity carbohydrates occur

abundantly in the living systems. The economical exploitation of carbohydrates started with the fermentation of carbohydrates to oxygenated hydrocarbons such as alcohol or organic acids. It was realized in 1970's that glucose could be converted into other useful chemicals through acid catalysed oxidation, hydrogenation and dehydration.[29] Among them, the dehydration of glucose gave various products like 5-hydroxymethyl-2-furaldehyde (HMF), formic acid, 4-oxopentanoic acid.[30] Extensive dehydration also led to the carbonization of the reaction products to form water-insoluble residues. Most of these reactions have been well characterized in the temperature range of 130 - 180 ^{o}C.[30] However, it was only recently that the water-insoluble residue came into the limelight, following the report of Li et al, where an aqueous solution of glucose was heated above 160 ^{o}C without an external addition of acid catalyst in a sealed container.[31] Surprisingly, the insoluble residue obtained in this reaction was found to contain uniformly sized colloidal spheres made up of functionalized amorphous carbon. Since then, a host of reasons have encouraged the material scientists to employ this form of carbon in a variety of applications which are described in the following sections. Henceforth, carbon materials derived from carbohydrates by hydrothermal treatment is abbreviated as HC and if glucose is used as the precursor it is mentioned as CSP for carbon spheres.

1.6. Glucose derived carbon - Synthesis, structure and properties:

Synthesis of HC comprises the heating of carbohydrates and water in closed containers at 150 - 180 ^{o}C for several hours ranging from 6 to 18 (Figure 9). A number of sources like glucose, fructose, maltose, sucrose, starch, cellulose and cyclodextrin have been employed as carbon precursors.[32] As the temperature employed is higher than the normal glycosidation temperature, the carbohydrates undergo dehydration followed by carbonization and aromatisation (Figure 10).

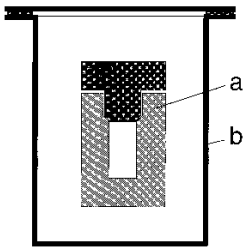

Figure 9: Cartoon showing the longitudinal cross section of the autoclave in which (a) represents the teflon lining in which the glucose solution is placed and (b) represents the steel jacket surrounding it.

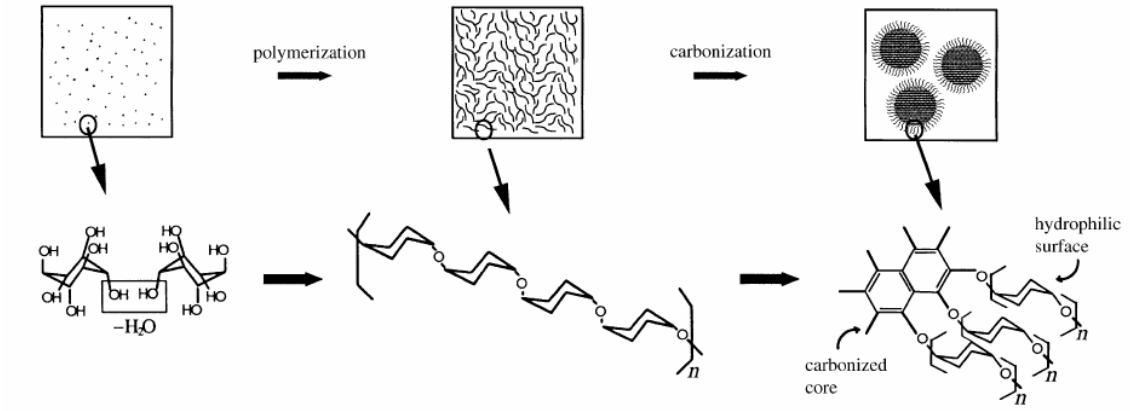

Figure 10: Scheme explaining the formation of carbon spheres from glucose. Ref 31.

The reaction mechanism for the case of glucose, fructose and cyclodextrin has been studied using ^{13}C NMR, Raman and FT-IR spectroscopy.[33] The intramolecular dehydration pathway usually involves the initial formation of HMF which further rehydrates to 4-oxopentanoic acid (levulinic acid) which in turn catalyses the dehydration of the remaining carbohydrates. Further polycondensation is believed to be mediated via the formation of a kind of –OH group containing amphiphilic intermediates which self organise to form spherical aggregate.[34] Following the nucleation, the surface hydroxyls continue to polymerise with the neighbouring free molecules leading to the growth of the sphere. This model is in accordance with the LaMer growth model.[35] A schematic explaining the formation is given below. But when glucose was used as the precursor, HMF was not detected at temperatures less than 180 ^{o}C suggesting that carbon spheres were most likely formed via an intermolecular dehydration followed by the carbonization. The mechanism has an impact over the final morphology of the spheres obtained. HC spheres of glucose origin are smooth due to dominant

intermolecular dehydration, while an aqueous fructose solution initially forms HMF by intramolecular dehydration followed by polymerisation of microscopic carbon-containing spheres that then assemble to larger spheres, generating a final raspberry like structure.[33] It must therefore be possible to obtain carbon spheres of few tens of nm diameter by optimising the reaction pathway using fructose. Cyclodextrin, on the other hand undergo hydrolysis to form glucose intermediate before forming smooth surfaced carbon spheres.[33] Furanose units in fructose are more reactive than pyranose units in glucose. Hence the glucose solution requires relatively high temperature to polymerise than the fructose solution. The internal structure of the HC differs drastically from the carbons prepared via high temperature pyrolytic routes. HC retains a large amount of oxygen and hydrogen (carbon content 70-80%) from the carbohydrates while the latter predominantly is graphitic.

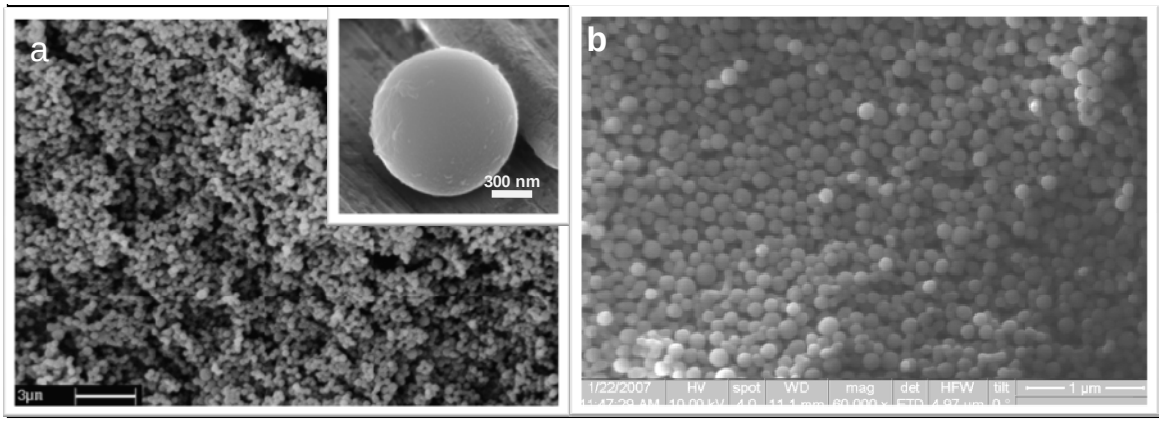

Figure 11: SEM images of CSP synthesized from 0.5 M aqueous solution of glucose at 180 ^{o}C. The reaction duration is a) 16 h and b) 6 h.

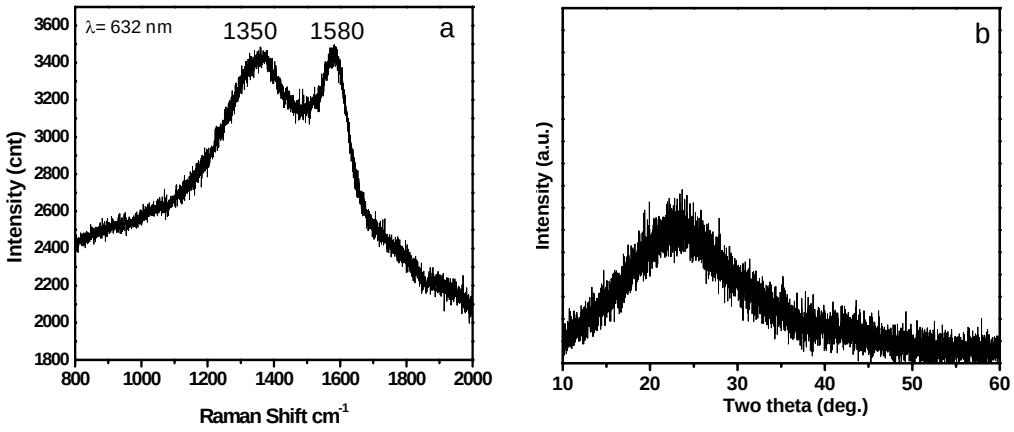

Figure 12: a) Raman Spectrum b) X-ray diffraction of glucose derived CSP.

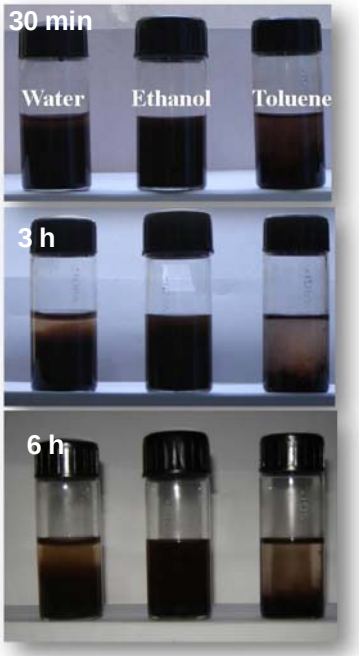

Figure 13: Dispersion of glucose derived CSP in different solvents (2 mg/mL). The samples were sonicated for 30 min initially.

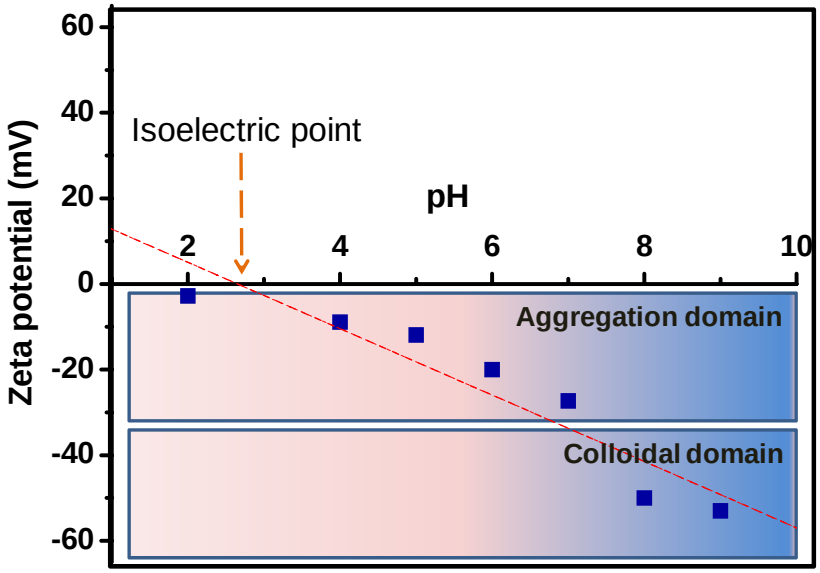

Figure 14: Variation of zeta potential with pH. The samples (300 µg in 2.5 mL water) were equilibrated for 20 h at 25 ^{o}C before the measurement. The pH was adjusted using 0.01 N HCl and 0.01 N NaOH.

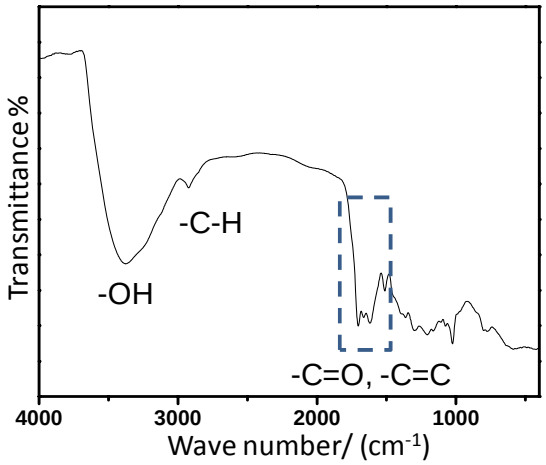

Figure 15: FT-IR spectrum of glucose derived CSP. 1 mg of sample mixed well with 80 mg of KBr and pelletized under a uniaxial pressure.

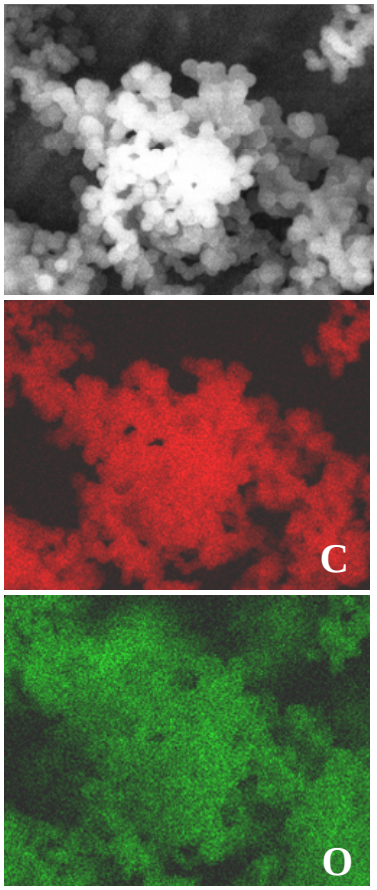

Figure 16: Elemental mapping using energy dispersive X-ray analysis. From top - SEM image of the area of analysis. The lower images show the distribution of carbon and oxygen from the functional groups of the sample.

In Figure 11, the SEM images of CSP are shown. It can be seen that by changing the reaction duration from 6 h to 16 h, one can tune the surface of these spheres from 40 nm to 400 nm. Raman spectrum shows two broad and equally intense bands at 1580 and 1350 cm^{-1} which are due to graphitic and disordered structures respectively of the carbon **(**Figure 12a). Thus CSP is predominantly amorphous with occasional graphitic structures. XRD show broad peaks characteristic of disordered system (Figure 12b**).** The dispersion of CSP in solvents of different polarity like water, ethanol and toluene were studied. It was found that the CSP were easily dispersible in all the solvents suggesting that the surface has both hydrophilic and hydrophobic functional groups (Figure 13). The stability of dispersion was found to be in the order of ethanol >water > toluene showing that the surface is amphiphilic with more amount of hydrophilicity than hydrophobicity. The surface charge of the CSP was measured in a wide range of pH from 2 to 10 and the data is shown in Figure 14. CSP are negatively charged in the entire pH range but tend to become less negative towards acidic pH with a possible isoelectric point falling at pH 2.8. The observation reiterates the presence of functional groups (e.g. organic acids) that can ionise in the basic medium. Detailed FT-IR spectra analysis suggests the presence of –OH, -COOH, -C=C and -CHO groups (Figure 15). Energy dispersive X-ray analysis (EDX) also shows the mapping of the oxygen element distributed throughout the CSP (Figure 16).

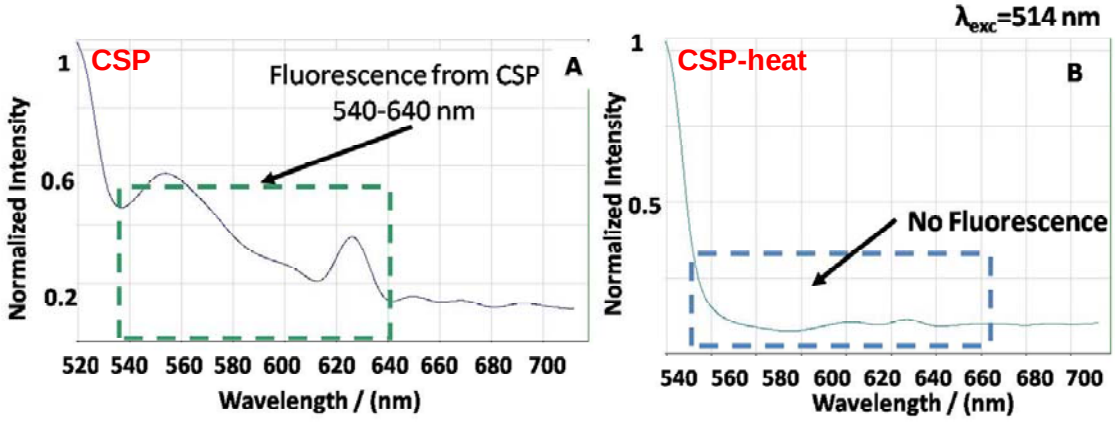

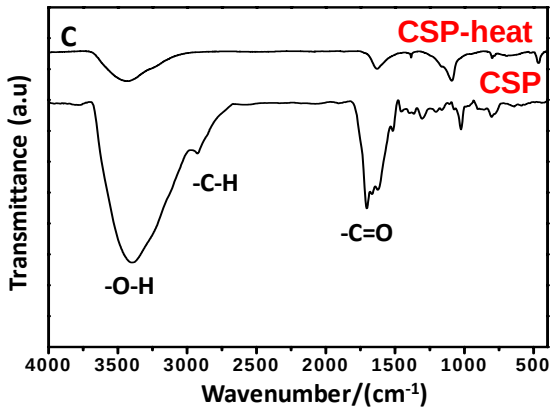

Figure 17: a) Emission spectrum of glucose derived CSP. b) Emission spectrum of heat treated carbon without functional groups (CSP-heat). CSP-heat is made by heating the CSP in N_2 atmosphere at 800 ^{o}C for 5 h. c) FT-IR spectrum of CSP and CSP-heat showing the absence of functional groups in CSP-heat sample.

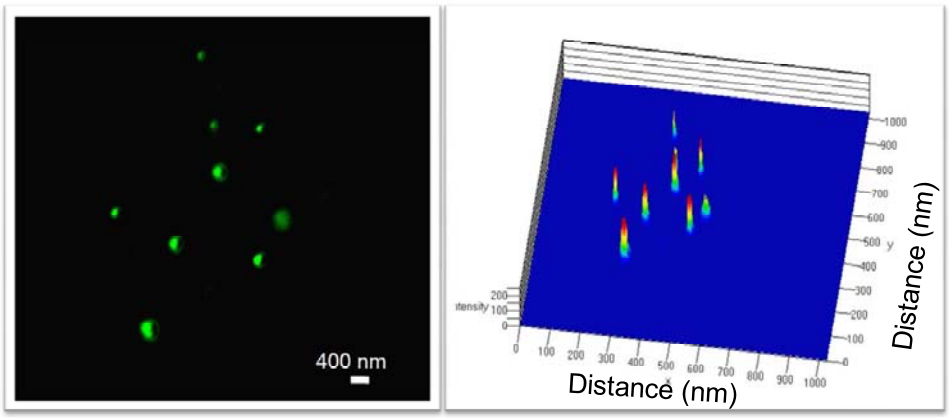

Figure 18: Confocal laser scanning microscopy image of CSP excited at 514 nm (left side). The intensity of emission plotted in space for the corresponding image (right side).

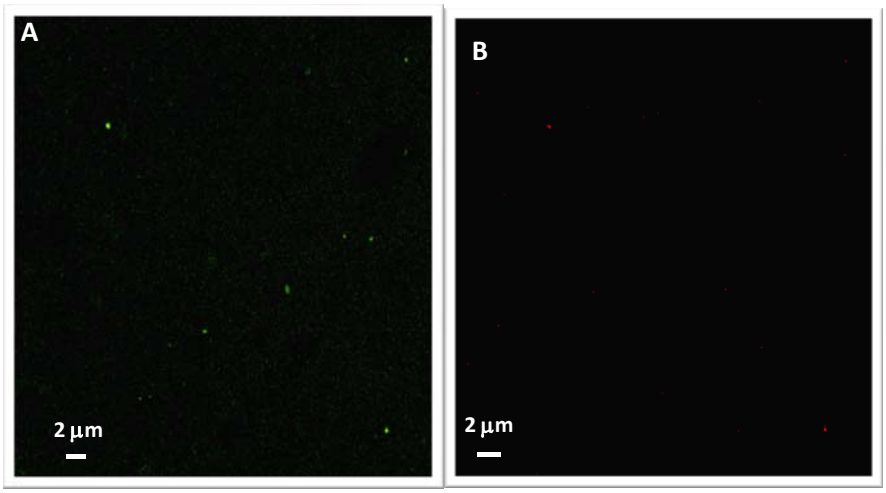

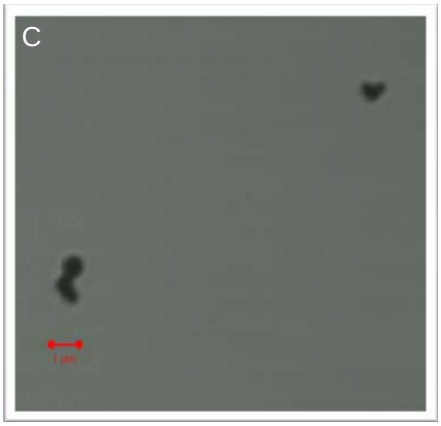

Figure 19: Confocal laser scanning microscopy image of CSP excited at 514 nm and observed using the a) band pass filter 540-589 nm images the spheres using the fluorescence from green and red emission b) band pass filter 600-650 nm images the spheres using the fluorescence from red emission. c) Confocal image of CSP-heat sample which does not show any fluorescence.

The growth model suggests that the well carbonized aromatic hydrophobic groups are at the core while the functional groups are distributed on its surface. In other words, the core resembles the disordered amorphous carbon while the periphery is more polymeric with abundant functional groups. The presence of functional groups also introduces fluorescence in this material. When as prepared CSP are excited at 514 nm, a wide emission band is observed ranging from 540 nm to 640 nm. The emission band has maxima at 550 nm and at 625 nm (Figure 17 A). When the functional groups of the CSP are removed by heating them at high temperature in an inert atmosphere, the fluorescence is lost (Figure 17 B). The Figure 17 C shows the confirmation of the removal of functional groups in CSP-heat sample. In Figure 18, we have imaged the CSP in confocal microscopy taking advantage of their intrinsic fluorescence. Figure 19 a and b are imaged using the different emission maxima regions of the CSP (green and red) using suitable filters. Figure 19c is the image of the carbon without functional groups (CSP-heat) where fluorescence is lost.

It was also possible to adsorb charged molecules on the surface of CSP. To demonstrate a few, adsorption of both positively charged molecule like

polydiallyldimethylammonium chloride (PDADMAC) (Figure 20) and negatively charged molecule like DNA (Figure 21) was successfully carried out. The spheres soaked in a 20 % aqueous solution of PDADMAC for 20 minutes show a good adsorption as indicated by the shift in the surface potential to +40 mV. This also suggests the possibility of loading cationic polypeptides onto the surface of CSP by simple adsorption. The adsorption of DNA was carried out by soaking 250 µg dispersed in 10 ml of deionised water containing 5 mg of DNA at pH7.3 showing signs of adsorption of DNA on CSP. But, increased number of washing in water restores the zeta potential back to -24 mV suggesting a weak adsorption. EDX analysis of CSP adsorbed with DNA after three cycles of washing with water shows the zeta potential close to the original value suggesting complete removal of DNA.

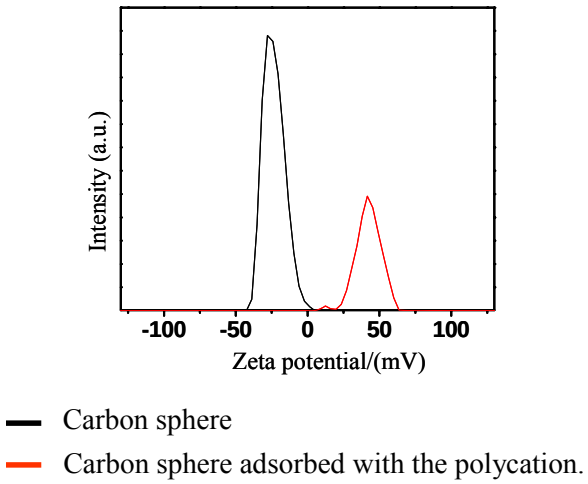

Figure 20: Zeta potential of carbon sphere dispersed in water at pH 7.3 is at -24 mV.

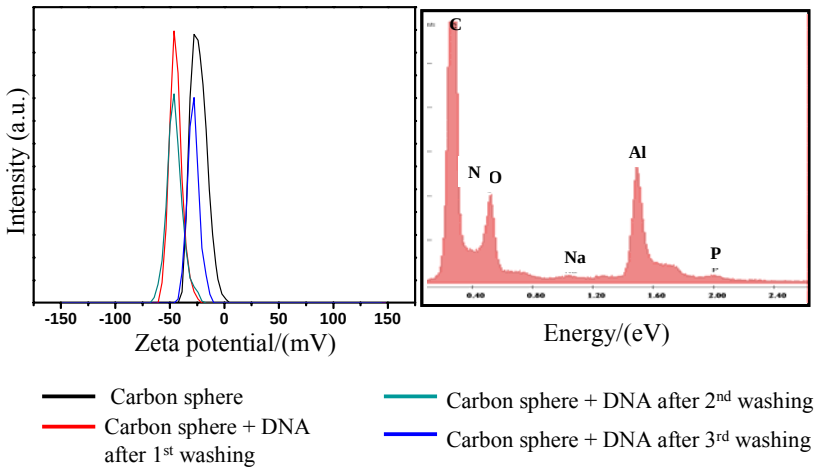

Figure 21: Adsorption of a negatively charged molecule like DNA was studied on the surface of the CSP.

1.7. Applications of HC:

The uniqueness of the HC stems from the rich functional groups they possess on their surface. Applications such as functional nanocomposites,[36] photonic band gap materials,[37] drug delivery[38] etc demand the synthesis of tightly controlled size and surface properties. Though there are many methods in literature to synthesise monodispersed silica or polymer materials,[39] their relatively inert surface makes the surface modification unavoidable.[40] The presence of a 'chemical handle' (functional groups) on the surface of HC greatly enhances the possibilities of integration of other functions like magnetic, catalytic, optical etc onto them. A short account on the development HC as a versatile material is given below.

a. Materials Synthesis:

Polymers with oxygen containing functional groups (like polyethyleneoxide or polyvinylalcohol) have been widely used as capping agent in the synthesis of nanoparticles.[41a] In a similar way, the rich functional groups like –COOH, -OH on the surface of HC is expected to bind to specific crystal planes of noble metals and stabilize them from aggregating to lager particles. Indeed, nanoparticles like Ag, Au, and Pt have been stabilized on their surface by simply reducing the respective metal precursor in the presence of the HC spheres.[41b] It is also known that prior to the carbonization steps, the polymerised glucose chains itself can be used as capping agents for Au nanoparticles.[42] As opposed to most inorganic templates, the glucose-derived polymer capping is dispersible in water to form stable suspensions. They also possess thermal stability and resistance to electrolytes. Such Au particles also possessed catalytic activity in the room temperature oxidation of CO.[42]

Templating can be defined as the replication of one structure into another under structural inversion. Among various methods to synthesise them, use of hard templates have been proved to be one of the most widely applied procedure. However, most of the available templates usually need further surface modification. HC spheres were readily put to use directly as a template to synthesise hollow structures without any special surface

modifications. More details are given in chapter 2 of this thesis. Another interesting aspect of the HC templates was indicated in a spontaneous combustion reaction for synthesising Pt hollow spheres.[43] The removal of the HC core at room temperature was apparently catalysed by the Pt nanoparticles of specific size that were previously deposited on the surface of HC. The observation was unique with the HC as there are many Pt composites with other forms are carbon which is stable enough to be commercially available. The reason was attributed to the presence of high hydrogen content of 2.57 wt% in HC as against 0.203 wt% in the commercially available Pt/C catalysts.[43]

b. **Catalysis:**

Selective partial oxidation of hydroxyl aromatic derivatives has been achieved with Pd@HC as catalyst.[44] The high selectivity in the conversion was attributed to the organisation of the sample used containing catalytically active Pd nanoparticles in a more confined environment of hydrophilic shell. The reactants get access to the catalyst at the core through the hydrophilic pores across the HC shell. The property is very relevant in case of industrially important conversion of phenol to cyclohexanol or cyclohehexanone by partial hydrogenation. The separation of products and unreacted reactants has remained a major challenge due to the possible formation of azeotropic mixtures of reactant and products. This can be circumvented by employing a catalyst that would have 100% conversion. Phenol, being a strongly H-bridge interacting system gets enriched in the hydrophilic pockets of the catalyst. On the other hand, the hydrophobic product like cyclohexanone gets expelled from the catalyst at a faster rate leading to a mechanistically biomimetic system. The catalyst was also shown to be effective on various other reactants.

c. **Energy and Fuel Cells:**

Lithium ion batteries have progressively replaced many conventional batteries based on acid, alkaline and metal hydrides in consumer electronics. Despite their efficiency in terms of high energy and high power density, constant efforts are put in order to improve their

cyclability and rate capability. As a result, a number of alternatives to the existing graphitic carbon anodes are pursued. Though materials like Sn or SnO_2 have higher theoretical specific capacity than the graphite, their commercial use is hindered due to the drastic volume variation (>300%) during the Li insertion/extraction (alloying/dealloying) cycles leading to fragmentation of the particles that remain electrically isolated. Dimensional integrity of the electrode material during alloying/dealloying process was maintained by coating them with amorphous carbon.[45]

1.8. Conclusions:

Looking at the number of reports that employed HC based carbon structures in recent years, it is sure to be considered as an emerging material. The future directions would be guided by efforts in the unexplored areas which would possibly lead to HCs of improved properties. As the method of synthesis remains simple, the possibility of utilising different solvent combinations can be tried in a view to obtain HC with different morphologies and surface properties. New synthetic route for multiferroic materials by utilising the reactive carbon interface is one such example. The potential of HC in biology is also yet to be fully exploited. Extending the current knowledge of HC coating would certainly evolve into a general strategy of making any inorganic material cell permeable but yet remain biocompatible. However, it would also be worthy to study the leaching of toxic encapsulations within the carbon structures.

1.9. References:

1. Fowler, W. A., *Rev. Mod. Phys.,* **1984,** 56, 149
2. http://en.wikipedia.org/wiki/Carbon
3. a) Dresselhaus, M. S.; Dresselhaus, G.; Eklund, P. C. *Science of Fullerenes and Carbon nanotubes* Academic Press, California, **1995**. b) Bundy, F. P. *J. Geophys. Res.* **1980**, *85*, 6930. c) Bundy, F. P.; Minomura, In S.; (ed.) *Solid State Physics Under Pressure*: *Recent Advances with Anvil Devices*, Reidel, Dordrecht, **1985**.

4. Kittel, C. *Introduction to Solid State Physics*. John Wiley and Son, New York, 6th ed. **1986**.
5. Robertson, J. *Advances in Physics*, **1986**, *35*, 317.
6. a) Novoselov, K. S., *et al.*, *Science,* **2004,** 306, 666. b) Novoselov, K. S. *et al.*, *Proc. Natl. Acad. Sci. USA,* **2005**, 102, 10451.
7. Kroto, H. W.;. Heath, J. R.; ÒBrien, S. C.; Curl, R. F.; Smalley, R. E. *Nature* **1985**, *318*, 162.
8. Krätschmer, W.; Lamb, L. D.; Fostiropoulos, K.; Huffman, D. R. *Nature* **1990**, *347*, 352.
9. a) Ijima, S. *Nature* **1991**, *354*, 56. b) Hiraoka, T.; Yamada, T.; Hata, K.; Futaba, D. N.; Kurachi, H.; Uemura, S.; Yumura, M.; Iijima, S. *J. Am. Chem. Soc*. **2006**, *128*, 1338. c) Panchakarla, L. S.; Govindaraj, A.; Rao, C. N. R. *ACS Nano* **2007**, *1*, 494. d) Hofmann, S.; Sharma, R.; Ducati, C.; Du, G.; Mattevi, C.; Cepek, C.; Cantoro, M.; Pisana, S.; Parvez, A.; F. C.-Sodi, Ferrari, A. C.; R. D-Borkowski, Lizzit, S.; Petaccia, L.; Goldoni, A.; Robertson, J. *Nano Lett.* **2007**, *2*, 602.
10. Tuinstra, F.; Koenig, J. L.; *J. Chem. Phys.* **1970**, *53*, 1126.
11. a) Bi, X.-X.; Jagtoyen, M.; Derbyshire, F. J.; Eklund, P. C.; Endo, M.; Chowdhury, K. D.; Dresselhaus, M. S. *J. Mat. Res.* **1995**, 10. b) Knight, D. S.; White, W. B. *J. Mat. Res*. **1989**, *4*, 385.
12. a) Dresselhaus, M. S.; Dresselhaus, G.; Eklund, P. C.; Saito, R. *Optical and Electronic Properties of Fullerenes and Fullerene Based Materials* Shinar, J.; Vardeny, Z. V.; Kafafi, Z. H. (eds.), Dekker, New York, **1999**, *8*, 217. b) Zhang, L.; Jia, Z.; Huang, L.; ÒBrien, S.; Yu, Z. *J. Phys. Chem. C.* **2008**, *112,*13893. c) Ando, Y.; Zhao, X.; Shimoyama, H.; Sakai, G.; Kaneto, K.; *J. Inorg. Mater*. **1999**, *1*, 77.
13. a) Koidl, In P.; Oelhafen, P. (eds.), *Amorphous Hydrogenated Carbon Films* **1987** European Materials Research Society, Les Editions de Physique, France, Vol. XVII.

b) Pollock, J. T. A.; Wichinski. L. S.; Hanker, In J. S.; Giammara, B. L. (eds.), *Biomedical Materials and Devices* **1987**, vol. 110. Materials Research Society, Pittsburgh, PA.

14. Katnelson, M. I. *Mat. Today*. **2007**, *10*, 1.
15. Tutt, L. W.; Kost, A. *Nature* **1992**, *356*, 225.
16. Sariciftci, N. C.; Heeger, A. J. *Int. J. Mod. Phys. B*. **1994**, *8*, 237.
17. Regueiro, M. N.; Monceau, P.; Hodeau, J-L. *Nature* **1992**, *355*, 237.
18. Tong, Q.-Y.; Eom, C.B.; Gösele, U.; Hebard, A. F. *J. Electrochem. Soc.* **1994**, *141*, L137.
19. Balooch, M.; Hamza, A. V.; *Appl. Phys. Lett.* **1993**, *63*, 150.
20. Wu, H. J.; Hirschon, A. S.; Malhotra, R.; Wilson, R. B. *Preprints of Papers ACS, Fuel Chemistry Div.* **1994**, *39*, 1233.
21. Shigematsu, K.; Abe, K.; Mitani, M.; Tanaka. K. *Fullerene Sci & Tech.* **1993**, *1*, 309.
22. Cohen, J.; Lawandy, N. M.; Suuberg, E. M. *Energy & Fuels*, **1994**, *8*, 810.
23. a) Ellis, A. V.; Vijaymohanan, K.; Goswami, R.; et al. *Nano Lett*, **2003**, 3, 279. b) Ou, Y.-Y.; Huang, M. H. *J. Phys. Chem. B.* **2006**, *110*, 2031.
24. Jiang, K.; Eitan, A.; Schadler, L. S.; Ajayan, P. M.; Siegel, R. W.; Grobert, N.; Mayne, M.; Reyes-Reyes, M.; Terrones, H.; Terrones, M. *Nano Lett.* **2003**, *3*, 275.
25. Tsang, S. C.; Chen, Y. K.; Harris, P. J. F.; Green, M. L. H. *Nature* **1994**, *372*, 159.
26. a) Hiura, T.; Ebbesen, T. W.; Tanigaki, K. *Adv. Mater*, **1995,** *7*, 275. b) Hwang, K. C. *J. Chem. Soc. Chem. Commun.* **1995**, 173. c) Lago, R. M.; Tsang, S. C.; Lu, K. L.; Chen, Y. K.; Green, M. L. H. *J. Chem. Soc. Chem. Commun.* **1995**, 1355.
27. Georgakilas, V.; Pantarotto, D.; Bianco, A.; Briand, J. P.; Prato, M. *Chem. Commun.* **2002**, *24*, 3050.
28. Zubay, G. L.; Parson, W. W.; Vance, D. E. *Principles of Biochemistry*. **1995**, Wm. C. Brown Publishers.

29. a) Kieboom, A. P. G.; van Bekkum, H. *Starch Conversion Technology*, Dekker: New York, **1986**. b) Kuster, B. F. M.; *Carbohydr. Res.* **1977**, *54*, 177. c) Kuster, B. F. M.; Temmink, H. M. *G. Carbohydr. Res.* **1977,** *54***,** 185. d) Kuster, B. F. M.; van der Baan, H. S. *Carbohydr. Res.* **1977,** *54***,** 165. e) McKibbins, S. W.; Harris, J. F.; Saeman, J. F.; Neill, W. K. *For. Prod. J.* **1962,** *12***,** 17. f) Pecina, R.; Bonn, G.; Burtscher, E.; Bobleter, *J. Chrornatogr.* **1984**, *287*, 245.

30. a) Lourvaniji. Rorrer, *Ind. Eng. Che. Res*, **1993**, *2*, 3, 11. b) Lourvaniji. Rorrer, *Appl. Catal. A.***1994**, *109*, 147.

31. Sun, X.; Li, Y. *Angew. Chem. Int. Ed.*, **2004**, *43*, 597.

32. a) Yu, S-H.; Cui, X.; Li, L.; Li, K.; Yu, B.; Antoneitti, M.; Cölfen, H. *Adv. Mat*. **2004**, *16*, 1636. b) Sun, X.; Li, Y.; *Adv. Mat*. **2005**, *17*, 2626. c) Zheng, M.; Cao, J.; Chang, X.; Wang, J.; Liu, J.; Ma, X. *Mater. Lett.* **2006**, *60*, 2991.

33. a) Yao, C. et al. *J. Phys. Chem. C*., **2007**, 111, 15141. b) Shin, Y.; Wang, Li-Q.; Bae, In-T.; Arey, B. W.; Exarhos, G. J. *J. Phys. Chem. C*. **2008**, *112*, 37, 14236.

34. Wang, Q.; Li, H.; Chen, L. Q.; Huang, X. J. *Solid State Ionics* **2002**, 43.

35. LaMer, V. K. *Ind. Eng. Chem.* **1952***, 44,* 1270.

36. Jiang, P.; McFarland, M. J. *J. Am. Chem. Soc.* **2004**, *126*, 13778.

37. Wostyn, K.; Zhao, Y.; Schaetzen, G de.; Hellemans, L.; Matsuda, N.; Clays, K.; Persoons, A. *Langmuir* **2003**, *19*, 4465.

38. Caruso, F. *Top. Curr. Chem*. **2003**, *227*, 145.

39. Jiang, P.; Bertone, J. F.; Colvin, V. L. *Science* **2001**, *291*, 453.

40. Caruso, F. *Adv. Mater*, **2001**, *13*, 11.

41. a) Kattumuri, V.; Chandrasekar, M.; Guha, S.; Raghuraman, K.; Katti, K. V.; Gosh, K.; Patel, R. J. *Appl. Phys. Lett.*, **2006**, *88*, 153114. b) Sun, X.; Li, Y. *Langmuir*, **2005**, *21*, 6019.

42. Zhong, Z.; Sim, D.; Teo, J.; Luo, J.; Zhang, H.; Gedanken, A. *Langmuir*, **2008**, *24*, 4655.

43. Yang, R.; Li, H.; Qiu, X.; Chen, L. *Chem. Eur. J*., **2006**, *12*, 4083.

44. Makowski, P.; Cakan, R. D.; Antoneitti, M.; Goettmann, F.; Titirici, M-M. *Chem Comm*. **2008**, 999.

45. Sun, X.; Liu, J.; Li, Y. *Chem. Mater*., **2006**, *18,* 3486.

Summary

This chapter deals with the use of templates in the synthesis of nanomaterials. Hydrothermal treatment of aqueous solution of glucose leads to the formation of highly functionalised amorphous carbon structures as a result of continuous dehydration and polymerisation. These structures are usually spherical. The carbon spheres have been used directly without any modifications as templates to synthesise hollow spheres of metal oxides. Using the same technique, functionalised amorphous carbon was successfully coated on the surface of other inorganic nanostructures. The amorphous carbon was also obtained in the form of nanotube brushes by using polycarbonate membranes as templates. The as-synthesized nanotube brushes retain all the functionalities as that of the carbon spheres. Further Ga_2O_3 and GaN nanotube brushes were synthesized using these carbon nanotube brushes as templates.

A paper based on this study has been published as a letter in *J. Phys. Chem. C,* **2008**, *111 (2)*, 510.

2.1. Introduction:

The synthesis of inorganic nano structures is an evergreen field, constantly aiming for better standards of quality, yield and generic approach. In a growing number of challenges in catalysis, cosmetics, drug / gene delivery, hydrogen production / storage, photonics, photovoltaics and rechargeable batteries the use of nanomaterials is certainly expected to improve the performance. For example, the large surface to volume ratios, which is unique for nanomaterials can significantly contribute to their performance by providing large areas of interfaces.[1] Of late, the interests in hollow nanostructures also increased due to their low density, confined environment, ability to store and controlled release. A number of applications like solid state lubricants,[2] hydrogen storage,[3] catalysis,[4] biomolecule detection,[5] pollution treatment,[6] encapsulation of nuclear fusion materials[7] and nanoreactors[8] involve hollow structures. In few other applications, the void in hollow particles has been used to modulate refractive index while in some cases it has been used to accommodate the cyclic changes in volume accompanying intercalations/phase changes. This chapter mainly deals with the synthesis of hollow nanostructures.

Before 1998, most hollow particles were of spherical shape and were using micro scale methods such as spray-drying or gas-blowing.[9] Templating process in the synthesis of nanomaterials was inspired in 1970s and 1980s by the works by Matijevic´[10a] and others who demonstrated core/shell type colloids, primarily in the context of surface functionalization. Synthesis of hollow spheres using microemulsions is also known in the literature.[10b] Microemulsions of oil in water or water in oil stabilized by suitably charged surfactants have been used to electrostatically assemble the metal precursors at the interface. The template here can be removed by warming the solution. In 1998 Caruso's[11] report established the synthesis of hollow nanospheres using colloidal templates. Around the same time, C. R. Martin's[12] group also demonstrated the use of anodic alumina discs as hard templates to

synthesise nanotubes of oxides and conductive polymers. Both approaches lead to a new, more versatile, synthesis paradigm for hollow structures based on hard-templating methods. Indeed, starting around 2001, there has been a large increase in research activity focused on synthesis of hollow micro/nanostructures based on hard and soft templates. Reviews of specialized elements of the literature, for example, synthesis of core/shell structures[13] or synthesis of hollow particles based on specific approaches, such as the Kirkendall effect, [14] Ostwald ripening[15] can also be found.

The common synthetic approaches to obtain hollow nanostructures can be broadly classified into three categories:[16] (1) conventional hard templating synthesis (e.g. silica, polymer nanostructures etc) (2) soft templating synthesis (e.g. gels, DNA etc) and (3) template-free methods (e.g. gas bubbles). Irrespective of the type of templates used, the primary requisite is the availability of the functional groups on the surface of the templates to interact with the precursors of the material interested. The general protocol of the template based synthesis is given below.

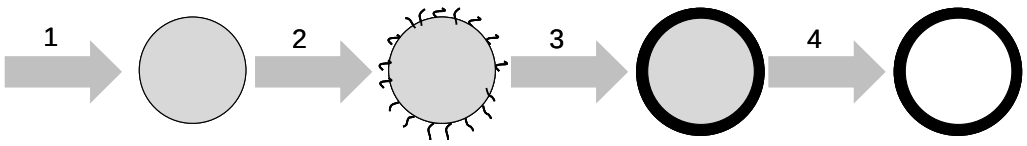

Scheme 1: Schematic illustration of hard template approach to synthesise hollow structures.

Preparation of hollow structures by templating is conceptually straightforward. In general, it involves the four major steps as illustrated in Scheme 1:

(1) Preparation of templates.

(2) Functionalization/modification of template surface to achieve favourable surface properties.

(3) Coating the templates with designed materials or their precursors by various approaches, possibly with post-treatment to form compact shells.

(4) Selective removal of the templates to obtain hollow structures.

In general, the narrow size distribution, ready availability in relatively large amounts, availability in a wide range of sizes from commercial sources, and simplicity of their synthesis must be considered important in the making of hard templates. Other colloidal systems, such as carbon nanospheres and nanoparticles of metals and metal oxides, have also been used as templates for preparation of hollow structures.[17] Step 4 is in principle the simplest. It typically entails selective etching of the template in appropriate solvents or calcination of the template at high temperatures. In both the approaches, special care is required to prevent collapse of the shells during template removal. For example, when using organic solvent to dissolve template latex particles, swelling of the polymer can cause rupture of the hollow structure, causing the shell to manifest uncontrolled shape change. Removing carbon rich templates can lead to good crystallinity in the product because of the exothermic reaction involved. Step 3 is generally regarded as the most challenging because it requires robust methods for efficiently precipitating shell materials on substrates with sizes in the nano-/micrometer range. Incompatibility between the template surface and shell material can be overcome by functionalizing / modifying the template with special functional groups like –OH, -COOH,[18] -SO_3H,[19] electrostatic charges[20] etc, before applying subsequent coating/deposition of shell materials. Step 2 and Step 3 together therefore constitute a coating scheme to form compact shells on any arbitrary template particles. Unsurprisingly, the most exciting research in the field has focused on developing flexible coating schemes suitable for a broad range of materials. This effort has led to considerable progress during the past decade.

2.2. Scope of the present investigation:

It has been realized that the hydrothermal treatment of glucose (chapter 1) produces carbon spheres with their surface rich in functional groups like -CHO, -OH and -COOH. The carbon spheres derived from glucose has been abbreviated as CSP in this chapter and other chapters. An impressive way to utilise the presence of surface functional groups on CSP is to employ them as templates. Thus the as synthesized CSP when soaked in the metal salt solution followed by a heat treatment in air will simultaneously remove the template carbon spheres at the core and also form metal oxide hollow spheres. Many technologically important hollow spheres can be synthesized using a functionalised template which was obtained at a lower temperature. It was almost at the same time as we obtained our results on hollow spheres that Y. Li's group also demonstrated the use of glucose derived carbon spheres as templates to synthesise hollow spheres.[21] An important observation described in chapter 1 concerning the amphiphilicity of the CSP surface has been testified in this chapter. CSP could interact well with both hydrophilic precursors (metal salts) and hydrophobic precursors (TEOS and Titanium isopropoxide) to form hollow spheres. This is one of the unique properties of CSP. Secondly, coating of inorganic nanostructures with CSP was also identified as an important problem. The motivation for this work is as follows. As it will be seen in chapter 5, the CSP were proved to be permeable and non toxic to the mammalian cells, it would be necessary to develop a method to coat many potentially useful inorganic structures (like Fe_3O_4, CdSe, $MnFe_2O_4$ etc) with CSP so that they can be successfully carried inside the cells without causing any cytotoxicity. In these cases the inorganic nanostructures which are to be coated with HC will act as a template. Besides that, we also obtained the functionalised carbon template in a different morphology of nanotube brushes.[22] However; it was our interest to obtain the nanotube brushes of GaN as there were not many reports on

chemical routes to obtain them. GaN nanotubes obtained through this method can be considered as the first chemical route to obtain aligned structure.[23]

2.3. Experimental section:

a. Materials:

α D(+) glucose**,** $Zn(NO_3)_2.6H_2O$, $Al(NO_3)_3.9H_2O$, Ga_2O_3, tetraethylorthosilicate (TEOS), cetyltrimethylammonium bromide (CTAB), ethylene glycol, polyethylene glycol, tetramethylorthoxysilane (TMOS), $FeCl_3.6H_2O$, $FeCl_2$, $MnCl_2.4H_2O$, ethanol, methanol, sodium acetate, NaOH, poly(diallyldimethylammonium) chloride 20% in water (PDADMAC) (M.wt 400000-500000) and $SnCl_2.2H_2O$ were purchased at an analytical pure grade and were used without any further purification. A 25 mL and 60 mL Teflon lined and sealed autoclaves were fabricated locally. Aqueous NH_3 used was 10 % in concentration. For gaseous ammonia 99.95% pure UHP gas was used. Polycarbonate membranes of 220 nm average diameter, 7-22 μm in thickness, pore density 109 pores per cm^2 (Millipore-GTTP 04700) was purchased. Muffle furnace used in this work was purchased from Elite thermal systems (UK).

b. Synthesis of carbon spheres from glucose (CSP):

2.5 g of glucose was dissolved in 22 mL of water to form a clear solution. It was placed in a 25 mL Teflon sealed stainless steel container at 180 ^oC for 12 h. In some cases, 60 mL volume autoclave was used during which a solution of 5 g of glucose in 50 mL water was used. The puce products were isolated and purified by repeated washing ethanol after which the samples were dried at 80 ^oC for 4 h. The as- carbon spheres were used as templates to synthesise the hollow spheres.

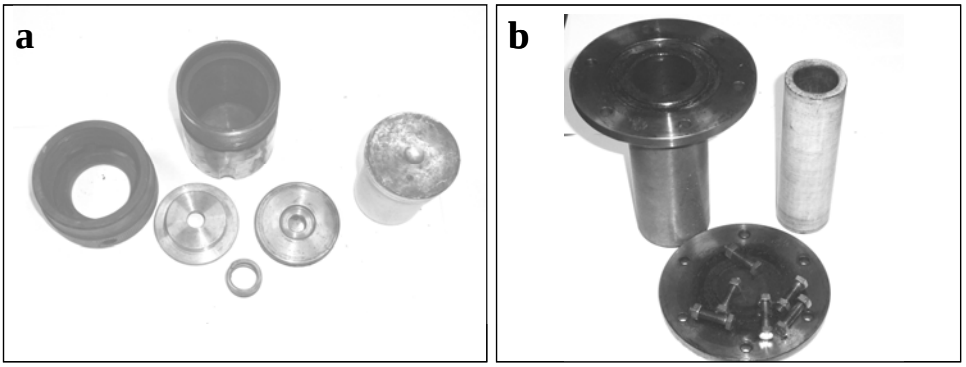

Figure 1: Digital photograph of Teflon lined stainless steel autoclave. a) 25 mL b) 60 mL volume.

c. $ZnAl_2O_4$ hollow spheres:

4.65 g of $Zn(NO_3)_2.6H_2O$ and 11.63 g of $Al(NO_3)_3.9H_2O$ were dissolved in 30 mL of water. The CSP (0.25 g) were added to the above solution and the whole mixture was sonicated for 15 min, followed by 12 h of aging. The supernatant solution was decanted out and the black residue obtained was centrifuged five times with water and ethanol. Desired amount of aq. NH_3 solution was added to make its pH 8-10. The mixture was transferred to a 25 mL teflon lined stainless steel autoclave and the temperature was maintained at 180 ^oC for 20 h after which it was allowed to air cool to room temperature. The supernatant was decanted out and the residue obtained was washed with ethanol and dried at 80 ^oC for 3 h. The template was finally removed by heating at 600 ^oC for 5 h in air.

d. SiO_2 hollow spheres:

0.1 g of as-prepared CSP were sonicated in 3 mL of TEOS for 15 min. The TEOS coated CSP were separated by centrifuging at 5000 rpm for 5 min. The supernatant was discarded. The residual carbon spheres were dried at 80 ^oC for 6 h. The process was repeated thrice to get a coating of desired thickness. The template was finally removed by calcination at 500 ^oC for 5 h in air and then at 1000 ^oC for 30 min to get a well condensed SiO_2 walls.

e. SnO_2 hollow spheres:

SnO_2 hollow spheres were according to a modified procedure.[24] 2.3 g of ethanol and 0.282 g of $SnCl_2.2H_2O$ (0.0025 mole) were mixed together and stirred thoroughly for 15 min. Water was added to this solution in a volume ratio of 3:1 respectively at room temperature. 0.1 g of the CSP were added to the above solution and sonicated for 15 min. The mixture was maintained at 45 ^oC for four days for the hydrolysis and condensation. The CSP were later separated by centrifugation and dried at 80 ^oC for 3 h. The template was removed by heating at 550 ^oC for 5 h in air.

f. Synthesis of Fe_3O_4 nanoparticles:

To a 25 mL of 0.4 N HCl solution, 5.2 g of $FeCl_3 \cdot 6H_2O$ and 2.0 g of $FeCl_2$ were successively dissolved in the solution with stirring. The resulting solution was added drop-wise into 250 mL of 1.5 M NaOH solution under vigorous stirring. The last step generated an instant black precipitate. The precipitate was isolated by centrifuge, and the supernatant was discarded. Purified deoxygenated water was added to the precipitate and the solution decanted after centrifugation at 4000 rpm.[25]

g. Synthesis of Fe_3O_4 and $MnFe_2O_4$ submicron spheres:

The magnetic submicron spheres were synthesized according to the procedure reported.[26] $FeCl_3 \cdot 6H_2O$ (1.35 g, 5 mmol) was dissolved in ethylene glycol (40 mL) to form a clear solution, followed by the addition of sodium acetate (3.6 g) and polyethylene glycol (1.0 g). The mixture was stirred vigorously for 30 min and then sealed in a teflon lined stainless-steel autoclave (50 mL capacity). The autoclave was heated to and maintained at 200 ^oC for 8-14 h, and allowed to cool to room temperature. The black products were washed several times with ethanol and dried at 60 ^oC for 6 h. The above process can be extended to the synthesis of MFe_2O_4 microspheres by coprecipitation of M^{II} and Fe^{III} chlorides (M^{2+}/Fe^{3+}=0.5). For example, a mixture of $MnCl_2 \cdot 4H_2O$ (0.50 g, 2.5 mmol) and $FeCl_3 \cdot 6H_2O$

(1.35 g, 5 mmol) under the same reaction conditions as used for the synthesis of Fe_3O_4 microspheres, produced microspheres of $MnFe_2O_4$.

h. Synthesis of mesoporous SiO_2 spheres:

Monodispersed spherical mesoporous silica spheres were synthesized using a reported procedure.[27] 3.52 g of CTAB and 2.28 ml of 1 M sodium hydroxide solution were dissolved in 800 g of methanol/water (50/50 w/w). Then 1.32 g of TMOS was added to the solution with vigorous stirring at 25 ^oC. After the addition of TMOS, the clear solution turned opaque suddenly and resulted in a white precipitate. After 8 h of continuous stirring the mixture was aged overnight. The white powder was then filtered and washed with distilled water at least three times, and dried at 100 ^oC for 24 h. The powder obtained was calcined in air at 700 ^oC for 6 h to remove the organic species.

i. Synthesis of inorganic core and carbon shell nanoparticles:

A common protocol was developed to coat the inorganic nanostructures with functionalised carbon. A suspension of PDADMAC solution in water (1 g in 25 mL H_2O) was made. To this 100 mg of the nanoparticles were added and homogenised using a glass rod. The adsorption was allowed to occur by keeping the suspension undisturbed for 1 h after which the nanoparticles were removed either magnetically or by centrifuging at 10000 rpm for 10 min. The as obtained precipitate was usually washed with water twice before transferring into an autoclave (60 mL) containing 0.5 M aqueous glucose solution. The autoclave was maintained at 180 ^oC for 12 h. After the desired time the autoclave was allowed to cool naturally. The nanoparticles@HC was separated using a magnetic bar and dried at 40 ^oC for 4 h.

j. Synthesis of amorphous carbon nanotube brushes (a-CNT):

The thermal decomposition of glucose as done in the synthesis of carbon spheres was performed in the presence of polycarbonate membranes. The reaction occurred inside the

pores of a polycarbonate membranes under hydrothermal condition. In a typical procedure, polycarbonate membranes (3 numbers) were taken in a 25 mL Teflon lined and sealed autoclave containing 22 mL of 0.5 M glucose (Aldrich) solution in water. The temperature of the autoclave was maintained at 180 °C for 6 h after which it was allowed to cool to room temperature. The brownish liquid, rich in CSP was discarded. The membranes that had turned brown are a composite of amorphous carbon deposited along the inner walls of polycarbonate membrane. This was washed with deionized water and ethanol several times. They were later oven dried at 40 °C for 1 h. The a-CNT as such can also be liberated from the membrane by treating the composite with CH_2Cl_2 which selectively dissolves polycarbonate.

k. Synthesis of GaN nanotube brushes:

The precursor for gallium was $GaCl_3$ which was prepared by dissolving 0.4 g of Ga_2O_3 in 10 mL of hot HCl. The a-CNT-polycarbonate composite membranes were soaked in the HCl solution for over 12 h. This was followed by washing the sample twice in water followed by drying at 80 ^oC for 4 h. No treatment with dichloromethane need to be performed. The polycarbonate and amorphous carbon templates are removed simultaneously during calcination step. The gallium adsorbed carbon tubes were finally calcined at 500 ^oC for 5 h. The as prepared Ga_2O_3 nanotube brushes were heated in the presence of gaseous NH_3 at 800 ^oC for 3 h to form GaN analogues.

2.4. Characterization:

Morphology of the samples was analyzed by a FESEM (FEI Nova-Nano SEM-600, Netherlands). TEM images were recorded with a JEOL JEM 3010 instrument (Japan) operated with an accelerating voltage of 300 kV. XRD characterization was done at 25 ^oC with a Bruker-D8 and Rich-Siefert 3000-TT diffractometer employing Cu Kα. Magnetic measurements were carried out with vibrating sample magnetometer in a physical property measurement system (Quantum Design, US) at 298 K.

2.5. Results and discussion:

The Figure 2 shows the digital photograph of carbon spheres and carbon tubes. In case of a-CNT, the dissolution of polycarbonate membrane left behind aligned nanotubes. At the macroscopic level, the sample after CH_2Cl_2 treatment looks silver to violet coloured under sunlight probably due to the presence of array of the dielectric nanotubes. Though this phenomenon is similar to those observed in photonic crystals, more in-depth study will be interesting.

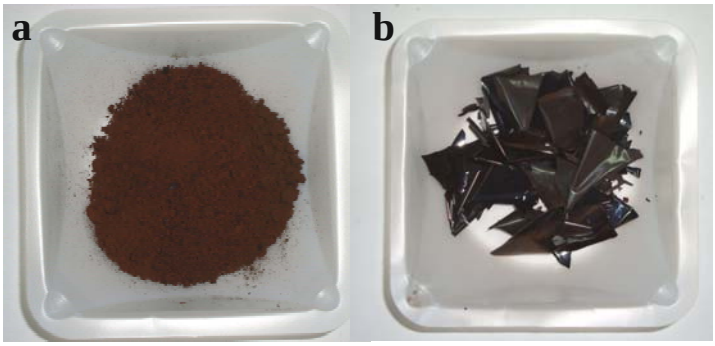

Figure 2: Digital photography image of a) CSP b) a-CNT-polycarbonate composite.

The microscopic features of CSP and a-CNTs were studied using electron microscopes. For the sample prepared from hydrothermal decomposition of glucose at 180 ^{o}C for 16 h, the size of the CSP varied from 300 – 500 nm (Figure 3). One can also bring down the size of these spheres to 40 – 100 nm by reducing the reaction time to 6 h. The TEM image of the CSP showed they are all dense spheres without any pores (Figure 4a). The continued use (for more than four reactions) of the autoclave for the synthesis of CSP produced a number of chain-like structures formed by linking of spheres (Figure 4b).

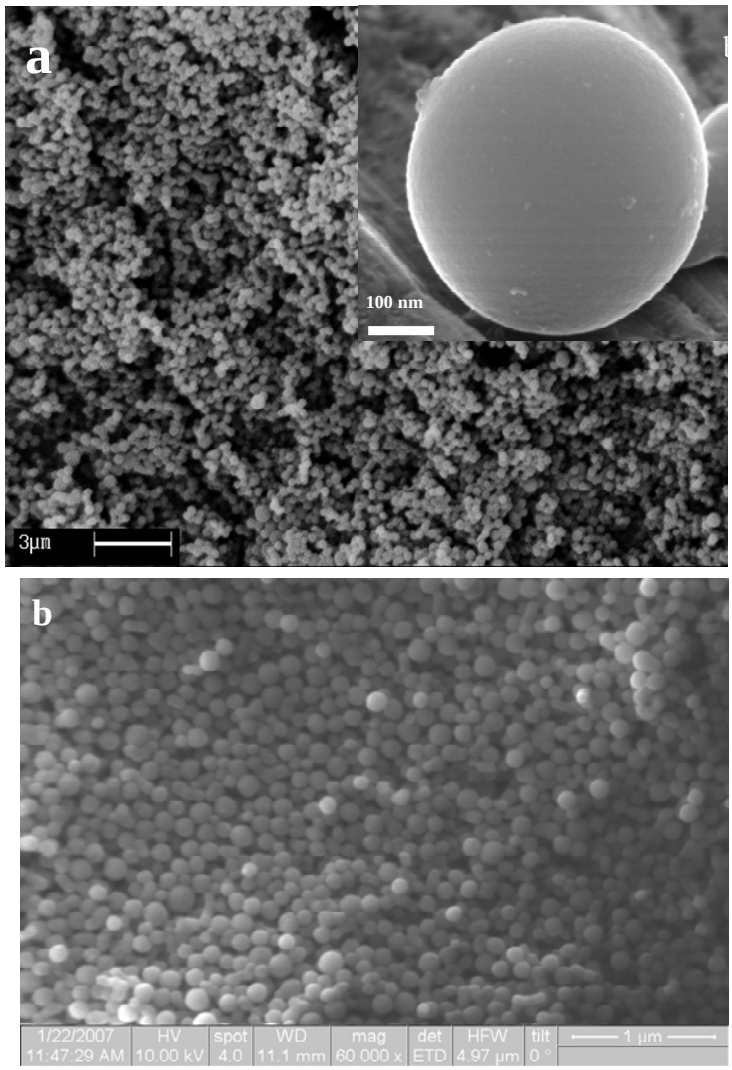

Figure 3: a) SEM image of CSP prepared at 180 ^{o}C for 16 h. Inset is the higher magnification image of a CSP prepared for 16 h. b) FESEM image of CSP prepared at 180 ^{o}C for 6 h.

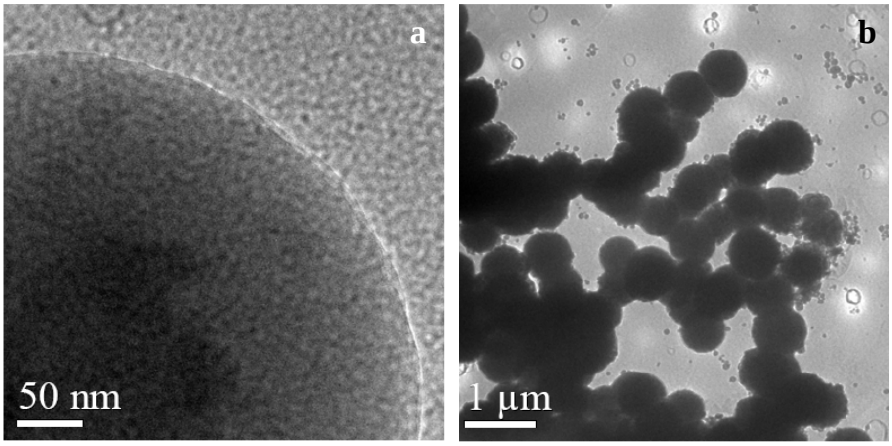

Figure 4: a) TEM image of CSP prepared at 180 ^{o}C for 16 h. b) TEM image showing chain-like structures of CSP.

In most cases, the walls of the Teflon container having the CSP of a previous batch could have nucleated the formation of CSP in subsequent reaction. A similar effect was also observed if acid impurities are present in the autoclave. It is therefore advised to take care of these parameters if one desires to have good quality spheres. Though the chemical composition and internal structure of the CSP differs drastically from the carbons prepared via high temperature pyrolytic routes (see chapter 1), it remains unaltered for CSP of various sizes and also with a-CNT. CSP and a-CNT retain a large amount of oxygen and hydrogen from the carbohydrates while the carbon structures derived from high temperature routes are predominantly graphitic. Our experiments suggest that the surface of the carbon spheres possess a negative zeta potential (ξ = -24 mV at pH 7.3). The Raman spectrum shows two broad and equally intense bands at 1580 and 1380 cm^{-1} which are due to graphitic and disordered structures respectively of the carbon (see chapter 1).

The as-synthesized CSP was used as template to make inorganic hollow structures. The simplified protocol was to adsorb the surface of the template with metal ions by placing them in a metal salt solution. The surface of the HC spheres being negatively charged due to the presence of –COOH and –OH groups readily adsorb the metal cations. On a subsequent calcination step, the metal ions form metal oxide network with the simultaneous removal of the HC template as CO_2 leading to the formation of hollow spheres.

Hollow Spheres

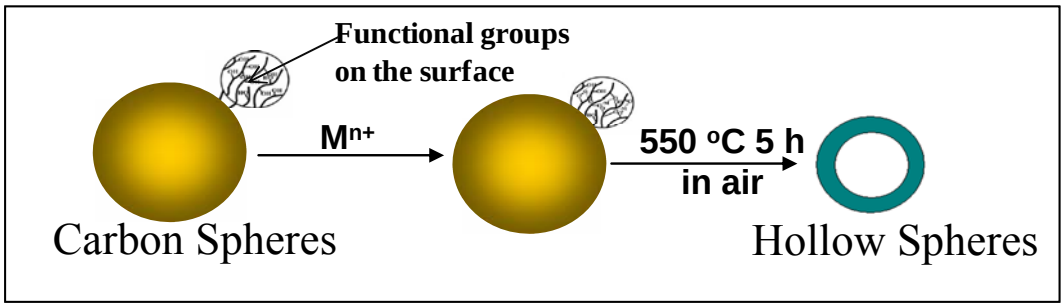

Figure 5: Synthesis of inorganic hollow spheres using carbon spheres as templates.

The general scheme for the formation of hollow spheres using HC spheres as templates is shown in Figure 5

Advantages of using CSP as template over other templates:

- No acid reflux or polyelectrolyte is required for functionalizing the template.
- Precursors can be simple metal salts or alkoxide.
- Thickness of the surface layer is determined by the time of soaking.

FESEM, TEM images and XRD patterns of $ZnAl_2O_4$, SnO_2 and SiO_2 hollow spheres are given in Figure 6, 7 and 8 respectively. The FESEM image shows that the spheres have retained their shape even after the calcination. They are uniform in size and high yield suggesting the high efficiency of the method employed.

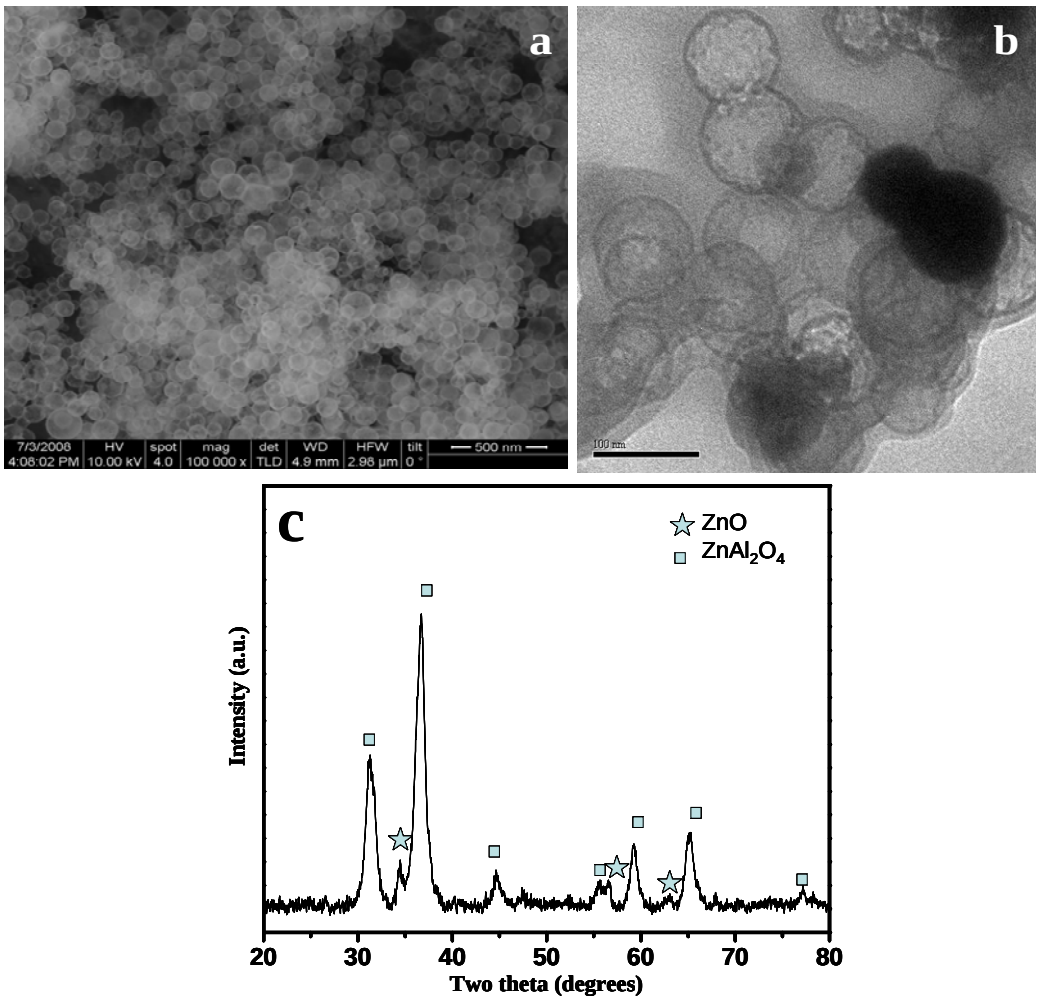

Figure 6: a) FESEM image b) TEM image and c) XRD pattern of $ZnAl_2O_4$ hollow sphere.

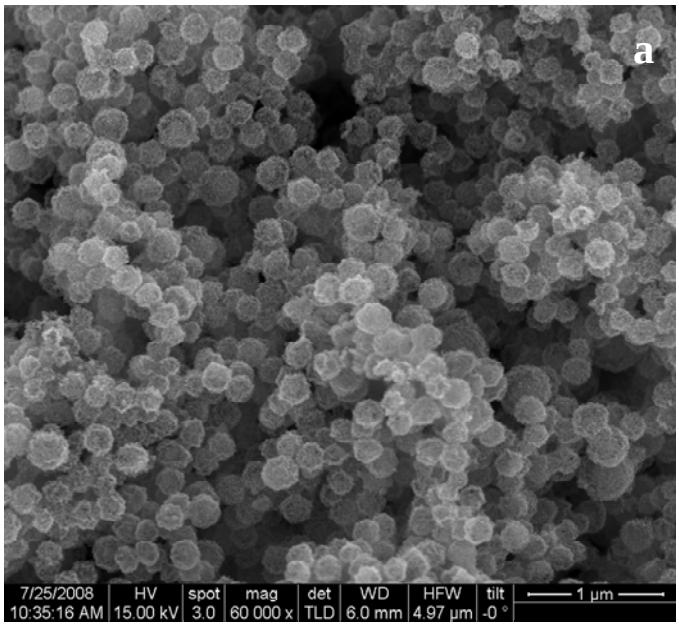
a
7/25/2008 | HV | spot | mag | det | WD | HFW | tilt
10:35:16 AM | 15.00 kV | 3.0 | 60 000 x | TLD | 6.0 mm | 4.97 µm | -0 °
1 µm

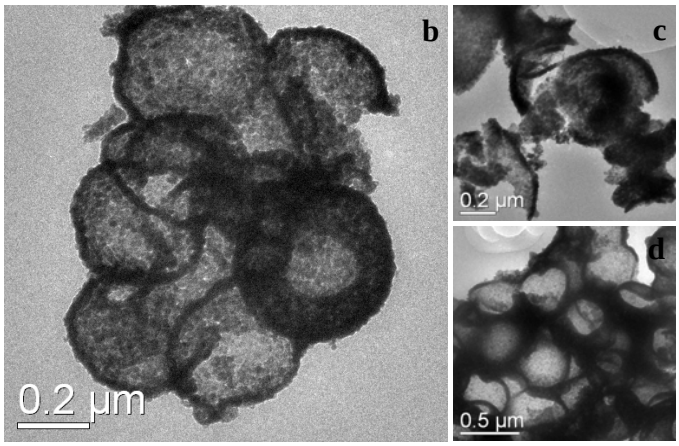
b
0.2 µm
c
0.2 µm
d
0.5 µm

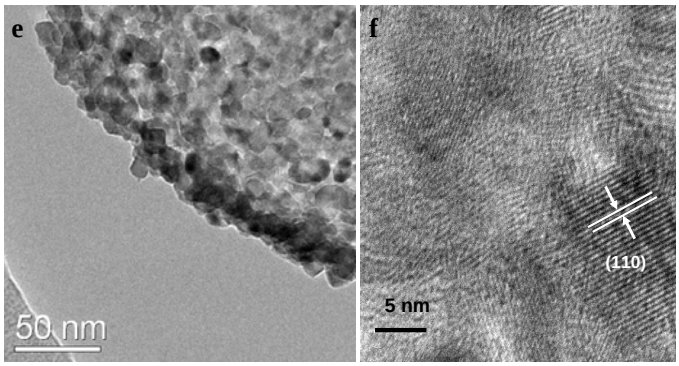
e
50 nm
f
(110)
5 nm

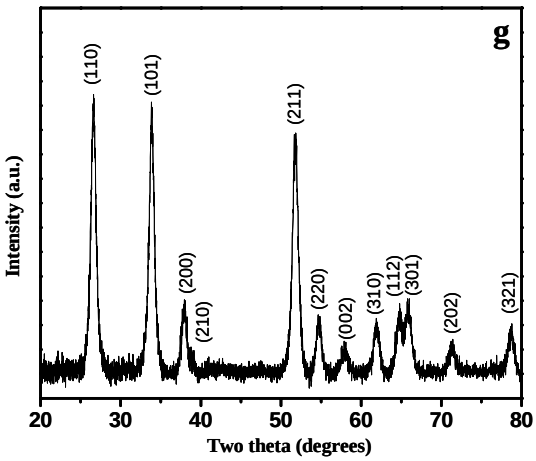

Figure 7: a) FESEM image b, c, d, e) TEM images f) HREM image g) XRD pattern of SnO_2 hollow spheres.

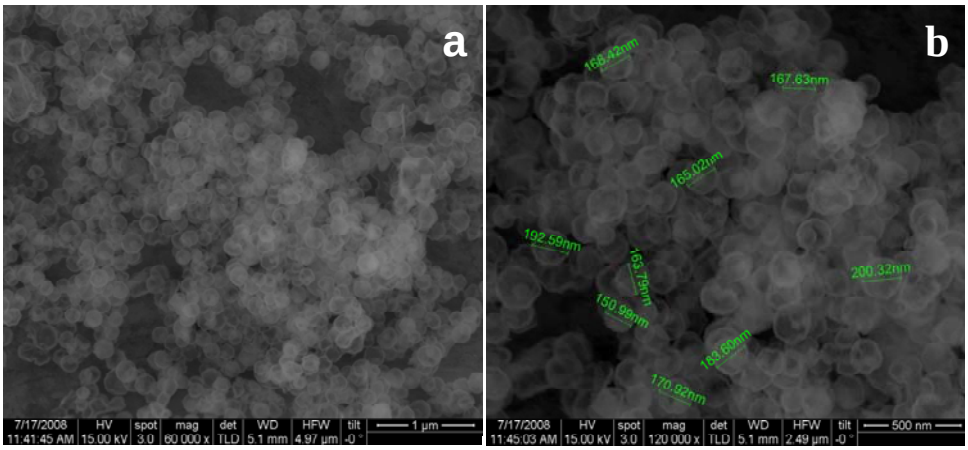

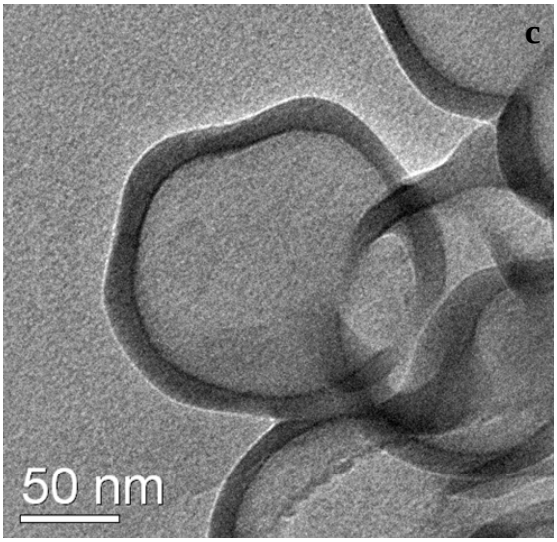

Figure 8: a, b) FESEM images, c) TEM image of amorphous SiO_2 hollow spheres.

The size of the hollow spheres are around 100 - 300 nm in diameter compared to a 400 nm diameter CSP template. This reduction in the size is expected as the precursors adsorbed on the surface of the template undergo hydrolysis and condensation to form highly dense oxide spheres. TEM analysis of the hollow spheres was also consistent with the FESEM images. The thickness of the walls of the hollow spheres varied from 10 – 25 nm. The walls of $ZnAl_2O_4$ and SnO_2 appeared to be porous made up of nanoparticles of 3 - 5 nm in size. However, SiO_2 hollow spheres appeared smooth without any clear distinction of particles. HREM image of the walls of SnO_2 hollow spheres showed a clear lattice spacing of 0.337 nm corresponding to the (110) plane of the cassiterite SnO_2.

XRD patterns suggests that $ZnAl_2O_4$ and SnO_2 are crystalline, while SiO_2 is amorphous with a broad peak at $2\theta = 20^o - 30^o$. XRD pattern of $ZnAl_2O_4$ hollow spheres showed traces of ZnO phase. Increasing the temperature of calcination, further favoured the formation of ZnO. In case of SnO_2, a single phase was formed with the diffraction peaks positioned at $2\theta = 26$, 33, 37 and 51^o which are respectively assigned to (110), (101), (200), (211) planes of the cassiterite phase of the tin oxide (JCPDF NO 05-0467). Amorphous nature of silica was confirmed by the absence of electron diffraction pattern and a broad XRD in the range of 2θ, $20 - 30^o$. As described earlier, it has been successfully shown that CSP can interact with both hydrophilic and hydrophobic precursors to form hollow spheres.

Core / shell structures:

As already described in the section 2, the motivation of obtaining inorganic core and functionalised carbon shell structures are for their potential biological applications. Materials like Fe_3O_4 and $MnFe_2O_4$ were chosen because they are widely applied as MRI contrast agents. Another important material is mesoporous silica which by virtue of ordered pores in the range of 2-50 nm has a large surface area which can be used for carrying drugs, labelling agents, antibodies etc.

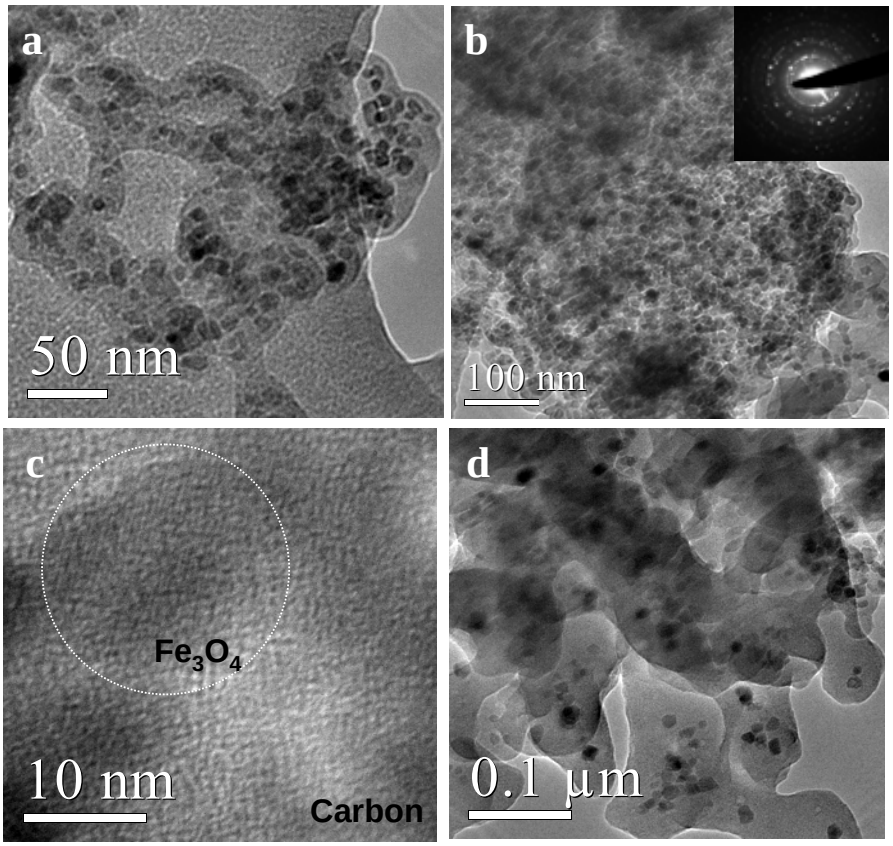

Figure 9: Coating of HC on Fe_3O_4 nanoparticles of size < 30 nm. a, b and d) TEM image. ED pattern of crystalline Fe_3O_4 is shown in inset of b. c) HREM image showing the composite structure of Fe_3O_4 particles well dispersed in HC matrix.

The presence of nanoparticles/submicron particles in the autoclave containing glucose, provides nucleation centres around which the coating of HC occurs. Surface of the nanoparticles which are already coated with polycation PDADMAC effectively interact with negatively charged oligomers of HC (Figure 14, chapter 1). However when Fe_3O_4 particles of 15 - 30 nm were used, it was observed that many nanoparticles were encapsulated within the carbon matrix (Figure 9). It is probable that the polymer wraps around many particles owing to their smaller size. In order to have a controlled coating, Fe_3O_4 particles were prepared by ethylene glycol route in which, monodispersed submicron spheres of Fe_3O_4 (100 nm) are formed by aggregation of Fe_3O_4 nanoparticles (10 nm). The FESEM image of Fe_3O_4 submicron spheres are given in Figure 10. The procedure is also versatile to prepare $MnFe_2O_4$

and other ferrite structure of similar morphologies. An inherent advantage of this morphology is that these particles can have higher magnetic moment than the isolated particles of similar size and also maintain their superparamagnetic behaviour. Both these properties are advantageous in biomedical applications wherein high magnetic moment can be used for field guided delivery and superparamagnetic behaviour can be used for MRI contrast purposes.

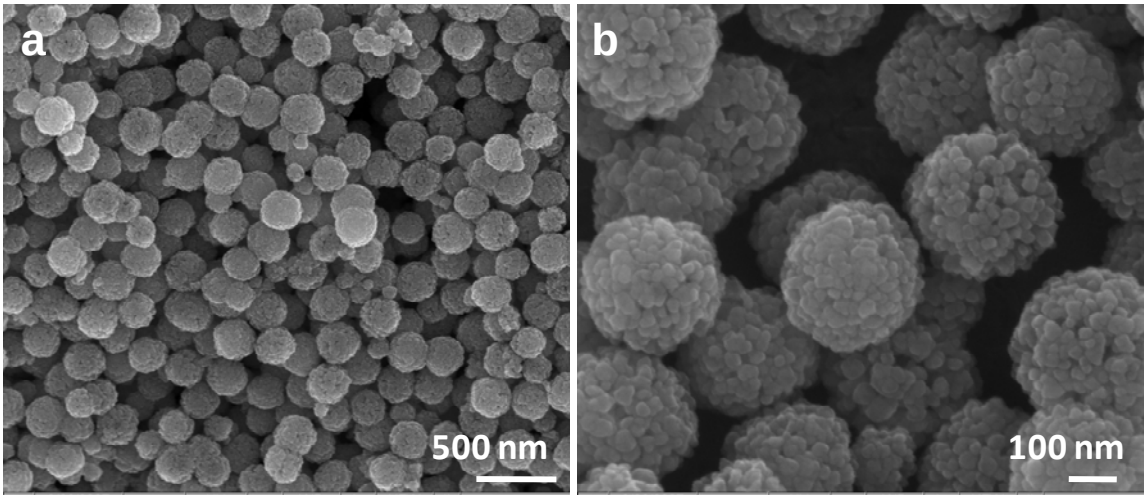

Figure 10: FESEM images of Fe_3O_4 submicron spheresa) low magnification and b) High magnification

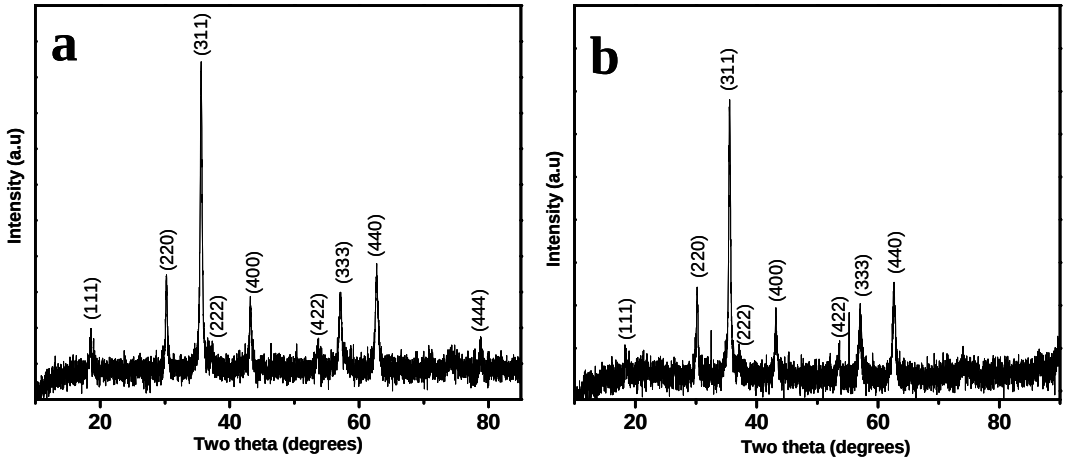

Figure 11: XRD patterns of submicron spheres of a) Fe_3O_4 and b) $MnFe_2O_4$.

Figure 11 shows the XRD patterns of the as synthesized Fe_3O_4 and $MnFe_2O_4$ (JCPDF 89-0950, 72-2403 respectively) submicron spheres. Figure 12 shows the low magnification

TEM images of Fe_3O_4 spheres coated with HC. In Figure 13 b, the thickness of coating can be measured around 20 nm. Figure 13a shows the HREM at the interface of Fe_3O_4 and HC. While Fe_3O_4 shows lattice fringes of crystalline Fe_3O_4, HC remains amorphous. In Figure 13c, ED pattern taken at the core suggests the polycrystalline nature of Fe_3O_4.

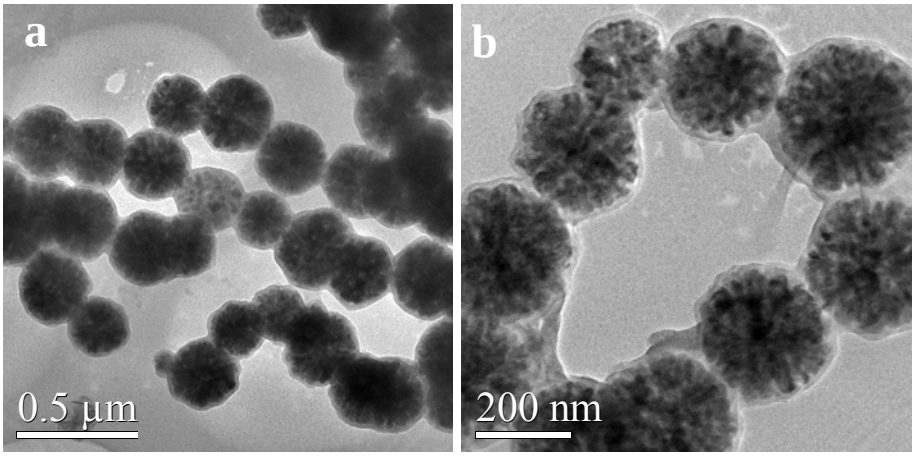

Figure 12: a and b) TEM image of Fe_3O_4 spheres coated with HC.

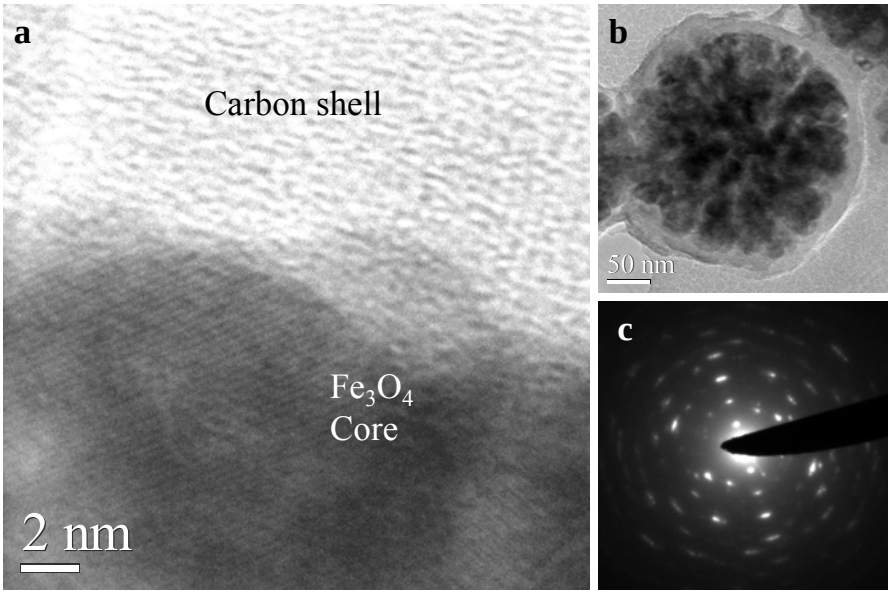

Figure 13: a) HREM image of Fe_3O_4 submicron spheres coated with HC (carbon shell). b) TEM image of a single sphere coated with HC. c) ED pattern of the crystalline Fe_3O_4 core.

The magnetisation curve of Fe_3O_4 submicron spheres prepared for different time durations (8 and 14 h) are given below. Both the samples are superparamagnetic which is suggested by

absence of coercivity. But the magnetic moment of 8 h sample is slightly higher than that of 14 h sample (Figure 14a) though their sizes are in similar distribution. In Figure 14 b, the effect of carbon coating on the magnetic spheres is shown wherein a decrease of the moment upto 25% is observed. In a similar way, mesoporous silica spheres were also successfully coated with HC as seen in the TEM image (Figure 15).

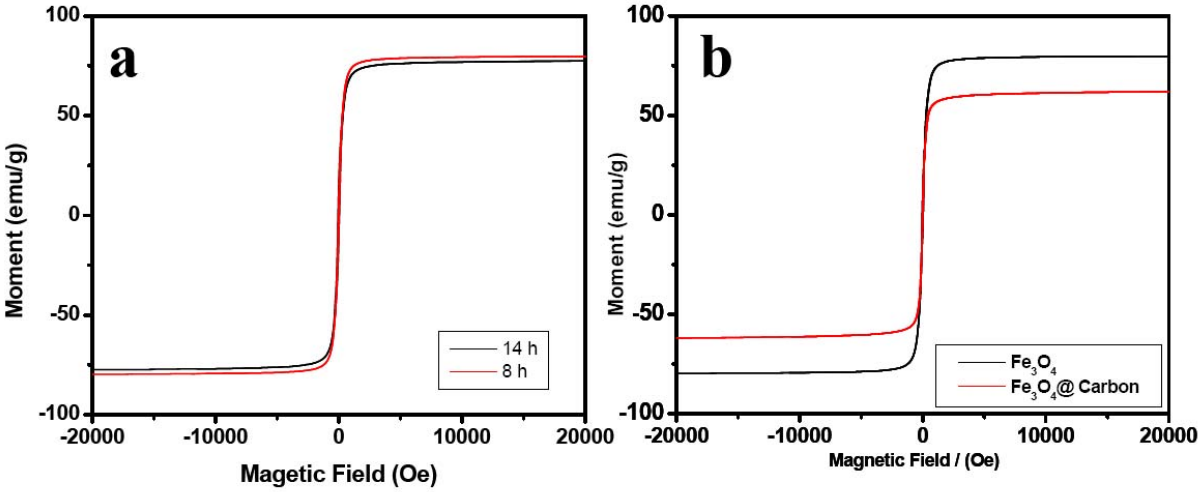

Figure 14: a) M vs H plot of Fe_3O_4 submicron spheres synthesized by a reaction of duration 8 and 14 h. b) M vs H plot of Fe_3O_4 spheres synthesized at 8h was coated with HC. The measurement was performed at 298 K.

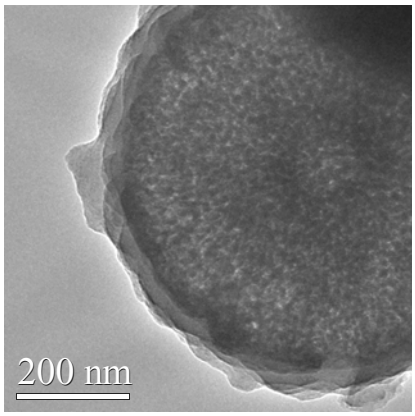

Figure 15: TEM image of mesoporous silica sphere coated with HC.

Aligned Nanotubes Brushes:

As mentioned earlier, it was also possible to obtain glucose derived carbon in the form of aligned nanotubes by using porous polycarbonate membrane or anodic alumina disc

as templates. The template could be removed by dissolving the polycarbonate-HC composite in CH_2Cl_2. Figure 16 explains the protocol to obtain a-CNT using this method

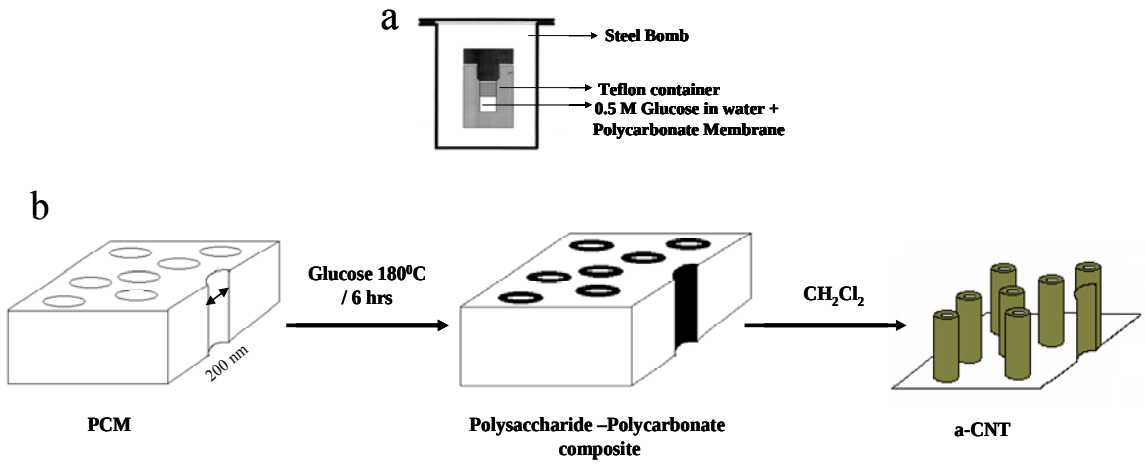

Figure 16: a) Cartoon of cross section of autoclave. b) Scheme showing the formation of a-CNT from polycarbonate membrane (PCM).

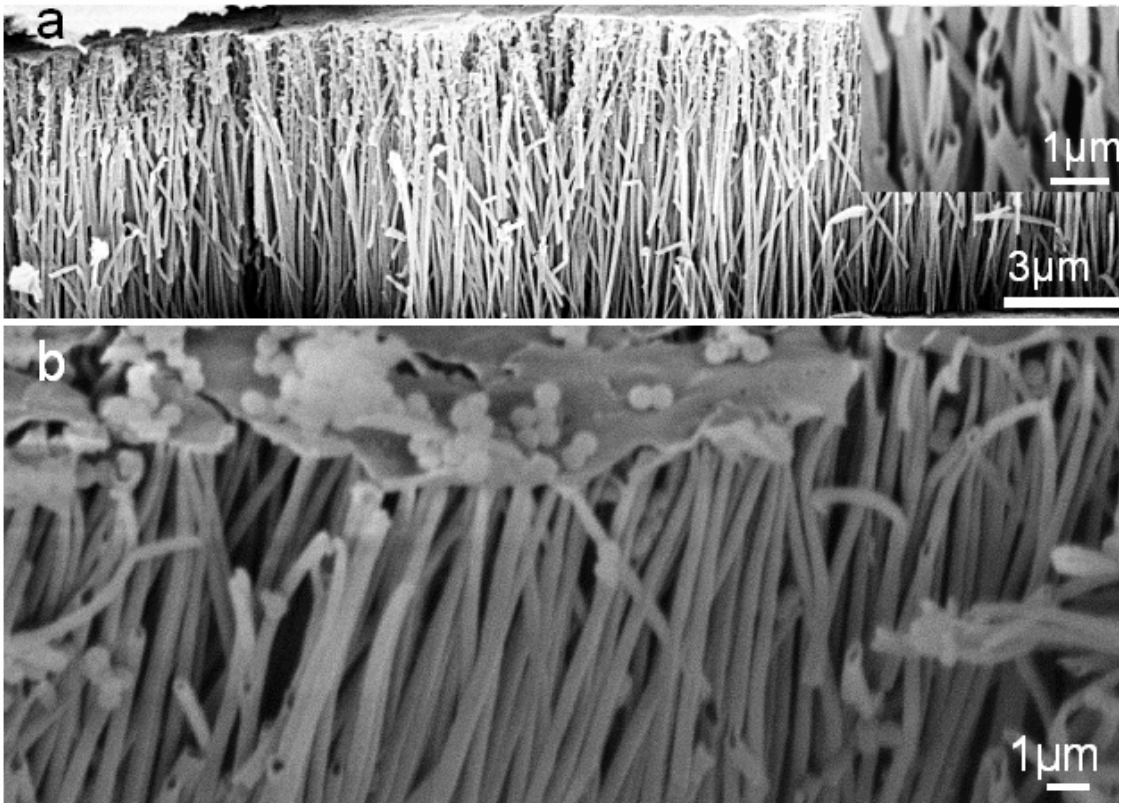

Figure 17: a) SEM image of amorphous carbon nanotube brushes. Inset shows openings of the nanotubes. b) SEM image showing the nanotubes held together by a thin carbon film giving it a brush-like morphology.

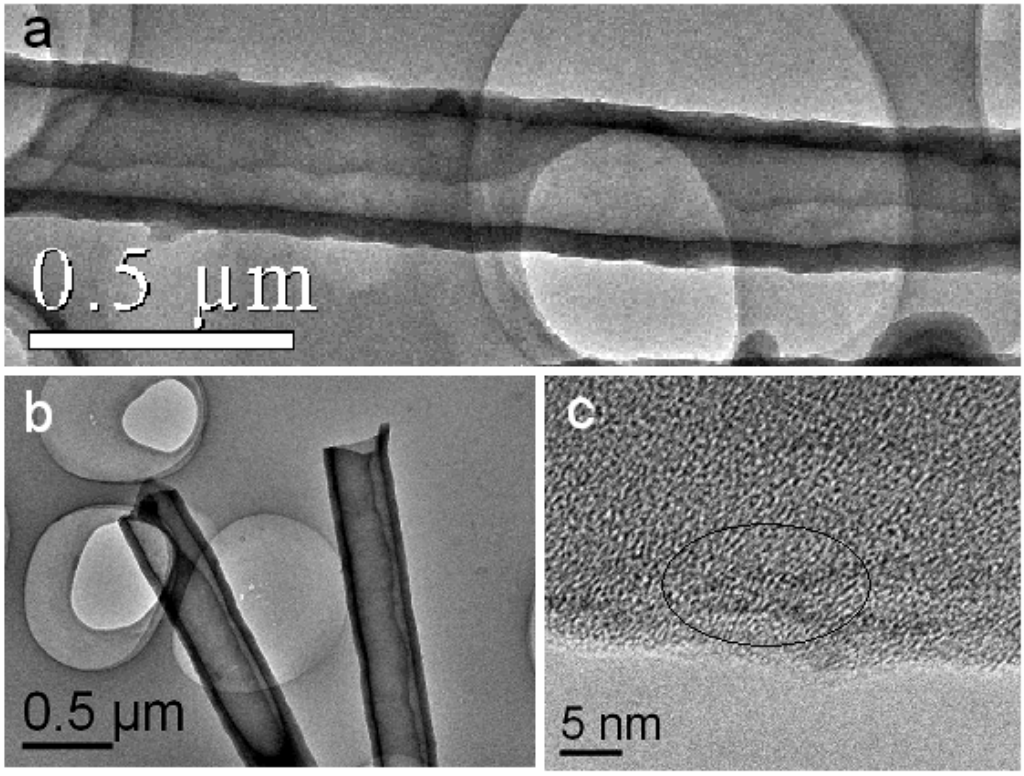

Figure 18: a) TEM image of a single a-CNT. b) TEM image showing cleavage along the length of the nanotube of diameter 340 nm. c) HREM image showing occasional graphitic layers (encircled).

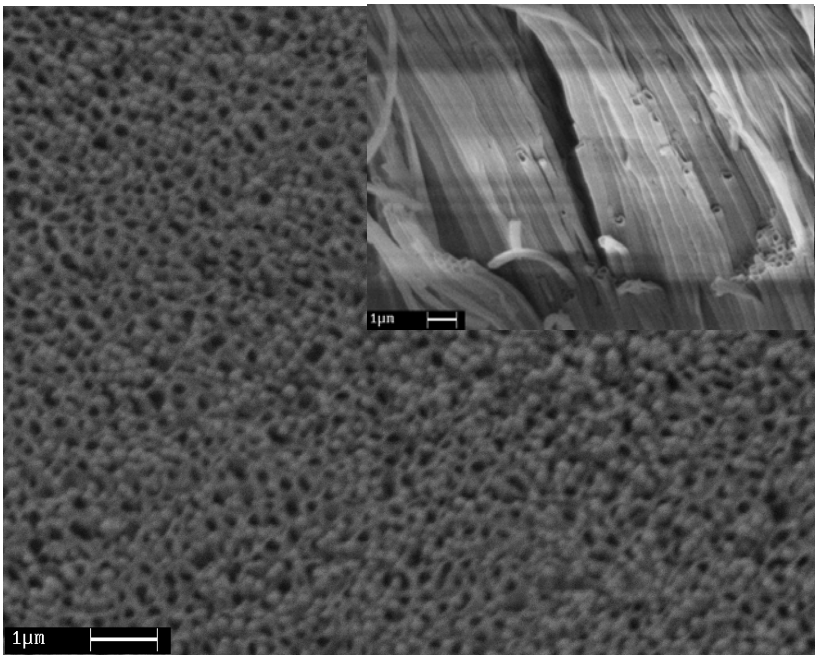

Figure 19: SEM image of a-CNT brushes prepared using anodic alumina disc as templates (top view). Inset shows the side view.

In Figure 17a, we show a SEM image of the aligned carbon nanotubes after dissolving the polycarbonate membrane using dichloromethane. The tubules are 7-10 μm long. They are broken in a few places because of the discontinuities along the pores in the polycarbonate membrane. The openings of the tubules can be seen in the SEM image in Figure 17a (see inset). A thin layer of broken carbon film, a few nanometers thick, deposited on the surface of the membrane loosely holds the tubules together (Figure 17b). In Figure 18, we show a TEM image of an amorphous carbon nanotube. The nanotubes have an inner diameter of around 170 nm and a wall thickness of 45 nm. Where the diameters of the tubes exceed 340 nm, we observe a cleavage along the length of the nanotubes (Figure 18b). Since the polycarbonate membrane has a 20% variation in porosity, a diameter greater than 260 nm can result from the expansion of the walls due to the outburst reaction accompanying carbonization of glucose within the pores of the membrane during the hydrothermal treatment. High-resolution electron microscope (HREM) images reveal the presence of graphitic layers occasionally along the walls showing that the nanotubes in the brush are by and large amorphous (Figure 18c). Similar type of amorphous carbon nanotubes was also made by using anodic alumina disc as templates (Figure 19).

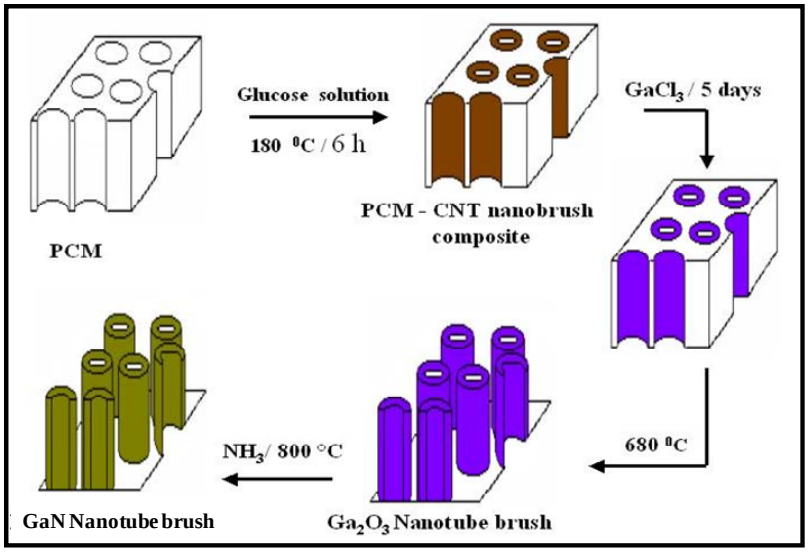

Figure 20: Scheme showing the use of a-CNT as templates to make Ga_2O_3 and GaN nanotube brushes.

In order to prepare GaN brushes, we first prepared Ga_2O_3 brushes by making use of the amorphous CNT brushes as templates. In a typical procedure, to prepare Ga_2O_3 nanotube brushes, the as-prepared amorphous carbon nanotube-polycarbonate composite was soaked in 0.5 M $GaCl_3$ solution for 12 h to 5 days (Figure 20). The membranes were later filtered and washed with deionized water before calcination. The calcination step involved heating of the $GaCl_3$ enriched composite in an alumina boat at 450 °C for 5 h in air followed by a further heating at 680 °C for 1 h in air. The rate of heating was maintained at 0.5 °C/min throughout. A white wool-like powder was obtained after cooling. The SEM image showing Ga_2O_3 nanotube brushes is given in Figure 21. The bristles in the brushes have diameters in the range of 90-200 nm with lengths of around 6-7 μm. Tubes of diameters greater than 250 nm also occur due to the variation in diameters of the carbon tubes. The TEM image shown in the inset of Figure 21b reveals a tube of 200 nm diameter, with a wall thickness of around 10 nm. The Ga_2O_3 nanotubes are poorly crystalline showing broad reflections in the X-ray diffraction pattern.

Conversion of Ga_2O_3 nanostructures to GaN nanostructures on heating in NH_3 is known.[28] The Ga_2O_3 nanobrushes were kept in a quartz tubular furnace, and a constant flow of mixture of ammonia (99.95%) (100 sccm) and argon (200 sccm) was maintained throughout the reaction. Heating was carried out at a rate of 3 °C/min till 800 °C where it was kept for 3 h. The sample obtained was light yellow in color and was allowed to cool to room temperature. A FESEM image shown in Figure 22 reveals the close packing of GaN nanotubes in a brush-like morphology. This brush-like morphology was inherited from Ga_2O_3 nanotube brushes without any damage due to thermal treatments. The diameter of the nanotubes varies from 100 to 230 nm. The tubes are open at one end and their surface appears to be smooth. The TEM image in Figure 23a shows a nanotube with an outer diameter of 200 nm. The wall thickness is in the range of 10-15 nm (Figure 23b). A HREM image of the wall

of a GaN nanotube shows the lattice spacing of 0.244 nm corresponding to the *d*-spacing of (101) planes of the wurtzite phase (Figure 23c). The XRD pattern (Figure 24) of the GaN nanotube brushes was characteristic of wurtzite structure (JCPDF 02-1078).

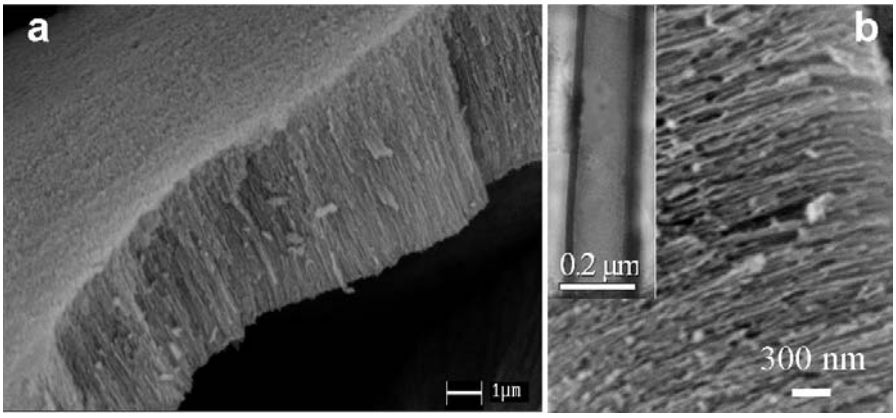

Figure 21: a) Low-magnification SEM image of Ga_2O_3 nanotube brush. b) High-magnification image of a Ga_2O_3 nanotube brush. Inset shows the TEM image of a Ga_2O_3 nanotube.

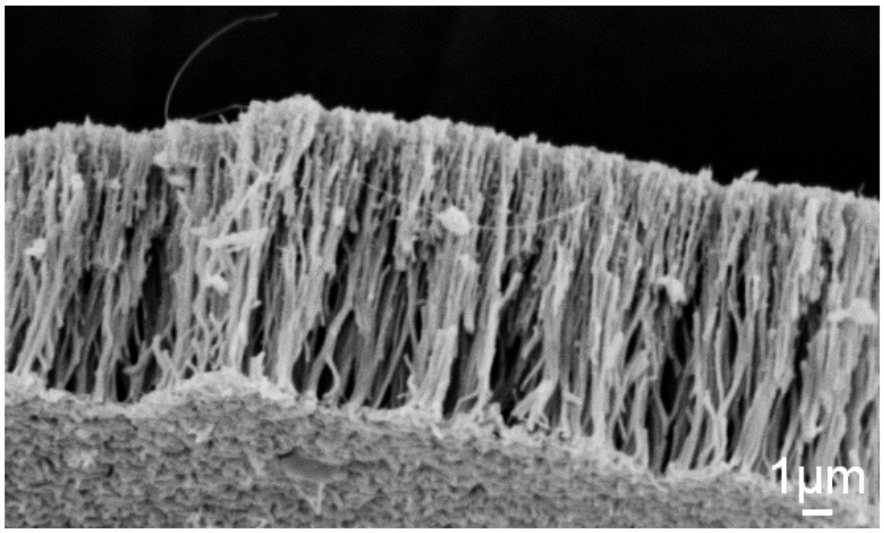

Figure 22: SEM image of GaN nanotube brush.

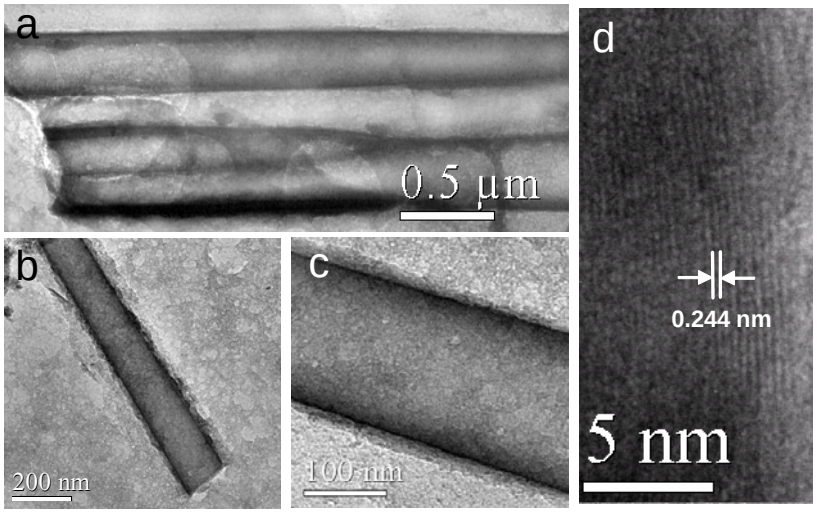

Figure 23: (a) (b) and (c) TEM images of GaN nanotubes. d) HREM image of the wall of a GaN nanotube.

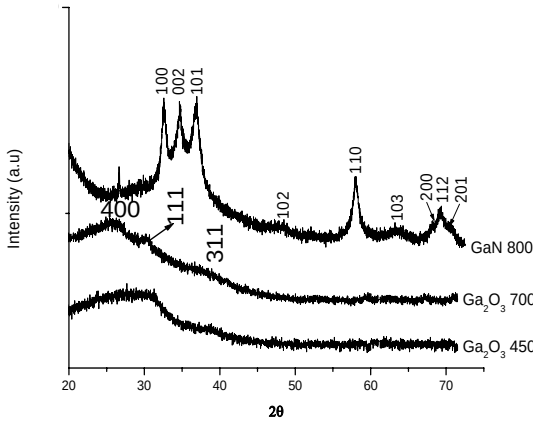

Figure 24: XRD patterns of Ga_2O_3 nanotube brushes calcined at 450 and 700 ^oC and GaN nanotubes brushes synthesized at 800 ^oC.

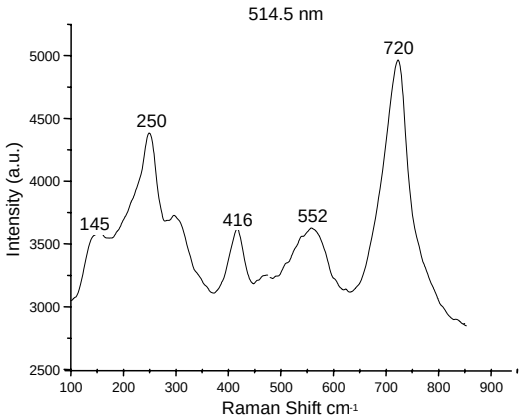

Figure 25: Raman spectrum of GaN nanotubes brushes recorded using 514.5 nm laser.

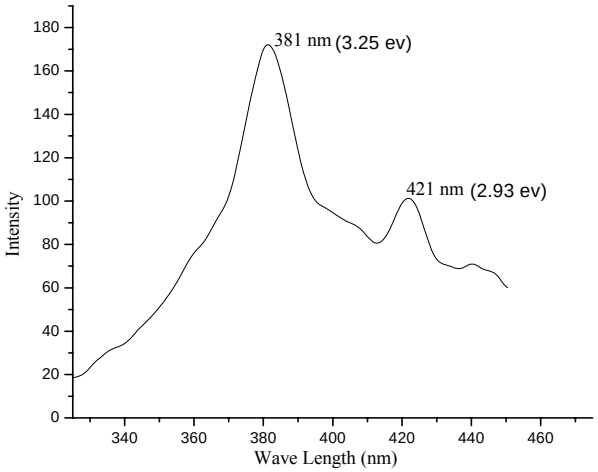

Figure 26: PL spectrum of GaN nanotubes brushes excited at 220 nm.

The Raman spectrum (Figure 25) shows broad peaks at 145, 250, 416, 553, and 720 cm^{-1}. The bands at 145 and 720 cm^{-1} can be assigned to E2 (low) and A1 (LO) modes of first-order Raman phonon modes of wurtzite GaN. The bands corresponding to A1 (TO), E2 (high), and E1 (TO) merge to give the broadband centered at 550 cm^{-1}. The band at 250 cm^{-1} is due to zone boundary phonons. The band edge emission peak of GaN in photoluminescence (PL) starts from 360 nm with a peak maximum at 380 nm (Figure 26). The lower wavelength region is associated with quantum confinement caused by the nanotubes of less than 10 nm wall thickness. The broadband edge emission could result from the wide variation in the wall thickness. The less intense peak at 420 nm is attributed to defects.

2.6. Conclusions:

In conclusion, we have successfully functionalised carbon nanostructures by low temperature route using glucose as the precursor. Two different morphologies like spheres and tubes of the same material were synthesized. Besides using them as templates to obtain hollow spheres of $ZnAl_2O_4$, SnO_2, SiO_2 and nanotubes of Ga_2O_3 and GaN, we also successfully coated them around the surface of biologically important inorganic submicron

spheres like Fe_3O_4, $MnFe_2O_4$ and mesoporous SiO_2. At this point, two more interesting possibilities turn out. The core Fe_3O_4 can be dissolved using HCl and hollow functionalised carbon spheres can be obtained. One can also optimize the dissolution of the core using dilute acids and retain the magnetic functionality. Such materials would have ball in ball architecture and can have potential applications in storage and controlled release. The other interesting extension of the problem could be the use of Fe_3O_4@HC to synthesise multiferroic materials. The outermost layer HC being functionalised can uptake ions like Bi^{+3} from solutions. After suitable thermal cycle, the adsorbed Bi^{+3} ions can react diffusively along the interface of iron oxide core to form $BiFeO_3$ while the core Fe_3O_4 could phase change to γ-Fe_2O_3. This material will have ferromagnetic core and a ferroelectric shell. A wide range of materials can be synthesized and a possible coupling between these two properties could lead to multiferroics.

2.7. References:

1. Bhushan, Bharat (Ed.), *Springer Handbook of Nanotechnology*, **2007**.
2. Rapport, L.; et al *Nature* **1997**, *387*, 791.
3. Gordon, P. A.; Sneger, P. B. *Ind. Eng. Chem. Res*. **1999**, *38*, 4647.
4. Shivalingappa, L.; Sheng, J.; Fukami, T. *Vacuum* **1997**, *48*, 413.
5. Bao, J. C.; Xu, D. P.; Zhao, Q. F.; Xu , Z. *Chem. Mater.* **2002**,*14*, 4709.
6. Li, J.; et al. *Nano Lett.* **2003**, *3,* 597.
7. Bhatkhande, D.S.; Pangarkar, V. G.; Beenackers, A. A. C. M.; *J. Chem. Techno. Biotech.* **2001**, *77*, 102.
8. Chen, X. Y.; Kawai, S. *Chem. Commun*. **2001**, 1354.
9. *Hollow and Solid Spheres and Microspheres: Science and Technology Associated with Their Fabrication and Applications*, (Eds: Wilcox, D. L.; Berg, M.; Bernat, T.;

Kellerman, D.; Cochran Jr. J. K.;) *Mater. Res. Soc. Symp. Proc.* **1995**, *372*, MRS Pittsburgh, PA.

10. a) Matijevic, E. *Chem. Mater.* **1993**, *5*, 412. b) Wang, X.; Peng, Q.; Li, Y. *Acc. Chem. Res.* **2007**, *40*, 635.
11. a) Caruso, F.; Caruso, R.A.; Möhwald, H. *Science,* **1998**, *282*, 1111. b) Caruso, F. *Adv. Mater*., **2001**, *13*, 11.
12. Parthasarathy, R. V.; Martin, C. R. *Chem. Mater*. **1994**, *6*, 1627.
13. a) Antelmi, D. A.; Spalla, O. *Langmuir* **1999**, *15*, 7478. b) Sato, T.; Ruch, R.; *Stabilization of Colloidal Dispersions by Polymer Adsorption; Surfactant Science Series*, No. 9, Marcel Dekker, New York **1980**.
14. a) Yin, Y.; Erdonmez, C.; Aloni, S.; Alivisatos, A. P. *J. Am. Chem. Soc*. **2006**, *128*, 12671. b) Raidongia, K.; Rao, C. N. R. *J. Phys. Chem. C*. **2008**, *112*,13366.
15. Yang, H.G.; Zeng, H.C. J. *Phys. Chem. B.* **2004**, *108*, 3492.
16. Lou, X. W.; Archer, L. A.; Yang, Z. *Adv. Mater*. **2008**, 20, 3987.
17. Lu, X.; Chen, J.; Skrabalak, S. E.; Xia, Y. *Proc. IMechE, Part N: J. Nanoeng. Nanosys.*, **2007**, *221*, 1.
18. Gomathi, A.; Vivekchand, S. R. C.; Govindaraj, A.; Rao, C. N. R. *Adv. Mater.* **2005**, *17*, 2757.
19. Yang, M.; Ma, J.; Zhang, C.; Yang, Z.; Lu, Y. *Angew. Chem. Int. Ed.* **2005**, *44*, 6727.
20. Caruso, F. *Adv. Mater*. **2001**, *13*, 11.
21. a) Sun, X.; Liu, J.; Li, Y.; *Chem. Eur. J*. **2006**, *12*, 2039. b) Sun, X.; Li, Y. *Angew. Chem. Int. Ed*. **2004**, *43*, 3827.
22. Dinesh, J.; Eswaramoorthy, M.; Rao, C. N. R. *J. Phys. Chem. C*. **2007**, *111*, 510.
23. Han, W.; Fan, S.; Li, Q.; Hu, Y. *Science* **1997**, *277*, 1287. b) Deepak, F. L.; Govindaraj, A.; Rao, C. N. R. *J. Nanosci. Nanotechnol.* **2001**, *1*, 303.

24. Gu, Q.; et al *Chem. Mater.* **2005**, *17*, 1115.

25. Soo Kang, Y.; Risbud, S.; Rabolt, J. F.; Stroeve, P. *Chem. Mater*. **1996**, *8*, 2209.

26. Deng, H.; Li, X.; Peng, Q.; Wang, X.; Chen, J.; Li, Y. *Angew. Chem. Int. Ed*. **2005**, *44*, 2782.

27. Yano, K.; Fukushima, Y. *J. Mater. Chem*. **2004**, *14*, 1579.

28. Hu, J.; Bando, Y.; Golberg, D.; Liu, Q. *Angew. Chem., Int. Ed.* **2003**, *42*, 3493.

Summary

A simple chemical route has been developed in tuning the morphology of α-Fe_2O_3 from hollow spheres to nanocups. The transformation to nanocups occurs via the buckling of hollow spheres rather than breaking of hollow spheres. The method is based on coating of iron oxohydroxide polymer around the spherical template followed by thermal treatment. Magnetic properties of these nanostructures also vary with the morphology.

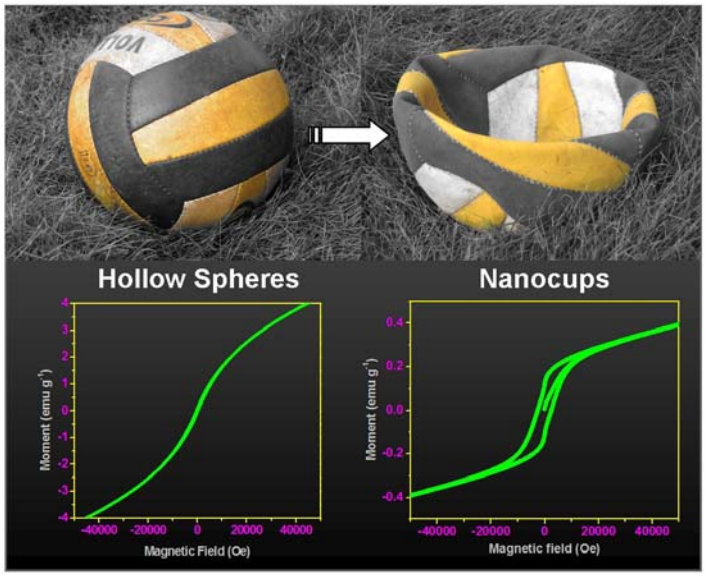

A paper based on this work has been published in *Angew. Chem. Int. Ed.*, **2008**, 47, 7685.

3.1. Introduction:

Futuristic technology to handle and manipulate reagents of very low volumes would certainly have immense impact on the chemical and biological research. They are expected to find applications in enzyme kinetics study,[1] immunoassays,[2] PCR analysis[3] and all other fields where quantity of the analyte is either extremely low or highly toxic to the environment. Synthesis of containers with nano or zeptolitre volume has therefore become a cardinal step in developing such a technology. While the mesoporous materials,[4] hollow capsules[5] and nanotubes[6] are also envisaged to serve the intended purpose, synthesis of more complex morphologies like a bowl/cup in large quantities is very challenging.

Some attempts have been made in the recent times to obtain micro and nanobowls.[7-10] Most of them are obtained by using a monolayer assembly of spheres as templates. Figure 1A summarises the experimental protocol for obtaining cups from monolayer assembly of the spheres. However, the cups obtained in this method are polycrystalline or amorphous and the yield is limited to only the monolayer arrangement of spheres. Thus, a simple bottom-up approach, not restricted to monolayer assembly of colloidal spheres, would be considered as an important step forward.

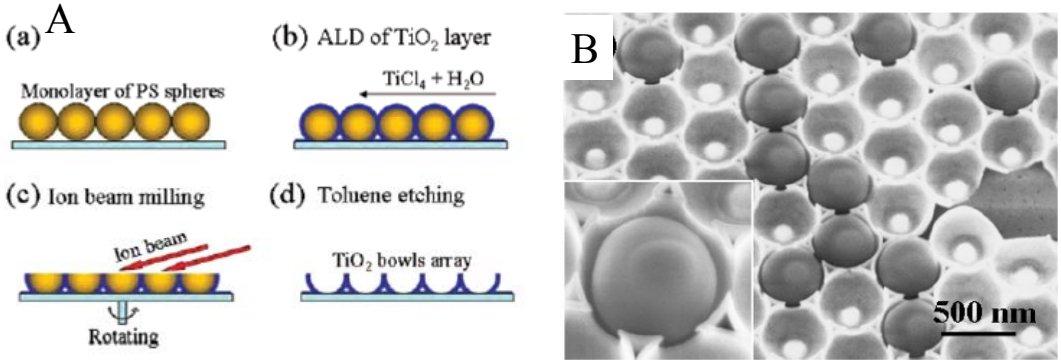

Figure 1: A) Scheme showing the formation of cups from the monolayer assembly of polystyrene spheres. a) Assembled polystyrene spheres. b) Atomic layer deposition of the precursor. c) Ion beam milling at an angle to remove a portion of the sphere. d) Toluene etching to remove the polystyrene spheres. B) SEM image of the TiO_2 nanobowls array prepared in this method. (ref 8).

There are also other methods to fabricate nanobowls but the procedures are usually restricted to a specific nature of the material like metals or polymers. An elegant method that was published by Gracias et al[11] utilised the surface tension effects of molten solder between the metal frames to cause their self folding. Though this method is good at obtaining containers of different shapes, it is restricted to metals. Further the size of the fabricated containers are of the order of 50-200 μm. Reducing the size further down is tedious as the fabrication involves photolithography. The method adopted by Kulkarni et al[9] to obtain femtolitre cups utilising the hydraulic jump of molten metal, through the pulsed laser ablation however is bound with the experimental limitation to scale-up.

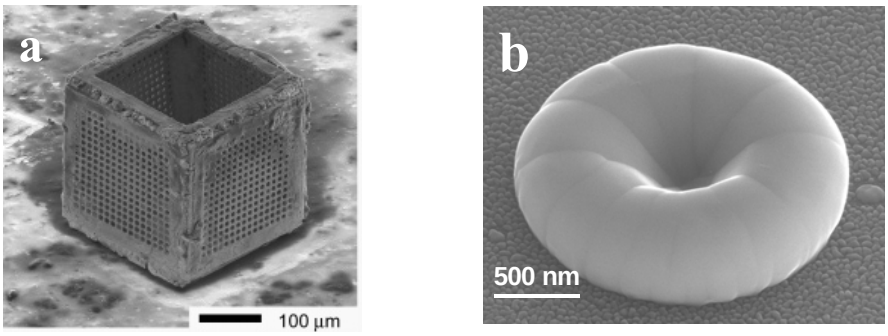

Figure 2: SEM images a) A fully formed microcontainer obtained by Gracias et al (ref 11) by the self folding of its faces b) Femtolitre metal cup prepared by John et al (ref 9) using the hydraulic jump of the molten metal drop during laser ablation.

It is intuitive to resort to the bottom-up approach rather than a top-down in order to evolve a versatile and easily scalable procedure. For example, Xia et al[12] have devised synthetic procedure to make polymer hollow particles with controllable holes based on the ability of a solvent like toluene to swell certain polymers.

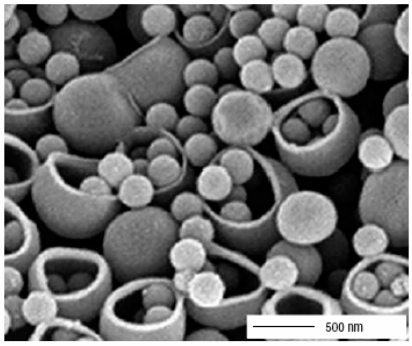

Figure 3: SEM image of polymer cups synthesized by Xia and coworkers (ref 12).

3.2. Scope of the present investigation:

A similar bottom-up approach to obtain nanocups / bowls of single crystalline metal oxide is yet to be pursued. This study describes a new approach to tune the morphology of α-Fe_2O_3 from hollow spheres to nanocups using carbonaceous spheres. It is interesting to note that our observation is seemingly against the well documented tradition of obtaining hollow spheres alone from such spherical templates.[13] It is also interesting to study the changes that the shape of a material has on its magnetic properties. As the material has been obtained in the single crystalline form and they are of comparable size, all the differences in the magnetic properties that arise between hollow spheres and nanocups can be attributed to their differences in shape.

3.3. Experimental section:

a. Materials:

D (+) glucose was purchased from Sigma Aldrich. $Fe(NO_3)_3.9H_2O$ was purchased from SD fine Chemicals. Teflon lined sealed stainless steel autoclave (60 mL) was fabricated. Millipore water and absolute ethanol were used wherever essential.

b. Synthesis of spherical carbonaceous templates (CSP):

CSP were synthesized by previously reported method.[14] An aqueous solution of α-D-glucose (55 mL of 0.5 M) was placed in a 60 mL teflon lined stainless steel autoclave. The

solution was maintained at 180 ^{o}C for 16 h after which it was allowed to cool down naturally to room temperature. The solid brown product was collected by centrifuging at 10000 rpm for 5 min. It was thoroughly washed with ethanol and water and dried at 80 ^{o}C in air for 4 h. CSP possess functional groups like –OH and –COOH groups as confirmed by FT-IR. Their surface is negatively charged at pH 7.3 (ζ = -24 mV). On dispersing CSP in the salt solution, the Fe^{+3} cations strongly bound to the surface of CSP as indicated by the change in zeta potential to +40 mV at pH 7.3.

c. Formation of thixotropic gel by hydrolytic polymerisation:

In a typical synthesis, 10 mL of 0.5 M solution of $Fe(NO_3)_3.9H_2O$ was prepared in absolute ethanol. The synthesized CSP (0.1 g) were added to it and the solution was sonicated in a water bath for 45 min. The fine suspension of CSP in ferric nitrate was magnetically stirred at 35 to 38 ^{o}C in a beaker to facilitate the gradual evaporation of ethanol. After stirring for certain period of time under normal conditions (this time period is called strirring time), the formation of the gel was induced by increasing the relative humidity beyond 85% and temperature to 38 ^{o}C for a continuous period of 4 to 5 h (this time period is called gel induction time). The total contact time of the CSP in the ferric nitrate solution till it attained the gel has been taken as 'gelation time' and was adjusted to 6, 12 and 20 h by suitably accommodating both stirring time and gel induction. The CSP containing gel thus obtained was washed with water (Millipore) and ethanol thoroughly and finally dried at 40 ^{o}C in air for 8 h. Different morphologies of α-Fe_2O_3 were obtained by calcining the sample (CSP coated with gel) at a suitable temperature depending on the gelation time.

d. Maintaining the relative humidity:

A simple apparatus was designed to carry out the experiments in a controlled humidity atmosphere (Figure 4). A thermo Cole chamber was made with two halves which can be closed. A provision was made along the top side of the partition through which a

humidity meter was inserted. The humidity meter measured both relative humidity and temperature. The sample (CSP suspension in ethanol solution of ferric nitrate) was placed in a beaker on the left side of the box. It was continuously stirred at room temperature using a magnetic stirrer. The sample was actually placed on a cold water bath in order to maintain the temperature. The moisture content in the air inside the chamber was increased by heating a trough of salt water at 80 – 90 ^{o}C. The salt water trough was placed on a hot plate on the right half of the chamber. An exhaust fan was used to carry water vapour from the right side of the chamber towards the sample.

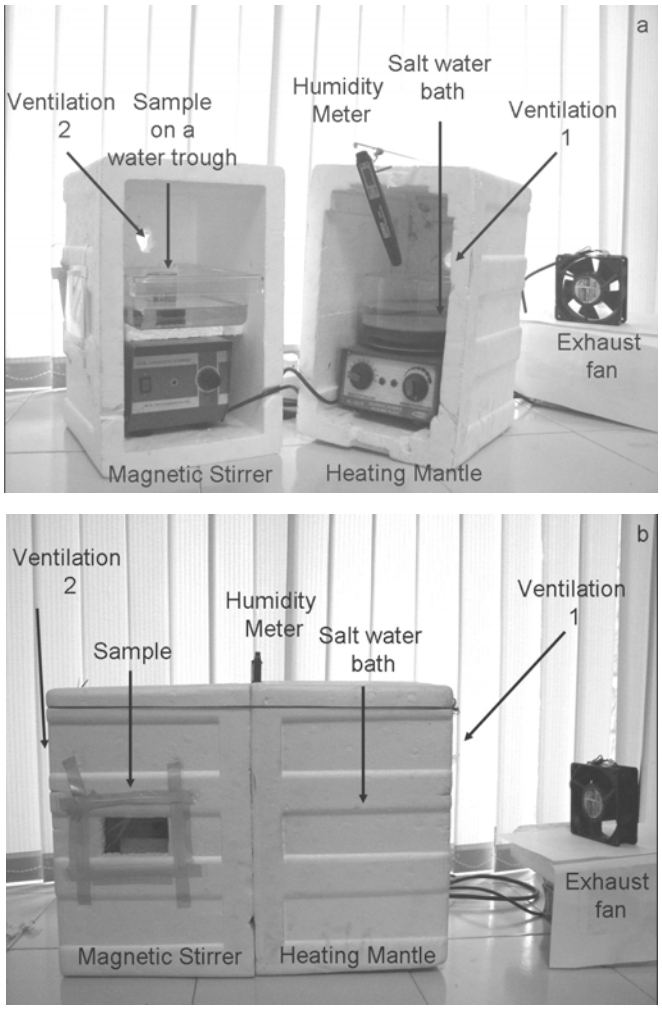

Figure 4: Apparatus for controlled humidity experiments a) Opened view and b) closed view

After a certain period of stirring, the gel was formed in the sample. At this point, the gel possessed a thixotropic property (i.e), when the magnetic stirring was stopped, the viscosity of the medium reduced and when stirring was restarted, its thickness resumed (Figure 5).

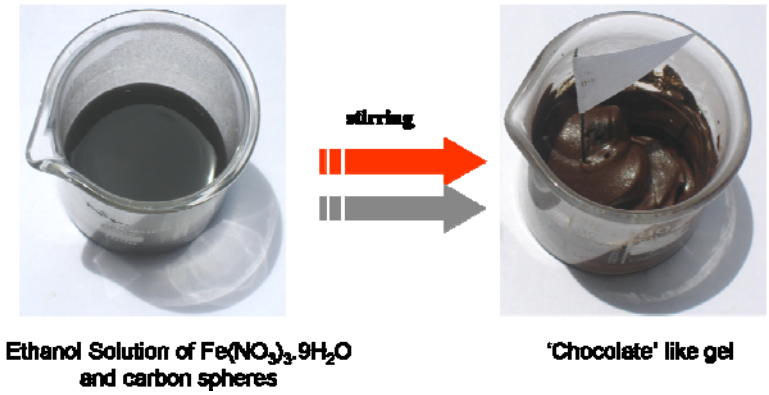

Figure 5: Digital photography images of the suspension of CSP in ferric nitrate solution in ethanol (left) and the thixotropic gel that was obtained after a continuous stirring for 12 h.

3.4. Characterization:

The morphology of the samples were analysed using FESEM, FEI, Nova-Nano SEM-600 (Netherlands). TEM analysis was done using a JEOL JEM 3010 instrument (Japan) operated with an accelerating voltage of 300 kV. Tilting experiment in TEM was done in Technai Instrument operated at 300 kV. XRD was measured at 25 ^{o}C in Bruker D8 (Germany) using CuK_{α} radiation. Relative humidity measurements were done using Extech instruments (China). Magnetic measurements were carried out with vibrating sample magnetometer in a physical property measurement system (Quantum Design, US). Zero field cooled (ZFC) and field cooled (FC) data were recorded in the temperature range of 5 to 400 K at an applied magnetic field of 500 Oe.

3.5. Results and discussion

The formation of gel is associated with the hydrolysis of ferric nitrate to iron oxohydroxide polymer.[15] Forming the thixotropic gel before calcination was found to be a mandatory step towards any well defined morphology like hollow spheres and nanocups.

Samples calcined before attaining the gel stage resulted in a porous network made up of α-Fe_2O_3 nanostructure (Figure 6).

The FESEM image of α-Fe_2O_3 hollow spheres obtained by calcining the sample (with a gelation time of 12 h) at 400 ^oC for 5 h shows a size variation from 100 to 400 nm (Figure 7a) which is considerably lower than the size of the CSP (300 – 800 nm) used as the template. This is quite understandable as the calcination leads to a significant shrinkage in its size due to sintering and condensation of metal oxide. These hollow spheres possess a very thin wall of few nm thick and are transparent to the electron beam. The TEM image in Figure 7b further shows that the thickness of the wall is around 20 nm or less. The appearance of roughened wall surface in FESEM made us to believe that the spheres are polycrystalline. However, the electron diffraction (ED) pattern on these hollow spheres shows that they are single crystalline in nature (inset of figure 3c). The HREM image shows the lattice spacing corresponding to (012) and (104) planes of α-Fe_2O_3 (Figure 7c and Figure 8).

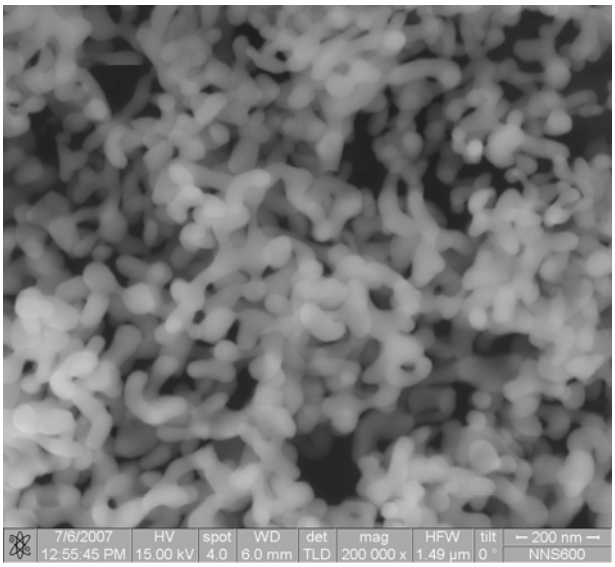

Figure 6: FESEM image of porous network of α-Fe_2O_3 when the sample was calcined before reaching the gel state.

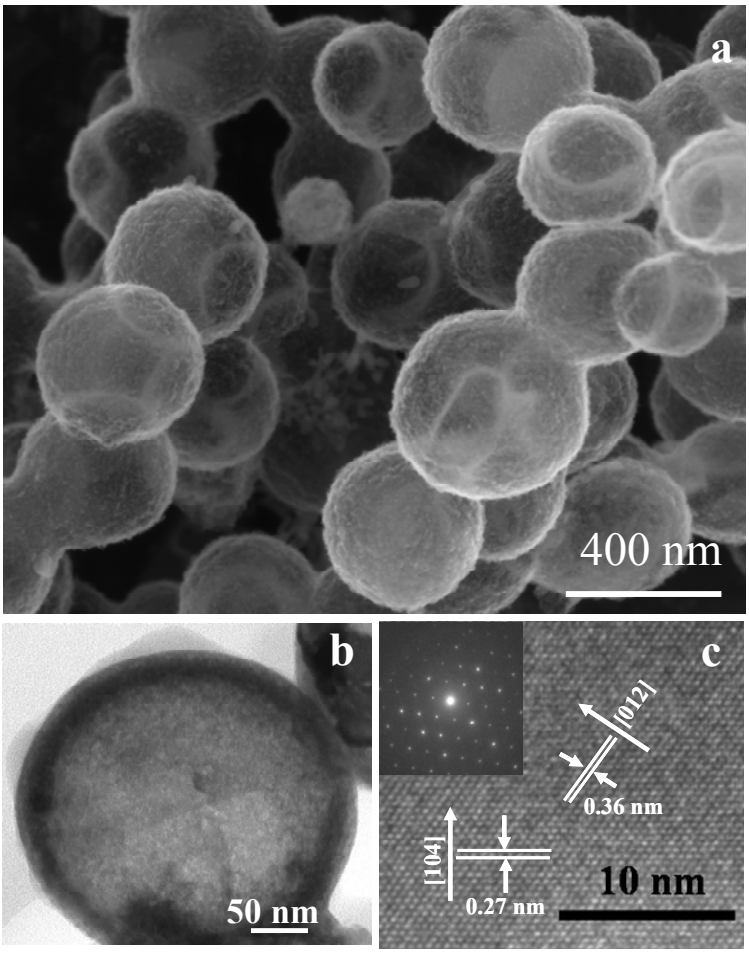

Figure 7: a) FESEM image of α-Fe_2O_3 hollow spheres. b) TEM image of an isolated hollow sphere. c) HREM showing the lattice fringes of (012) and (104) planes. Inset shows the ED pattern obtained on a single sphere.

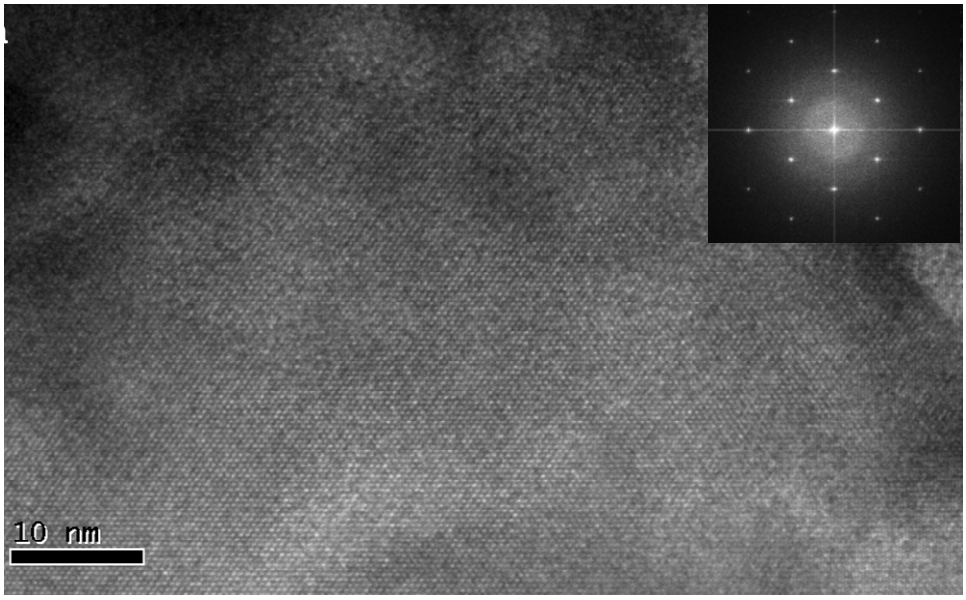

Figure 8: HREM image obtained on a single hollow sphere shows an extended area of single crystalline nature. Inset is the FFT pattern which did not change throughout the sample suggesting the long range ordering of the crystal.

Figure 9 and Figure 10a, show the low magnification FESEM image of α-Fe_2O_3 nanocups of sizes ranging from 100 to 300 nm. The images suggest the high yield of the metal oxide nanocups obtained by this procedure. The nanocups were obtained by calcining the sample (gelation time in 12 h) at 500 ^oC in air for 5 h. A double wall with the folding along the rim of the cup was routinely observed in most of these cups. Further, the inward folding of these thin α-Fe_2O_3 walls at the rim of the cup can be clearly seen in the FESEM image (Figure 9). The exposure of underneath layer in the broken up regions shows that the inner and outer walls of the cups are not completely merged together (white arrow in Figure 10c and 10b). A gold coated cup with an improved contrast shown in Figure 10d does not display the double wall as it is covered with a gold layer. TEM image shows that the thickness of the double-wall at the rim of a cup is about 20 nm. HREM (Figure 10f and Figure 11) image and ED pattern (inset) besides confirm the single crystalline nature of these α-Fe_2O_3 nanocups.

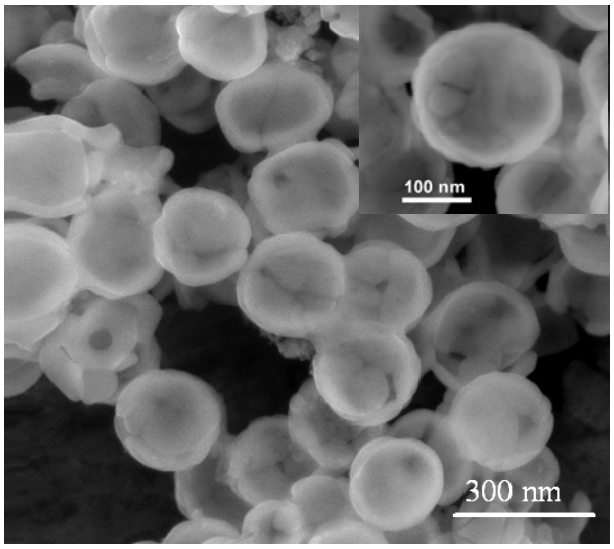

Figure 9: FESEM images of α-Fe_2O_3 cups

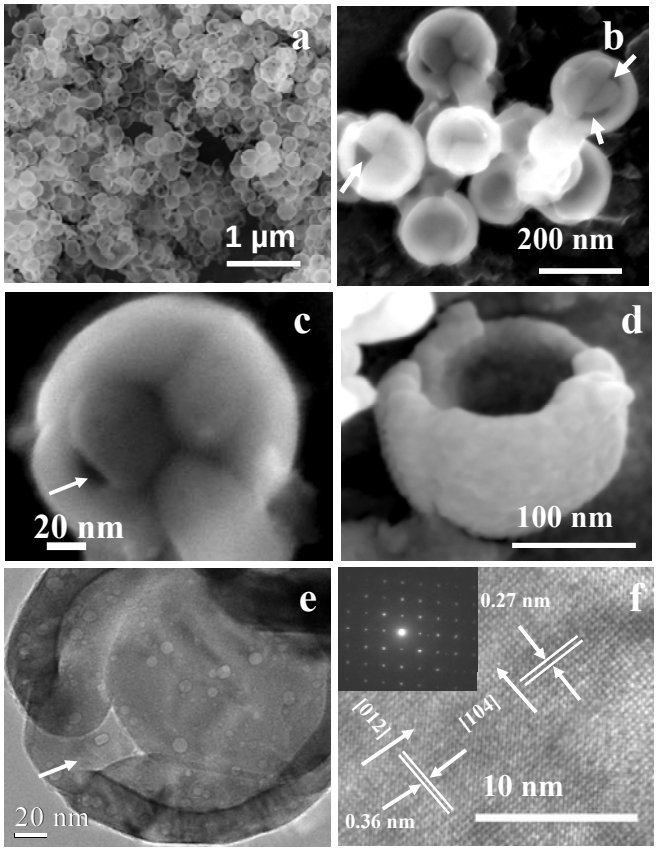

Figure 10*:* a) Low-magnification FESEM image of the α-Fe_2O_3 nanocups. b, c) Higher-magnification FESEM images of the nanocups showing the double-walled folding along the rim. White arrows indicate the broken-up regions. d) FESEM image of a single nanocup coated with gold. e) TEM image of a nanocup showing double-walled folding along the rim (white arrows). f) HREM image showing the lattice fringes of (012) and (104) planes. Inset: ED pattern of the nanocups.

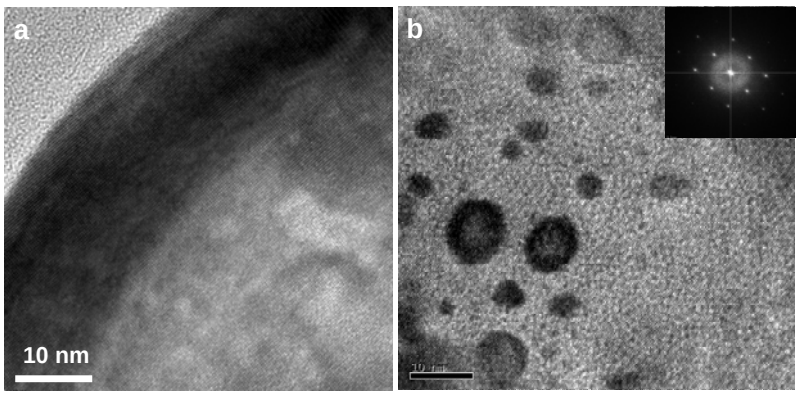

Figure 11: HREM image obtained on the bottom (floor) of the nanocup. Certain regions of darker contrast were observed which may be due to the pits that were formed during the folding process. The single crystalline nature of the nanocups are evident from its FFT pattern (inset) which remained same throughout the cup. The bottom

of the cup is decorated with a lot of tiny pits whose contrast in the electron beam is varied with its depth. The lattice fringes of the α-Fe_2O_3 cups at the rim and the extended inner wall of a cup is seen in the HREM image.

TEM α tilting (from $+40^o$ to -40^o) analysis (Figure 12) clearly distinguished the nanocups from hollow spheres by virtue of their prominent asymmetry along the rim created by the folding. This purpose of this analysis was to rule out any artefacts that could have occurred in FESEM images. The experiment clearly distinguishes the cups from the hollow spheres. The triangle in the cartoon represents the discontinuity that occurs along the rim of the cups during the folding process of the walls. This is a common feature among the cups and becomes clearly evident as the tilting angle changes. On the other hand, TEM image of hollow spheres shows a symmetrical rim at all angles of tilting. All the TEM images were recorded at the same magnification.

The formation of a cup-like nanostructure rather than a hollow sphere from a spherical template is an interesting observation in this work. To understand the mechanism of cup formation the samples prepared at different gelation times 6, 12 and 20 h were subjected to thermal analysis and morphology studies. Thermogravimetric analysis (TGA) of the CSP (separated from the thixotropic gels after a thorough washing) shows that the iron content on them increases with longer gelation times (Figure 13A). For example, samples with gelation time 6, 12 and 20 h show 10, 14 and 25 wt % of residual mass respectively in TG analysis accounting for the inorganic content, iron oxide in this case. The increased loading of inorganic iron content for the samples with increased time of gelation is evident from the increase in the residual weight. When the sample with gelation time 6 h (of low iron content) was calcined at 250 ^oC in air for 5 h, only 27% of the carbon is removed and the spherical morphology is still preserved.

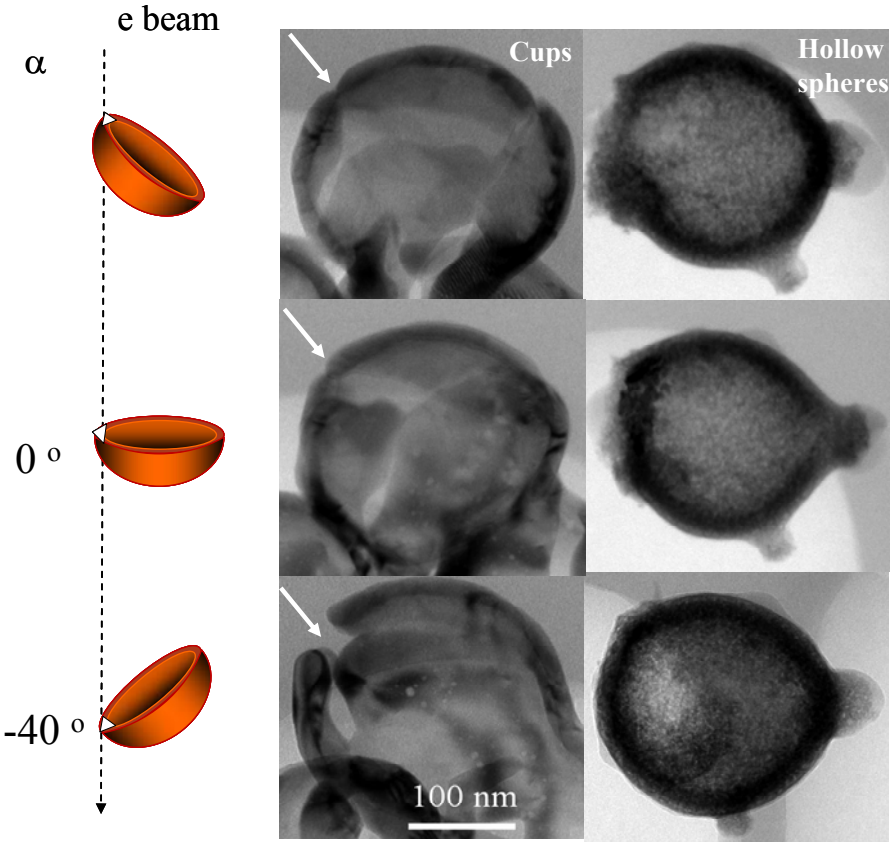

Figure 12: TEM image of the nanocups and hollow spheres tilted at different angles of α = +40° to -40°.

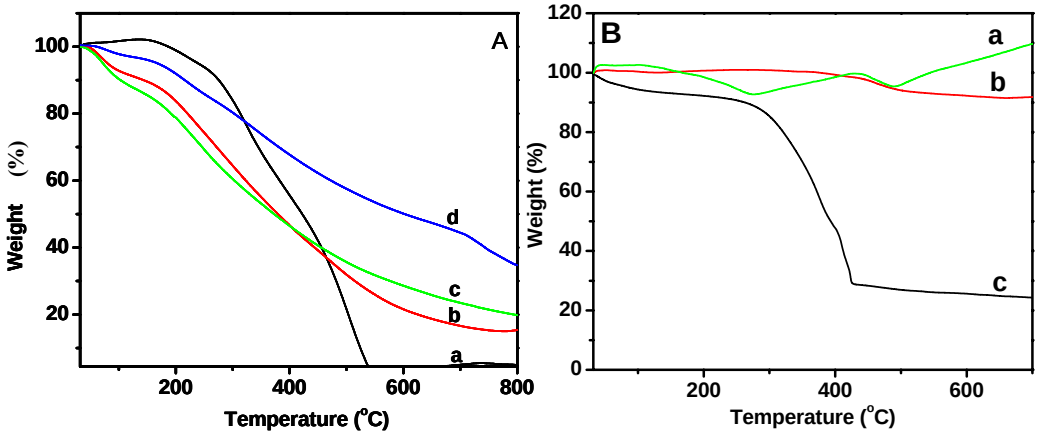

Figure 13A: a) TGA of pure CSP and the CSP coated with polymeric iron species obtained at various gelation time. b) 6 h, c) 12 h and d) 20 h. 13B**)** TGA of CSP coated with the polymeric iron species with gelation time - 6 h, calcined at a) 250, b) 350 and c) 400 °C for 5 h. Nearly 70% of the carbon remains even after heating the sample at 250 °C for 5 h.

XRD pattern for the sample at this condition indicates that transformation of amorphous iron oxohydroxide to crystalline Fe_2O_3 begins well before the complete decomposition of CSP (Figure 14). Calculation of the particle size using Debye-Scherrer formula considering FWHM of (104) peak suggests that there is not much increase in the growth of the crystal size with increased calcination temperature. However, the improved crystallinity at higher calcinations temperature like 600 ^oC is evident from exhibition of peaks of increased intensity. This result can also be interpreted as the formation single crystalline nanostructures occur right from the beginning of the thermal treatment without undergoing through any polycrystalline intermediate. TG analysis of as synthesized CSP shows a gradual weight loss from 200 to 530 ^oC due to decomposition of amorphous and graphitic regions. However, when the sample with the gelation time 6 h was calcined at 350 ^oC for 5 h almost 96 % of the carbon was removed and the spheres show buckling of walls (Figure 13B and Figure 15).

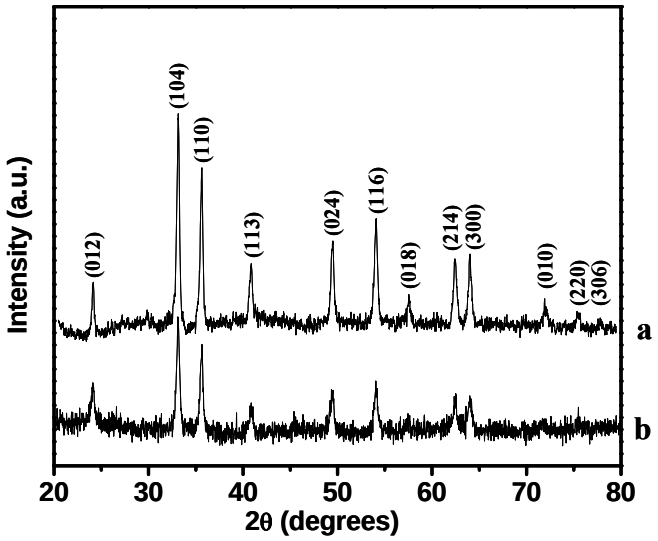

Figure 14: XRD of Fe_2O_3 obtained by calcining the CSP coated with the polymeric iron gel (gelation time 6 h) at a) 600 ^oC /5h and b) 250 ^oC /5 h. All the peaks are indexed to corundum structure of α-Fe_2O_3

The thin walls of the spheres could not withstand the stress caused by the crystallization and sintering of the iron oxide once the CSP are decomposed. This stress is eventually relieved

via bucking into a controlled three dimensional shapes.[16] If the sample was heated at 400 ^{o}C for 5 h, the buckling process completes as the top layer touches the bottom of the wall resulting in a cup-like morphology. The carbon is almost completely removed in this sample. In addition, the local heat generated during the nitrate and CSP decomposition facilitates the formation of single crystalline α-Fe_2O_3.

Thus formation of nanocups occur via the folding of the walls of the hollow spheres rather than through their break-up. To confirm this, a number of intermediate stages of folding were obtained by subjecting the sample to different calcination conditions like 250, 350, 450 and 500 ^{o}C for 5 h each (Figure 15). The morphologies showed a constant evolution of structures from a sphere to a fully formed nanocup aided by buckling of the walls. This is predominantly driven by the transformation of the amorphous polymeric iron oxohydroxide to crystalline iron oxide. The scheme is given below in Figure 16.

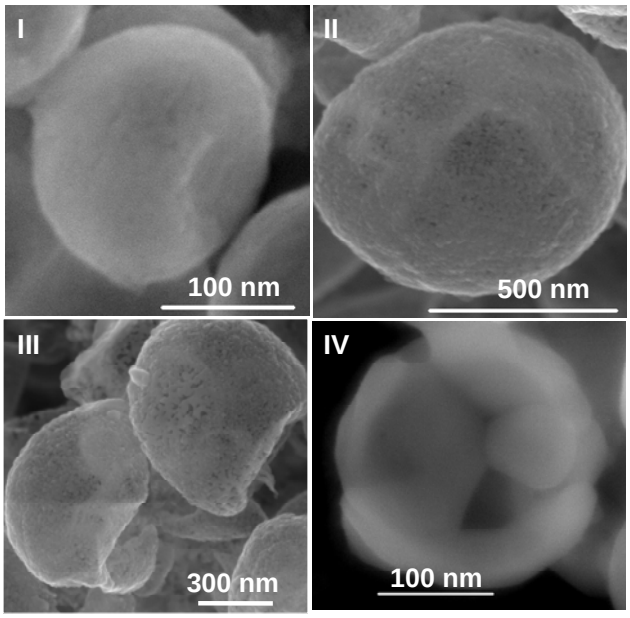

Figure 15: FESEM images of intermediate stages of cup formation upon thermal treatment (I = 250, II = 350, III = 450 and IV = 500 ^{o}C for 5 h). The images show the buckling of the walls of the hollow spheres (I, II, II). Cracks developed on the buckled inner walls due to sintering (IV).

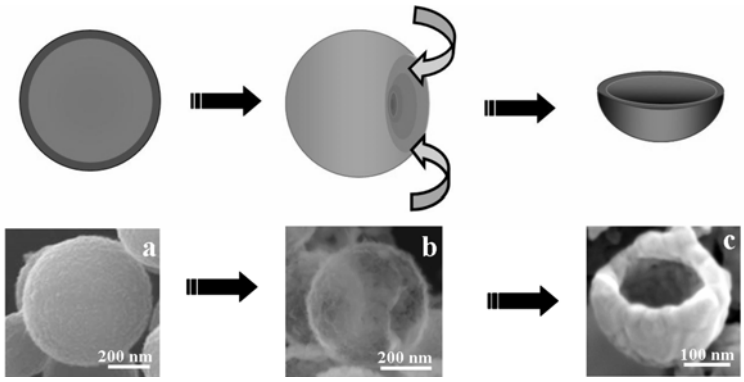

Figure 16: Temperature induced shape evolution of α-Fe_2O_3 nanocups. FESEM image of CSP coated with the gel (gelation time 6 h) calcined at a) 250, b) 350 and c) 400 ^oC for 5 h (coated with gold).

The most intriguing fact that remained unanswered was the formation of nanocups from spherical templates. From our earlier results (Chapter 2) and other reports, it is well understood that only hollow spheres form when spherical templates are used. Interistingly, we have observed an exclusive formation of either hollow spheres or nanocups in high yields depending on the conditions. The results are graphically tabulated below in Figure 17.

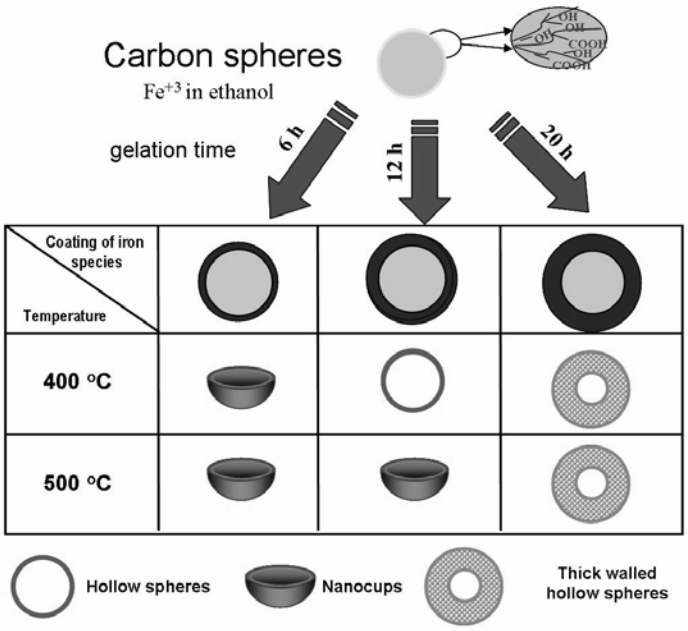

Figure 17: Scheme showing the formation of different morphologies of α-Fe_2O_3 when the samples with different gelation times (6, 12 and 20 h) were calcined at 400 and 500 ^oC in air.

As seen from the Figure 17, the samples that attained gel in 6 h formed only nanocups irrespective of the temperature of calcination. On the other hand, sample with higher iron content prepared by increasing the gelation time to 12 h shows the cup-like morphology only when it was calcined at 500 ^{o}C for 5 h. The formation of hollow spheres on calcination at 400 ^{o}C suggests that the walls of the hollow spheres are thick enough to withstand the stress at that temperature. In other words, if the wall is thick buckling occurs at higher calcination temperature. However, if the iron loading is too high, the resulting morphology was always spherical irrespective of calcination temperature (Figure 18). This is evident from the retention of spherical structure for the sample with the gelation time 20 h, despite its calcination at 500 or 600 ^{o}C for 5 h. Moreover, the resulting α-Fe_2O_3 spheres are polycrystalline in nature and the wall thickness is around 40 nm. At higher loading the local heat generated at the surface of the CSP on calcination may not evenly be felt throughout the thick iron oxohydroxide coating leading to smaller α-Fe_2O_3 crystals. This polycrystalline structure eventually helps to absorb the stress and blocks its propagation during the carbon removal compared to a single crystalline α-Fe_2O_3. If the gelation time goes beyond 24 h, the thickness of the resulting α-Fe_2O_3 hollow spheres also increases up to 50 nm. Increasing the ratio (wt/wt) of CSP to ferric nitrate to three times gives a bowl-like morphology with a porous network on calcination at 500 ^{o}C (Figure 19).

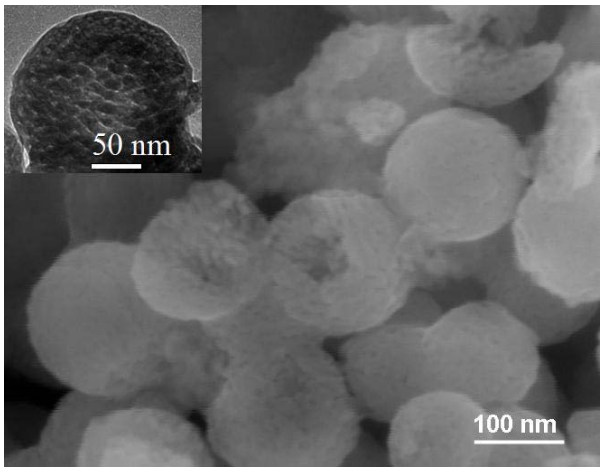

Figure 18: FESEM image of the thick walled spheres obtained by calcining the samples that attained gel in 20 h at 500 ^{o}C / 5 h in air. Inset is the TEM image.

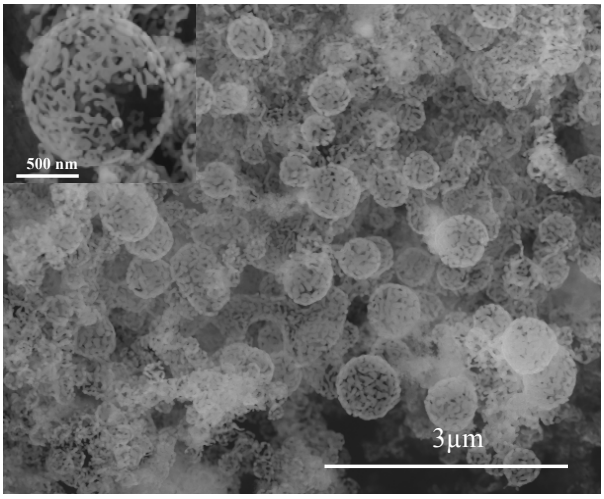

Figure 19: FESEM image of porous nanostructures obtained when CSP ratio was increased three times more for the same concentration of the ferric nitrate solution. Inset is the high magnification image of a single porous nanostructure.

One dimensional α-Fe_2O_3 nanorods, tubes and wires by virtue of their shapes are known to show anisotropic magnetic properties compared to their spherical counterparts.[17] However, change in the magnetic properties with respect to change in three dimensional complex morphology of single crystalline α-Fe_2O_3, for example, from hollow sphere to nanocup is not yet known. The bulk form of α-Fe_2O_3 is a canted antiferromagnet with high Néel temperature of T_N = 953 K. At T ~ 263 K, it undergoes Morin transition (MT) where

there is a magnetic spin reorientation, below which the weak ferromagnanetic component disappears.[18] Temperature dependence of zero field cooled (ZFC) and field cooled (FC) susceptibilities of the hollow spheres of α-Fe_2O_3 is shown in Figure 20a. This is typical of a superparamagnetic material with blocking temperature of 100 K.

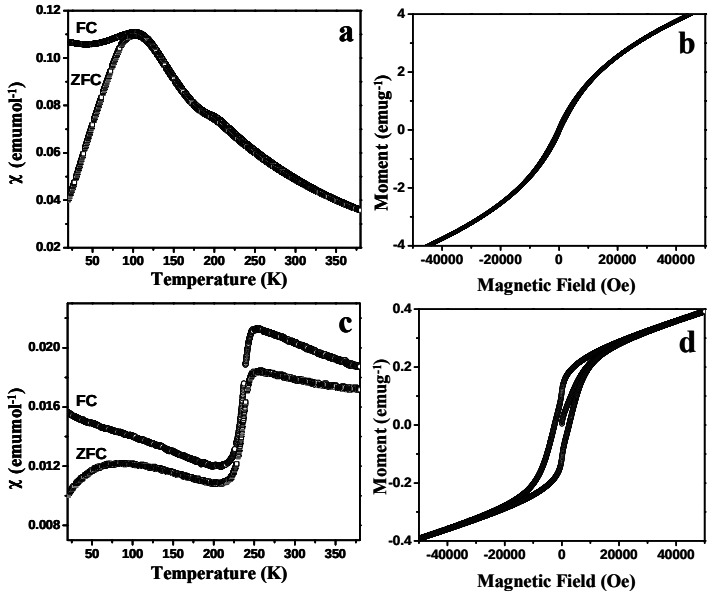

Figure 20*:* ZFC/FC (at 500 Oe) and M-H plot (at 300 K) of hollow spheres (a and b) ZFC/FC (at 500 Oe) and M-H plot (at 300 K) of nanocups (c and d).

The room temperature magnetization data further confirms the superparamagnetic behaviour of the hollow spheres (Figure 20b). Superparamagnetic properties is usually found in α-Fe_2O_3 particles of size less than 20 nm.[19] This property can therefore be attributed to the wall thickness of the single crystalline hollow spheres which is around 20 nm. Interestingly, it also shows a very weak transition at 200 K which cannot be attributed to the superparamagnetic hollow spheres. This would probably be accounted for the Morin transition associated with a very few buckling spheres which are at the beginning of transformation into cups. In sharp contrast to the superparamagnetic hollow spheres, nanocups with the wall thickness around 10 nm show bulk α-Fe_2O_3 behaviour with a prominent Morin transition around 250 K (Figure 20c). It is to be noted that Morin transition

is unlikely to be seen above 4 K if the particle sizes are in the range of 8 to 20 nm. Studies over crystalline, mesoporous α-Fe_2O_3 further revealed that the walls of confined dimensions tend to suppress the Morin transition.[20] However, unlike bulk, the irreversibility between zero-field cooled (ZFC) and field cooled (FC) below Morin transition strongly suggest a spin canting. Room Temperature M-H curve clearly confirms the canted antiferromagnetism in nanocups (Figure 20d). The shape anisotropy of nanocups indeed has a significant influence on their magnetic properties[22] exhibiting a very high coercivity of 2587 Oe. This value to our knowledge is highest among all other morphologies of α-Fe_2O_3 reported so far.[21]

3.6. Conclusions:

In summary, we have reported a simple chemical route to synthesise single crystalline α- Fe_2O_3 in the form of hollow spheres and nanocups using glucose derived CSP as templates. Nanocups have been found to form from the buckling of hollow spheres. The observation could not be reproduced with spherical templates made of polystyrene. The magnetic properties are shown to be different for the two morphologies. The nanocups show a very large coercivity owing to their complex shape anisotropy. Metal ions that are amphoteric, form oxohydroxide polymer in acidic or basic conditions and therefore, it should be possible to extend this procedure to obtain other metal oxide nanocups.

3.7. References:

1. Song, H.; Ismagilov, R. F. *J. Am. Chem. Soc.* **2003**, *125*, 14613.

2. Lagally, E. T.; Medintz, ; Mathies, R. A. *Anal. Chem.* **2001**, *73*, 565.

3. Hatch, Kamholz, A. E.; Hawkins, K. R.; Munson, M. S.; Schilling, E. A.; Weigl, B. H.; Yager, P. *Nat. Biotechnol.* **2001**, *19*, 461.

4. Han, Y-J.; Watson, J. T.; Stucky, G. D. *J. Molecular Catlysis B: Enzymatic*, **2002**, *17*, 1.

5. a) Zelikin, A. L.; Becker, A. L.; Johnston, A. P. R.; Wark, K. L.; Turatti, F.; Caruso, F. *ACS Nano,* **2007**, *1*, 63-69. b) Eswaramoorthy, M.; Walsh, D.; Mann, S.; *Adv. Mat.* **2002,**

14, 969-972. c) Shchukin, D.; Möhwald, H. *Adv. Funct. Mater.* **2007**, *17*, 1451.

6. a) Ajayan, P. M.; Ijima, S. *Nature* **1993**, *361*, 333-334. b) Gao, Y.; Bando, Y. *Nature* **2002**, *415*, 599.

7. Love, J. C.; Gates, B. D.; Wolfe, D. B.; Paul, K. E.; Whitesides, G. M. *Nano Lett.* **2002,** *2*, 891.

8. Wang, X. D.; Lao, C. S.; Graugnard, E.; Summers, C. J.; Wang, Z. L. *Nano Lett.* **2005**, *5*, 1784.

9. John, N. S.; Selvi, N. R.; Mathur, M.; Govindarajan, R.; Kulkarni, G. U. *J. Phys. Chem. B.* **2006,** *110,* 22975.

10. a) Deotare, P .B.; Kameoka, J. *Nanotechnology* **2006,** *17*, 1380. b) Li, X.; Peng, J.; Kang, J-H.; Choy, J-H.; Steinhart, M.; Knoll, W.; Kim, D. H. *Soft Matter* **2008**, *4*, 515. c) Srivastava, A. K.; White, T. J.; Ramanujan, R. V. *Thin Solid films* **2006**, *505*, 93.

11. Leong, Gu, Z.; Koh, T.; Gracias, D. H. *J. Am. Chem. Soc.* **2006**, *128,* 11336.

12. Im, S. H.; Jeong, U.; Xia, Y. *Nature Mater.* **2005**, *4*, 671.

13. a) Sun, X.; Liu, J.; Li, Y. *Chem.- Eur. J.* **2006**, *12*, 2039. b) Titirici, M-M.; Antonietti, M.; Thomas, A. *Chem. Mater.* **2006**, *18*, 3808.

14. Sun, X.; Li, Y. *Angew. Chem. Int. Ed.* **2004**, *43*, 597.

15. Schwertmann, U.; Cornell, R. M. Iron Oxides in the laboratory, *VCH Publishers, Verlagsgesellschaft mbH, Weinheim (Germany) and New York (USA),* **1991**.

16. Klein, Y.; Efrati, E.; Sharon, E. *Science* **2007**, *315*, 1116.

17. a) Dumustre, F.; Chaudret, B.; Amiens, C.; Fromen, M. C.; Casanove, M. J.; Renaud, P.; Zurcher, P.*Angew. Chem. Int. Ed.* **2002**, *41*, 4286. b) Liu, Z.; Chang, P-C.; Chang, C-C.; Galaktionov, E.; Bergmann, G.; Lu, J. G. *Adv. Funct. Mater.* **2008**, *18*, 1573.

18. Morin, F. J. *Phys. Rev.* **1950**, *78*, 819.

19.Bødker, F.; Hansen, M. F.; Koch, C. B.; Lefmann, K.; Mørup, S. *Phys. Rev. B.* **2000**, *61*,

6826.

20. Jiao, F.; Harrison, A.; Jumas, J.-C.; Chadwick, A. V.; Kockelmann, W.; Bruce, P. G.; *J. Amer.Chem. Soc.* **2006**, *128*, 5468.

21. a) Liu, L.; Kou, H. Z.; Mo, H.; Liu, Y.; Wang, Y. *J. Phys. Chem. B.* **2006**, *110*, 15218. b) Chueh, Y. L.; Lai, M. W.; Liang, J. Q.; Chou, L. J.; Wang, Z. L. *Adv. Funct.Mater.***2006,** *16*, 2243. c) Zhu, L. P.; Xiao, H. M.; Liu, X. M.; Fu, S. Y. *J. Mater.Chem.* **2006,** *16,* 1794. d) Yu, X.; Cao, C.; An, X. *Chem. Mater.* **2008,** *20*, 1936. e) Mitra, S.; Das, S.; Mandal, K.; Chaudhuri, S. *Nanotechnology* **2007**, *18,* 275608. f) Cao, M.; Liu, T.; Gao, S.; Sun, G.; Wu, X.; Hu, C.; Wang, Z. L. *Angew. Chem. Int. Ed.* **2005**, *44*, 4197. g) Wu, J.J.; Lee, Y. L.; Chiang, H. H.; Wong, D. K. P. *J. Phys. Chem. B.* **2006**,*110*, 18108. h) Tang, B.; Wang, G.; Zhuo, L.; Ge, J.; Cui, L. *Inorg. Chem.* **2006**, *45*,5196.

Summary

This chapter deals with the synthesis and characterisation of hierarchically porous bioactive glass (MBGH). The walls of the macroporous (0.3 - 0.5 μm) MBGH contains orderly arranged mesopores of 5 nm diameter. The pores are generated using a template based approach wherin, the self-assembled pluoronic P123 polymer was used to create mesopores and glucose derived amorphous carbon microspheres were used to create macropores. The as synthesized MBGH exhibits a high surface area of 270 m^2/g. Besides serving as a template for macropores, the negatively charged CSP favour the local enrichment of calcium ions around the surface and favour the formation of hydroxycarbonate apatite – silica nanocomposite on calcination. MBGH also exhibits an accelerated growth of monoclinic like apatite growth under *in vitro* conditions. The reason for such high bioactivity is attributed to the presence of nanocrystals of hydroxycarbonate apatite which is supported by X-ray diffraction, Fourier transform-IR spectroscopy and electron microscopy.

A paper based on this study has been published as an article in *J. Phys. Chem. C*, **2008**, 112 (19), 7379-7384.

4.1. Introduction

Bone is a natural composite of collagen (polymer), which provides a framework, and inorganic mineral (ceramic), which provides strength.[1] As every other living tissue, bone is also prone to continuous degeneration over a period of time. Osteoporosis is one such disease where bone resorption (dissolution) occurs faster than the new bone formation leading to a reduction in total bone density and strength.[2] Figure 1 summarizes the effect of time on bone strength and density from the age of 30 years onward.

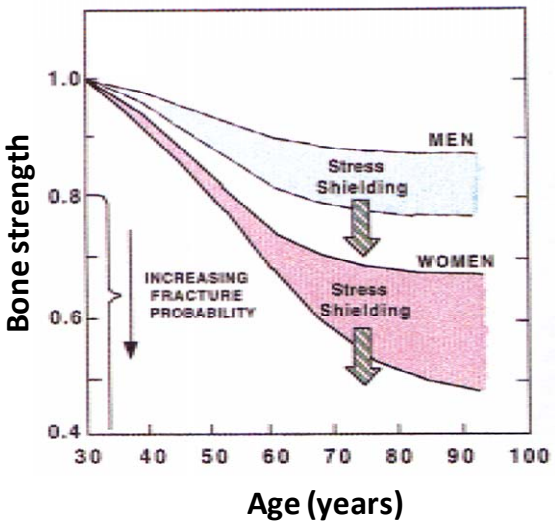

Figure 1: Plot showing the loss of bone density in humans with age. (ref 2)

The lower bone density leads to a constant deterioration of bone strength in the ends of long bones and vertebrae. An unfortunate consequence of this is that many old people fracture their hips, wrist, knee or spine. The effect is even more severe in women because of hormonal changes during menopause. The major cause of this disease is that the osteoblasts (bone producing cells) become progressively less productive in making new bone and repairing minor wears and tears.

In the present situation, such osteoporotic fractures are treated by total replacement of the bone tissue via painful surgeries. However, many issues like mismatch of the Youngs

modulus between bone and the implant and their compatibility have made subsequent surgeries an inevitable option. Nevertheless, this has also put an enormous thrust on the choice of material to be used as an implant. Some of the biomaterials that have been developed include metals, alumina, zirconia, calcium phosphates etc. It has been proved beyond doubt that no impalnt remains inert in the body and all the materials elicit a response from living tissue. The implant materials in the past 20 years show that the failure originates from the biomaterial-tissue interface. Accordingly, the tissue-implant response has been classified into four types.[3]

- If the material is toxic, the surrounding tissue dies.
- If the material is non-toxic and biologically inactive, a fibrous tissue of variable thickness forms.
- If the material is non-toxic and biologically active, an interfacial bond forms.
- If the material is non-toxic and dissolves, the surrounding tissue replaces it.

A common drawback associated with most of the present day implants is that they lack three of the most critical characteristics of living tissues.[4]

- The ability to self-repair
- The ability to maintain the blood supply at the implant site
- The ability to modify their structure and properties in response to environmental factors such as mechanical load.

Assuming that an implanted material is expected to perform for at least 20 years, it is proposed that a shift in emphasis from ‘replacement of tissues’ to ‘regeneration of tissues’ is required. In other words, the fourth type of tissue-implant response must be fully exploited to evolve a new class of materials called tissue engineering materials.

Tissue Engineering:

Tissue Engineering is the persuasion of the body to heal itself, achieved by the delivery of biomolecules and supporting structures to the appropriate site of tissue.[5] The essence of tissue engineering is that those cells capable of initiating and sustaining the regeneration process are 'switched on', through growth factors or genes, so that they generate new functional tissue of the required variety.

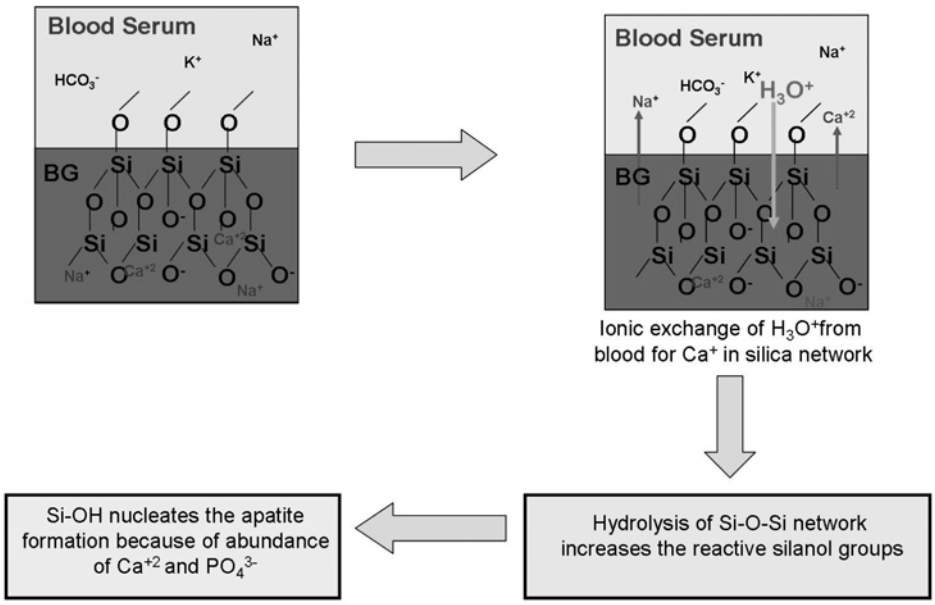

Scheme 1: The mechanism of formation of hydroxyapatite on the bioactive glass in simulated body fluid.

Bioactive glass ceramics of composition $CaO\text{-}P_2O_5\text{-}SiO_2\text{-}MO$ (M = Na, Mg, etc) are much sought-after materials in tissue engineering due to their ability to form chemical bond with the bone through the formation of biologically compatible hydroxycarbonate apatite formation (HCA) when implanted in the body (see scheme 1).[1] Findings that the bioactive glasses can also up-regulate different genes of primary human osteoblast cells evoke a great deal of interest in such materials.[6] Scheme 1 depicted above explains the mechanism of formation of HCA on the surface of a bioactive glass when placed in the simulated body fluid. The key point in the mechanism is the exchange of Ca^{+2} for H_3O^+ leading to the hydrolysis of silica network. It becomes more vivid that the entire bioactivity is a result of the

chemical reaction occurring at the interface (limited by diffusion). So, a large interfacial area would mean an increased bioactivity. Thus the efficiency of a bioactive glass greatly depends on the rate at which HCA forms on its surface in presence of the body fluid.

4.2. Scope of the present investigation

When the rate of formation of HCA is slow, no bond forms, and the material is no longer bioactive. Hence, there have been continuous efforts to develop materials with enhanced rate of the HCA growth in the body fluid in order to blend well with the bone. A layer of HCA can also form on the bioglass when soaked in a simulated body fluid (SBF). The formation rate of HCA in SBF referred to as *in vitro* bioactivity is used to predict the performance of the material when implanted in the body. The classical, melt-derived bioglasses take a month long time to crystallize apatite on their surface in SBF.[7] On the other hand, sol-gel derived bioglasses are able to crystallize HCA within 5 to 15 days time owing to their reactive silanol groups and increased porosity.[8] Calcium phosphate surrounded by mesoporous silica was reported to have very high *in vitro* bioactivity (less than 24 h) due to the presence of a highly soluble $NaCaPO_4$ phase coexisting with hydroxyapatite.[9] Recent report claims that mesostructured bioglass (MBG) is a better candidate for the fast crystallization of HCA in 4-8 h in SBF.[10]

In this study the synthesis of hierarchically porous bioactive glass (MBGH) showing exceptional growth for monoclinic like HCA in SBF in a very short period of 1 h is discussed. The hierarchy in the porosity arises from the macropores (300-800 nm) with their walls made of orderly arranged mesopores (3-5 nm). The former is templated by glucose derived CSP and the latter is templated by the pluoronic polymer P123. Removal of CSP and polymer P123 on calcinations leads to inherently premixed porous composite containing HCA nanocrystals embedded on the walls of mesoporous silica. MBGH refers to the calcined sample. This is very different from the known glass reinforced apatites[11] where the

composites are usually obtained by physical mixing of the bioactive glass powder and synthetic hydroxyapatite crystals at microscale. Mixing at the nanoscale can offer many advantages besides the fact that such a material would closely resemble the natural bone. HCA nanocrystals also serve as nuclei for the further growth of HCA in SBF. The macropores described in MBGH may not serve the biological scaffold requirements to support the cell growth but would certainly enhance the cell adhesion due to increased nanoscale-roughness on the surface.[12] Coating of these materials along with the existing scaffolds can be expected to have improved *in vivo* performance of the implants. Further, formation of monoclinic-like HCA is expected to have bioelectric effects in bone growth.[13]

4.3. Experimental section

a. Materials

D (+) glucose, Pluoronic polymer P123 and tetraethyl orthosilicate (TEOS) 2-[4-(2-hydroxyethyl)-1-piperazinyl]ethanesulfonic acid were purchased from Sigma Aldrich. Analar grade salts used for preparing SBF (NaCl, $NaHCO_3$, Na_2CO_3, KCl, $K_2HPO_4.3H_2O$, $MgCl_2.6H_2O$, $CaCl_2$ and Na_2SO_4) were purchased from Sd-fine Chemicals. Human foreskin fibroblasts (HFF) were purchased from American Type Culture Collection (ATCC, SRC-1040). Milli-Q water was used in all the experiments.

b. Synthesis of amorphous carbon additive (CSP)

Amorphous CSP were synthesized by solvothermal treatment of glucose. A slight modification in the synthetic procedure was adopted wherein, 2.0 g of glucose was dissolved in 8 mL of water and an equal volume of n-octane was added to it. The whole mixture was kept at 180 ^oC for 14 h in a 25 mL Teflon lined stainless steel autoclave. After cooling down the autoclave to room temperature the octane layer was decanted and the dark brown paste found at the bottom of the container was carefully collected and stirred in ethanol for 2 hours.

The CSP were separated by centrifugation and dried at 80 ^{o}C in air for 4 h. The size of the as-synthesized CSP was in the range of 500 nm to 10 μm.

c. Synthesis of hierarchically porous bioactive glass

A general protocol for the synthesis of hierarchically porous mesostructured bioactive glass (MBGH) included making slurry of CSP with calcium and phosphorous containing silica sol. The silica sol was prepared by the following procedure. P123 (4.0 g), TEOS, 6.7 g, $Ca(NO_3)_2{\cdot}4H_2O$ (1.4 g), triethyl phosphate (TEP, 0.73 g) and 0.5 M HCl (1.0 g) were dissolved in ethanol (60 g) and stirred at room temperature for 1 day. The slurry was obtained by physically mixing the CSP and silica sol in a definite ratio. The slurry was allowed to dry at room temperature overnight to aid the evaporation induced self-assembly (EISA) process of polymers to form mesostructure around the CSP. The dried powder was calcined at 700 ^{o}C for 5 h to obtain the final MBGH products. MBG was also prepared in a similar way except that the CSP were not added to the initial silica sol.

d. Synthesis of simulated body fluid (SBF)

SBF was prepared according to the procedure reported in the literatutre.[14] It contains all the salts that are present in the human blood in an appropriate ratio at pH 7.4. It does not possess any proteins or cells. For a 160 mL of SBF solution the salts are added as given below. The order of addition of salts must also be maintained as given in the table (from top to bottom).

Ingredients in SBF	Weight (g)
NaCl	0.864
$NaHCO_3$	0.080
Na_2CO_3	0.068
KCl	0.036
$K_2HPO_4.3H_2O$	0.036
$MgCl_2.6H_2O$	0.049
HEPES	2.862
$CaCl_2$	0.046
Na_2SO_4	0.011

Table 1: Preparation of SBF. pH 7.2 was obtained by adding suitable amount of 1M HCl solution after the addition of HEPES.

e. *In vitro* studies

In vitro studies were performed by soaking the powder samples of MBGH in a SBF (40 mg in 40 mL). The samples were soaked in SBF kept at 37 ^oC and a pH of 7.2 over a period of 1h, 3h, 6h, 12h, 3 days and 14 days. Accordingly the samples were labelled as MBGH-1 h, MBGH-3 h, MBGH-6 h, MBGH-12 h, MBGH-3 d and MBGH-2 w. Finally, the samples were recovered by filtration using a polycarbonate membrane containing pores of 200 nm in diameter (Millipore GTTP04700) and washed thrice with acetone and dried in air for 1 hour.

f. Preliminary biocompatibility test of MBG, MBGH and MBGH-3d samples on human fibroblasts cells *in vitro*

HFF are primary culture cells that grow by attaching to the substratum. Human fibroblasts are a widely distributed cell type in the body. The use of neonatal-derived cell cultures adds further significance to these studies as they most closely mimic cells in the body in terms of their growth and survival characteristics. A defined number of cells were

seeded and monitored for survival and growth in the presence of mesoporous bioglasses. The cells were maintained in Dulbeccos modified eagle's medium (DMEM) supplemented with 10% foetal calf serum (FCS), 1 mM sodium pyruvate and 2 mM glutamine. The cells were seeded in 24-well plates at a concentration of 1 x 10^5 cells/well in 0.5 mL of medium. The cells were incubated in a humidified incubator at 37° C and 5% CO_2 atmosphere. They were cultured for 2 h before addition of any material onto them. The cells were exposed to MBG, as synthesized MBGH and MBGH-3 d samples at concentrations of 0.5, 1.0 and 1.5 mg/mL. The morphology of the incubation cells were monitored over a period of 24 h, 48 h and 72 h.

4.4. Characterization

Morphology of the samples was analyzed by a field emission scanning electron microscope (FESEM, FEI Nova-Nano SEM-600, Netherlands). TEM images were recorded using a JEOL JEM 3010 instrument (Japan) operated with an accelerating voltage of 300 kV. Low angle X-ray diffraction (XRD) characterization was done at 25 ^oC with a Rich-Siefert 3000-TT diffractometer employing Cu Kα radiation. Wide angle X-ray diffraction (XRD) characterization was done at 25 ^oC with a Bruker-D8 X-ray diffractometer employing Cu Kα radiation. N_2 adsorption-desorption isotherms were measured using QUANTACHROME AUTOSORB-1C at liquid N_2 temperature (77 K). The morphology of the cells in biocompatibility studies were studied at 100X magnification using an Olympus IX70 microscope fitted with a Coolsnap pro camera.

4.5. Results and discussion

The sample was first characterized for the hierarchy in porosity. Figure 2 shows the field emission scanning electron microscopy (FESEM) image of MBGH and MBG wherin MBGH clearly is seen with macropores of size 200 nm to a few microns templated by the CSP. The density of the macropores could be increased by increasing the amount of CSP used to form the slurry.

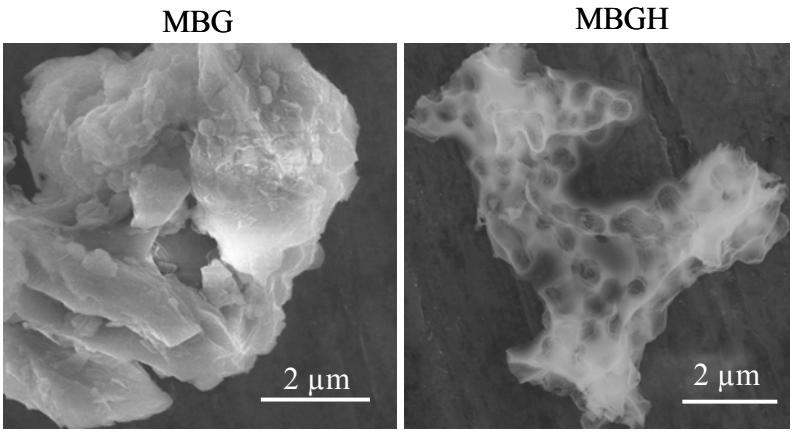

Figure 2: FESEM image of MBG and MBGH.

Figure 3 also shows the FESEM image of MBGH obtained at higher magnification. The inset of Figure 3 is a TEM image of the fragmented wall showing uniform mesoporous channels viewed perpendicular to the channel direction. The low angle peak observed in XRD at $2\theta = 1.19^{o}$ for MBG and at 1.04^{o} for MBGH (Figure 4) is associated with ordered arrangement of the mesopores in the silica matrix templated by the pluronic polymer, P123. This also suggests that MBGH has thicker mesopore walls than MBG.

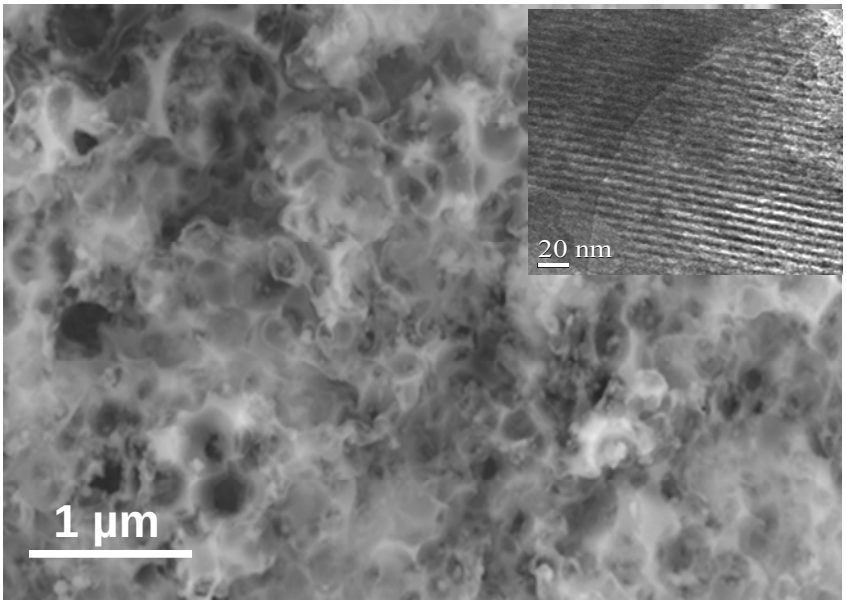

Figure 3: FESEM image of MBGH taken at higher magnification. Inset is the TEM image of the wall of MBGH.

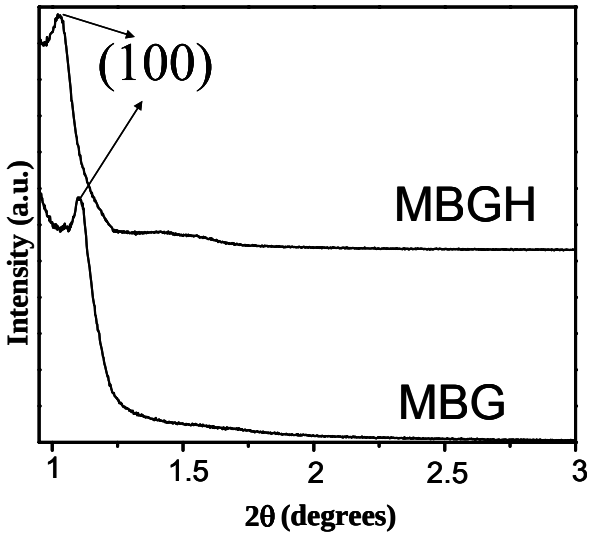

Figure 4: Low angle X-ray diffraction of MBG and MBGH showing the reflection of (100) plane of mesostructured silica network.

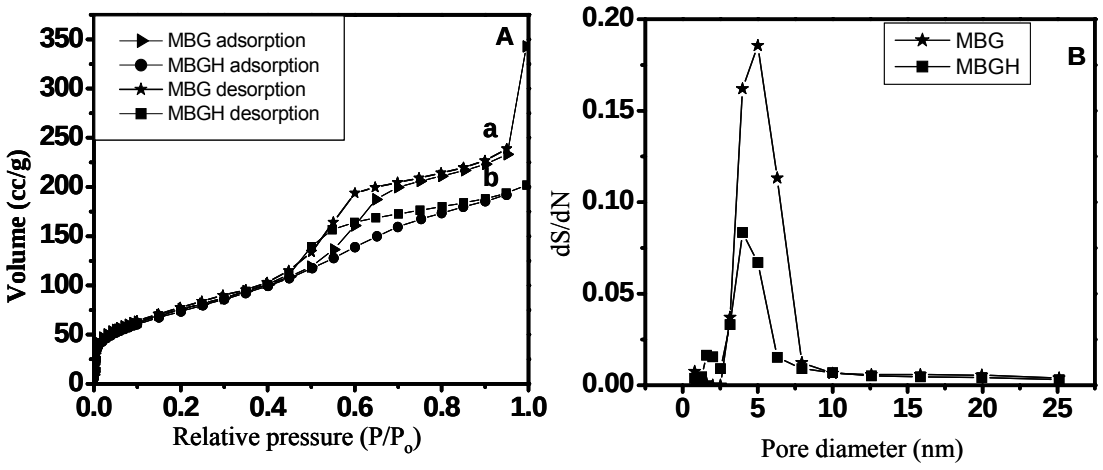

Figure 5: A) Adsorption isotherm of a) MBG and b) MBGH. B) Pore size distribution of MBG and MBGH.

Nitrogen adsorption isotherms of calcined MBG and MBGH samples show type-IV isotherm with H1 type hysterisis identified with the cylindrical mesopores in Figure 5A. The pore volume (at $P/P_0 = 0.98$) and pore size of MBGH (Figure 5B) obtained from nitrogen adsorption isotherm were 0.49 cm^3/g and 5 nm respectively. The low BET surface area (270 m^2/g) obtained for MBGH compared to MBG sample (351 m^2/g) is attributed to the presence

of macropores. The presence of thicker mesopore walls as suggested by XRD data also supports this inference. All the above data establishes that the physical structure of MBGH is hierarchically porous wherein, the pores of size 300 nm to a few μm are formed by CSP and the walls of these pores are inturn made up of mesopores of 5 nm diameter.

TEM analysis of MBGH in Figure 6a reveals the presence of dark contrast crystals of 5 to 10 nm in size (indicated by white arrows) specifically located in and around the macropores templated by the CSP. The ED pattern (Figure 6b) displays a polycrystalline pattern, typical of hydroxyapatite nanocrystals. The HREM image (Figure 6c) of a nanoparticle shows the lattice spacing of 0.280 nm charcteristic of a hydroxyapatite crystal. The study suggests that MBGH possess apatite nanocrystals in the initial stage itself (before soaking in SBF) which was also confirmed by other means. Figure 7 shows the wide angle XRD pattern of the MBG and MBGH samples after calcination. In contrast to MBG sample, MBGH shows reflections for hydroxyapatite nanocrystals at 2θ; 25.8, 31.7 and 32.9 degrees. However, it would be difficult to assign these peaks to a particular phase (hexagonal or monoclinic) of hydroxyapatite as there are only a limited number of diffraction peaks in the XRD pattern. FT-IR spectrum of MBG and MBGH are compared in Figure 8. The O-P-O bending frequencies at 600 to 570 cm^{-1} and P-O stretching frequency at 960 cm^{-1} are present in the case of MBGH. The bands at 1490 and 1423 cm^{-1} seen in MBGH correspond to CO_3^{2-} stretching frequencies. Thus as synthesized MBGH contains crystals of hydroxycarbonate apatite (HCA).

The presence of HCA nanocrystals in MBGH and not in MBG hinted the role of CSP which was originally introduced to create macropores. The binding capacity of the CSP with divalent calcium ions was studied by soaking the CSP in calcium nitrate solution for an hour followed by an extensive washing with water. The effecient adsorption of Ca^{+2} ions on the surface of the CSP is evident from the EDX mapping (Figure 9).

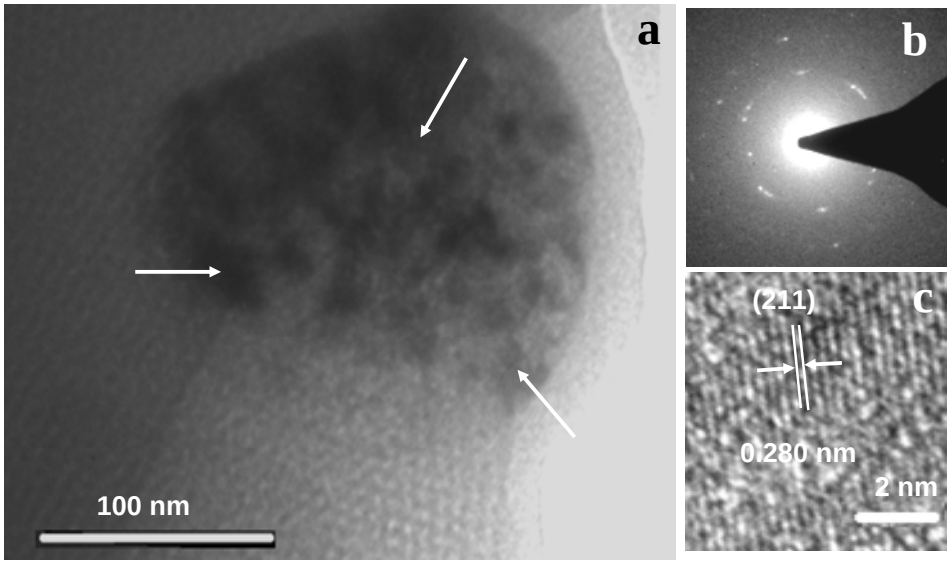

Figure 6: a) TEM image of MBGH showing HCA nanocrystals (patches of dark contrast) around the macropore region b) corresponding ED pattern. c) HREM image of an HCA nanocrystal.

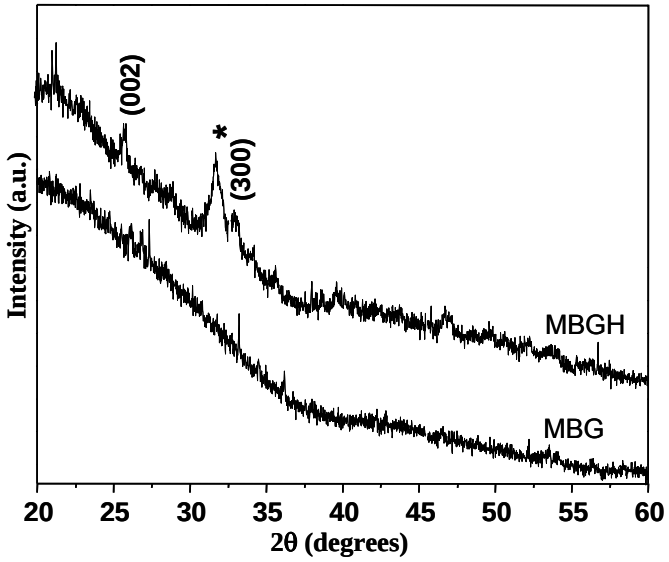

Figure 7: Wide-angle XRD pattern of calcined MBG and MBGH samples. (*) This peak can be assigned to (211) plane of hexagonal or (221) plane of monoclinic phase of HCA.

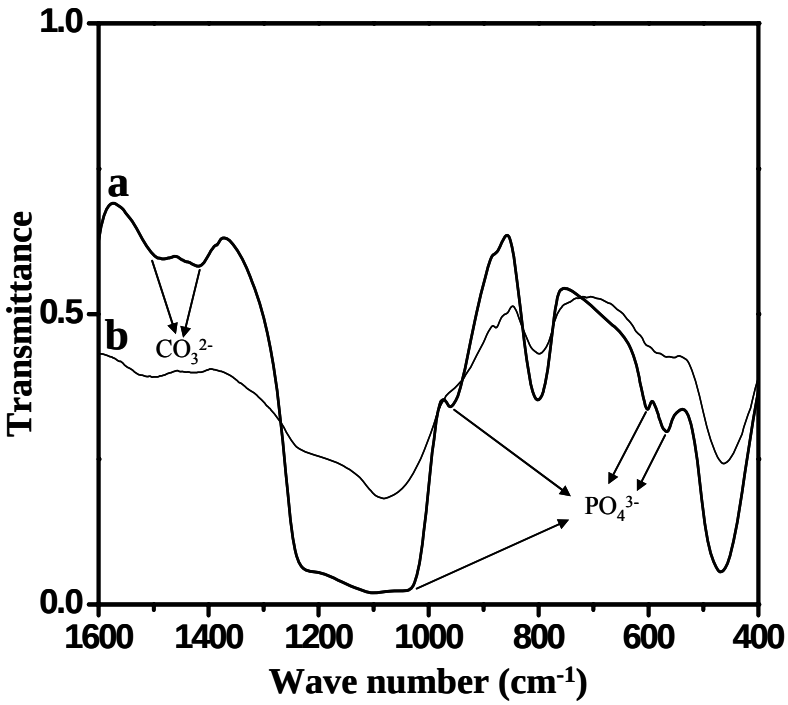

Figure 8: FTIR of a) calcined MBGH and b) calcined MBG before soaking in SBF.

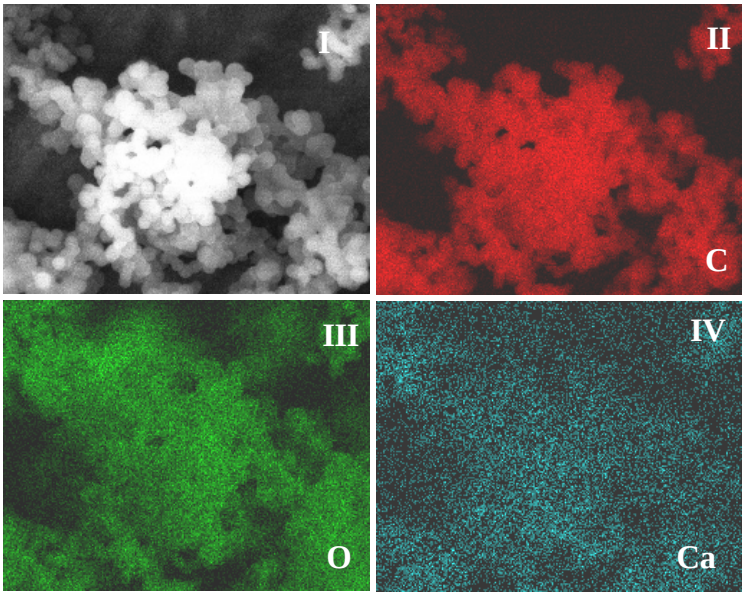

Figure 9: Images I) SEM image of 500 nm CSP treated with 0.5 M calcium nitrate solution for an hour and washed thoroughly with water. EDX mapping of CSP showing the compositional elements II) carbon, III) oxygen and IV) calcium. The image suggests the strong binding ability of CSP to the divalent cation Ca^{+2}.

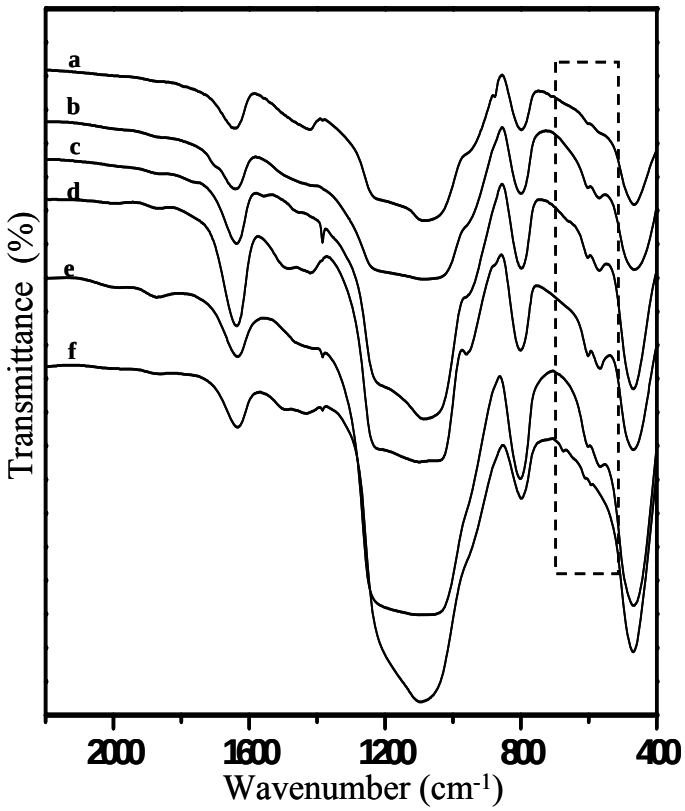

Figure 10: FTIR studies of MBGH prepared with various CSP content. C/Ca weight ratio for a) 0, b) 0.5, c) 4, d) 10, e) 50 and f) 500.

Synthesis of MBGH at different weight ratios of CSP to calcium nitrate (C/Ca = 0, 0.5, 4, 10, 50 and 500) was carried out and their FT-IR spectrum after calcination is presented in the Figure 10. The O-P-O bending frequency region from 570 to 600 cm^{-1} was monitored to study the formation of crystalline HCA at different carbon content. The initial increase in intensity of HCA bands at 568 and 603 cm^{-1} with increase in the C/Ca ratio (from 0 to 10) confirms the role of CSP in the formation of crystalline HCA nuclei. At higher ratios (C/Ca = 50 and above) the distinction between the two peaks disappeared.

The growth of HCA crystals on the surface of MBGH (C/Ca ratio = 10) soaked in SBF at different periods of time was monitored using XRD. Within 10 min of soaking SBF, the growth of HCA nanocrystals was noticed. The growth of the crystals started within few minutes of soaking the sample in SBF. The integral intensity of the peak at two theta 31.7^{o}

corresponding to (221) was found to increase 4.5 times within 10 min of soaking the sample in SBF (Figure 11).

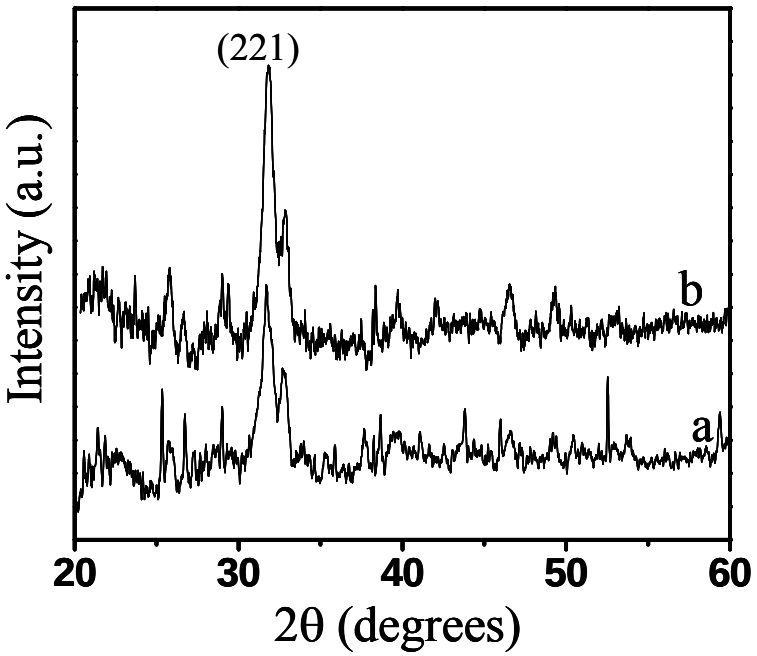

Figure 11: XRD patterns of a) MBGH as prepared. b) MBGH soaked in SBF for 10 min.

Soaking MBGH in SBF for 1 h resulted in two prominent peaks at 2θ range 31.7 and 45.3 degrees followed by a very weak peak at 56.3 degree. Increasing the soaking time from 1 h to 12 h did not show any significant change in the intensity of XRD peaks indicating a slow down in the rate of crystal growth (Figure 12A). Samples soaked for longer period of time (3 days) show increase in intensity for the original peaks along with some additional peaks (Figure 12A inset) that could be indexed to monoclinic HCA.

The calculated pattern for the samples soaked in SBF for less than 24 h also fits well for the monoclinic rather than hexagonal phase. MBGH soaked in SBF for two weeks showed very well resolved peaks (Figure 12B). The peaks were indexed using the program DICVOL91 TREOR90 in CRYSFIRE. No best solutions were obtained when the indexing was restricted to the hexagonal phase (P63/m) but yielded solutions to monoclinic phase

(JCPDF 76-0694). The XRD patterns were further refined for the cell parameters using TOPAS (Figure 13).

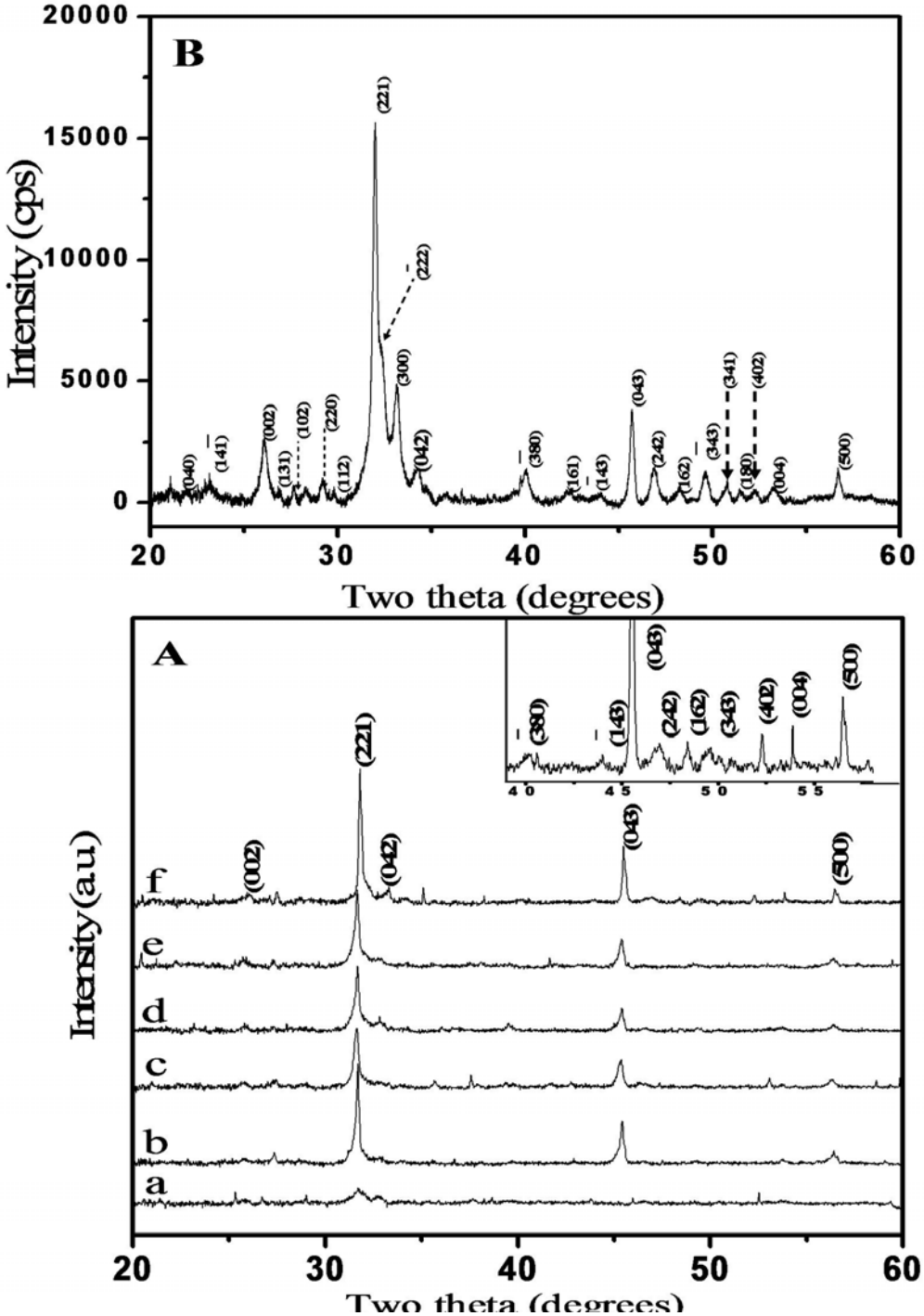

Figure 12: A) XRD patterns of a) MBGH (without SBF treatment), and MBGH soaked in SBF for various period of time b) 1 h, c) 3 h, d) 6 h,e) 12 h and f) 3 days. Inset shows the magnified (two times) region of (f) in

the 2 θ range from 38° to 60° degrees. B) XRD of MBGH soaked in SBF for 2 weeks, indexed to monoclinic HCA.

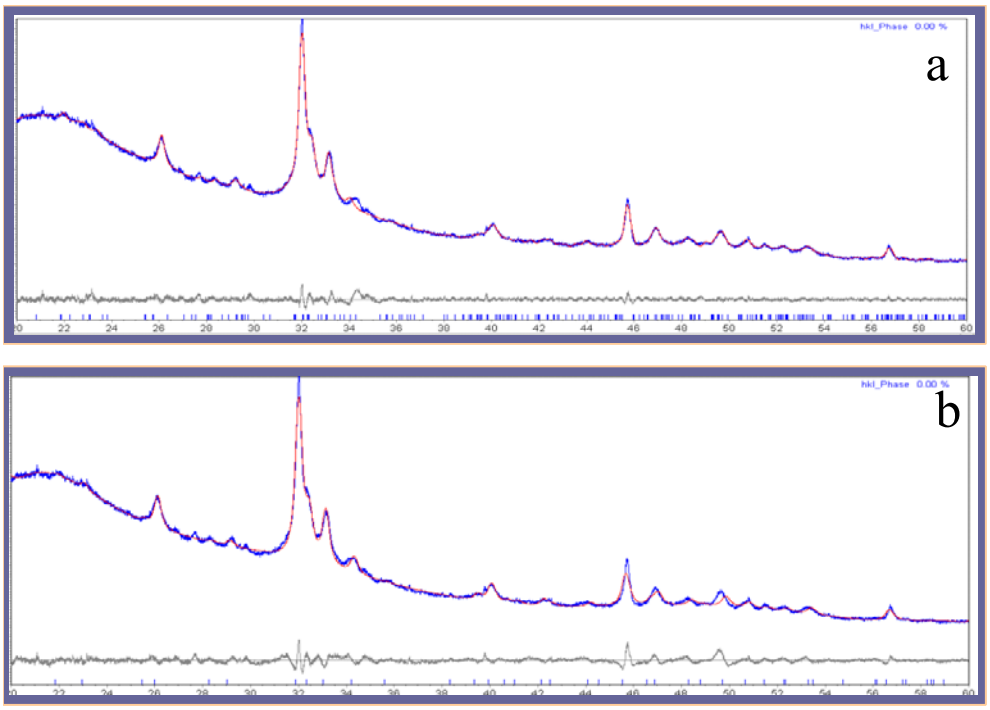

Figure 13: Profile matching done for MBGH- 2 weeks sample using TOPAS programme. a) Monoclinic P21/b b) Hexagonal P63/m. The blue line is the experimentally obtained XRD pattern of MBGH-2 weeks sample. The red line is the fitted pattern. The grey line at the bottom represents the difference between the calculated and the obtained pattern.

Monoclinic phase

R Values

Rexp : 1.13 Rwp : 1.98 Rp : 1.47 GOF : 1.75

Rexp`: 1.41 Rwp`: 2.48 Rp` : 1.93 DW : 0.65

a (Å) 9.2831206

b (Å) 18.5487097

c (Å) 6.9096479

gamma (°) 118.8773

Hexagonal P63/m

R-Values

Rexp : 1.15 Rwp : 2.89 Rp : 2.02 GOF : 2.51

Rexp`: 1.69 Rwp`: 4.25 Rp` : 3.03 DW : 0.31

The FTIR spectra of MBGH before and after soaking in SBF at different periods of time is shown in Figure 14. The O-P-O bending frequency region showed two distinguisable bands for the samples soaked in SBF for 1h. However, with increased time of soaking the spectral region from 570 – 610 cm^{-1}displayed three broad bands. The restoration of three bands into two was observed in the sample soaked in SBF for over 2 weeks.

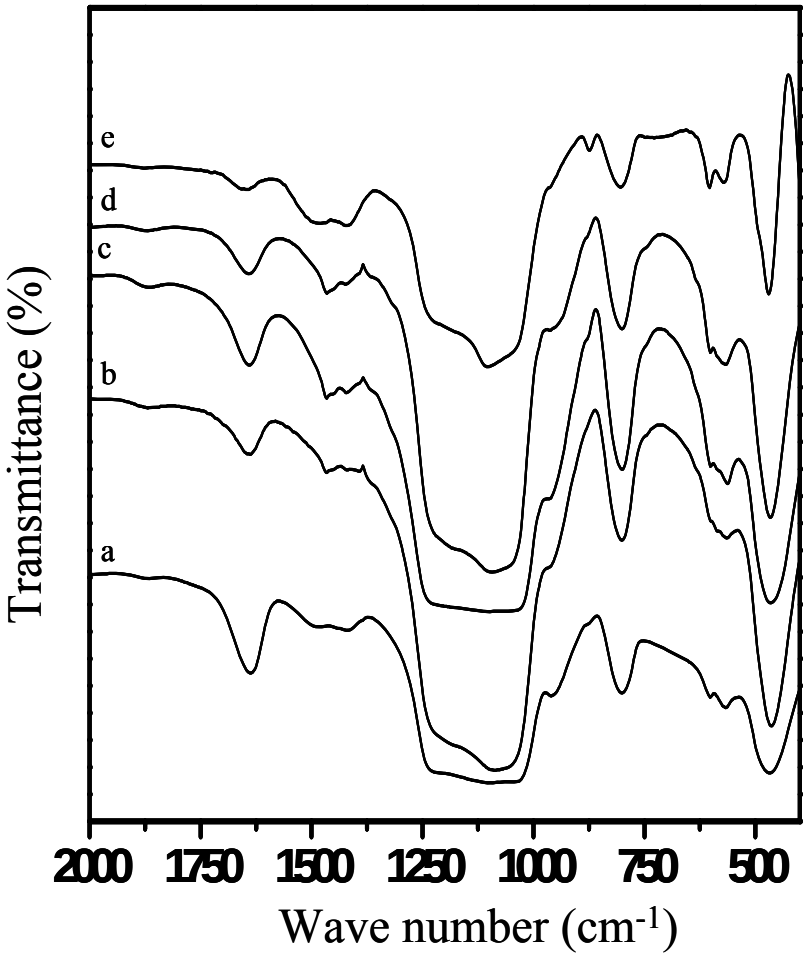

Figure 14: FT-IR spectrum of a) calcined MBGH, and MBGH soaked in SBF at different periods of time b) 1 h, c) 12 h, d) 3 days and e) 2 weeks.

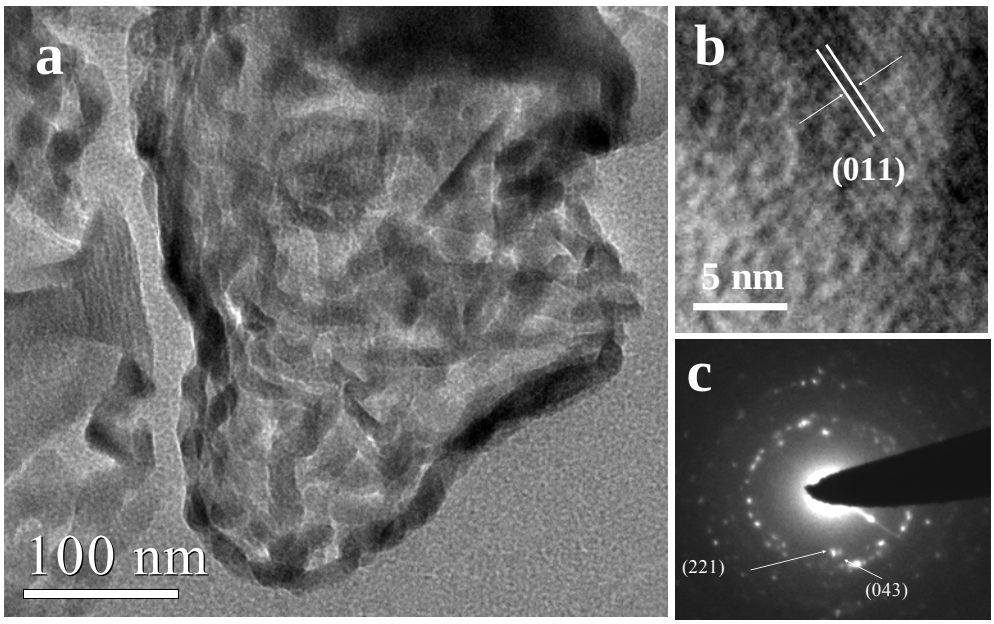

Figure 15: a) TEM image of hollow structure of MBGH-1h showing the HCA crystals. b) HREM of the crystal. c) ED pattern of the HCA crystal.

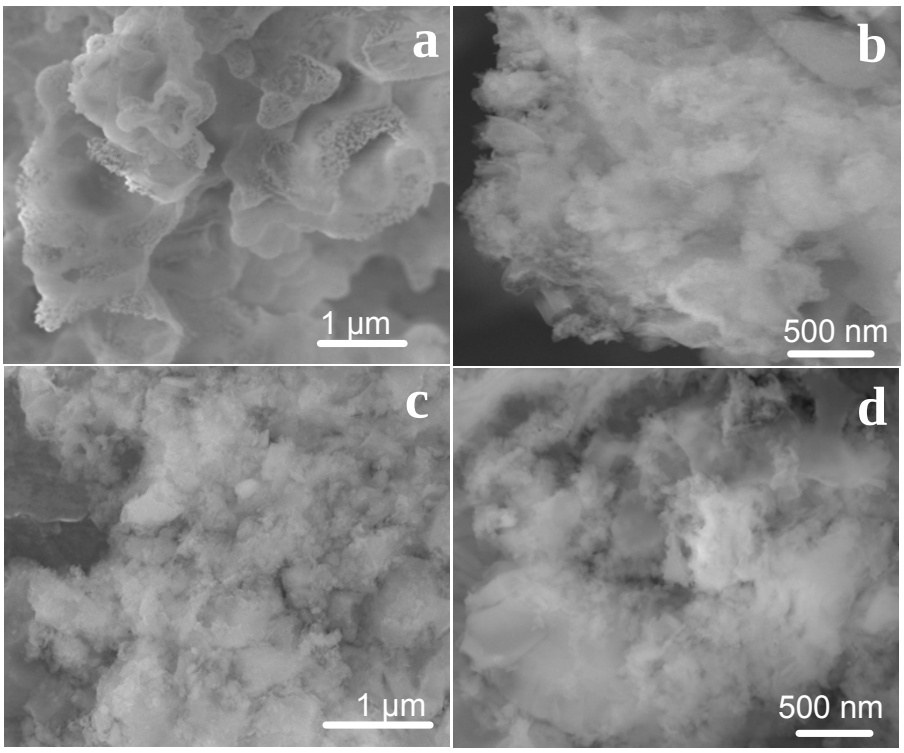

Figure 16: FESEM images of a) MBGH-1h, b) MBGH-3d, c) MBGH-6d, d) MBGH-2 weeks.

In Figure 15a, the TEM image of MBGH -1 h shows the presence of HCA crystals around 50 nm forming network like structures on the surface of MBGH. The crystallinity of the sample was evident from HREM image showing the (011) plane (Figure 15b). The ED pattern (Figure 15c) shows polycrystalline nature whose rings could be indexed to (221) and (043) planes. The macropores of MBGH are gradually covered with the nanocrystals of HCA on soaking for longer duration in SBF as analysed using FESEM (Figure 16).

The role of CSP additive in obtaining HCA nuclei can be explained as follows. The CSP possess a negatively charged surface with a zeta potential of -24 mV in water at pH 7.2. Besides, the FTIR spectrum of the CSP showed intense bands at 1702 and 3369 cm^{-1} corresponding to the presence of -C=O and O-H stretches respectively. Therefore, adsorption of divalent and trivalent metal ions on the surface of the CSP is expected and has already been exploited to make metal oxide and nitride hollow structures.[15,16] In the present case, the negatively charged surface of the CSP increases the local concentration of Ca^{2+} around them and facilitates the nucleation of calcium phosphates (Scheme 2). Attempts to synthesize mesostructured silica in absence of calcium nitrate were not successful due to the interference of charged surface of the CSP on the formation of micelles. On the other hand, presence of calcium ions passivates the surface charge of CSP and hence allows the formation of micelles, a prerequisite to the development of mesostructure. The strong binding affinity of CSP with calcium ions was unambiguously proved by elemental mapping (Figure 9) and from the formation of HCA on the surface of MBGH synthesized at diffrent carbon content (FT-IR studies). However, at higher ratios (C/Ca = 50 and above in Figure 10) the distinction between the two peaks (indicating the presnce of crystalline HCA) disappeared suggesting a substantial reduction in the concentration of calcium ions on each sphere which, in turn reduces the calcium phosphate formation in presence of phosphate ions. The enormous amount of heat generated locally during the calcination of carbon rich CSP plays a very

important role in converting amorphous calcium phosphates into crystalline HCA. XRD patterns of the CSP soaked in bioactive silica sol for 6 h did not show any peak assigned to the crystalline HCA, indicating the importance of calcination.

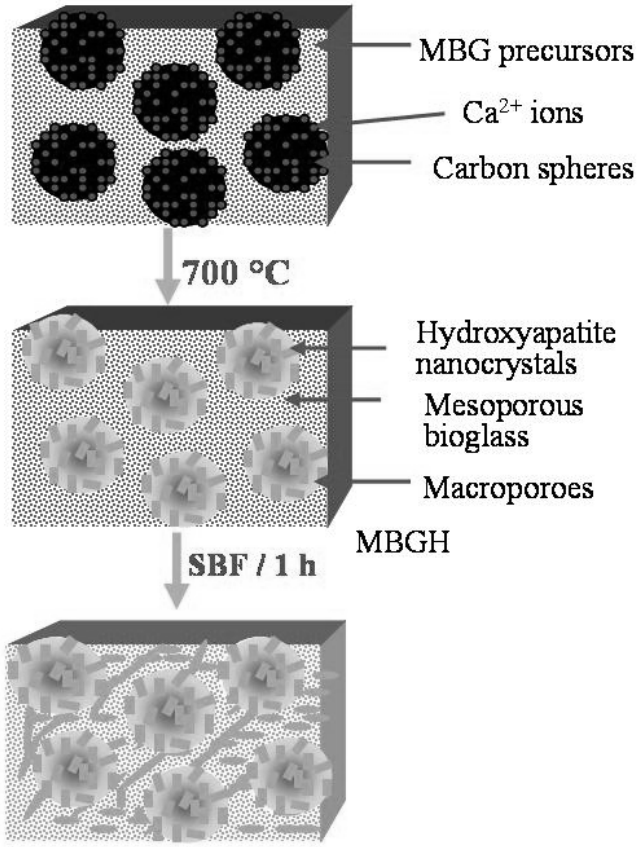

Scheme 2: Scheme showing the role of carbon in the formation of hierarchically porous bioactive glass.

The deconvolution analysis of absorption bands in the FT-IR spectrum of the samples soaked in SBF at various time periods was informative (Figure 17). Amorphous calcium phosphates are known to give a broad band[17] in the region 600 to 570 cm^{-1} while, the crystalline phosphates exhibit two distinct bands at 570 and 604cm^{-1} for O-P-O bending mode vibrations. The presence of two distinguishable bands at 570 and 604 cm^{-1} for the calcined MBGH sample clearly indicates the formation of HCA crystals nucleated by the CSP. Soaking the sample in SBF for 1 h resulted in broadening of these bands possibly due to the formation of amorphous calcium phosphate in addition to crystalline

HCA. The deconvoluted, O-P-O bending region shows three possible absorption bands with the broad, middle one being assigned to amorphous calcium phosphate (Figure 17). The decrease in intensity of the amorphous peak with increase in soaking time is attributed to the transformation of amorphous calcium phosphate to crystalline one. This is further supported by the clear restoriation of the O-P-O bending modes for MBGH soaked in the SBF for over 2 weeks.

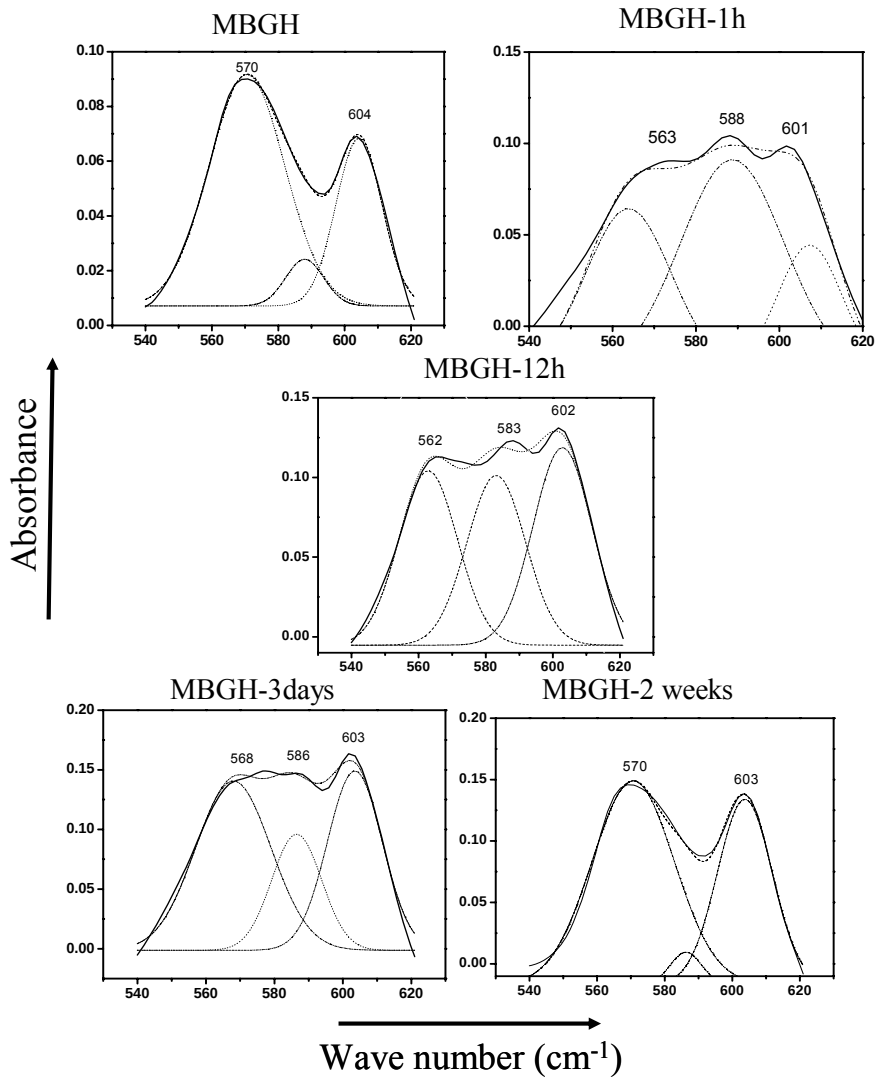

Figure 17: Deconvolution of FT-IR spectra of MBGH, MBGH-1h, MBGH-12 h, MBGH-3days and MBGH-2 weeks.

Any biomaterial must be subjected to thorough tests on their compatibility with the living tissue. The most preliminary biocompatibility test would be to see the physical

interactions between the synthesized bioglass and the human cells. The ideal cell line would ofcourse be the osteoblasts but human fibroblasts cells were used in the study because of its availability. Figure 18 shows the optical phase contrast microscopy images of the interaction of cells and MBG and MBGH incubated for different periods of time. No change in cell morphology or growth characteristics as compared to controls (A, cover slip and B, MBG) could be observed by phase-contrast microscopy. The white arrow mark indicates the samples. MBGH-3d sticks to the fibroblast cells more than the other samples (D 72 h) as seen after the PBS wash which removes most loosely bound material in the medium.

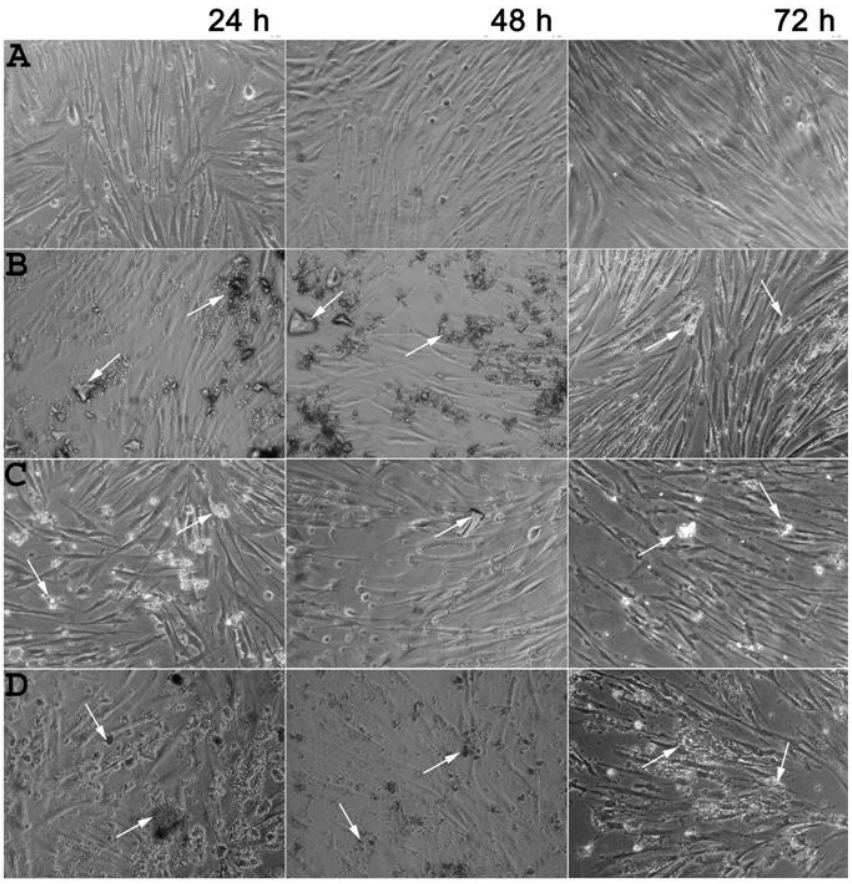

Figure 18: Phase contrast microscopy images of Human foreskin fibroblasts (HFF) cells cultured along with the A) Blank coverslip, 1.5 mg/mL of the samples B) MBG, C) as synthesized MBGH, D) MBGH – 3d.

4.6. Conclusion

In conclusion, we have synthesized hierarchically porous bioactive glass with improved bioactivity employing amorphous CSP as a macroporous template. CSP act as templates to form macropores. The CSP are also found to be instrumental in creating HCA nuclei. Thus when MBGH is soaked in SBF, a very high *in vitro* bioactivity is exhibited owing to its high surface area derived from the mesopores and HCA nuclei derived from the CSP.

4.7. References

1. a) Rho, J., *Medical Engineering and Physics*, **1998**, *20*, 92. b) Peters, F.; Schwarz, K.; Epple, M, *Thermochimica Acta*, **2000**, *361*, 131.
2. Hench, L. L. *J. Am. Ceram. Soc.* **1998**, *81*,1705.
3. Hench, L. L.; Wilson, J. *Science*, **1984**, *226*, 630.
4. Jones, J. R.; Hench, L. L. *Curr. Opi. Solid State & Mater. Sci*. **2003**, *7*, 301.
5. Williams. D. F., The Williams Dictionary of Biomaterials, Liverpool University Press, Liverpool, (**1999**).
6. Xynos, I. D.; Edgar, A. J.; Buttery, L. D. K.; Hench, L. L.; Polak, J. M. *J. Biomed. Mater.* Res. **2001**, *55*,151.
7. Hench, L. L.; Splinter, R. J.; Allen, W. C.; Greenlee, T. K., Jr. *J. Biomed. Mater. Res.* **1971**, *2*, 117.
8. Li, P.; Nakanishi, K.; Kokubo, T.; Klaas de Groot, *Biomaterials,* **1993**, *14*, 963.
9. Andersson, J.; Johannessen, E.; Areva, S.; Baccile, N.; Azaïs, T.; Lindén, M. *J.Mater. Chem,* **2007**, *17*, 463.
10. Yan, X.; Yu, C.; Zhou, X.; Tang, J.; Zhao, D. *Angew. Chem. Int. Ed.* **2004**, *43*, 5980.
11. Knowles, J. C.; Bonfield, W. *J. Biomed. Mater. Res.* **1993**, *27*, 1591.

12. Aryal, S.; Bhattarai, S. R.; Bahadhur, K. C. R.; Khil, M. S.; Lee, D. R.; Kim, H. Y. *Mater. Sci. Eng. A.* **2006**, *426,* 202.

13. Elliott, J. C.; Mackie, P. E.; Young, R. A. *Science* **1973**, *180*, 1055.

14. Oyane, A.; Kim, H. M.; Furuya, T.; Kokubo, T.; Miyazaki, T.; Nakamura, T. *J. Biomed. Mater. Res.* **2003**, *65A,* 188.

15. Sun, X.; Liu, J.; Li, Y. *Chem. Eur. J.* **2006**, *12*, 2039.

16. Dinesh, J.; Eswaramoorthy, M.; Rao, C. N. R.; *J. Phys. Chem. C.* **2007**, *111,* 510.

17. Yan, H.; Zhang, K.; Blanford, C. F.; Francis, L. F.; Stein, A. *Chem. Mater*. **2001**, *13*, 1374.

Summary

This Chapter deals with the studies that demonstrate the glucose-derived carbon spheres (CSP),[1] as an emerging class of intracellular carriers. Properties like amphiphilicity and mild intrinsic fluorescence have made this material a suitable choice for the applications of intra cellular transport. CSP are found to target the nucleus of the mammalian cells without causing any toxicity. Detailed characterization based on zeta potential experiments, time dependent, temperature dependent studies of cellular uptake of CSP suggest that besides the surface charge reversal, the cellular uptake is an active energy dependent process. Further, CSP were used to ferry the membrane impermeable, CTPB (N-(4-chloro-3-trifluoromethylphenyl)-2-ethoxybenzamide), the only known small molecule activator of histone acetyltransferase (HAT) p300. The delivered molecules lead to transcriptional activation thereby establishing an alternative path for activating gene expression mediated by HAT activation instead of HDAC inhibition.

A paper based on this work has been published in *Nano Letters*, **2008**, 8, 10, 3182.

5.1. Introduction:

Delivery of drugs can be considered as important and expensive as the drug discovery itself. One of the principal pharmacokinetic properties of drugs - *bioavailability,* is used to describe the fraction of an administered dose of drug that reaches the systemic circulation (with the ultimate target being some part in the body). When a drug is administered, its bioavailability decreases due to incomplete absorption and first-pass metabolism. Delivery of drugs or essential biomolecules (peptides, proteins, DNA etc) directly into the cell is a promising approach in the field of medicine to increase their bioavailability while its eventual impact on the economy can be many fold.[1a,b]

However, there are many challenges present in achieving an efficient delivery. The first being the administered drug though water soluble must cross the hydrophobic cell membrane. The second important factor is the stability of the drug in hostile physiological conditions (presence of enzymes etc) of the cell. Therefore, a vehicle or a vector that can safely transport the molecular cargo inside the cell would be an ideal way to transport them to the desired target inside the cell. The ability of a virus[1c] (e.g T4 bacteriophage) to enter the bacterial cell and transfer its genetic material into the bacterial nucleus during the infection stands as nature's testimony to the vector based delivery approach. However one cannot rely on the viral vectors for the drug delivery due to their lack of specificity and unintentional germline gene transfer after the therapy. Consequently use of viruses will imposes serious safety and ethical concerns.[2] Therefore, the non viral vectors that are less risky, easily amenable to mass production and with high delivery efficiency will be most desired. Different types of delivery vectors are classified below in Figure 1.[3] There is a lot of scope for inorganic nanoparticles to emerge as an ideal delivery vector if their efficiency is improved.[3]

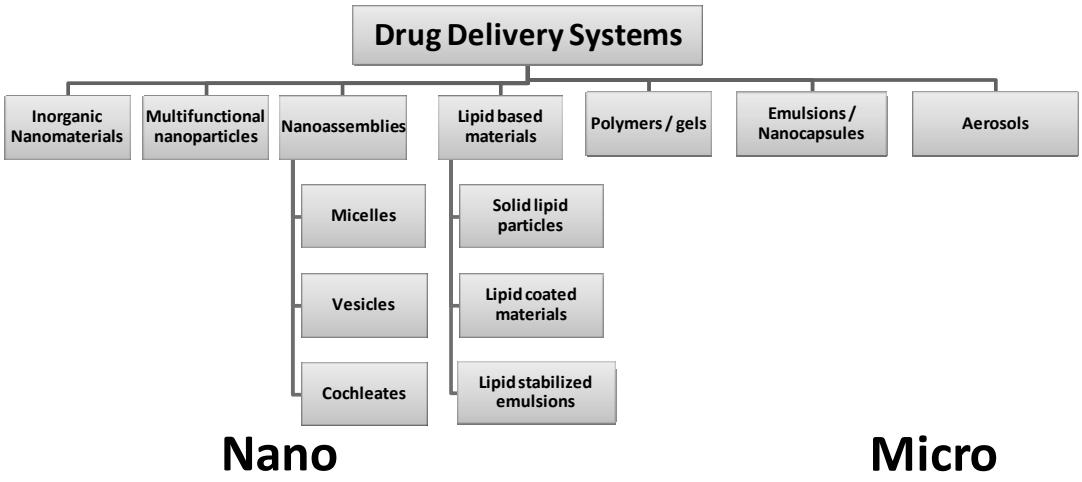

Figure 1: Classification of drug delivery systems. Polymer/gels include materials in both nano and micro regime.

5.2. Scope of present investigation:

Nanoparticles such as silica,[4] LDH clay,[5] micelles,[6] polymer nanoparticles[7] and carbon nanotubes (CNTs)[8,9] are actively being explored for the intracellular drug delivery purpose. The interaction of nanoparticles with the cell and their subsequent internalization occurs at various steps. The first being adhesion of the nanoparticles on the cell membrane. For example, magnetic nanoparticles modified with dextran show a strong adhesion to the membrane of human fibroblasts, which retains the nanoparticles just outside the cell.[10] The second step involves the internalization of the nanoparticle. The functional groups on the surface of the nanoparticles play the deciding role in the entry of nanoparicles into the cell, besides their biocompatibility and biodegradability are no trivial issues. However, functionalization of the surfaces of materials like CNTs involve elaborate synthetic procedures followed by surface functionalization by strong acids or 1,3-dipolar cylcoaddition of azomethine ylides.[11] The major draw back with all of the existing nanomaterials is the need for an external fluorescent agent to track their path inside the cells which is usually achieved by tagging them with quantum dots or with fluorescent organic dyes. The use of quantum dots like CdSe further poses severe toxicity problems in case of

leaching of heavy metals into the cells. On the other hand, poor photostability of organic dyes limits their use over extended periods of study. Most often, the chemical modifications adopted to carry the drug molecules and fluorescent tags[11,12] inevitably affect their surface properties, cellular uptake and metabolism. Another important aspect that may prevent their use is their inability to cross the nuclear membrane where most important activities of the cells occur. Despite their use in transporting nucleic acids, proteins, and drug molecules across the cell membrane, the inefficiency to breach the nuclear membrane limits their use in many applications. On the other hand, nuclear targeting carriers like peptides and polyethyleneimines face intense serum inhibition due to their highly positive charged surfaces.[13]

The motivation for this works stems from our prior knowledge that the surface of the CSP is rich in functional groups and may not need any further functionalization. The freedom available to exploit the surface functional groups to covalently link any drug increases the probability of making CSP as a new class of non-viral vector for intra cellular delivery of molecular cargos. Besides, the intrinsic fluorescence of the CSP will avoid any additional steps to tag fluorescent molecules. Above all, preparation of CSP is inexpensive as the precursor involves only glucose. The present work has focussed to emphasis on three important issues.

a) *Cell entry:* Cell membranes are made up of lipid bilayers. These self assembled layers separate the cell interior from its external surroundings both of which are aqueous. Therefore, a particle that has both the nature of hydrophilicity and hydrophobicity must be needed to achieve a successful entry into the cells. The CSP being amphiphilic (described in chapter 1) must be an ideal candidate for cellular entry.

b) *Mechanism of entry:* The mechanistic studies related to the entry of CSP into the cells must be established in order to aid any future efforts to maximise the uptake of CSP inside the cells.

c) *Delivery:* Use the CSP to carry a membrane impermeable but therapeutically important molecule (CTPB) and show its effect inside the cell.

5.3. Experimental section:

a. Synthesis of CSP:

5 g of D (+) glucose was dissolved in 50 mL of deionised water to form a clear solution. It was placed in a 60 mL teflon lined sealed stainless steel autoclave and maintained at 180 ^{o}C for 18 h. The puce products were isolated by centrifuging at 10000 rpm for 10 min. They were later purified by repeated washings using water and ethanol before being dried in the oven at 80 ^{o}C for 4 h. The final product is a brownish powder which had spheres with an average size of 400 nm. The CSP of 40 – 100 nm size can also be synthesized by reducing the reaction duration from 18 h to 6 h.

b. Zeta potential measurements:

A suspension of 1 mg of CSP in 10 mL of water (milliQ) was made by sonicating it for 5 min. The measurements were carried out using a NanoZS (Malvern UK) employing a 532 nm laser at a back scattering angle of 173^{o}. Cuvettes fitted with gold electrodes were used.

c. Confocal microscopy imaging:

Confocal microscopy imaging was taken at room temperature using a Zeiss LSM 510 META laser scanning confocal microscope. The microscope objective of 40X (NA 0.75) and 100X (NA 1.3) were employed. To excite CSP, a 514 nm line (Argon laser) with a band pass filter of 525-670 nm was used. For samples involving cellular system, a two photon excitation of

NIR 790 nm (diode laser) was used. Emission spectrum was recorded using a META PMT detector array.

d. Adsorption of CTPB on CSP:

1 mL of 30 μM solution of CTPB (M.wt 501) in HPLC grade methanol was prepared. 10 μg of CSP was added to the solution and sonicated for 15 min. The solution was later incubated at 37 ^{o}C for 12 h. CSP were separated by centrifuging at 10000 rpm for 10 min. Amount of CTPB adsorbed on the CSP was calculated by measuring the absorbance of the supernatant methanol solution of CTPB at 258 nm using a UV-vis spectrometer (Perkin-Elmer lambda 90) at 25 ^{o}C. A prior calibration plot was obtained by measuring the absorbance of CTPB solution at various known concentrations. 4.15×10^{-9} moles of CTPB was adsorbed on 10 μg of CSP. Carbon spheres adsorbed with CTPB are referred as CTPB-CSP.

e. Preparation of the DMEM medium:

DMEM stands for Dulbecco's modified eagle's medium. It is a liquid containing all the essential growth supplements for the cells along with antibiotics. The medium is prepared from DMEM supplemented with 10 % foetal bovine serum (10X FBS) and 1 % penicillin-streptamycin-amphotericin.

f. Cell revival:

HeLa Cells were usually stored in frozen conditions at liquid N_2 temperature in (50% serum, 40 % DMEM and 10% DMSO). The revival of the cells was done by rapid thawing to 37 ^{o}C by placing them in the incubator. Care should be taken not to disturb the cells by any mechanical agitation. The cell suspension was then centrifuged at 700 rpm for 4 min. The cells that settle at the bottom are redispersed in a tissue flask containing FBS and DMEM (25 mL) and incubated at 37 ^{o}C for nearly 6-8 h after which the media was changed.

g. Maintenance of cell culture:

Following the revival of the cells, they were cultured in tissue culture flasks (25 mL or 75 mL) in DMEM with 10 vol % FBS. HeLa cells usually took 24 h to reach 60% confluence (monolayer covering the floor of the culture flask). Fresh medium was replaced for every 24 h during which the cell debris (if formed) are removed by centrifuge followed by washing using DMEM. Usually HeLa cells reached 80-90% confluence in 36-48 h after which the shape of the cells became spherical due to stress. This stage was suitable for *splitting* the cells into different flasks so as to provide the cells more surface for growth. *Cell splitting* was done carefully by first discarding the DMEM followed by a washing using fresh medium (3-4 mL) to completely remove the FBS already present. The first step in cell splitting involved trypsinization - a process by which cells adhered to the flask are removed to form cell suspension. Trypsin is known to degrade some of the membrane proteins of the cells used for adherence to the flask. Cells are well exposed to the trypsin (0.5 mL of 10X trypsin) by gently rotating the flask. Excessive contact to the trypsin can damage the cells. Keeping the cells in trypsin at 37 ^{o}C for 2 min gave good results. This was followed by the addition of 0.5 mL of FBS to neutralize the action of trypsin. The loosely adhered cells were gently removed using a pipette and the process must be continued till all the cells were transferred completely to form a suspension in 8 mL of DMEM medium. The cell suspension was centrifuged at 700 rpm for 4 min during which the cells settled at the bottom leaving the cell debris in the supernatant. The pelletized cells were washed by recessing them with fresh 8 mL of DMEM. The process of washing was carried out once or twice depending on the amount of debris present. Finally the cells were extracted by recessing them in FBS and transferred to tissue culture flasks containing growth medium (75 mL flasks will contain 13.5 mL of DMEM medium and 25 mL flasks will contain 4.5 mL of the medium.

Accordingly, 1.5 mL of serum is added to the former and 0.5 mL is added to the latter). The cell suspension in serum is added according to the flask volume. The tissue flasks are safely kept at 37 ^{o}C incubator in 5% CO_2 environment.

h. Preparation of the cover slips:

The cover slips were first washed using a solution of 70% ethanol, 10% HCl solution followed by a thorough rinsing in 90% ethanol. Followed by this, they were treated with 0.25 M of aqueous ammonium acetate solution for 30 min and dried at 60 ^{o}C for 1 h. The cover slips were then exposed to polylysine solution (50 μg/mL in 10 mM Tris HCl) for 30 min followed by air drying. Both the sides of each cover slip were subjected to this treatment procedure by individually turning those using forceps. Polylysine imparts positive charge to the cover slips which will facilitate the cell adhesion.

i. Seeding the cells for experiments:

The *in vitro* experiments were performed with the CSP suspension of known concentration in water. But prior to the addition of CSP, the cells were cultured in 30 mm or 60 mm diameter culture dishes with polylysine coated cover slips placed in it. After 6 h, the culture medium attained more than 80 % confluence and was ready for the experiments. The cells at this stage were found to be adhered to the cover slips. A media change is given at this stage along with the addition of CSP and other required reagents. Usually FBS was added 1 h after the addition of the CSP unless otherwise mentioned as in section 5.3 k.

j. Preparation of the samples for confocal microscopy studies:

This process was carried out after the completion of the experiment. Cover slips were carefully taken out using forceps and placed in plastic wells. The cover slips were thoroughly washed with 1X Phosphate buffer solution (PBS) (3×1mL) and a 0.2 mL of 4%

paraformaldehyde for 20 min at 25 ^{o}C. Treating cells with paraformaldehyde cross-links free amino groups of the proteins maintaining the overall architecture of the cell. After a wash using 1X PBS (3×1mL), 0.2 mL of 0.1% TritonX100 for 5 min at 25 ^{o}C which permeabilizes cell membranes, and allows reagents to access to both the cytosol and nuclear material. After a cycle of washing with PBS, the cells were treated with 1.2 mL of 0.02 % of Hoechst stain (bis-benzimide dye) in dark at 25 ^{o}C for 20 min. The bis-benzimide dye being lipophilic penetrates the cell membrane and readily intercalates with the DNA in the nucleus. The dye absorbs in UV region and emits in blue. This is followed by another cycle of washing in PBS before mounting on glass slides using 70% glycerol. The cells were treated with the above mentioned concentration for 24 h before processing for confocal microscopy.

k. Effect of serum on the uptake of CSP:

Cells were cultured with CSP (50 μg) in DMEM medium. However FBS was added at different time points (no addition, addition after 6 h and present all throughout).

l. Temperature dependent uptake of CSP:

Three temperatures of incubation (4, 25 and 37 ^{o}C) were chosen to study the dependence of temperature on the CSP uptake by the cells. In all the cases 50 μg of CSP was incubated for 12 h. However, to maintain the uniformity the reaction was performed in the absence of CO_2 atmosphere. A control experiment was also done in each case to study the effect of CO_2 absence on the viability of the cells.

m. ATP dependent uptake of CSP:

HeLa cells were pre-incubated in 1X PBS supplemented with 10 mM of NaN_3 for 30 min at 37 ^{o}C. This was followed by changing the growth medium to DMEM with 10 % FBS and CSP

(50 μg). The incubation time was 12 h. Control experiments were performed under the same conditions without the addition of CSP.

n. Hypertonic solution studies:

Cells were pre-incubated in 1X PBS supplemented with 0.45 M aqueous sucrose solution at 37 ^{o}C. This was followed by changing the growth medium to DMEM with 10 % FBS and CSP (50 μg). The incubation time was 12 h. Control experiments were performed under the same conditions without the addition of CSP.

o. Cytotoxicity of CSP:

HeLa cells (5000 cells) were seeded in 96 well plate. The cells were treated with carbon nanospheres (CSP) and apoptosis inducing compound plumbagin, for the indicated time points. Following the period of treatment the Cell Titre Aqueous reagent (20 μL) was added (as per the manufacturer's instructions). After incubation with the reagent for 3h, the absorbance was recorded at 490 nm in an ELISA reader (VERSA Max microplate reader, Molecular Devices).

5.4. Results and discussion:

As described in the first chapter of this thesis and the experimental section, CSP were synthesized by the hydrothermal treatment of glucose. CSP used in these experiments were 300-500 nm in diameter. Based on the data available from our measurements and from the literature,[14] it was proposed that the CSP (300- 500 nm) were made up of dense hydrophobic core of polyaromatic units covered by layers of carbon chains functionalized with polymeric alcohols, carboxylic acids, with a negatively charged surface (zeta potential of -24 mV at pH 7.3) giving these spheres an amphiphilic property.

The amphiphicity of the CSP becomes very relevant with the results published by H. Dai et al[15] which demonstrates that a carrier must posses an optimal presence of hydrophilicity and

hydrophobicity for an efficient uptake by the cells. For CNTs modified with PEG, it was observed that a certain degree of both hydrophilicity (brought about by PEG) and hydrophobicity (due to CNTs) are essential in increasing the internalization.[15]

HeLa cells derived from cervical cancer cells were used in the studies. These cells proliferate abnormally rapidly, even compared to other cancer cells. HeLa cells have an active version of the enzyme telomerase during cell division, which prevents the incremental shortening of telomeres (a region of repetitive DNA at the end of chromosomes, to protect them from destruction) that is implicated in aging and eventual cell death.[17] In this way, HeLa cells circumvent the limited number of cell divisions that most normal cells can later undergo before dying out in cell culture.

The permeation of CSP inside the HeLa cell was monitored with time using the CLSM and the results are shown in Figure 2. Interestingly, with time the CSP cross not only the plasma membrane but also the nuclear membrane before being retained in the nucleoplasm. The time required for the CSP to reach the plasma membrane was about 30 min at 37 ºC and the time required to reach the perinuclear region was about 1 h. Entry of CSP inside the nucleus was observed within a period of 3 h. Eventually, the CSP got distributed throughout the nuclear region by the end of 24 h which was confirmed by the presence of uniformly spread fluorescence intensity of the CSP across the nucleus.

In Figure 3, a Z scan spatial-intensity profile of the fluorescence along the red trace is shown. One can observe a spatial localization of the blue emission from the nucleus of the cells (stained with Hoechst dye) and the CSP emission. This suggests that the CSP is predominantly found inside the nucleus of the cells. It is worth noting that the CSP is one of the few classes of intra cellular drug delivery vehicles with an ability to traverse through the nuclear membrane.

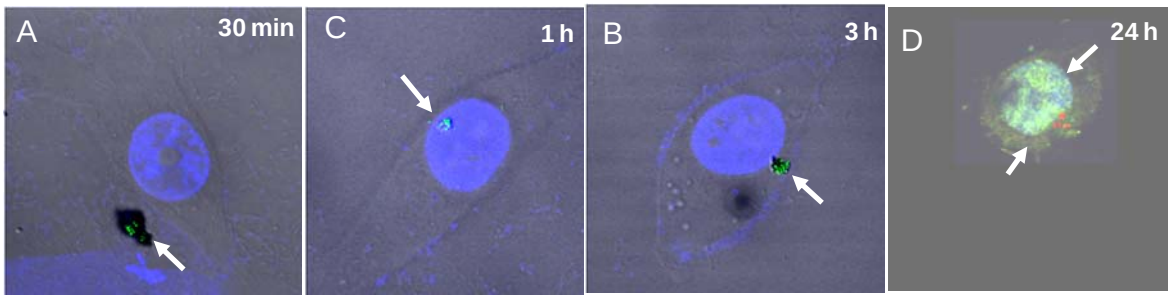

Figure 2: Time dependent study of entry of CSP in HeLa cells after 30 min, 1 h, 3 h and 24 h. White arrows point out the CSP.

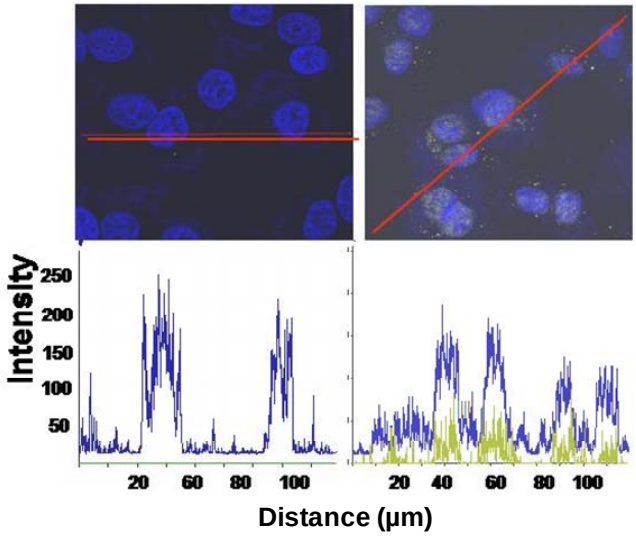

Figure 3: a) Confocal image of CSP inside the HeLa cells (Z scan). Blue fluorescence is from Hoechst stained nucleus of the HeLa cells. Pale green is due to fluorescence from CSP. b) Intensity profile of fluorescence from nucleus and CSP along the trace of red line. X axis is distance in μm.

In the next step the mechanism of uptake of CSP by the cells was studied. The uptake of the CSP by the cells consists of two steps: i) Attachment of the particle onto the membrane of the cell - This step is mainly determined by the surface property of the particles and the type of cells under the study. For example, in T cells the attachment of particles has been aided by the hydrophobicity while in case of many other cell lines, an electrostatic interaction has been responsible.[15] As the cell membrane is negatively charged, nanoparticles that acquire partly

neutral or positive charge near the membrane site can overcome the serum inhibition and expedite their entry.[18] However, there are no hard and fast rules to predict the type of interaction between the cell and the particles. Besides the confluence of cell culture, the distribution and aggregation of the particles in the culture medium can also affect the attachment of the particles on the surface of the cells. ii) The uptake of the particles by the cells or entry of the particles into the cellular compartment. This process could be a simple diffusion or osmosis which is a passive (or energy independent) way of uptake. The passive ways could also be aided by the transmembrane proteins. In case of many macromolecules, the process of uptake usually occurs via an energy dependent route called endocytosis. Endocytosis involves the formation of membrane bound vesicles which in turn can occur via a receptor mediated cell signalling process or receptor independent processes.

The following paragraphs describe the experimental results on cellular uptake of CSP. It is important to note that the surface charge of the nanoparticles also plays a pivotal role in negotiating with the cell membrane during the attachment of CSP. Since the pH of the cellular compartments varies, the surface charge of CSP at different pH was studied. The zeta potential of the CSP showed a charge reversal with increasing acidity. It varied from a value of -24 mV at pH 7.3 to -4 mV at pH 4 (Figure 4a). However, the surface potential at pH 4 has a good overlap in the positive region (Figure 4b). When the zeta potential was measured in the cell medium containing serum and other inorganic salts at pH 7.3, a rapid adsorption of inorganic cations (Na^+) occurred on the negatively charged CSP decreasing its potential to -17 mV within 30 min (Figure 4c). Thus both the factors modulate the surface charge of the CSP thereby favouring their entry into the cells.

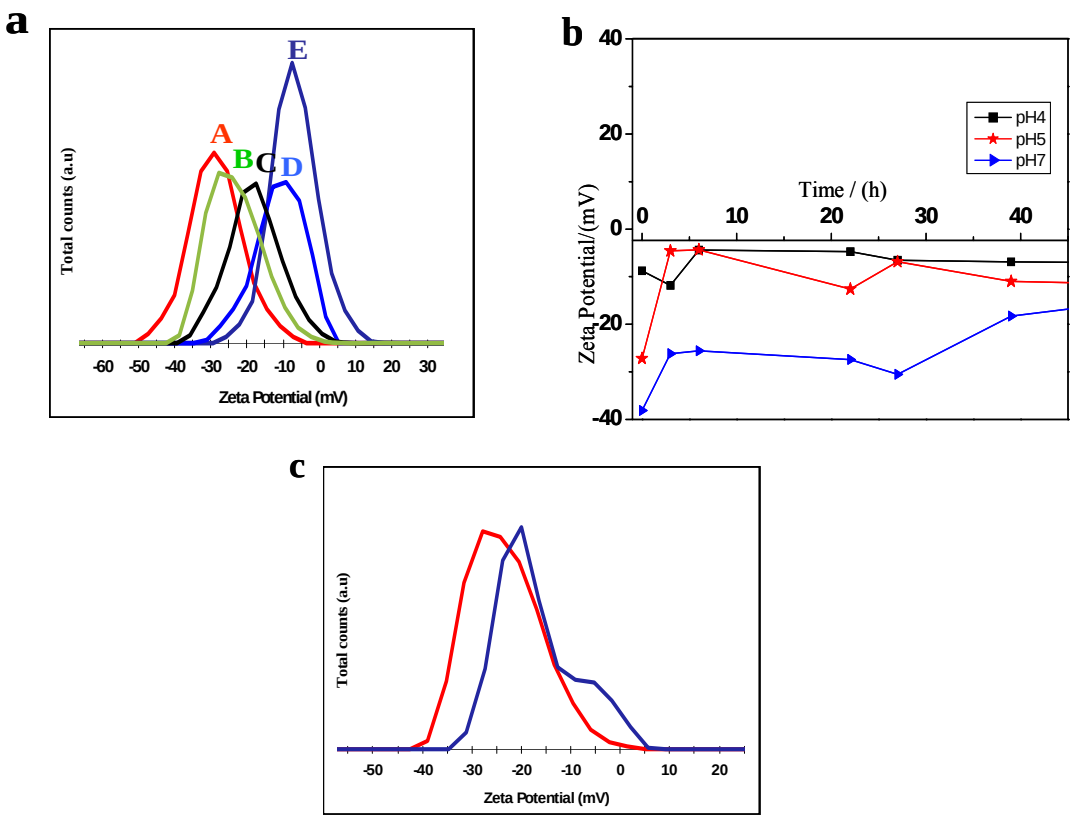

Figure 4: Zeta potential of CSP dispersed in water at different pH values A) 8, B) 7.3, C) 6, D) 5, E) 4. The zeta potential was measured after an equilibration time of 2 h. (b**)** Zeta potential of the CSP at different pH was observed over a period of 56 h. (c**)** Zeta potential of CSP in water at pH 7.3 (red), CSP soaked in the DMEM with 10% FBS at pH 7.3 (blue).

In Figure 10c, it is shown that the surface potential of the CSP becomes more positive when soaked in FBS suggesting that CSP adsorbs specifically the positively charged components on the its surface. This could have two impacts on the uptake of the cells. Firstly, the positive charge that has been imparted on the surface of the CSP can increase its cellular uptake by favouring the electrostatic mediated attachment of the particles on the cell membrane. On the other hand, as there is also a constant decrease in the surface potential of the CSP with the adsorption of FBS, CSP enters into an aggregation domain (colloids are stable only beyond ± 30 mV) which could affect its cellular uptake. The effect of FBS on the uptake of CSP by the cells

was therefore studied. It is seen from the Figure 5 that there is an increase in the cellular uptake with increase in contact with FBS. Thus one can come to the conclusion that the attachment of CSP on to the cell membrane may involve electrostatic interaction between the CSP and the membrane.

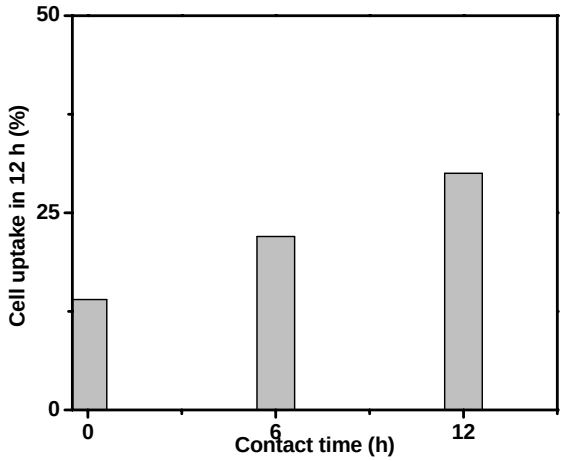

Figure 5: Effect of FBS on the uptake of CSP by HeLa cells. FBS was added to the DMEM at different time intervals. Experiment was performed by incubating 50 µg of CSP to HeLa cells at 37 ^{o}C for 12 h in 10 % CO_2 environment. Contact time 0 h (no FBS was added throughout the experiment). Contact time 6 h (FBS was added 6h after the addition of CSP to the cells). Contact time 12 h (FBS was added right in the beginning of the experiment).

To verify the energy dependence of the uptake of the CSP by HeLa cells, we incubated CSP with HeLa cells at different temperature like 37, 25 and 4 ^{o}C. While 37 ^{o}C is the normal incubation temperature of the cells which is essential for all the energy dependent metabolic processes, reduction in the incubation temperature will bring most metabolic processes to a halt. The results are shown Figure 6. It is seen clearly that the uptake of CSP is maximum at the normal incubation of 37 ^{o}C, while it is reduced with the reduction in the temperature suggesting that the uptake is an energy dependent process or endocytosis.

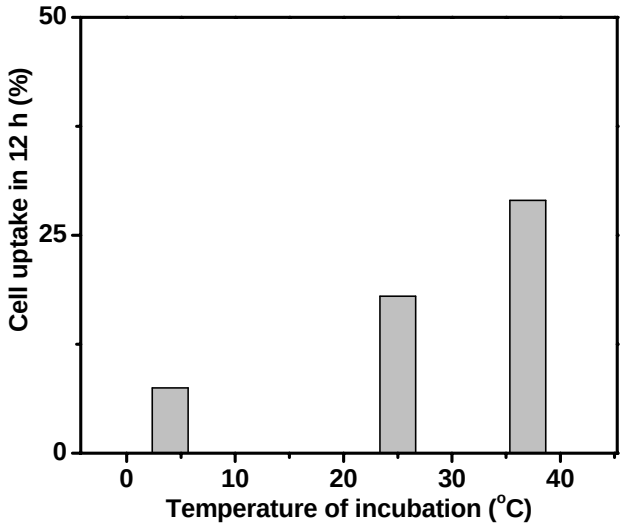

Figure 6: Cellular uptake of CSP by HeLa cells at different incubation temperatures 4, 25 and 37 ^{o}C.

The hydrolysis of adenosine triphosphate (ATP) to diphosphate is an important energy yielding step that occurs in parallel with all the metabolic activities demanding energy. By depleting the cells from ATP, all the energy dependent processes of the cells can be affected. This was done by pre-treating the cells with NaN_3, the molecule known to hinder the ATP dependent processes in the cells. In the Figure 7, it is seen that no CSP is seen inside the cells that have been depleted from ATP using NaN_3. In addition, one can also observe that no CSP is also seen attached to the cell membrane of the cells. For sure, one can conclude that the cellular uptake of CSP is an ATP dependent endocytosis processes. However, the data also suggests that the attachment of CSP onto the membrane may also be an energy dependent process.

The next step was to identify whether the process of CSP uptake by the cells is a receptor mediated process or is an uptake - independent of any receptors. The receptor mediated processes usually involves the clathrin coated vesicle formation. Clathrin, a soluble protein found in the cytoplasm of the cells undergo polymerisation to form lattices.

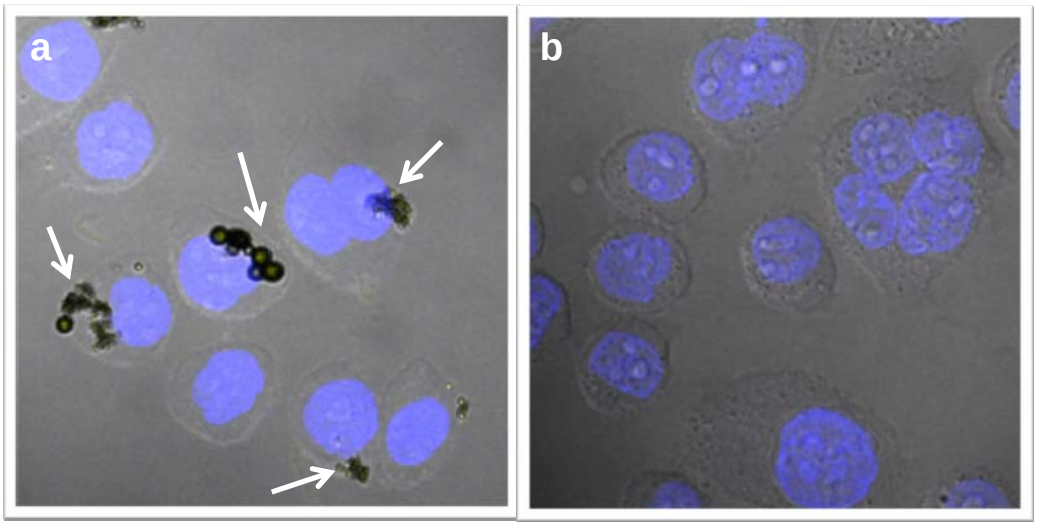

Figure 7: ATP dependent uptake of CSP by HeLa cells. a) ATP present and b) ATP absent. 50 µg of CSP was incubated for 12 h at 37 ^{o}C. ATP was depleted by pre-treating the cells with NaN_3 (see experimental section). White arrows point out CSP.

However, this process of polymerisation of is initiated by a cell signalling mechanism which in turn is triggered by the attachment of the particle onto the receptors present on the cell membrane. Thus receptors induce the formation of vesicles coated by clathrin. The subsequent pinching off of the clathrin coated vesicles and their transportation to a target organelle are accelerated by clathrin. By treating the cells with a hypertonic solution of sucrose, the exosmosis of the cells increase the acidity inside the cells. The increased acidity can also initiate a random and non-specific polymerisation of clathrin throughout the membrane ultimately leading to the depletion of the clathrin. Such a hypertonic pre-treatment will totally avoid any further formation of clathrin coated vesicles even if the cell signalling process may occur. In the Figure 8 below, we show the experimental results of the CSP uptake by HeLa cells which are pre-treated with hypertonic sucrose solution. The results show no CSP uptake suggesting the process is most likely to be a receptor mediated process.

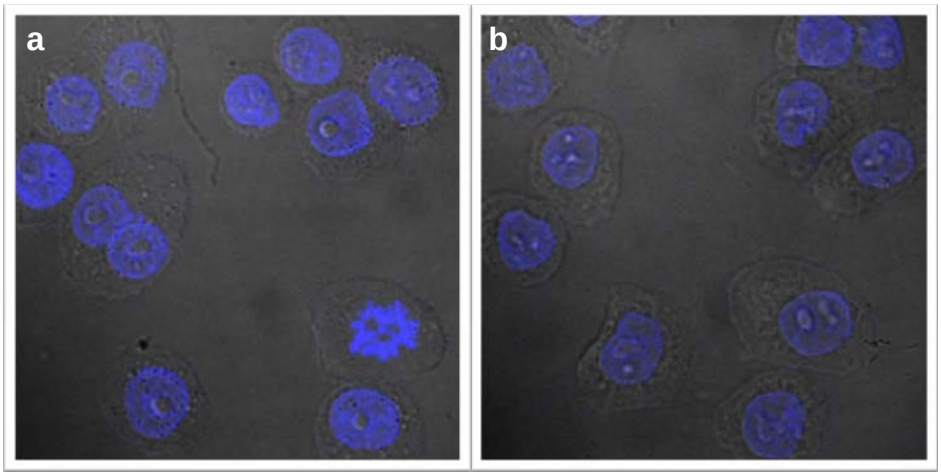

Figure 8: Clathrin dependent endocytosis. Clathrin formation was prevented by pre-treating the cells with 0.45 M sucrose. a) control – no CSP added. b) CSP added.

Any possible cytotoxicity due to the nanomaterials must be tested. One parameter used as the basis for colorimetric assays is the metabolic activity of viable cells. For example, a microtiter plate assay which uses the tetrazolium salt (3-(4,5-Dimethyl-2-thiazolyl)-2,5-diphenyl-2H-tetrazolium bromide) (MTT) is now widely used to quantify cell proliferation and cytotoxicity. Because tetrazolium salts are reduced to a colored formazan only by metabolically active cells, these assays detect viable cells exclusively. For instance, in the MTT assay, MTT is reduced by viable cells to a colored, water-insoluble formazan salt. After it is solubilized, the formazan formed can easily and rapidly be quantified in a conventional ELISA plate reader at 570 nm (maximum absorbance).

However, an inherent problem associated with the standard MTT (3-(4,5-Dimethyl-2-thiazolyl)-2,5-diphenyl-2H-tetrazolium bromide) assay is that some carbon based nanomaterials have been shown to strongly bind to the crystals of insoluble formazan. So, an incomplete extraction of the formazan would imply a toxicity of the material which may not be the actual case. In order to have a more reliable assay, it is suggested to use the water soluble form of

tetrazolium salt which can be converted by the viable cells to water soluble formazan. [19] This protocol avoids the experimental limitations due to incomplete extractions. MTS ([3-(4,5-dimethylthiazol-2-yl)-5-(3-carboxymethoxyphenul)-2-(4-sulfophenyl)-2-H-tetrazolium),(see Figure 9) a sulfonic acid derivative of MTT can be used for this purpose.

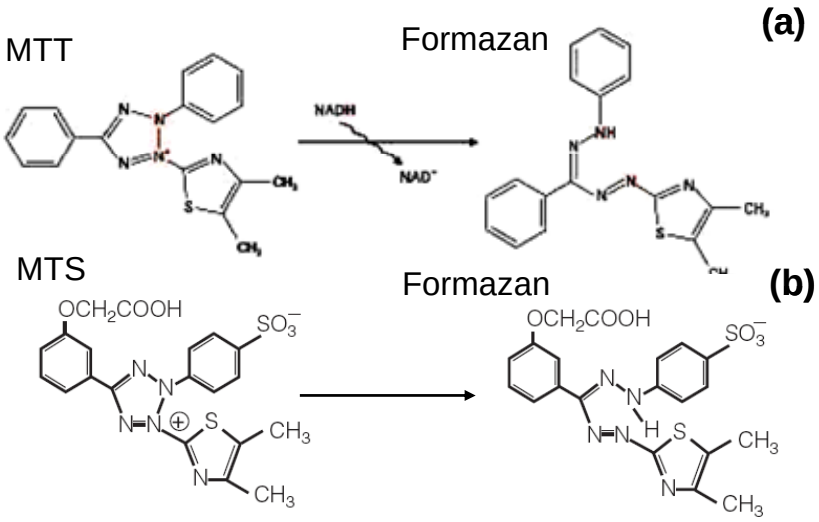

Figure 9: a) Schematic showing the reduction of MTT to formazan and b) MTS to formazan.

The viable cells are capable of reducing the MTS salt to a water soluble formazan by the action of mitochondrial reductases. Thus, the reduction of MTS to formazan gives a yellow product which is estimated as a measure of cell viability. The presence of CSP within the nucleus did not cause any cytotoxicity even after 24 h of treatment as evident from the absorbance values which were constant throughout the experiment (Figure 10). A known apoptosis inducing compound, plumbagin, was used as a positive control. The assay was carried out with the concentration of CSP as high as 200 μg/mL while the working concentration used for the other cellular experiments was only 10 μg/mL. The cell viability was monitored for 24 h which is the time taken for the cellular hyperacetylation experiments and it was observed that the nanospheres are nontoxic to the cells. MTT reduction to the purple formazan recorded at 550 nm is an indication

of cell viability. As compared to the control untreated cells (lane a), there was not much significant loss of cell viability on CSP treatment (lane b- 10 µg/ml; lane c- 20 µg/ml; lane d- 50 µg/ml; lane e- 100 µg/ml; lane f- 200 µg/ml) indicating that these are nontoxic. However, the known apoptosis inducing plumbagin was able to induce cytotoxicity at the same experimental conditions. A careful analysis of the MTT assay suggests that the ability of the cells to reduce MTT (a mark of its viability) gets marginally decreased in nanosphere treated cells. Any additional component added externally during the process of cell culturing can interfere with the cellular viability to a minimal extent[b]. Therefore the initial decrease in percentage reduction of MTT should not be attributed to the toxicity of the introduced nanomaterial. The observation of toxicity is validated only if there is dose dependent decrease in the reduction of MTT as observed in the case of plumbagin, a known toxin.

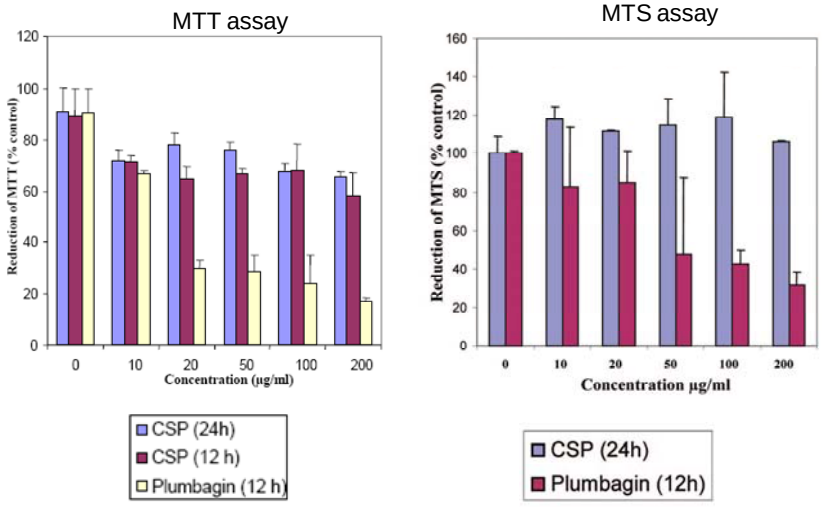

Figure 10: MTT and MTS assay performed to check the cytotoxicity of CSP on HeLa cells. Plumbagin is a known apoptosis causing agent.

Within the cell nucleus, exists a highly compact and dynamic nucleoprotein structure, chromatin, composed of DNA, RNA and different proteins (histones and nonhistones). Reversible acetylation of histone proteins in the chromatin, by histone acetyltransferases (HATs) and histone deacetylases (HDACs) enzymes play a pivotal role in the dynamicity of chromatin

thus regulating transcription, replication and repair.[21] During normal conditions, the enzymatic activity of HATs and HDACs regulate chromatin and transcription factor acetylation in a controlled fashion whereas their imbalance leads to diseases such as cancer, diabetes and asthma.[22] The well-known new generation drug candidates are the HDAC inhibitors[23] (HDACi), that indirectly induce hyperacetylation which is predominantly nonspecific in nature. Direct activation of a specific HAT is therefore a promising alternative.[24] However, the only known small molecule HAT activator which could be useful in this context is CTPB (Figure 11), but its impermeability to the human cells limits its use for molecular probing and therapeutic purposes.[20a] Thus, a carrier capable of localizing CTPB directly into the nucleus could circumvent the limitations of HDACi leading to a high therapeutic efficacy.

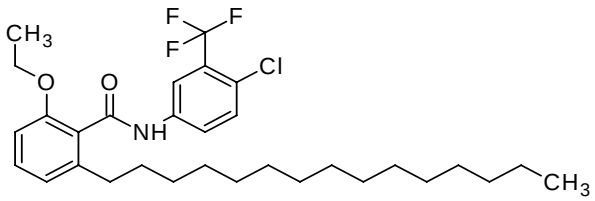

Figure 11: The molecular structure of CTPB.[20]

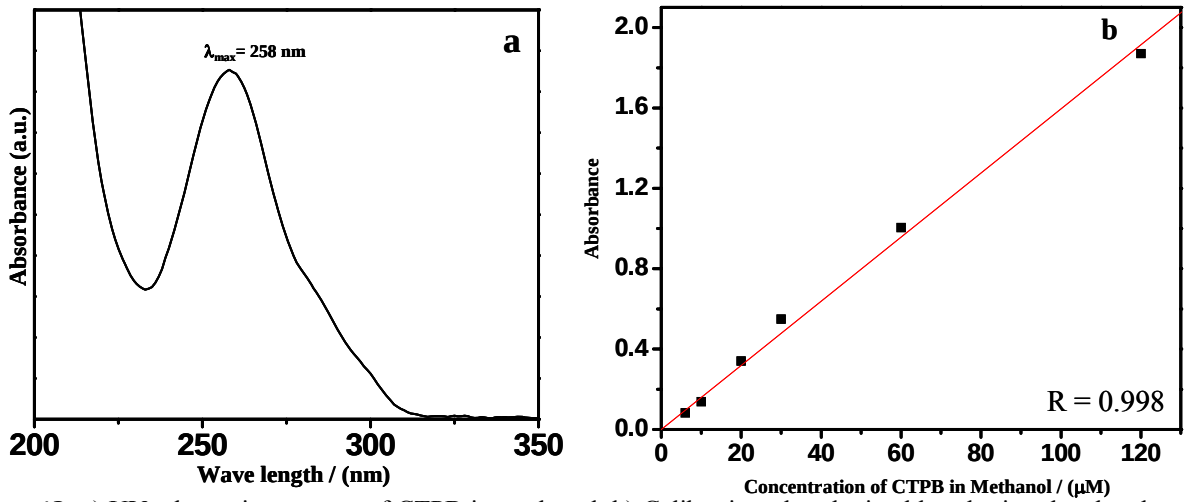

Figure 12: a) UV absorption spectra of CTPB in methanol. b) Calibration plot obtained by plotting the absorbance at 258 nm against the concentration of CTPB in methanol.

The nuclear targeted entry of CSP was effectively used to carry the CTPB inside the mammalian cell nuclei. When the CTPB adsorbed CSP enter the nucleus, it comes in close contact with the nucleus. The amount of CTPB adsorbed on the surface of CSP was quantified using the absorbance value at 258 nm where CTPB was known to absorb (Figure 12 a and b). An approximate calculation was done to estimate the number of molecules adsorbed on the surface of CSP. After keeping a known weight of CSP in a standard methanol solution of CTPB for more than 12 h (see experimental section), they were centrifuged and the supernatant was measured for absorbance value at 258 nm. The absorbance value in the calibration plot suggested nearly 10^{-9} moles of CTPB were adsorbed on 10 μg of CSP. Considering the density of CSP as 160 mg/mL (measured experimentally) and their diameter around 400 nm, one can calculate that nearly 10^5 molecules would occupy the surface of each CSP. EDX mapping of the CSP adsorbed with CTPB (Figure 13) showed a uniform distribution of the fluorine signal (red region, Panel IV) suggesting an efficient adsorption of CTPB on the surface. Considering the surface area of one CSP to be 5×10^5 nm^2, and the surface area of one molecule of CTPB to be 0.09 nm^2, a sphere can maximum hold upto 10^7 molecules which accounts for a surface coverage of less than 5%. Less than 5% coverage of CTPB on CSP surface also ensures that the presence of CTPB does not alter the surface properties of CSP by far. As expected, the uptake of CSP and the CTPB adsorbed CSP (CTPB-CSP) by the mammalian cells as monitored by fluorescence analysis did not show any significant difference. The activity of CTPB inside the cell is the hyperacetylation of histones of the chromatin. This is monitored by the fluorescence from the acetylated H3 antibody. Figure 14 I - shows that the fluorescence of H3 antibody is minimal indicating that CSP does not by itself induce any hyperacetylation. Since CTPB, as such is impermeable to the cell membrane, it does not show any significant increase in the

hyperacetylation (Figure 14 II). On the other hand, addition of CTPB - CSP showed remarkable increase of 3-4 fold in the localized fluorescence intensity of the acetylated H3 antibody (Figure 14 III).

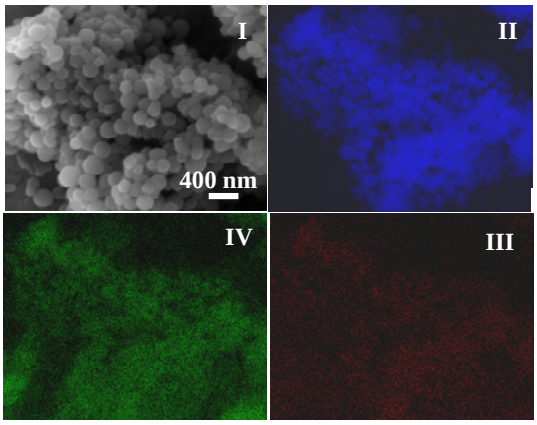

Figure 13: SEM image of the CSP, adsorbed with CTPB (Panel I). A specific area of the sample was excited with the electron beam of energy suitable for the constituent elements to emit the X-rays of their characteristic wavelength. The appearance of the K line of fluorine; red – (Panel III) was observed specifically from the sample alone confirming the adsorption of CTPB. The blue (Panel II) and the green (Panel IV) signals from the same region are due to K lines of oxygen and carbon respectively.

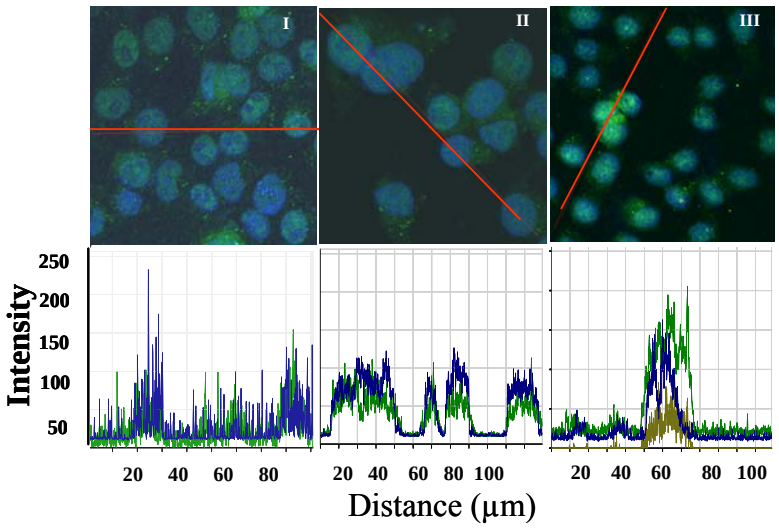

Figure 14: Fluorescence Image showing the activity of CTPB-CSP, I) untreated CSP, probed with antibody against acetylated histone H3. II) treated with HAT activator CTPB (300 μM), probed with antibody against acetylated

histone H3. III) treated with CTPB-CSP, probed with antibody against acetylated histone H3. Blue colour represent the nucleus of the cell. Dark green represent the antibody. Pale brown represent CSP.

5.5. Conclusions:

In conclusion, the CSP described here are unique intracellular molecular transporters owing to their intrinsic fluorescence, amphiphilicity, non-toxicity and nuclear targeting ability. The affinity of CSP for positively charged molecules like polycations (PDADMAC) and negatively charged molecules widen the scope of their use in peptides and gene delivery. Its immense potential in nuclear-targeted entry has been harnessed by trafficking the cell impermeable HAT activator molecule CTPB into the nucleus to induce hyperacetylation *in vitro.* This gives a positive impetus to the field of therapeutics involving direct HAT activation. The in vivo experiments performed in mice showed that the CSP localized in liver, spleen and brain.[20c] A continuous removal of CSP from these tissues was also observed over a period of 9 days. The entry of CSP into the brain suggests that CSP is capable of crossing the blood brain barrier.

5.6. References:

1. a) Dietz, G. P. H.; Bahr, M. *Mol. and cell. Nanosci.* **2004**, *27*, 85. b) Dinesh J.; Eswaramoorthy, M. *Nanomaterials for therapeutic drug delivery*, CRC handbook on nanobiomaterials, Taylor and Francis Publishers, 2009. c) Chibani-Chennoufi, S.; C. Canchaya, A. Bruttin, and H. Brussow. 2004. Comparative genomics of the T4-Like Escherichia coli phage JS98: implications for the evolution of T4 phages. J. Bacteriol. 186:8276-8286.

2. Marshal, E. *Science* **2001**, *294*, 1640.

3. Xu, Z. P.; Zeng, Q. H.; Lu, G. Q.; Yu, A. B. Chemical Engineering *Science*, **2006**, *61*, 1027.

4. Barbé, C.; et al. *Adv. Mater.* **2004,** *16,* 1959.

5. Choy, J. H.; Kwak, S.Y.; Jeong, Y. J.; Park, J.S. *Angew. Chem.Int. Ed.* **2000,** *39,* 4042.

6. Nasongkla, N.; et al. *Nano. Lett.* **2006**, *6,* 2427.

7. Zhu, H.; McShane, J. M. *J. Am. Chem. Soc.* **2005**, *127,* 13448.

8. Kam, N. W. S.; Jessop, T.C.; Wender, P.A.; Dai, H. *J. Am.Chem. Soc*, **2004**, *126,* 6850.

9. Liu, Z.; et al. *Nat. Nanotech*. **2007, *2***, 47.

10.Berry, C. C., Curtis, A. S. G., *J. Phys. D. Appl. Phys.* **2003**, *36*, R198-R206.

11.a) C. N. R. Rao, A. Govindaraj, *Acc. Chem. Res.* **2002**, *35*, 998-1007. b) K. Jiang et al, *Nano Lett*. **2003**, *3*, 275. c) S. C. Tsang, Y. K. Chen, P. J. F. Harris, M. L. H. Green, *Nature*, **1994**, *372*, 159. d) T. Hiura, T. W. Ebbessen, K. Tanigaki, *Adv. Mat*, **1995**, *7*, 275.

12.Lacerda, L.; et al. *Adv. Mater.* **2007**, *18,* 1480.

13.Eric, P.; et al. *Nat. Mater.* **2007**, *6*, 52.

14.Sun, X.; Li, Y. *Angew. Chem. Int. Ed*. **2004**, *43***,** 597.

15.Liu, Z.; Winters, M.; Holodniy, M.; Dai, H. *Angew. Chem. Int. Ed.* **2007**, *46*, 2023.

16.Bellezza, F.; Cipiciani, A.; Costantino, U.; Marmottini, F. *Langmuir* **2006**, *22*, 5064.

17.Masters, J. R. *Nature Reviews Cancer*, **2002**, *2*, 315.

18.Xu, P.; et al. *Angew. Chem. Int. Ed*., **2007**, *46,* 1.

19.Worle-Knirsch, J.M.; Pulskamp, K.; Krug, H.F.; *Nano. Lett.* **2006**, *6,* 1261.

20.a) Kundu et al, *J Biol Chem.* **2003,** 278, 19134-40. b) Ph.D thesis of Ms. Ruthrotha Selvi, MBGU, JNCASR, Bangalore. c) Selvi, R.; Dinesh, J.; Nagashankar, G.; Suma, B. S.; Arif, M.; Balasubramanyam, K.; Eswaramoorthy, M.; Kundu, T. K. *Nano. Lett*, **2008**,

21.Berger, S.L. *Nature* **2007**, *447*, 407. Review

22.Swaminathan, V. et al. *Chromatin and Disease, Springer press.* **2007**, *41*, 397.

23.Mai A. *Expert Opin Ther Targets* **2007**, *11*, 835. Review.

24.Roth, S.Y.; Denu, J. M.; Allis, C. D. *Annu Rev. Biochem*. **2001**, *70*, 81. Review.

Summary

Inorganic carbonates that occur abundantly on the earth are the cheap and natural source of organic carbon. We have carried out thermal decomposition of various transition metal carbonates of composition $MCa(CO_3)_2$ [M:Ca is 1:1 and M = Co, Ni or Fe] and $M_1M_2Ca(CO_3)_3$ [M_1:M_2:Ca is 1:1:2 and M_1M_2 = CoNi, NiFe or FeCo]. The decomposition conditions include heating at 550 ^oC in H_2 atmosphere for 5-6 h. The reduced transition metals act as catalysts for methanation of $CaCO_3$/$MgCO_3$ with high efficiency in the utilization of H_2.

A manuscript based on this work has been submitted for publication to *ChemSusChem* in 2009.

6.1. Introduction:

Energy and pollution-control are considered as two most important challenges in the 21st century. Presently we derive more than 80 % of our energy by burning the fossil fuels which include oil, coal and natural gas. Though the natural deposits of coal can continue to supply us the energy for next 200 years,[1] the resultant increase in pollution (in the form of CO_2 emission) presses for an immediate alternative sources of energy. Besides the combustion process, deforestation and other chemical process also continue to be most important anthropogenic sources[2] leading to global warming and consequent climate changes. The production of CO_2 by various countries of the world is presented in Figure 1.

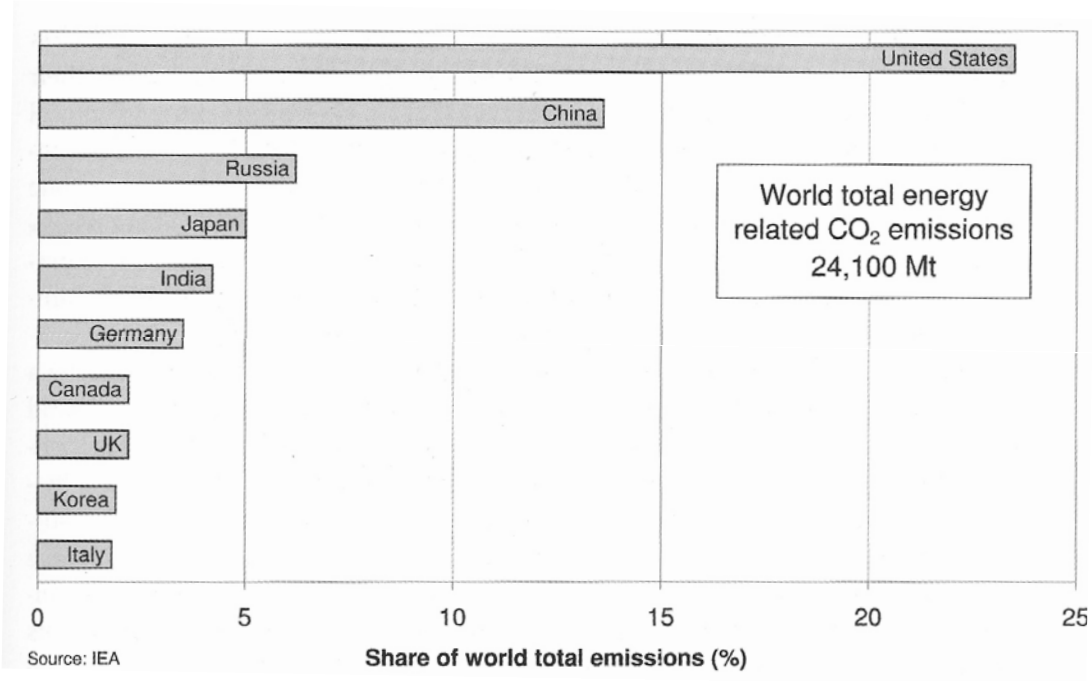

Figure 1: Contribution of various countries to energy related CO_2 production in the world. (Ref 7)

Keeping the current trend of energy consumption, following predictions are made for the next two decades,[1]

i) The global primary energy demand will rise by 53% leading to a 55% increase in global CO_2 emission related to energy.

ii) Fossil fuels will still remain the dominant source of energy worldwide meeting 83% of the increase in energy demand.

iii) As the demand for electricity rises, emission from power generation will account for 44% of global energy related emission.[3]

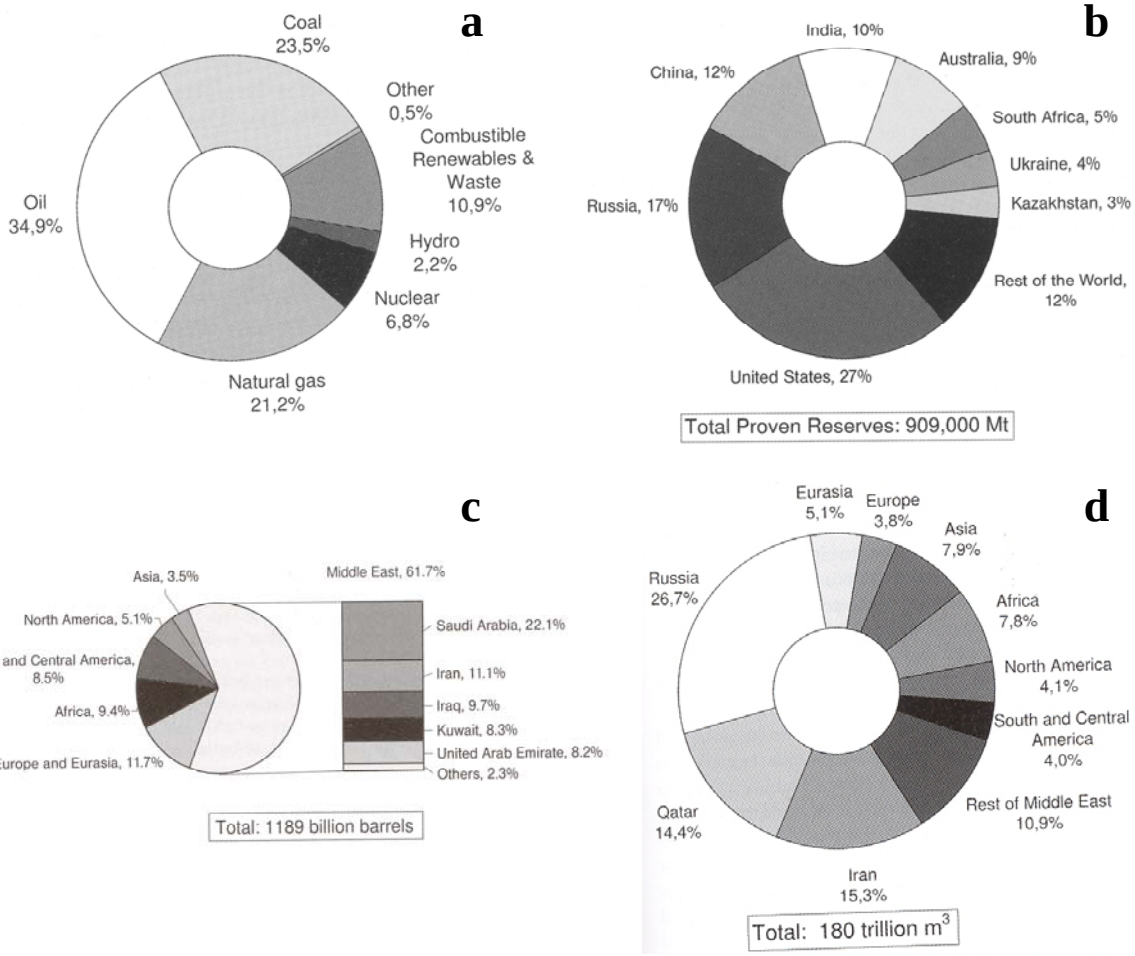

Figure 2: Charts showing various statistics of energy consumption and reserves. a) Contribution of various energy sources to the total energy demand in the world. b) World coal reserves c) World oil reserves and d) world natural gas reserves. The statistics are estimated during the year 2004-2005. Source: BP statistical review of world energy 2005.

In Figure 2, the estimated reserves of coal, oil and natural gases are presented. While this is the present state of affairs of our use of non-renewable sources of energy, the contributions of alternative renewable sources like hydro, solar, geothermal, wind and biomass can only complement and not replace our dependence on fossil fuels. Therefore, the solution to tackle the existing problem must not only be aimed at lowering the pollution from the existing sources of energy but also to provide alternative sources of energy that are economically sustainable, environmentally clean and renewable. A number of other energy sources based on H_2, nuclear, methanol, natural gas, formic acid etc have been under consideration. Figure 3 represents the scheme explaining the inter conversions of energy. Table 1 shows the energy content of various sources of fuel.

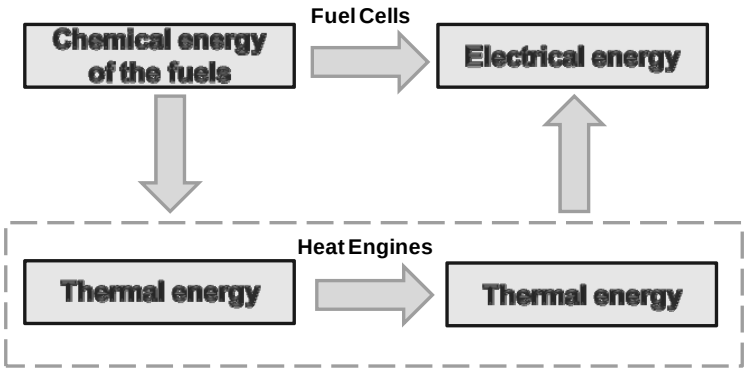

Figure 3: Scheme showing the fuel to energy conversions.

Fuel	Average Energy Content ($kcalg^{-1}$)
Wood	3.5
Coal	7
Oil	10
Natural gas	11
Uranium	150000

Table 1: Energy content of various fuels.

From the existing coal and oil economies, the possible migration towards other economies based on hydrogen or methanol is seriously considered. A brief account on various other sources of fuels, their advantages and disadvantages are discussed below.

a) The hydrogen economy:

The idea of hydrogen economy is quite straight forward. Hydrogen being the most plentiful element on earth can be burnt completely without any pollution. They can be used in the fuel cells to power cars, heat the houses and even generate electricity. Figure 4 summarizes the consumption of hydrogen in various sectors. The by product is water which can be used. Therefore, it is more than obligatory for governments, energy producing companies and automobile industries to explore the possibilities of utilising them. However, the challenges that are to be confronted to make this approach viable are enormous, the primary one being its production in large quantities. Though hydrogen as an element is abundant, its presence in the form of molecular hydrogen (H_2) is very limited on this planet. The possible methods of production are by reforming the fossil fuels or electrolysis of water.

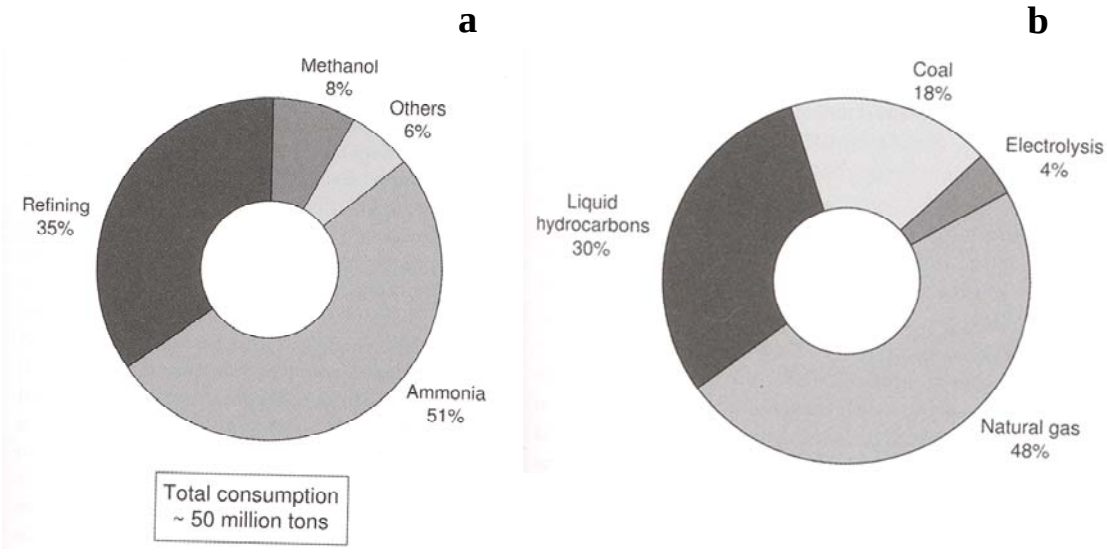

Figure 4: Scheme showing a) hydrogen consuming sectors and b) hydrogen producing sources.

But the steam reforming process of natural gas also produces large amounts of CO_2 via CO route.[4] The technology to produce H_2 locally at smaller scales such as in filling stations is more economically profitable only if there are means to capture CO_2. H_2 production via water electrolysis needs electricity which is currently generated by environmentally-polluting sources. Although H_2 from fossil fuels are produced at the cost of $1 per kg,[5] with substantial potential for improvement and further price reduction, there are no existing economical technologies to treat large amounts of CO_2 that will be produced. Though a very high quality of H_2 is assured by electrolysis, the high cost of the process has made it possible to contribute only 4% of the total H_2 production in the world.[5]

Producing H_2 is only the first step involved in the implementation of hydrogen economy. The next challenging aspect is to develop a technology that is economical, practical, safe and user-friendly to store hydrogen. H_2 being the lightest gas contains much less energy per unit volume than the liquid fuels like gasoline under the same pressure (Figure 5).

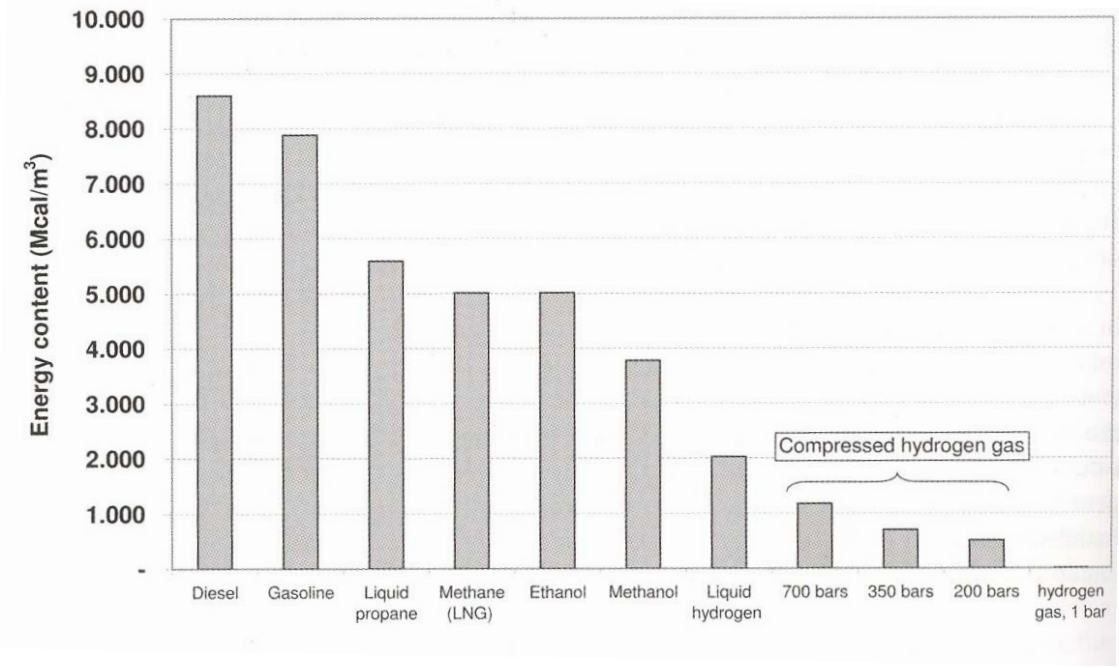

Figure 5: Volumetric energy content of hydrogen compared to other fuels.

Under normal conditions, H_2 requires 3000 times more space than gasoline. Thus H_2 must be liquefied, compressed or adsorbed on solid supports to be of any practical purpose. Interestingly, on the weight basis H_2 has the highest energy content of any known fuel (almost thrice that of gasoline). This makes the liquefaction of H_2 as an attractive means to store. A very high pressure and a low temperature of -258 ^oC require a multi stage cooling apparatus which makes the whole process an energy intensive.[6] Despite the use of thermally insulated containers it is difficult to store liquid H_2 without any leak. Typically it will evaporate at a rate of 1% per day. It also shares many of the same safety issues as other forms of hydrogen, as well as being cold enough to liquefy atmospheric oxygen which can be an explosion hazard. Most hydrogen fuel cell powered cars adopt energy storage by compression method. Though H_2 is stored at a pressure of 700 bar, its energy content is 4.6 times lesser than that of gasoline. This necessitates the use of many numbers of voluminous tanks. Though H_2 storage by compression consumes lesser energy than by liquefaction, it still utilises an equivalent of 10% of the energy that is stored.[6] Presently, the use of hydrogen as the fuel is limited to rocket propellants and some advanced cars.

b) Nuclear energy:

The nuclear energy made its first public impact in August 1945 in the form of atom bombs. The fact is that a tremendous amount of energy lies to be utilised in this technology (1 kg of pure ^{235}U can generate over 2 million times more energy than 1 kg of coal!)[6] but the irony is that the possibility of its constructive power was demonstrated much before it was used to make atom bombs (the first controlled nuclear fission was performed by a team of scientists lead by the famous physicist Enrico Fermi in 1942 at the football grounds of University of Chicago).[6] Relying on nuclear power can also make significant advances in hydrogen production, water desalination etc. With near zero emissions, nuclear power has clear advantages over fossil fuels

with regard to air pollution and climate change. Today there are about 440 commercial nuclear reactors in 30 countries with over 3,60,000 MW of total power production capacity.[7] In US, nearly 20% of the total electricity produced is of nuclear origin. In France and Belgium, it's about 78% and 55% respectively.[7] All the commercial plants use uranium as the fuel. Uranium, a slightly radioactive metal occurs throughout the earth's crust at about 500 times more abundant than gold. However the natural uranium consists of a mixture of two isotopes: uranium 235 (^{235}U) and uranium 238 (^{238}U) of which only ^{235}U - which represents merely 0.7% of the natural uranium, can undergo nuclear fission. The major challenge in this area lies in the engineering and design aspects of the reactors which can increase the efficiency, reduce the cost of maintenance and increase the safety disposal of the nuclear wastes. The cost of production of electricity using nuclear energy is expected to be at €0.03 kWh^{-1} in France[8] including the costs of decommissioning the older plants and construction capital. This is at a much lower value compared to the electricity produced from oil or coal. The introduction of breeder reactors makes recycling of fuel possible.[9]

Generation of power using nuclear fusion is also an important area where intensive research is being carried out. The amount of energy released would be 10 times more than that produced in nuclear fission for the same mass of the fuel. There are means to extract the required fuels namely tritium and deuterium from nature. Besides fusion reactors are intrinsically safe as only small amounts of fuel is present in the plasma chamber and any uncontrolled perturbation will lead to temperature drop which will immediately haul the chain reaction. Unlike fission reactors, in fusion reactors neither the fuel nor the final product is radioactive. However the process is yet to be commercialized because the energy gained must be at least equal to the amount of energy spent in maintaining the temperature of the reactions. However, there are

bright hopes in making this technology viable and a number of fusion reactors are under construction in countries like India, China etc.

The safety concerns run high in any energy related technology. Our history is well studded with a number of energy-related accidents that there are always activists groups which speak against their implementation. The famous explosion observed in zeppelin of Hindenburg[10] in 1937 was a major hindrance in developing H_2 as the fuel for transportation. Civilian nuclear disasters in Three Mile Island[11] in US in 1979 and chemical explosion in Chernobyl reactor[12] in former Soviet Union in 1986 are attributed to human errors and have caused huge radiation related damages. The failures have virtually stopped the construction of further nuclear reactors in the western world. Although this was the most serious nuclear accident, it should also be compared with other energy-related losses of life such as coal mining accidents which draw much less public attention but nevertheless cause thousands of deaths every year.

c) The methanol economy:

Methanol as an alternative fuel is expected to influence the transportation sector more profoundly than any other fields. In contrast to gasoline, which is a complex mixture of hydrocarbons and some additives, methanol is a simple chemical. It contains about half the energy density of gasoline, which means that 2L of methanol contains the same energy as 1L of gasoline. The world demand for methanol is given in Figure 6. Even though methanol's energy content is lower, it has a high octane number which means that fuel/air ratio mixture can be compressed to a smaller volume before being ignited. This increases the efficiency of the engine. Methanol also has high latent heat of vaporization which is about 3.7 times faster than gasoline,[6] so that methanol can absorb a much larger heat while passing from liquid to vapour phase. This helps to remove heat away from the engine so that it may be possible to have light-weight; air-

cooled radiators.[13] Methanol vehicles have shown to have low emissions of NO_x, hydrocarbons, SO_2 and particulates. Though the concept of using alcohol as a fuel is as old as the internal combustion engine itself, the support it received from the governments across the world had been fluctuating throughout the history. The major support was given in Germany during the world wars, which being poor in its oil reserves wanted energy independence. United States support for alcohol powered vehicles had been in accordance with their oil supplies.

The 1970 oil crises saw a surge in alcohol production while it declined fast after the crises ended. It was Thomas Reed of Massachusetts Institute of Technology who first advocated methanol as a fuel in US in 1973.[14] He suggested that adding just 10% of methanol to gasoline

can improve the vehicle's performance, reduce mileage and reduce pollution. Methanol derived products like dimethylether, dimethylcarbonate also possess great potential to be developed into commercial alternative fuels.

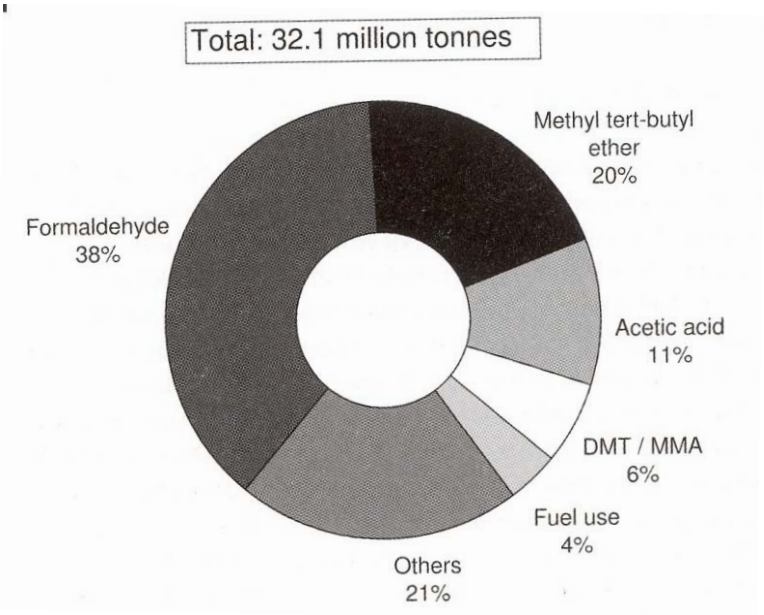

Figure 6: World demand for methanol in various sectors in 2005 (Ref 7).

Biodiesel – which is fatty acid methyl ester is again derived by transesterification of vegetable oil and animal fats using methanol. Methanol can also be considered as hydrogen storage molecule. Being the simplest alcohol, it does not have any C-C bonds which are difficult to cleave during reforming reactions. Thus, unlike gasoline, methanol reforming occurs at much lower temperatures and is portable for H_2 generation. Mitsubishi Gas Chemical has developed a process to produce high-purity H_2 by steam reforming of methanol using a highly active catalyst which allows operation at 240-300 ^oC and enables rapid start up and stop and flexible operations.[7]

d) The fuel cell technology:

Fuel cells are the devices which directly convert chemical energy into electrical energy. In contrast to heat engines, fuel cells can have high thermodynamic efficiencies as it does not involve any conversion to mechanical work. Thus they can have very high power densities at low temperatures. The possible applications of the fuel cells can range from operating mobile phones to running automobiles. Some major drawbacks in commercializing the fuel cell technology lie in reliability issues, mechanical durability, mass transport and catalyst utilization. Fuel cells can be designed to utilise H_2, CH_4, CH_3OH, HCOOH or NH_3. But they all operate under the same principle.[15]

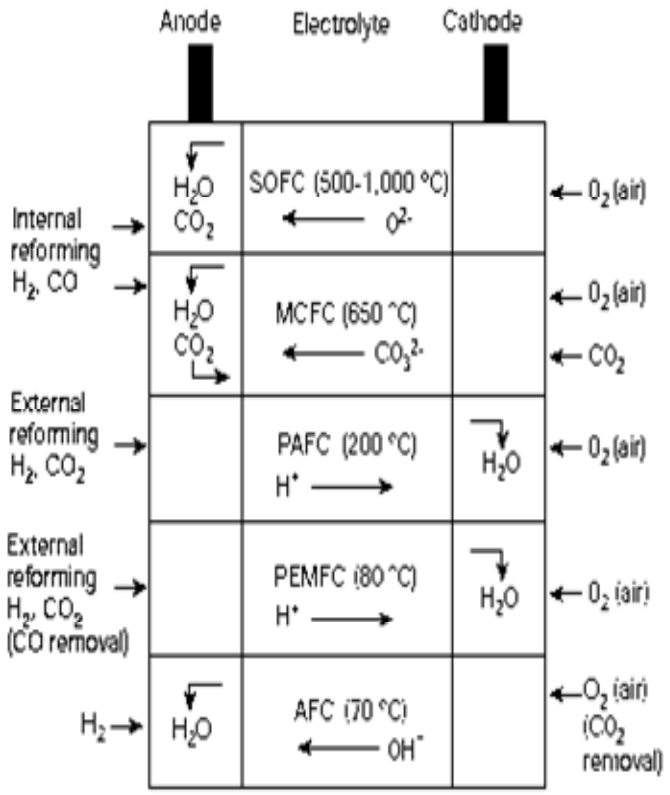

Figure 7: Major types of fuel cells.

Figure 7 shows a picture of major types of fuel cells. H_2 based fuel cells is also an important component of hydrogen economy. H_2 and O_2 are catalytically combined to form water, heat and electricity. The electrolytes can be polymers or ceramics with ion conducting properties (ions like H^+, OH^-, CO_3^{2-}, and O^{2-}). Accordingly, we have proton exchange membrane fuel cells (PEMFC), molten carbonate fuel cells (MCFC), phosphoric acid fuel cells (PAFC), solid oxide fuel cells (SOFC), alkali fuel cells (AFC) and direct methanol fuel cells (DMFC). The operating temperatures are about 200 ^oC for PAFC and 600-1000 ^oC for MCFC and SOFC. The power generation using fuel cell technology remains expensive at the cost of \$4500 kWh^{-1} as compared to \$1000 kWh^{-1} using conventional fossil fuels.[16] However, as the fuel cells do not have any movable parts; there is no maintenance expenditure associated with them.

6.2. Scope of the present investigation:

Natural gas, which is a clean alternative source of energy, is abundantly present in the earth's crust although localized to remote inaccessible areas of the world making its transportation expensive.[15] In this context, storage of CO_2 and its conversion to useful chemicals are important challenges facing the mankind.[16,17] For storage of CO_2, we have to design novel materials with engineered pores or surfaces.[18] Sequestration of CO_2 as carbonates is also probably considered.[15] The second approach is to utilize CO_2 as a cheap source of carbon to produce high value chemicals such as methane, higher hydrocarbons, methanol and formic acid.[19-28] On-site conversion of CO_2 to CH_4 on the industrial scale can be economically attractive as it can avoid the expensive distribution process of natural gas. The current conversion processes involve heating CO_2 and H_2 in the presence of metal or metal oxide catalysts.[29,30] Other processes involve electrochemical and photoreduction.[31,32] Most of these reactions, however utilize H_2 in excess which in turn is prepared by the water gas shift reaction which produces CO_2 as a by-product. In this context, we were interested in studying the efficiency in the conversion of inorganic carbonates instead of gaseous CO_2 as the source of carbon to form methane. Such a study would also be relevant to the conversion of carbonaceous inorganic rocks to organics, a futuristic problem of importance. Our study aims at optimizing conditions for the maximum conversion of inorganic carbonates to methane in high efficiency by the use of appropriate catalysts.

Replacing gaseous CO_2 with carbonates has many inherent advantages. Firstly, the abundantly present natural metal carbonates like calcite ($CaCO_3$) and dolomite ($MgCO_3$) are the starting materials. Furthermore, after the decomposition of the carbonates, the recarbonization process can be used to keep the resources renewable and minimise CO_2 emission. The observations made by Reller et al suggested that the presence of transition metals in carbonates

can decrease the temperature of decomposition of calcite in H_2 by 150 – 300 K.[33] Their conclusions were based on the results obtained from the reduction of carbonates at a high flow rate of H_2 in a continuous-flow TGA. Detailed studies are therefore essential to evaluate the commercial feasibility of using transition metal carbonates as the carbon source to synthesise hydrocarbons.

6.4. Experimental section

a. Materials:

$Ca(NO_3)_2.4H_2O$, $NaHCO_3$, $Co(NO_3)_2.6H_2O$, $Mn(NO_3)_2$, $FeCl_2$ (anhydrous), $Ni(NO_3)_2.6H_2O$ and 99.99% CO_2 gas. Double distilled water was used for the synthesis. Heating was done using a hot plate. Filtration was effectively done using a 200 nm pore polycarbonate membrane. Other materials include Buchner flask, suction pump, oven, quartz tube (12321), high temperature furnace (Elite Thermal systems, UK), quartz wool, stainless steel reactor tubes, alumina boat, gas chromatograph (Agilent 6890N) fitted with thermal conductivity detector (TCD) and flame ionisation detector (FID). Helium was used as the carrier gas. FID was supplied with the mixture of H_2 and air (zero grade) in the ratio of 1:10. The columns used were capillary columns HP-PLOT MoleSieve 5A (30 m × 320 µm × 10 µm) and HP-PLOT Al_2O_3 "S" deactivated (15 m × 530 µm × 15 µm) purchased from Agilent.

b. Synthesis of carbonates:

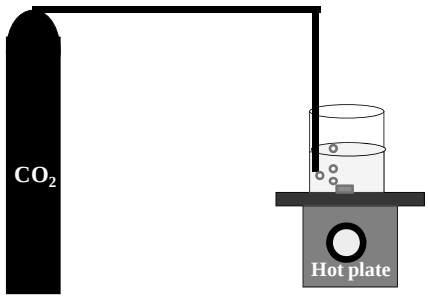

Figure 8: Schematic showing the experimental procedure for the synthesis of metal carbonates.

S.No	Sample	Precursor	Weight (g) M:Ca (1:1), M_1:M_2:Ca (1:1:2)
1	$CoCa(CO_3)_2$	$Co(NO_3)_2.6H_2O$ $Ca(NO_3)_2.4H_2O$	0.72 0.59
2	$NiCa(CO_3)_2$	$Ni(NO_3)_2.6H_2O$ $Ca(NO_3)_2.4H_2O$	0.72 0.59
3.	$MnCa(CO_3)_2$	$Mn(NO_3)_2$ $Ca(NO_3)_2.4H_2O$	0.50 0.59
4.	$FeCa(CO_3)_2$	$FeCl_2$ $Ca(NO_3)_2.4H_2O$	0.25 0.59
5.	$FeCoCa(CO_3)_2$	$FeCl_2$ $Co(NO_3)_2.6H_2O$ $Ca(NO_3)_2.4H_2O$	0.12 0.36 0.59
6	$NiCoCa(CO_3)_2$	$Ni(NO_3)_2.6H_2O$ $Co(NO_3)_2.6H_2O$ $Ca(NO_3)_2.4H_2O$	0.36 0.36 0.59
7	$FeNiCa(CO_3)_2$	$FeCl_2$ $Ni(NO_3)_2.6H_2O$ $Ca(NO_3)_2.4H_2O$	0.12 0.36 0.59

Table 2: A summary of weight of different metal salts added in making carbonate samples.

The carbonates were synthesized according to the procedure reported in the literature.[34] The scheme is shown in Figure 8. Mixed metal carbonates $MCa(CO_3)_2$ were synthesized in the M:Ca molar ratio of 1:1, where M is (Fe, Co, Ni, Mn). Incase of metal carbonates of composition $M_1M_2Ca(CO_3)_2$, the metal molar ratio M_1:M_2:Ca was maintained as 1:1:2, where M_1 and M_2 are any two combinations of Fe, Co and Ni. A 100 mL aqueous solution of 0.5 M $NaHCO_3$ was made. The solution was maintained at 80 ^oC with constant stirring using a magnetic pellet. CO_2 gas was constantly bubbled through the solution at the rate of 10 mL/min. To this $NaHCO_3$ solution, a 20 mL aqueous solution of metal salt and $Ca(NO_3)_2.4\ H_2O$ dissolved in an appropriate ratio (Table 2) was added drop by drop in 2 min. The precipitation begins to occur immediately as evident by the turbidity. The precipitate becomes more flocculent with time. The stirring was

allowed to continue for 1 h with constant bubbling of CO_2. Followed by this the precipitate was carefully removed by filtration using a suction filtration set up and polycarbonate membrane. The precipitate was washed with distilled water thrice before drying at 50 ^oC in air for 4-6 h.

c. Preparation of the catalyst:

A known weight of the as prepared metal carbonates was placed in an alumina boat and heated in the tube furnace at 550 ^oC for 10 h in presence of H_2. The rate of heating was kept at 5 ^oC /min and rate of flow of H_2 was around 3.5 mL/min. After the reaction temperature cooled, the black coloured sample was removed carefully and used for other experiments.

d. Characterization:

The morphology of the as prepared carbonate sample was characterized using FESEM. The presence of the carbonates was analysed using FT-IR spectroscopy and TGA. All the crystalline phases were analysed using XRD.

e. **Estimation of carbonates**:

Amount of carbonate in the samples was determined by decomposing them at 700 ^oC in N_2 flow and the CO_2 produced was dissolved in standard solution of $Ba(OH)_2$.[35] The concentration of excess $Ba(OH)_2$ after the reaction was estimated by titrating it against of 0.1 N HCl using thymolphthalein as the indicator. The end point was sharp change from blue to colourless against the precipitated white $BaCO_3$ allowing for an accurate estimation of CO_2 formed from transition metal carbonates.

f. Experimental setup for catalytic conversion of metal carbonates:

The catalytic reactions were performed in a stainless steel tube reactor whose dimensions are ¼ inch in diameter and 30 cm in length (Figure 11a). The supply of the reactant gas to the reactor and the exhaust from it was connected using to 1/8 inch stainless steel tubes via swagelok

connections. The exhaust is fed into a Gas chromatograph (GC). The details of the reactor setup are shown in Figure 9. H_2 was used for FID as the fuel gas as well as the reactant gas for the catalytic conversion. A "stainless steel - T" joint was placed at the source of H_2 in order to supply the gas for both the above mentioned purposes.

In the figures, the outlet for H_2 line meant for the reaction feed stock is connected to the reactor via the mass flow controller. By this, one can establish a controlled flow of reactant gas H_2 to the reaction. This assumes significance as the utility of H_2 gas is also an important parameter considered for commercialization of a process. H_2, which is the most clean and high-energy fuel is industrially very precious and therefore its judicious utilization in the conversion of a pollutant like CO_2 to other chemicals is recommended in order to keep the whole process attractive.

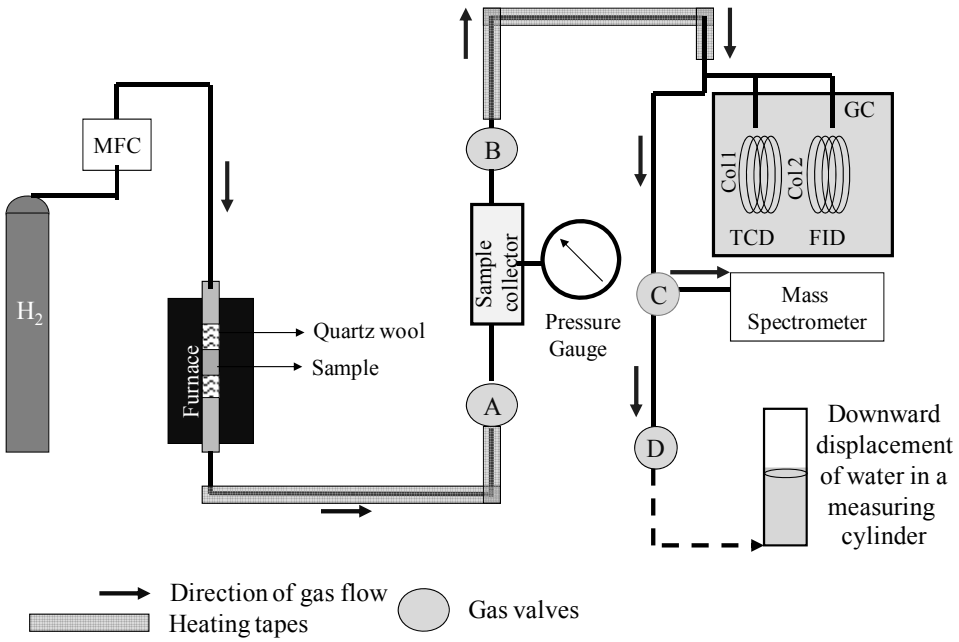

Figure 9: Scheme showing the experimental set up used in the catalytic conversion of inorganic carbonates into organic compounds.

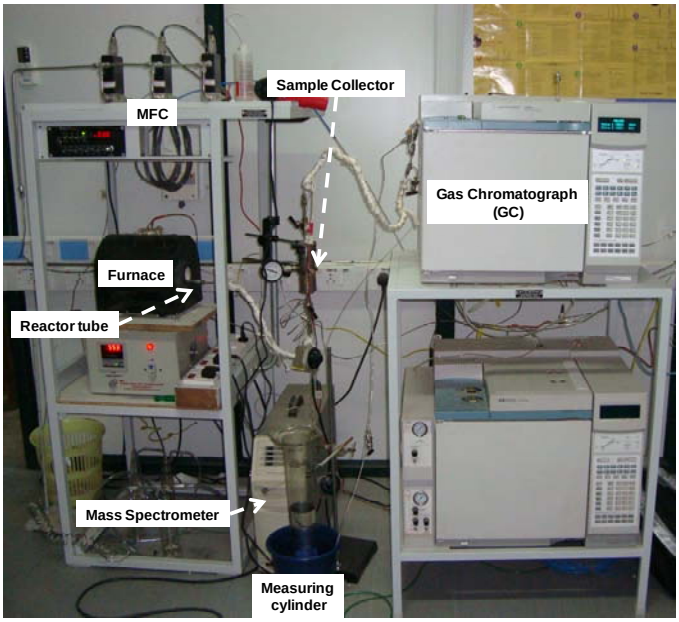

Figure 10: Digital photography image showing the experimental setup.

g. Sample packing:

The required amount of sample was packed with the catalyst in the reactor tube (Figure 11b). The tube was vertically clamped to a stand. A steel rod was inserted from the bottom of the reactor tube so that the tip of the rod reached the midpoint of the reactor tube.

Figure 11: a) Digital photography image showing the stainless steel reactor tube b) Cartoon depicting the packing of the catalyst and sample at the centre of the reactor tube.

Quartz wool, sample and the catalyst are packed alternatively in the order from the top opening till the length of the packed material is about 2.5 cm. The packing is usually begun by stuffing quartz wool which served as a support for the catalyst and sample. A minimal quantity

of quartz wool was added between the sample and the catalyst to avoid the formation of hot spots during the reaction. The whole packing is then pushed to the middle of the reactor tube using another rod so that it remains in the heating zone of the furnace.

h. Gas lines and plumbing:

The outlet of the reactor tube was connected to a sample collector which is controlled by valve A. The sample collector was a cylinder made of thick walled stainless steel (Figure 10) with an inlet, outlet and a side arm (which is permanently sealed). The sample collector was also fitted with a pressure gauge which can measure up to 2 atm. The outlet of the sample collector was connected to GC inlet via valve B. The plumbing at this point was fabricated in such a way that a simultaneous injection to both the columns can be achieved. A T-type connection followed by a reducing adapter from 1/8 to 1/16 inch was used for this purpose. The line also bypassed to mass spectrometer which was controlled by valve C. The length of the tube that connected the outlet of the reactor to the inlet of GC was kept minimal and heated with heating tapes (approx temp was 80 – 100 ^{o}C) to avoid the adsorption of gasses on the steel walls. Additionally a hot air gun was also used to heat the lines wherever required.

i. GC – configuration and measurement details:

The products of the reaction were analysed using GC via automatic gas sampling operated by a six port valve. The separation of the products is achieved independently using two columns (HP-molsieve and HP-PLOT Al_2O_3) which were placed one behind the other in parallel. The front column (HP-molsieve) is connected between TCD and the front inlet. The back column (HP-PLOT Al2O3) was connected between FID and the back inlet. Both the columns were placed in an oven and the separation was achieved in both the columns at the same temperature. The details of flow rates, retention times of the analytes and ramp programming of

oven are summarised in Table 3 and Figure 12. The inlets were maintained at are 200 ^{o}C throughout the measurement. The TCD and FID were maintained at 200 and 250 ^{o}C respectively throughout the measurement. The outlet of GC was carefully exhausted to outside.

component	Retention time (min)	Column temperature (^{o}C)	Column flow rate (mL/min)	column	Detector
H_2	1.9 1.7	40 100	1.7 1.7	HP-molsieve	TCD
CO	1.8	100	1.7	HP-molsieve	TCD
CO_2	10.0	180	1.2	HP-molsieve	TCD
CH_4	0.7 2.4 2.4	100 40 40	7 1.7 1.7	HP-PLOT Al_2O_3 HP-5 HP-molsieve	FID FID TCD

Table 3: Details of optimised measurements conditions using Gas Chromatograph. TCD – Thermal Conductivity Detector and FID – Flame Ionisation Detector.

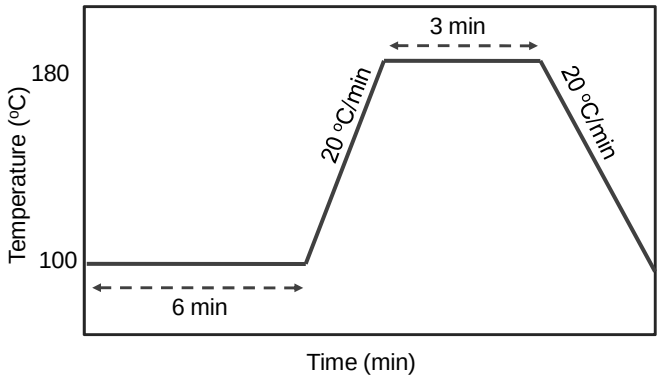

Figure 12: Optimised conditions of oven-programming in GC.

6.4. Results and discussion:

In Figure 13, digital photograph images of various carbonate samples prepared are given. The samples were coloured characteristic of the type of metal ion present. FESEM images of the

as prepared carbonate samples of composition $MCa(CO_3)_2$ where M= Fe, Co, Ni, Mn (M:Ca is 1:1) are presented along with the corresponding energy dispersive X-ray spectra in Figures 14 and 15. FESEM images suggested that the transition metal carbonates existed as large aggregates of particles with size varying between 50 – 500 nm.

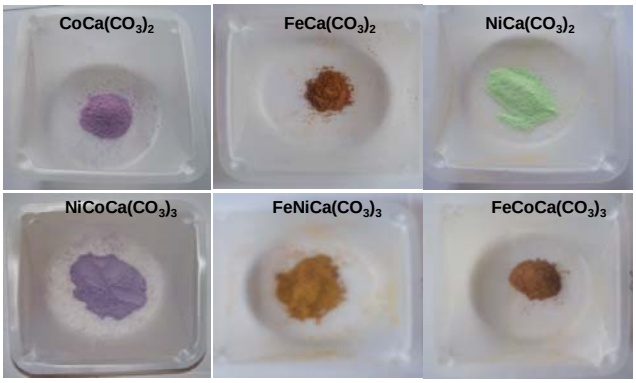

Figure 13: Digital photography images of the various carbonates prepared. M: Ca is 1:1 and M_1:M_2: Ca is 1:1:2.

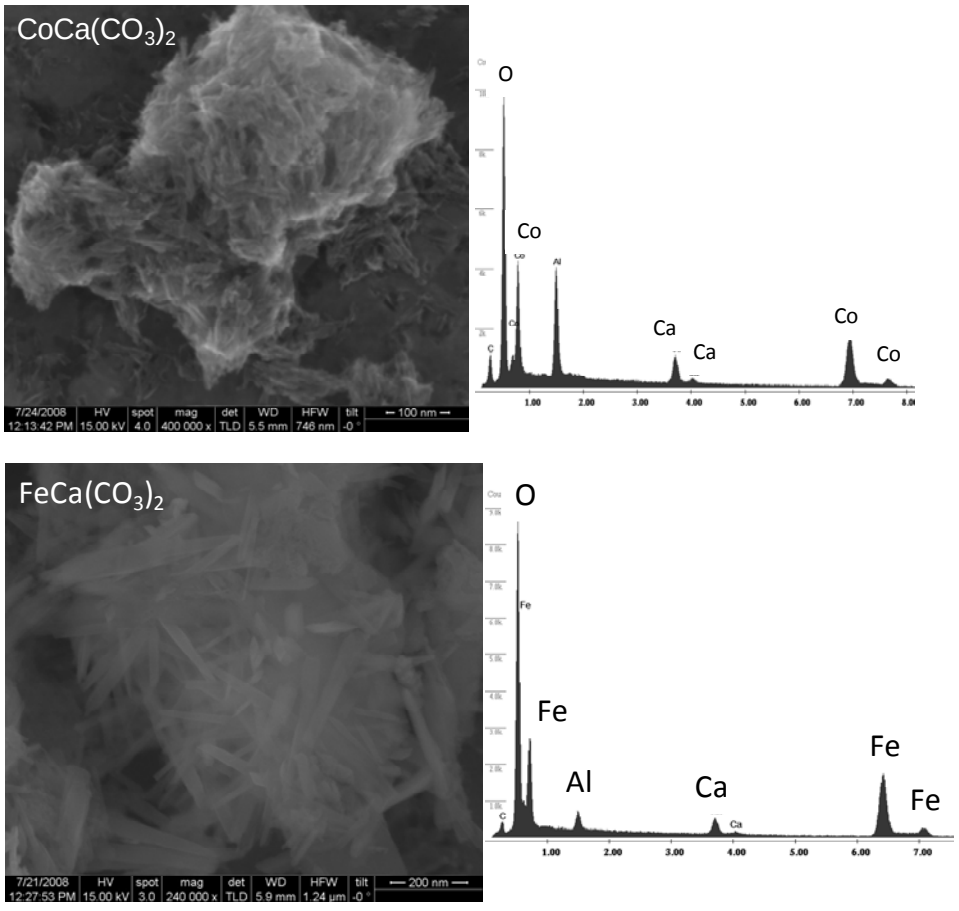

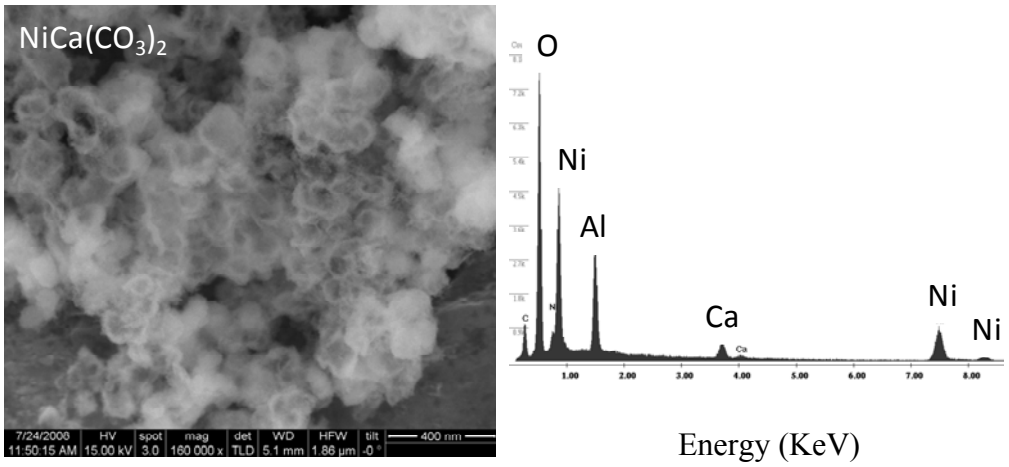

Figure 14: FESEM images and the corresponding EDX spectra of carbonates of formula $MCa(CO_3)_2$.

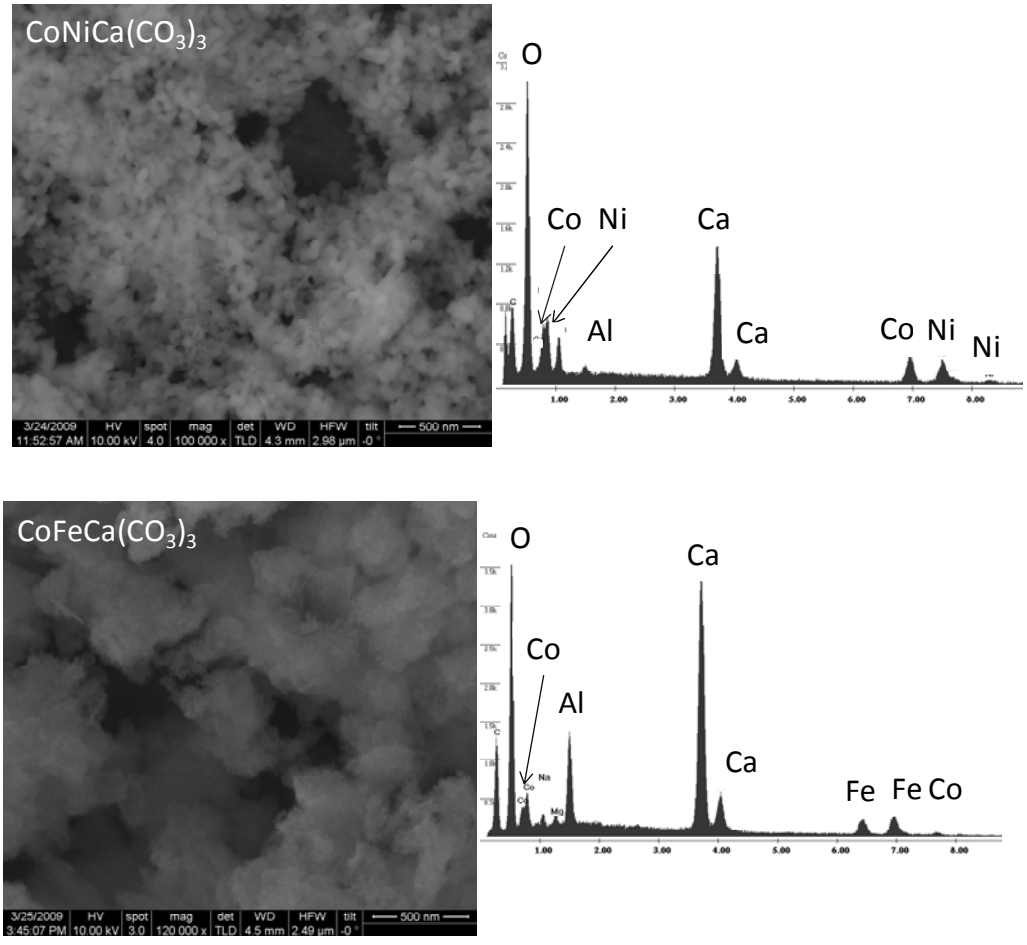

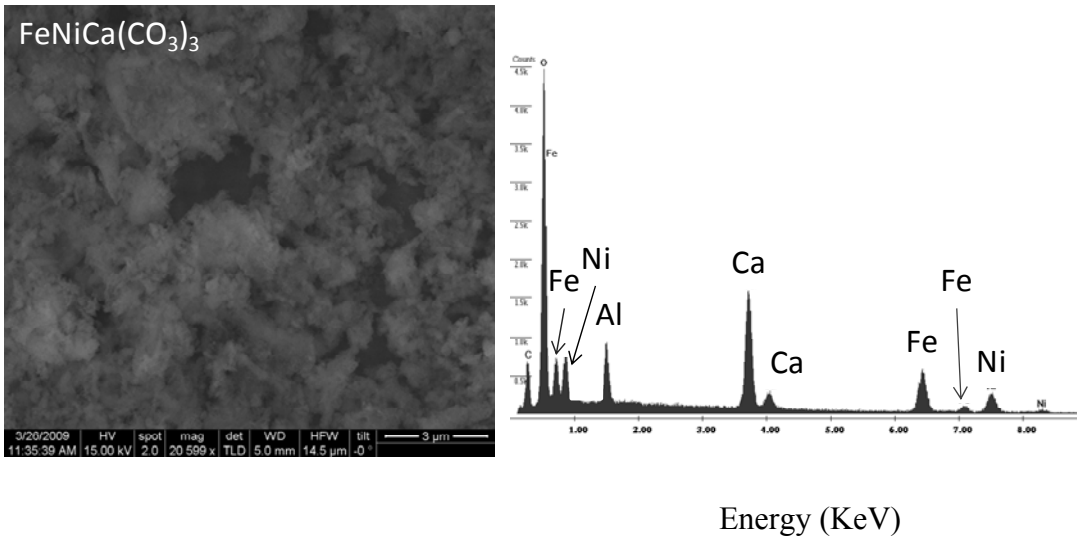

Figure 15: FESEM images and the corresponding EDX spectra of carbonates of formula $M_1M_2Ca(CO_3)_3$.

Carbonate formula	Volume of CO_2 at STP (mL) calculated by titrimetry
$CaCO_3$	9.0
$CoCa(CO_3)_2$	5.1
$NiCa(CO_3)_2$	6.8
$FeCa(CO_3)_2$	6.8
$CoNiCa(CO_3)_3$	6.8
$NiFeCa(CO_3)_3$	4.7
$FeCoCa(CO_3)_3$	5.1

Table 4: Volume of CO_2 at STP produced by decomposing 50 mg of the carbonates as estimated by titration method.

The amount of carbonates was estimated by titrimetry method and the results are given in table 4. The volume of CO_2 (in mL) varied significantly from the values calculated from their molecular formula. The deficiency in carbonates could be attributed to synthesis conditions. The percentage conversion in other reactions was calculated using the volume of CO_2 calculated by the titrimetry method and the amount of gaseous products (CO_2 or CH_4) after the reaction.

The decomposition of transition metal carbonates in H_2 was studied systematically in a view of increasing the efficiency of H_2 to have a maximum conversion and high selectivity for CH_4 (reaction 1). The decomposition of transition metal carbonates in H_2 initially produces products like CO_2, CO, H_2O and CH_4. But the process also leads to an in situ formation of reduced metal and metal oxide nanoparticles over calcium oxide which catalyses the formation of CH_4. Following this, we prepared metal/metal oxide/CaO catalysts separately (see experimental section) and tested their influence on the decomposition products by mixing with fresh transition metal carbonates (reaction 2) and with minerals like $CaCO_3$ and $MgCO_3$ (reaction 3).

Reaction 1:

$$MCa(CO_3)_2 \text{ or } M_1M_2Ca(CO_3)_3 \xrightarrow{H_2/550\,^oC/5\,h} CH_4$$

Where M = Co, Ni or Fe and M_1M_2 = CoNi, NiFe or FeCo

Reaction 2:

$$MCa(CO_3)_2 \text{ or } M_1M_2Ca(CO_3)_3 \xrightarrow[H_2/550\,^oC/5\,h]{\text{catalyst}} CH_4$$

Reaction 3:

$$CaCO_3 \text{ or } MgCO_3 \xrightarrow[H_2/550\,^oC/5\,h]{\text{catalyst}} CH_4$$

The transition metal carbonates of composition $MCa(CO_3)_2$, where M = Co, Ni, Fe and mole ratio M:Ca = 1:1 and $M_1M_2Ca(CO_3)_3$, where M_1M_2 = CoNi, NiFe and FeCo and mole ratio M_1:M_2:Ca = 1:1:2, were prepared as described in the experimental section. The decomposition of transition metal carbonates were carried out in presence of H_2 at 550 ^oC. We first optimised the reaction conditions such as flow rate of H_2 and amount of sample for the decomposition of $CoCa(CO_3)_2$ to obtain maximum conversion and selectivity for CH_4

and extended the study to other transition metal carbonates. Figure 16a shows the time dependent analysis of the product profile for the thermal decomposition of $CoCa(CO_3)_2$ without the catalyst at 5 mL/min flow rate of H_2. The two major products were CO_2 and CH_4 and we do not see the formation of CO or H_2O. For the first 4 h of the reaction formation of CO_2 and CH_4 show an opposite trend. At the end of first hour, CO_2 formation dominates the reaction. However, as the reaction proceeds, the formation of transition metal nanoparticles on the surface of carbonates facilitates the subsequent conversion of CO_2 to CH_4 as evident from the increasing trend observed for the methane formation up to 4th hour.

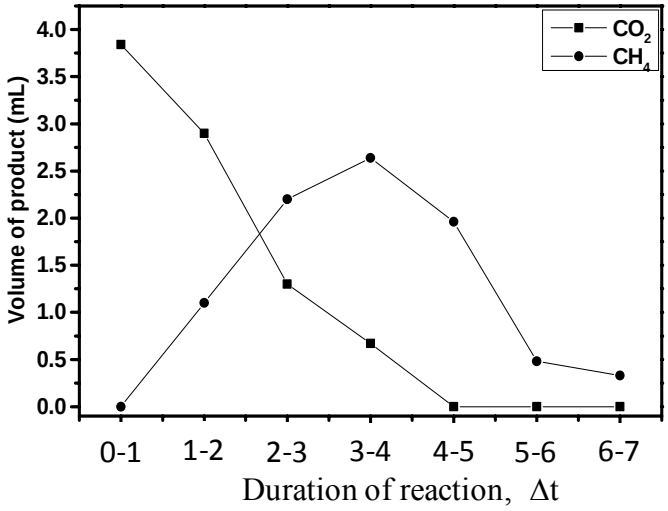

Figure 16: Time dependent product distribution of $CoCa(CO_3)_2$ in H_2 (5 mL/min) at 550 ^oC a) 50 mg of sample without catalyst.

$CaCO_3$ in the absence of transition metal carbonates was reported to give products like CO_2, CO and H_2O and not CH_4.[19] The results indicate that to get a maximum selectivity for methane, reduction of the transition metal must be accomplished. This is done by increasing the amount of H_2 available for the reduction of metal ions. The product distribution in the

decomposition of 50 mg of $CoCa(CO_3)_2$ at different flow rates of H_2 shows complete conversion of carbonates to CH_4 at a flow rate of 8 mL/min (Table 5).

Sample	Wt (mg)	T (°C)	H_2 (mL/min)	Conversion (%)	Yield (%)	
					CH_4	CO_2
$CoCa(CO_3)_2$	200	550	1	100	7	93
$CoCa(CO_3)_2$	200	550	3.5	100	31	69
$CoCa(CO_3)_2$	100	550	3.5	100	49	51
$CoCa(CO_3)_2$	50	550	8	100	80	20

Table 5: Optimization of flow rate of H_2 to get a maximum selectivity of methane

These results assume significance compared to the results of Reller et al, where there was a noticeable formation of CO and CO_2 even at high flow rates of hydrogen (30 mL/min for 10 mg of carbonates). The reason for the higher efficiency of H_2 in the conversion of CO_2 to methane in the present case could be the high proportion of transition metal nanoparticles available in the carbonates. FT-IR studies showed that the stretching frequency of the CO_3^{2-} disappear almost completely after the reaction indicating the complete decomposition of the carbonates (Figure 17 A). XRD studies of the decomposed $CoCa(CO_3)_2$ showed the presence of β Co, CaO and CoO (Figure 17 B). TEM studies showed particle diameters to be in the range of 20 – 200 nm range which could be a mixture of metals and metal oxides (Figure 17C).

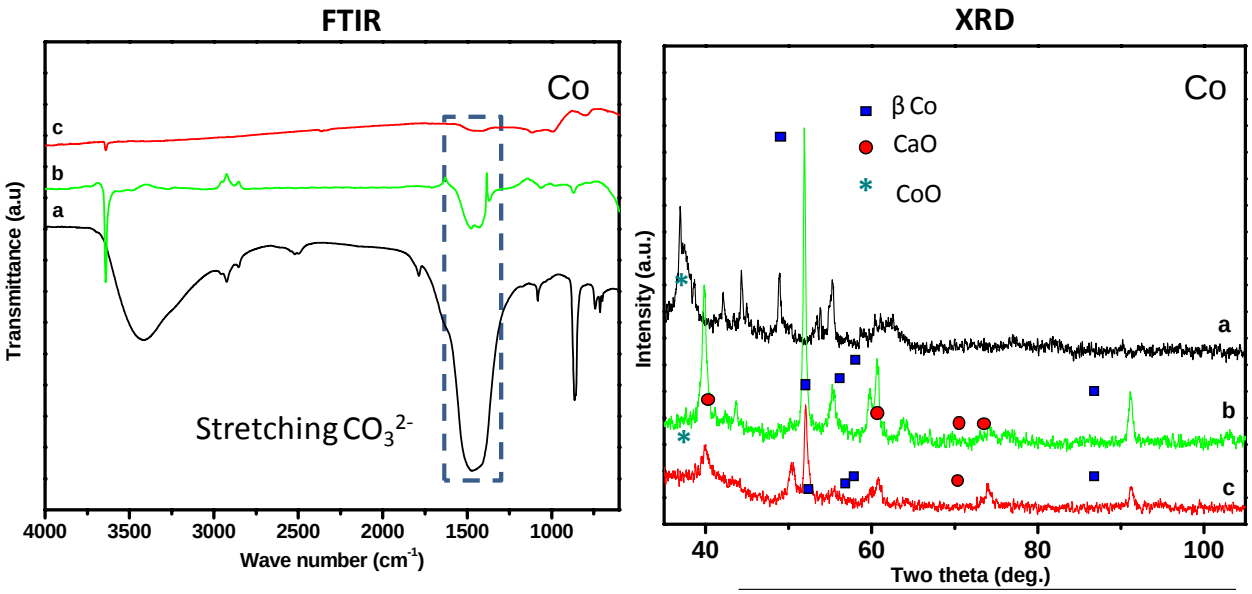

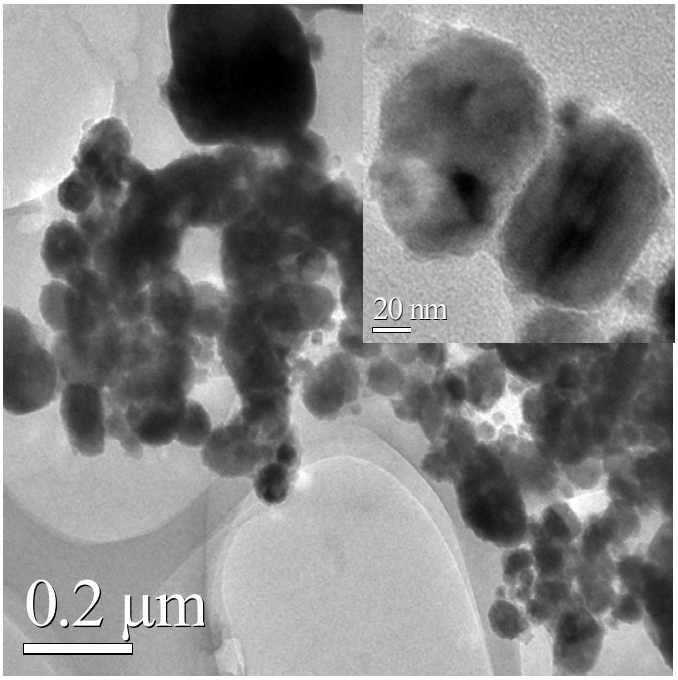

Figure 17: FTIR spectra and XRD of the $CoCa(CO_3)_2$ a) as prepared, b) catalyst before reaction and c) after reaction. Below is the TEM image of the catalyst. Inset is the magnified image of a crystalline region.

Sample	Conversion (%)	Yield (%)	
		CH_4	CO_2
$CoCa(CO_3)_2$	100	80	20
$NiCa(CO_3)_2$	81	100	0
$FeCa(CO_3)_2$	4	>99*	0
$CoNiCa(CO_3)_3$	77	100	0
$NiFeCa(CO_3)_3$	16	>99*	0
$FeCoCa(CO_3)_3$	76	>99*	0

Table 6: Product profile during the decomposition of various transition metal carbonates. The samples (50 mg) were heated at 550 ^oC for 5 h at a H_2 flow rate of 8 mL/min. *Traces of C1-C3 hydrocarbons.

The experimental conditions that gave maximum conversion and selectivity for 50 mg of $CoCa(CO_3)_2$ were employed to investigate the decomposition of other metal carbonates in H_2 and the results are given in Table 6. It clearly showed that the transition metal affects the composition of the reaction products. For example, at a flow rate of H_2 of 8 mL/min, when M=Co in $MCa(CO_3)_2$, complete conversion of carbonates occurs with 80 % selectivity for methane while, when M=Ni, we observe 80% conversion with 100 % selectivity for CH_4. Under similar conditions, Fe exhibits poor conversion as well as poor selectivity for CH_4. Nevertheless, the presence of Fe always leads to the formation of traces of higher hydrocarbons. Attempts to increase the higher hydrocarbon formation by introducing Pt or K in $FeCa(CO_3)_2$ did not show any significant results. As speculated earlier, if the reduced metal is essential in the high selectivity of CH_4, then it must be able to attain 100% selectivity for CH_4 using the decomposed remains of the transition metal carbonates which would contain reduced metal nanoparticles. Indeed, the amount of CH_4 formed was four times high in the first 2 h itself when $CoCa(CO_3)_2$ was mixed with the used sample compared to the fresh carbonate (Figure 18). Interestingly, the

presence of used sample totally removed the formation of CO_2 and also reduced the reaction temperature to 350 ^oC for complete conversion.

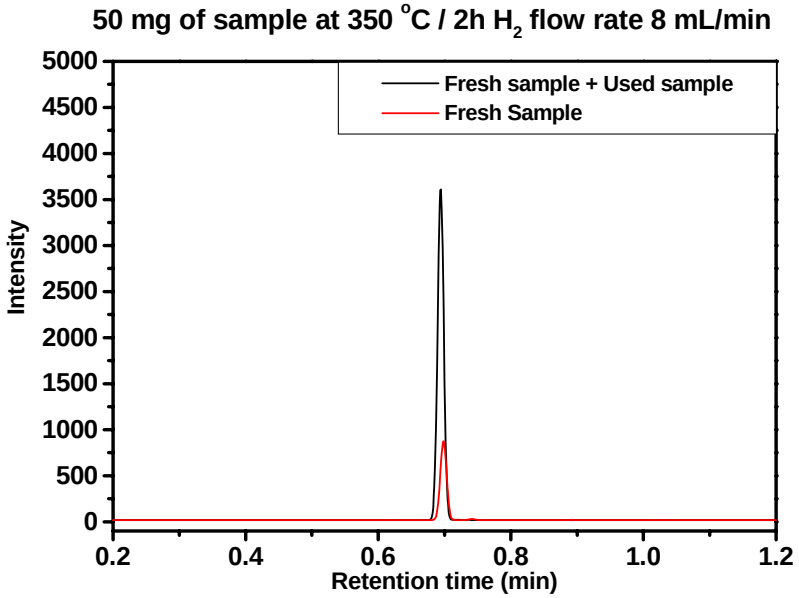

Figure 18: Enhanced formation of methane in FID signal from $CoCa(CO_3)_2$ using used sample (black trace)and without used sample (red trace) at 350 ^oC at the end of 2 h of reaction duration with H_2 flow rate of 8 mL/min.

Encouraged by the above results, we prepared catalysts by decomposing the transition metal carbonates in the presence of H_2 (see the experimental section) and tested their efficiency in the conversion of respective transition metal carbonates to methane (Figure 19) at 550 °C and at the flow rate of hydrogen 5 ml/min. All the reactions show complete selectivity for CH_4. Another notable feature is that, the initial hours of the reaction in the presence of catalyst did not produce any product (Figure 19) unlike the reaction without the catalyst (Figure 16a). Besides, the CH_4 formation reached the maximum within 2 h in presence of catalyst. This indicates a probable change in the kinetics of decomposition of carbonates in the presence of reduced metal. It could be assumed that the presence of catalyst can accelerate the decomposition of carbonates much more than without the catalyst. However, there is a possibility of adsorption of the formed

CO_2 on the surfaces of reduced metal and alkaline CaO which subsequently gets converted to CH_4.

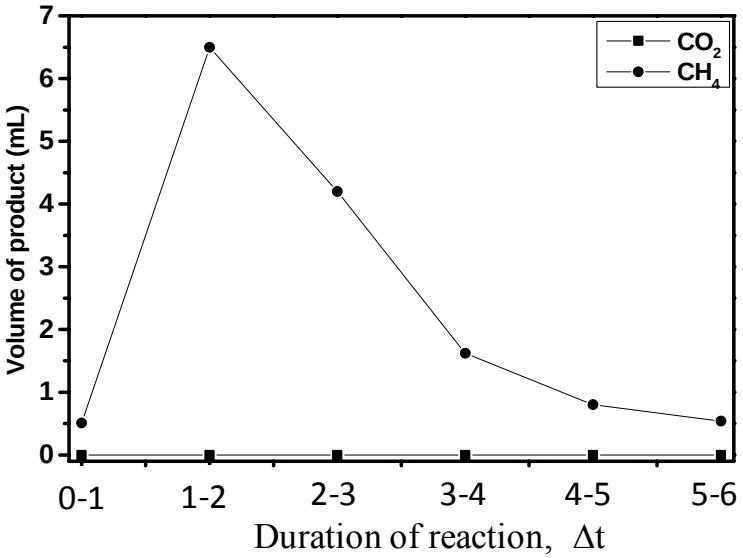

Figure 19: Time dependent product distribution of $CoCa(CO_3)_2$ in H_2 (5 mL/min) at 550 ^oC with 50 mg of catalyst Co/CoO/CaO in H_2

Sample	H_2 (mL/min)	Conversion (%)	Yield (%)	
			CH_4	CO_2
$CoCa(CO_3)_2$+Co/CaO/CoO	8	100	100	0
$CoCa(CO_3)_2$+Co/CaO/CoO	2.5	100	60	40
$CoCa(CO_3)_2$+Co/CaO/CoO	3.5	100	100	0
$NiCa(CO_3)_2$+Ni/CaO	3.5	15	100	0
$FeCa(CO_3)_2$+Fe/CaO/Fe_3O_4	8	87	70*	30
$CoNiCa(CO_3)_3$+CoNi/CaO/CoO	3.5	100	100	0
$NiFeCa(CO_3)_3$+NiFe/CaO/	3.5	64	>99*	0
$FeCoCa(CO_3)_3$+FeCo/CaO/CoO	3.5	50	>99*	0

Table 7: Decomposition of transition metal carbonates in the presence of catalysts. The samples and catalyst were mixed in 50: 50 weight ratio. The temperature of the reaction was 550 ^oC. *Traces of C1-C3 hydrocarbons.

In Table 7, the results of conversion and selectivity of reaction 2 for various carbonates are presented. A significant improvement in the H_2 efficiency was observed to obtain 100 %

selectivity for methane (in presence of catalyst 100 % selectivity for methane was obtained at 3.5 mL/min hydrogen flow rate as against 8 mL/min for the reactions without the catalyst). The results also suggest that the influence of Co in the methanation of carbonates is higher than any of the other metals or their combination. XRD and FT-IR spectra of all the carbonates before and after reaction are presented in Figure 20. XRD indicates the formation reduced metal species. Formation of metal oxide, CaO and alloy particles were also observed. In some cases, there were a few less intensity peaks which could not be ascertained. The results are tabulated in Table 8. FTIR results after the reaction show the disappearance of carbonate stretch indicating its decomposition.

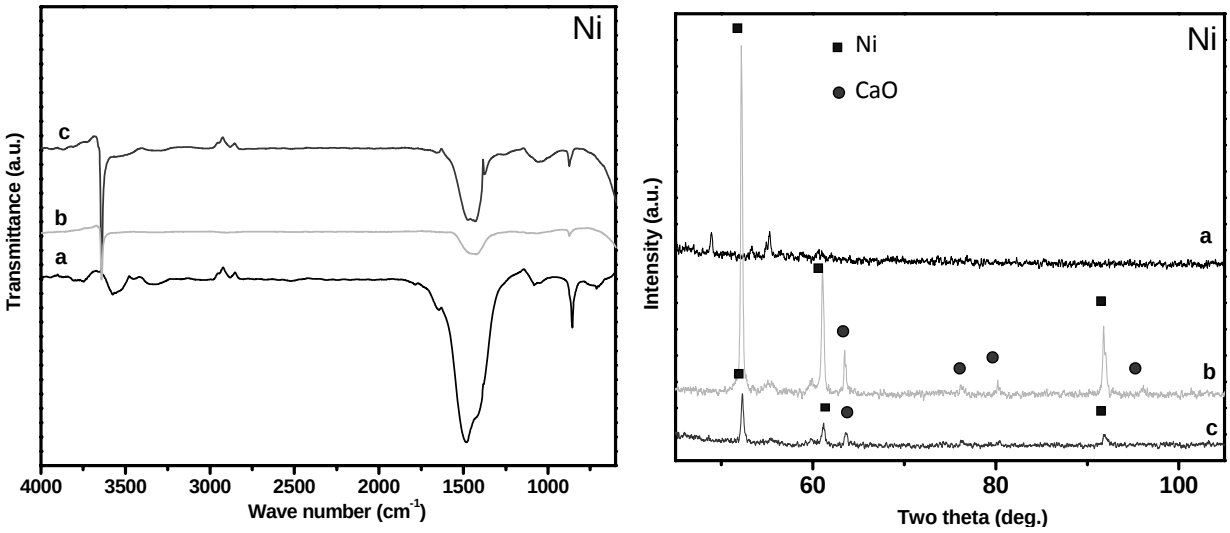

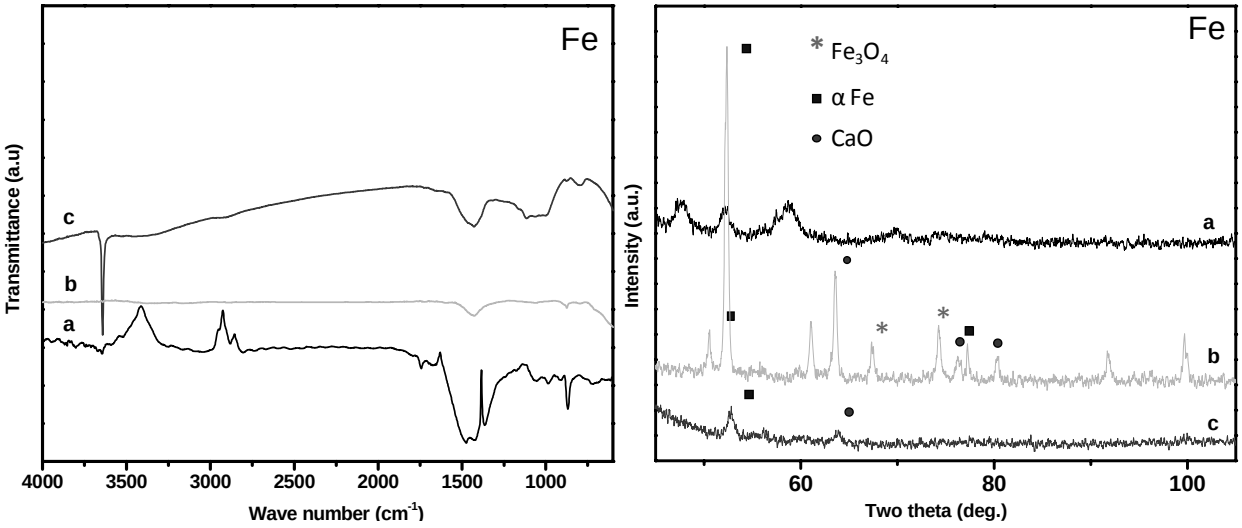
Fe
Transmittance (a.u)
Wave number (cm-1)
4000
3500
3000
2500
2000
1500
1000
a
b
c
Fe
* Fe3O4
■ α Fe
● CaO
Intensity (a.u.)
Two theta (deg.)
60
80
100

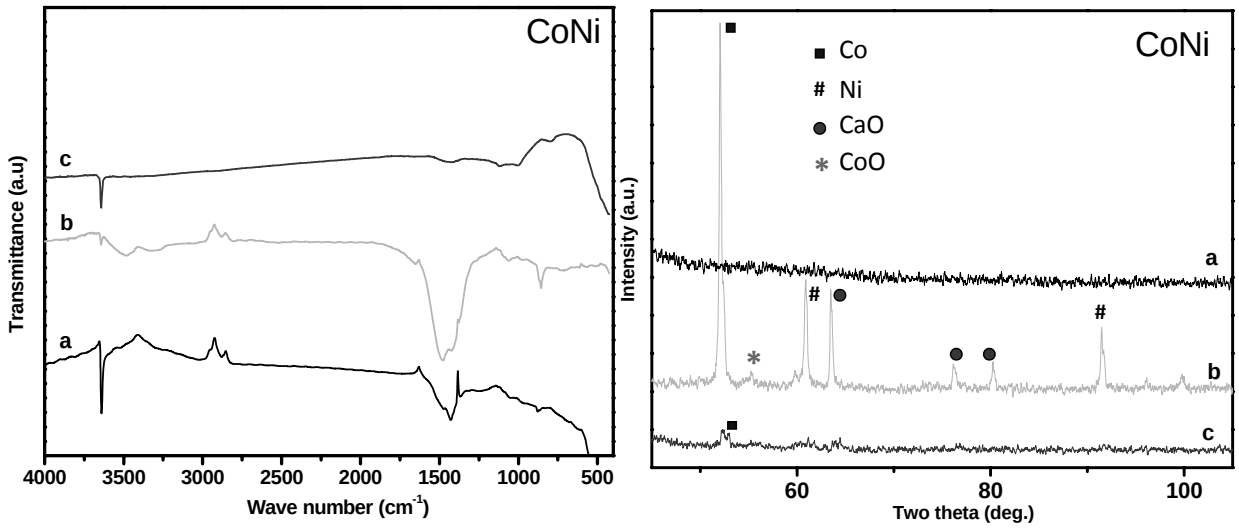
CoNi
Transmittance (a.u)
Wave number (cm-1)
4000
3500
3000
2500
2000
1500
1000
500
a
b
c
CoNi
■ Co
Ni
● CaO
* CoO
Intensity (a.u.)
Two theta (deg.)
60
80
100

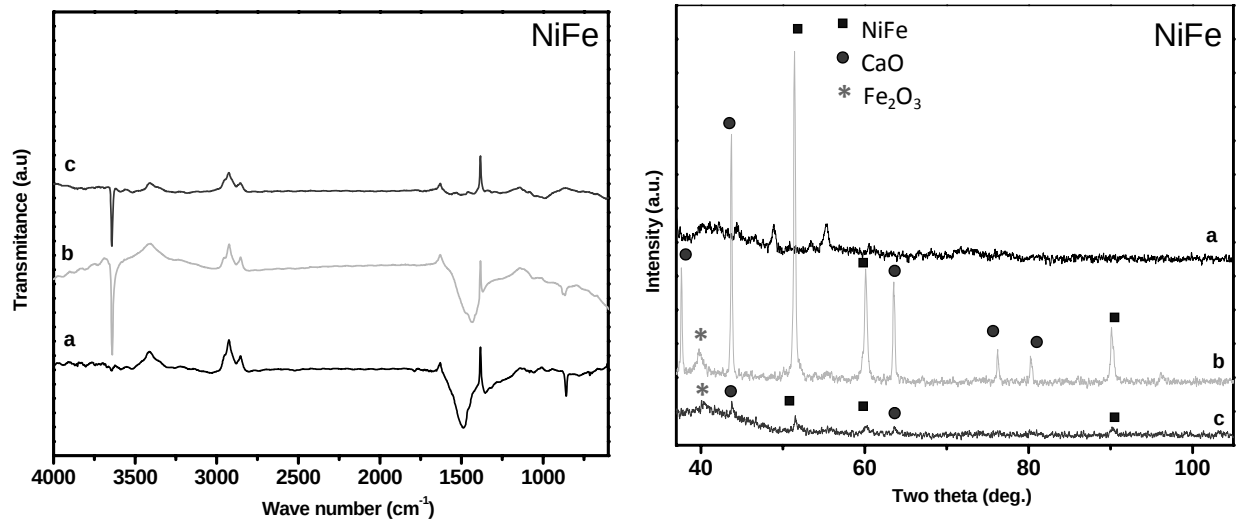
NiFe
Transmittance (a.u)
Wave number (cm-1)
4000
3500
3000
2500
2000
1500
1000
a
b
c
NiFe
■ NiFe
● CaO
* Fe2O3
Intensity (a.u.)
Two theta (deg.)
40
60
80
100

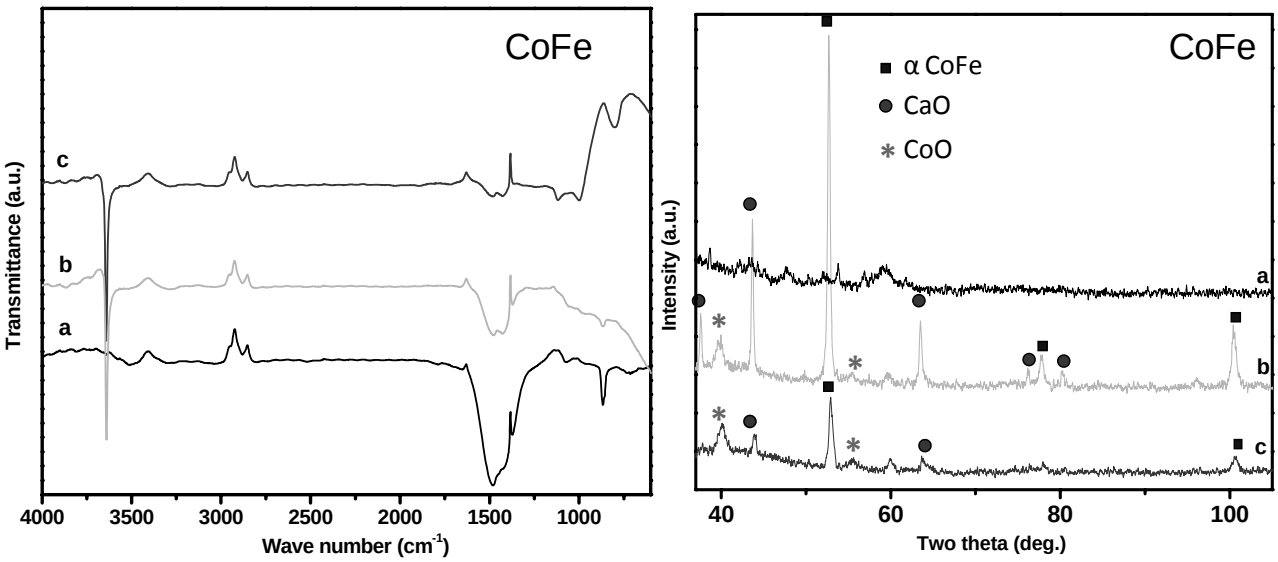

Figure 20: XRD and FT-IR spectra of all the carbonates before and after reaction. a) Freshly prepared transition metal carbonate b) catalyst before reaction, c) catalyst after reaction.

Carbonates	Phases in decomposed carbonates
$CoCa(CO_3)_2$	βCo, CoO, CaO
$NiCa(CO_3)_2$	Ni, CaO
$FeCa(CO_3)_2$	α Fe, Fe_3O_4, CaO
$CoNiCa(CO_3)_3$	Co, Ni, CaO
$NiFeCa(CO_3)_3$	NiFe, Fe_2O_3, CaO
$FeCoCa(CO_3)_3$	α CoFe, CoO, CaO

Table 8: Phases found in the catalysts as detected in XRD.

The catalysts prepared from FeCo and NiFe were found to contain alloys. The above catalysts were tested for their ability to decompose the natural minerals like calcite and dolomite. Table 9 summarizes the performance of various catalysts in the conversion of minerals such as calcium carbonates to CH_4. Complete conversion of magnesium carbonates to CH_4 was also achieved successfully.

Sample	Conversion (%)	Yield (%)	
		CH_4	CO_2
$CaCO_3$+Co/CaO/CoO	100	100	0
$CaCO_3$+Ni/CaO	80	100	0
$CaCO_3$+Fe/CaO/Fe_3O_4	18	>99*	0
$CaCO_3$+CoNi/CaO/CoO	34	65	35
$CaCO_3$+NiFe/CaO/	40	>99*	0
$CaCO_3$+CoFe/CaO/CoO	89	>99*	0

Table 9: Decomposition of calcium and magnesium carbonates in the presence of catalysts. The samples and catalyst were mixed in 50: 50 weight ratio. The temperature of the reaction was 550 ^oC at a H_2 flow rate of 3.5 mL/min. *Traces of C1-C3 hydrocarbons.

Again, the ability of the transition metals to convert calcium carbonates to gaseous products (CO_2 or CH_4) differs. For example, catalyst obtained from $FeCa(CO_3)_2$ shows only 18% $CaCO_3$ conversion with 99 % selectivity for methane. This decrease in conversion may be associated with difficulty in the reduction of $FeCa(CO_3)_2$ in presence of hydrogen at 550 °C. The catalyst obtained from $FeCa(CO_3)_2$ gave significant amount of gaseous CO_2 when heated in N_2 atmosphere at 700 °C suggesting the presence of unreduced $FeCa(CO_3)_2$. Apart from CO_2 and CH_4, no coke formation has been observed in any of these reactions as the decomposed carbonates when heated in presence of O_2 did not give CO_2 even at 550 ^oC. The FTIR studies also indicate the presence of traces of carbonates even after the reaction in case of Ni, Fe, FeNi and CoFe.

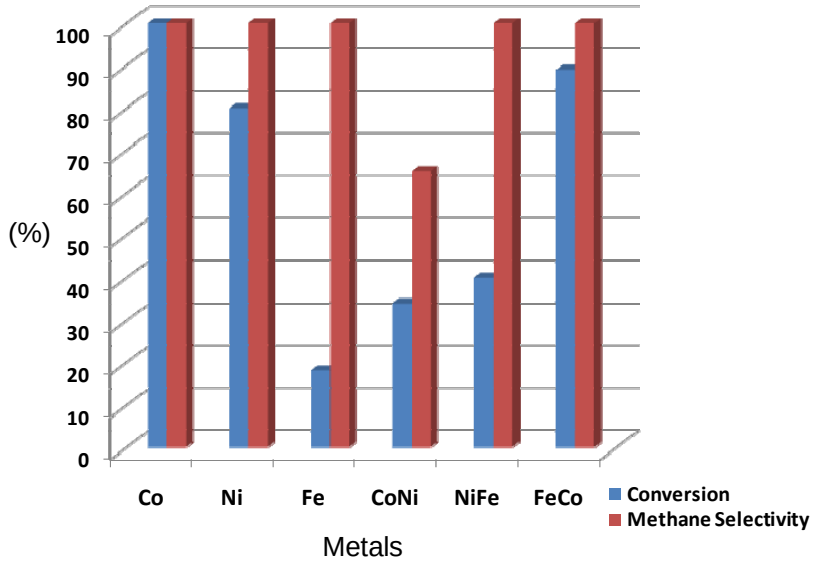

Figure 21: Effect of metal catalyst on conversion of calcium carbonate and the selectivity towards CH_4

Based on the results, following conclusions could be drawn. Most of the carbonates show an increase in the conversion of carbonates when mixed with the catalyst. However, Co and Ni show a decrease in the efficiency in the conversion of carbonates in the presence of the catalyst. Interestingly, the mixture of Co and Ni show an increased efficiency while the other metal combinations show an additive effect. Though individually Co and Ni are good in the decomposition of $CaCO_3$ (reaction 3), mixture of both found to be less active. On the other hand, Fe which is not very active by itself in catalysing reaction 3, has been found very effective in combination with Ni and more so with Co probably due to the formation of alloy. In Figure 21, we provide a graphical representation of the effect of the transition metal catalysts on the conversion of calcium carbonate and the selectivity. Under the conditions employed by us, all the transition metals show a high selectivity for CH_4. The percentage conversion however, varies in the order of Co>Ni>Fe and for the combination of transition metals, we see a trend of CoNi<NiFe<FeCo.

6.5. Conclusions:

In Summary, we have synthesized the transition metal carbonates of various compositions and studied their decomposition profiles in H_2 atmosphere. The major product is CH_4 and CO_2 without any other products like CO, H_2O or coke. The conditions were optimised to get maximum conversion and yield for CH_4. It has been proved that the decomposed remains of a transition metal carbonate can be used as catalyst for methanation of freshly prepared carbonates. This will certainly save a huge expenditure at the industrial level - not to forget the fact that the catalyst can also be recarbonized to precursor. However, the process would be economically very valuable if products like higher hydrocarbons are obtained.[36] Though there have been a number of Fe based catalysts to convert CO_2 to higher hydrocarbons, the conversions are poor. Alternatively, one can try calcium carbonates mixed with Fe and other transition metals so that the conversions are higher. However, the selectivity for higher hydrocarbons remains to be tuned in such materials.

6.6. References:

1. World Energy Council (WEC):, http://worldenegy.org/wec-geis/
2. Intergovernmental Panel on Climate Change, Fourth Assessment Report: Climate Change, **2007**; http://www.ipcc.ch/ipccreports/assessments-reports.htm.
3. International Energy Agency, World Energy Outlook **2007**-Executive Summary; Head of Communications and Information Office, France **2007**; http://www.iea.org/Textbase/npsum/WEO2007SUM.pdf
4. Crabtree, G. W.; Dresselhaus, M. S.; Buchanan, M. V. *The Hydrogen Economy*, December, **2004**.

5. *The Hydrogen Economy: Opportunities, Costs, Barriers and R&D Needs*, National Research Council and National Academy Engineering, The National Academic Press, Washington DC, **2004**.
6. Bossel, U.; Eliasson. B.; Taylor, G. *The Future of Hydrogen Economy: Bright or Bleak?*, **2003**, http://www.efcf.com/reports/
7. Olah, G. A.; Geoppert. A.; Prakash, G. K. S. Chapter 8, *Beyond oil and Gas: The Methanol Economy,* WILEY-VCH publishers, Weinheim, ISBN 3-527-31275-7, **2006.**
8. Key World Energy Statistics, International Energy Agency, **2004**.
9. A Technology Forum for Generation IV Nuclear Systems, US DOE Nuclear Energy Research Advisory Committee and the Generation IV International Forum, **2002**. http://www.gen-iv.ne.doe.gov/
10. Eckener. H. *My Zeppelins* Putnam & Co. Ltd., **1958**.
11. http://en.wikipedia.org/wiki/Three_Mile_Island_accident
12. http://en.wikipedia.org/wiki/Chernobyl_disaster
13. *The Road with Methanol: The Present and Future Benefits of Methanol Fuel*, Prepared for the Methanol Institute, **1994**.
14. Reed, T. B.; Lerner, R. M. *Science* **1973**, *182*, 1299.
15. Olah, G. A.; Geoppert. A.; Prakash, G. K. S.; Chapter 11, *Beyond oil and Gas: The Methanol economy,* WILEY-VCH publishers, Weinheim, ISBN 3-527-31275-7, **2006.**
16. US Department of Energy, Energy Efficiency and Renewable Energy.
17. Yu, K. M. K.; Curcic, I.; Gabriel. J.; Tsang, S. C. E. *ChemSusChem*, 2008, **1**, 893.
18. a) Milliward, A. R.; Yaghi, O. M. *J. Am. Chem. Soc*., **2005**, *127*, 17998. b) Raidongia, K.; Dinesh, J.; M. U-Kahalay, Waghmare, U. V.; Pati, S. K.; Eswaramoorthy, M.; Rao, C. N. R.;

J. Mater. Chem., **2008**, *18*, 83. c) Ghosh, A.; Subrahmanyam, K. S.; Saikrishna, K.; Datta, S.; Govindaraj, A.; Pati, S. K.; Rao, C. N. R. *J. Phys. Chem. C.,* **2008**, *112*, 15704.

19. Haggin, J.; *Chem. Eng. & News.,* **1994**, *72*, 29.
20. Zhao, T. S.; Han, Y. Z.; Sun, Y. H. *Fuel Process. Technol.,* **2000**, *62*, 187.
21. Lu, Y.; Jiang, Z. Y.; Xu, S. W.; Wu, H. *Catal. Today*, **2006**, *115*, 263.
22. Graf, E.; Leitner, W. *J. Chem. Soc., Chem. Commun*., **1992**, 623.
23. Sakakura, T.; Choi, J-C.; Yasuda, H. *Chem. Rev.,* **2007**, *107*, 2365.
24. Huang, W.; Xie, K-C.; Wang, J-P.; Gao, Z-H.; Yin, L-H.; Zhu, Q-M. *J. Catal.,* **2001**, *201*, 100.
25. Choudhury, V. R.; Choudhury, T. R. *Angew. Chem. Int. Ed.,* **2008**, *47*, 2.
26. Wilcox, E. M.; Roberts, G. W.; Spivey, J. W. *Catal. Today.,* **2003**, *88*, 83.
27. Barton, E. E.; Rampulla, D. M.; Bocarsly, A. B. *J. Am. Chem. Soc.,* **2008**, 130, 6342.
28. Choi, J. C.; Sakakura, T.; Sako, T.; *J. Am. Chem. Soc.,* **1999**, 121, 3793.
29. Weatherbee, G. D.; Bartholomew, C. H. *J. Catal.,* **1984**, *87*, 352.
30. Kim, J. S.; Lee, S.; Lee, S. B.; Choi, M. J.; Lee, K. W. *Catal. Today,* **2006**, *115*, 228 and referenced therein.
31. Centi, G.; Perathoner, S.; Winèab, G.; Gangeri, M. *Green Chem.,* **2007**, *9*, 671.
32. Nguyen, T. V.; Wu, J. C. S. *Appl. Catal. A: Gen.,* **2008**, *335*, 112.
33. a) Reller, A.; Padeste, C.; Hug, P. Nature, **1987**, *329*, 527. b) Padeste, C.; Reller, A.; Oswald, H. R.; *Mater. Res. Bull.,* **1990**, *25*, 1299.
34. Vidyasagar, K.; Gopalakrishnan, J.; Rao, C. N. R. *Inorg. Chem.,* **1984**, *23*, 1206.
35. Truog, E. *J. Ind. Eng. Chem.,* **1915**, *7*, 1045.

36. a) Lunsford, J. H. *Catal. Today.,* **2000**, *63*, 165 and references therein. b) Gesser, H. D.; Hunter, N. R.; Prakash, C. B. *Chem. Rev.,* **1985**, 85, 235. c) Riduan, S. N.; Zhang, Y.; Ying, J. Y.; *Angew. Chem. Int. Ed.,* **2009**, *48*, 3322.

Outlook

LIST OF PUBLICATIONS

From Thesis

1. Use of amorphous carbon nanotube brushes as templates to fabricate GaN nanotubes brushes and related materials. *J. Phys. Chem.C*, **2007**, 111 (2), 510.

2. Carbon spheres assisted synthesis of porous bioactive glass containing hydroxycarbonate apatite nanocrystals: A material with high *in vitro* bioactivity. *J.Phys. Chem.C*, **2008**, 112(19), 7379.

3. Intrinsically fluorescent carbon nanospheres as nucleus targeting vector: Delivery of membrane impermeable molecule to modulate gene expressions *in vivo*. *Nano Lett*, **2008**, 8, 10, 3182.

4. Hollow spheres to nanocups: Tuning the morphology and the magnetic properties of α-Fe_2O_3 nanostructures. *Angew. Chem. Int. Ed,* **2008**, 47, 40, 7685.

5. Investigations on the conversion of inorganic carbonates to methane. **2009** (Submitted to *ChemSusChem*).

6. Uptake mechanism of glucose derived carbon spheres by mammalian cells. **2009**. (Manuscript under preparation).

Miscellaneous

7. Synthesis, structure and properties of homogeneous BC_4N nanotube brushes. *J. Mater. Chem.* **2008**, 18, 83.

8. Construction of bi-functional inorganic-organic hybrid nanocomposites. *J. Mater. Chem.*, **2008**, 18, 5448.

9. pH sensitive breathing of clay sheets in the polymer matrix. **2009**. (Manuscript under preparation)

10. Clay templated synthesis of layered carbon and their adsorption properties. **2009**. (Manuscript under preparation)

11. Magnetic properties of non-magnetic inorganic hollow spheres. **2009**. (Manuscript under preparation).

12. Polymer induced assembly of CdS nanoparticles into nano onions. 2009. (Manuscript under preparation).

13. Nanomaterials for therapeutic drug delivery, *CRC Handbook on Nanobiomaterials,* **2009**, Taylor and Francis Publishers. (Submitted).

14. Functionalized Carbon Nanostructures: Sweeter Alternatives, **2009** (Submitted to Chemistry – An Asian Journal).

In summary glucose derived carbon nanostructures are sure to be considered as an emerging material with potential applications in many areas ranging from biology to materials synthesis. The inexpensive precursor, low temperature, green synthesis is expected to give this material an edge over many conventional carbon structures in biological applications. In general, the applications involving functionalized interfaces can use HC materials. However, there are a few areas of applications that need to be exploited namely functionalised mesostructured carbon with high surface area for adsorption properties. The surface of HC being functionalised can be expected to have preferential adsorption of solvents. However, there are also good opportunities to improve the mechanical strength of these materials. The possibility of utilising different solvent combinations can be tried in a view to obtain HC with different morphologies and surface properties. New synthetic route for multiferroic materials by utilising the reactive carbon interface is another interesting area of research. The potential of HC in biology is also yet to be fully exploited. Extending the current knowledge of HC coating would certainly evolve into a general strategy of making any inorganic material cell permeable but yet remain biocompatible and also permeable into blood brain barrier. However, it would also be worthy to study the leaching of toxic encapsulations within the carbon structures.

The final chapter involves the transition metal carbonates of various compositions and studied their decomposition profiles in H_2 atmosphere. It has been proved that the decomposed remains of a transition metal carbonate can be used as catalyst for methanation of freshly prepared carbonates. This will certainly save a huge expenditure at the industrial level - not to forget the fact that the catalyst can also be recarbonized to precursor. However, the process would be economically very valuable if products like higher hydrocarbons are obtained. Though there have been a number of Fe based catalysts to convert CO_2 to higher hydrocarbons, the conversions are poor. Alternatively, one can try calcium carbonates mixed with Fe and other transition metals so that the conversions are higher. However, the selectivity for higher hydrocarbons remains to be tuned in such materials. Another important direction in this field is to look for reactions that are in situ sources of H_2. For example, conversion of ethylbenzene to styrene can be coupled to carry out the carbonate conversion.

Appendix

List of Corrections

The following corrections were included in the thesis as suggested by the referees.

1. The list of abbreviations was replaced with a new list of alphabetically-arranged abbreviations in page XII and XIII.
2. A new paragraph was added at the end of chapter 1 to present an overview to the readers about the succeeding chapters.
3. Elemental analysis of carbon spheres was been included.
4. A one page write up on outlook of the work was included at the end of chapter 6 to discuss the future prospects of the work.